

# REPORT DOCUMENTATION PAGE

Form Approved  
OMB NO. 0704-0188

Public reporting burden for this collection of information is estimated to average 1 hour per response, including the time for reviewing instructions, searching existing data sources, gathering and maintaining the data needed, and completing and reviewing the collection of information. Send comment regarding this burden estimate or any other aspect of this collection of information, including suggestions for reducing this burden, to Washington Headquarters Services, Directorate for Information Operations and Reports, 1215 Jefferson Davis Highway, Suite 1204, Arlington, VA 22202-4302, and to the Office of Management and Budget, Paperwork Reduction Project (0704-0188), Washington, DC 20503.

1. AGENCY USE ONLY (Leave blank)		2. REPORT DATE March 1, 1996		3. REPORT TYPE AND DATES COVERED May 11, 1992 to May 10, 1995 <i>Final</i>	
4. TITLE AND SUBTITLE High Speed Integrated Light Modulators				5. FUNDING NUMBERS DAAL03-92-G-0232	
6. AUTHOR(S) F. S. A. Sandejas and D. M. Bloom					
7. PERFORMING ORGANIZATION NAME(S) AND ADDRESS(ES) Edward L. Ginzton Laboratory Stanford University Stanford, CA 94305-4085				8. PERFORMING ORGANIZATION REPORT NUMBER G. L. 5398	
9. SPONSORING / MONITORING AGENCY NAME(S) AND ADDRESS(ES) U.S. Army Research Office P.O. Box 12211 Research Triangle Park, NC 27709-2211				10. SPONSORING / MONITORING AGENCY REPORT NUMBER <i>ARO 29576-3-PH</i>	
11. SUPPLEMENTARY NOTES The views, opinions and/or findings contained in this report are those of the author(s) and should not be construed as an official Department of the Army position, policy or decision, unless so designated by other documentation.					
12a. DISTRIBUTION / AVAILABILITY STATEMENT  Approved for public release; distribution unlimited.					
13. ABSTRACT (Maximum 200 words)  This report describes the invention and development of the Grating Light Valve (GLV). The GLV is a deformable grating structure fabricated by silicon surface micromachining. It is a reflection phase grating; optical modulation is achieved by electromechanically controlling the grating amplitude. The GLV is a promising technology for spatial-light-modulators, and projection and head-mounted displays. Bistable switching of the grating at speeds as fast as 20 ns has been demonstrated. Single-pixel contrast ratios of 200:1 have been measured. The GLV is inherently capable of color selection and, with a proper optical system, produces the full NTSC color gamut. Arrays of 150-by-192 pixels have been fabricated and operated to demonstrate the GLV's potential as a color display. The device fabrication process for the GLV is simple and compatible with CMOS processing. However, the first generation GLV suffers from surface adhesion (stiction) since it contains optically-flat, compliant structures separated by sub-micron air gaps. Our second generation devices combine beam stiffening, surface modification, and novel self-aligned processes to avoid stiction and operate with high reliability.					
14. SUBJECT TERMS Color Display, Phase Grating, Silicon Micromachining, MEMS, Optical Modulator, Light Valve, Pixel, Projection, Head-Mounted Display				15. NUMBER OF PAGES 256	
				16. PRICE CODE NTIS only	
17. SECURITY CLASSIFICATION OR REPORT UNCLASSIFIED	18. SECURITY CLASSIFICATION OF THIS PAGE UNCLASSIFIED	19. SECURITY CLASSIFICATION OF ABSTRACT UNCLASSIFIED	20. LIMITATION OF ABSTRACT UL		

NSN 7540-01-280-5500

DTIC QUALITY INSPECTED 1

Standard Form 298 (Rev. 2-89)  
Prescribed by ANSI Std. Z39-18  
298-102

19960524 198

# DISCLAIMER NOTICE



**THIS DOCUMENT IS BEST QUALITY AVAILABLE. THE COPY FURNISHED TO DTIC CONTAINED A SIGNIFICANT NUMBER OF PAGES WHICH DO NOT REPRODUCE LEGIBLY.**

## Table of Contents

Abstract.....	Page 1
1. Introduction.....	Page 1
1.1 Basic Principle of the Grating Light Valve (GLV) .....	Page 1
1.2 Applications.....	Page 5
GLV as a Light Valve.....	Page 5
GLV as a Spatial Light Modulator.....	Page 5
2. Optics of the GLV .....	Page 6
Efficiency.....	Page 6
GLV Display Viewing Systems .....	Page 7
3. Beam Mechanics.....	Page 8
Other Mechanical Issues.....	Page 12
4. Process and Manufacturing.....	Page 12
4.1 Fabrication .....	Page 12
4.2 Stiction.....	Page 13
4.3 Staggered Support Structures.....	Page 15
4.4 Two-Dimensional Addressing .....	Page 17
4.5 Preliminary Development of a GLV Packaging Technology.....	Page 18
Conclusion on Process .....	Page 18
5. Conclusion.....	Page 19
Publications and Technical Reports .....	Page 21
Scientific Personnel .....	Page 21
Inventions .....	Page 21
Appendix A: Raj B. Apte, "Grating Light Valves for High Resolution Displays," Thesis (June 1994)	
Appendix B: Francisco S. A. Sandejas, "Silicon Microfabrication of Grating Light Valves," Thesis (July 1995)	

# GRATING LIGHT VALVES

## Abstract

The Grating Light Valve (GLV) is a micromechanical phase grating that can be used for black and white or color display applications. Operation is based on electrically controlling the mechanical positions of the grating elements to modulate the diffraction efficiency. Proper choice of the grating dimensions allows the structure to operate as a digital optical device.

Since the grating is inherently dispersive, the GLV can be used for color displays. In addition, the devices are bistable and may be able to operate with a passive matrix of contacts and still achieve the performance of an active matrix light valve. The fast (20 ns) switching speed of the GLV allows grayscale operation by pulsewidth modulation. The contrast ratio of the device is sensitive to processing; a contrast ratio of 200:1 has been measured for a monochrome pixel illuminated by a HeNe source.

Sticking of the micromachined grating elements to the substrate during the final wet processing step and during operation remains a problem. However, our current approach uses rough (150 Å-RMS) polysilicon films to reduce the area of contact. When doped, the polysilicon can be patterned to function as a bottom electrode for two-dimensional array applications. Although this structure suffers from the difficulties associated with non-planar processing, it was used to demonstrate two-dimensional arrays with switching voltages as low as 11V.

## 1. Introduction

### 1.1 Basic Principle of the Grating Light Valve (GLV)

The GLV is a microelectromechanical light valve. Particularly, it is a programmable mechanical reflection phase grating. The GLV modulates light by electrostatically adjusting the grating amplitude of the phase grating. Photo 1 is a scanning electron microscope (SEM) photograph of an actual GLV pixel. This particular pixel consists of 12 nitride beams stretched across a nitride frame. The beams are 25  $\mu\text{m}$  long, 1  $\mu\text{m}$  wide, and spaced with a 2.25  $\mu\text{m}$  period. The frames are 2.5  $\mu\text{m}$  wide.



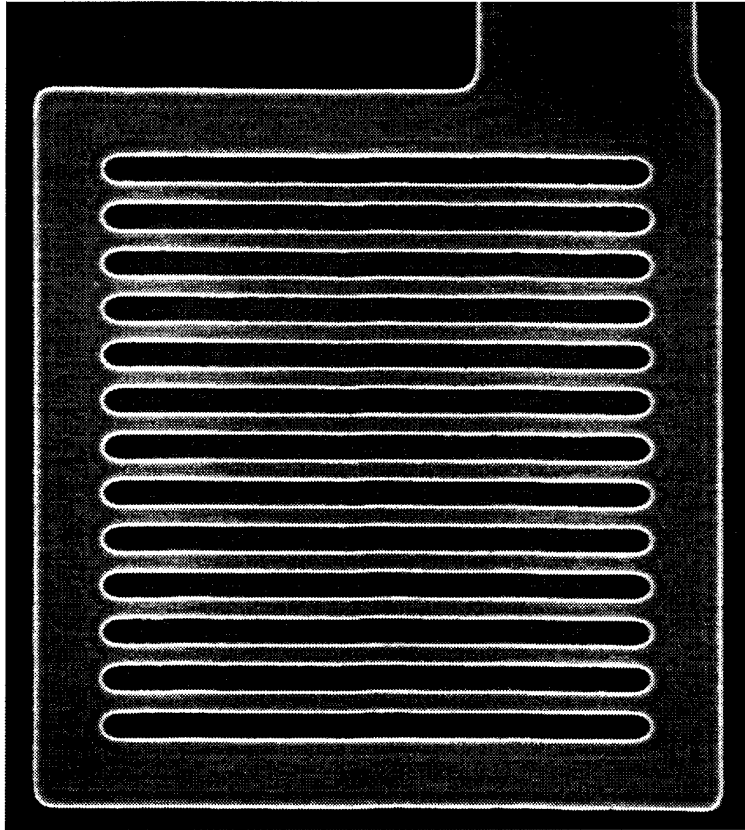
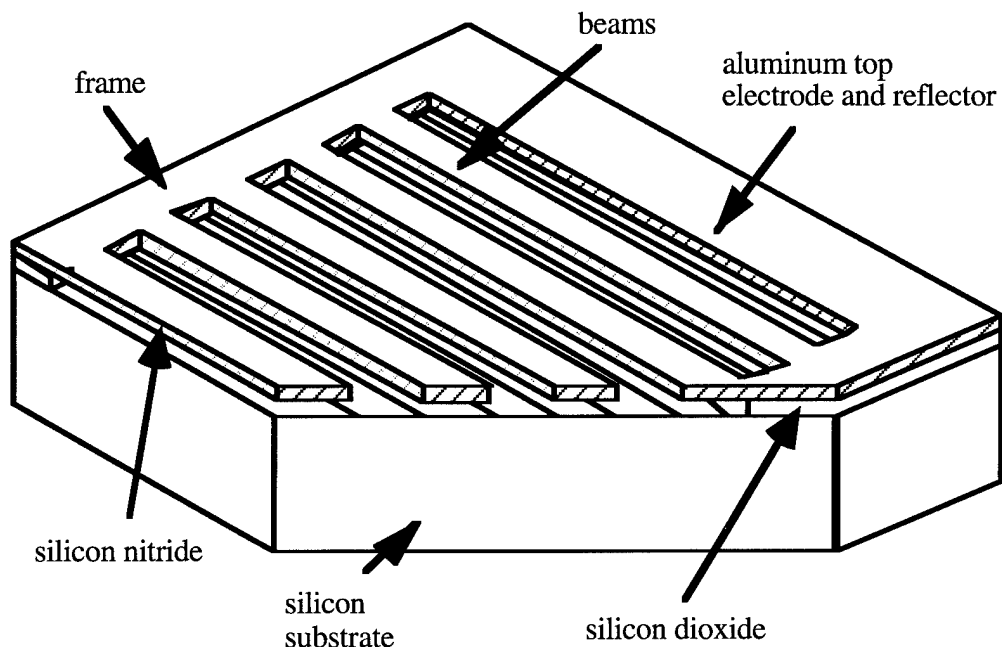


**Photo 1.** SEM of a GLV pixel with beams that are 25  $\mu\text{m}$  long, 1  $\mu\text{m}$  wide, and spaced with a 2.25  $\mu\text{m}$  period.

Figure 1 is a representation of the GLV with a portion of one corner cut out to show the different underlying layers. For ease of illustration, the picture is exaggerated in the vertical dimension and only four grating beam elements are drawn. We describe the drawing starting from the bottom. A silicon substrate supports the whole structure. On top of the substrate, a 132 nm thick oxide layer forms an O-ring that supports the nitride frame. Spanning the length of the nitride frame are the 132 nm thick. A thin aluminum layer is evaporated on top of all the vertically exposed surfaces, i.e. on the beams and on the surfaces of the spaces between the beams. This serves as a reflection layer and also as the top and bottom electrodes. There is no oxide underneath the beam area, so if a cross-section is taken along the length of the pixel then the picture will look like Fig. 2. The beams form microbridges supported and raised above the substrate by the oxide at their ends. Tension in the nitride film keeps the beam from collapsing into the substrate area. Figure 2b demonstrates what happens if a voltage is applied between the top electrode and the substrate electrode. The electrostatic load pulls the beams to the substrate. If the force is removed then the tension in the beams will provide a restoring force that pulls them back up.



#### LEGEND

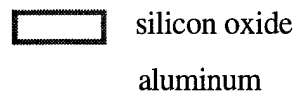
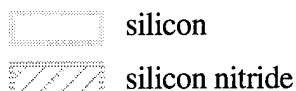
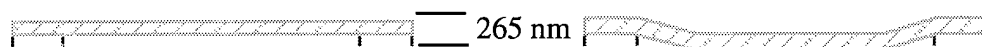


**Figure 1.** Illustration of an aerial view of a Grating Light Valve pixel with a corner cut-out to expose its underlying elements.



(a) Beams held up  
by tensile stress.

(b) Beams pulled down  
electrostatically.

**Figure 2.** Cross-sectional cut along the length of a GLV beam structure. On the left, the beam is up; on the right, down.

Silicon micromachining is the technology that has enabled the fabrication of such a grating structure. The manufacturing process for the GLV will be discussed later. For now, we will assume that such a micromechanical device can be made and will perform as described above.

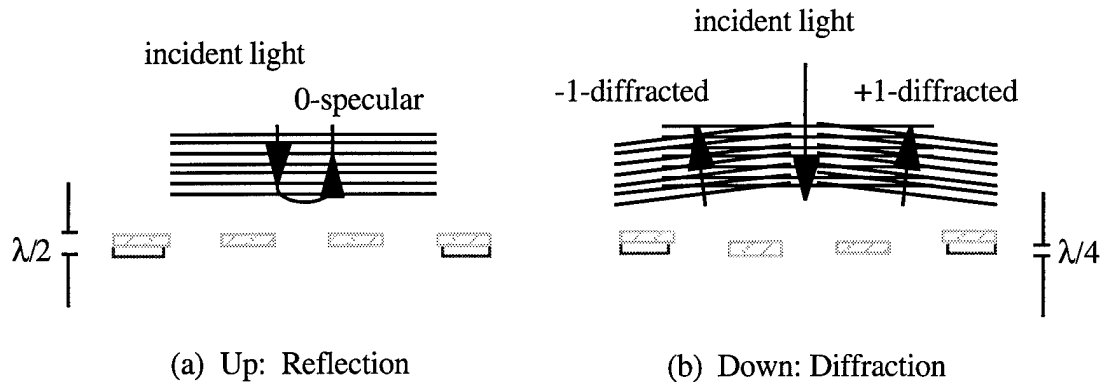


**Figure 3.** Cross-section perpendicular to the length of a GLV pixel. The device forms a reflection phase grating with two sets of diffraction elements, one of which is movable allowing control of the grating amplitude. In (a) the beams are up and the GLV reflects light; while in (b) the beams are down and diffract the light.

Typical thicknesses of the air gap and the nitride beams are 132 nm, which corresponds to a quarter wavelength of green light. The mechanical deflection of the beam is also equal to this quarter-wave distance. This tiny mechanical motion allows the grating to modulate reflected light. Taking a cross-section perpendicular to the length of the beam reveals a picture as in Fig. 3. The left side corresponds to the up-state and the right side corresponds to the down-state. Optically, the structure is a reflection phase grating with a grating amplitude that can be controlled via the electromechanical motion of the beams. The grating amplitude is defined as the height difference between the two sets of diffraction elements. The GLV's two sets of diffraction elements are the tops of the beams and the reflective metal in the spaces between the beams. A very simple way of analyzing this diffraction case starts by considering a source of monochromatic light normally incident on the GLV pixel. With no voltage applied between the bridges and the substrate, the grating amplitude is one half of the wavelength of the incoming light. Since the round-trip path difference between the light reflected from the top and bottom of the grating is one wavelength, the reflected light adds in-phase and constructive interference occurs. The grating acts like a flat mirror. However, when a voltage is applied between the bridges and the substrate, the electrostatic force pulls the bridges down. The grating amplitude is now one quarter of the wavelength, the round-trip path difference is half a wavelength, and diffraction from the bridges and the substrate add destructively. Light power is not sent into the specular direction but is instead diffracted into the odd diffraction modes. If the detection system for the reflected light has a numerical aperture which accepts only the zero-order light, a mechanical motion of only one quarter of a wavelength is sufficient to modulate the reflected light with high

contrast. This is the most basic way of analyzing the diffraction condition for the grating light valve.

## **1.2 Applications**

### **GLV as a Light Valve**

As a light valve, the GLV offers a number of attractive features. The obvious distinction is that it is a silicon micromachined device that is simple to fabricate. It can be made cheaply and integrated with CMOS circuitry. Mechanically, the device is fast and bistable; we have demonstrated high-speed switching as fast as 20 ns and have also demonstrated hysteretic behavior. This type of latching behavior simplifies system integration and possible drive circuitry since active transistors will not be necessary to maintain either the on or off states. Depending on the device geometry and material properties, the voltage levels required to switch the GLV range from 5 to 30 V, well within the range of display drivers today. Finally, the optical device is polarization insensitive, efficient, capable of high-brightness levels, and gives contrast ratios of up to 350:1 using laser illumination.

### **GLV as a Spatial Light Modulator**

There are also large-array applications for the grating light valve. Single columns of the GLV can be used in printers. GLV-based two-dimensional spatial light modulators (SLM's) can be used for optical computing or display applications. The display application area became a major focus of this research effort.

Beyond the strong points of the GLV as an individual light valve, it possesses attractive features for display systems. The grating device is inherently color dispersive and has demonstrated a full-NTSC color gamut without the use of color filters. Its bistability could enable a high-image-quality GLV display without active matrix addressing; while, the short switching times will allow 8 bits of gray-scale with time-division multiplexing schemes. Since it is efficient and reflective, the GLV can tolerate very high optical power levels, leading to brighter projection systems. Finally, high-density arrays of these valves can be fabricated using existing silicon technology.

## 2. Optics of the GLV

Regardless of the intended application of a particular light valve, a high contrast ratio and an efficient optical throughput are always desired. Contrast ratio is defined as the difference between the bright and dark-state luminance divided by the luminance of the pixel in its dark-state. For displays this is often considered as the most important visual characteristic. For power, brightness, and thermal issues, optical efficiency is also a strong concern. Optical efficiency is defined as the luminance of useful light out divided by the luminance of light used to illuminate a device. In the case of the GLV, this is mainly determined by the diffraction efficiency of the grating.

We have developed analytical expressions for the optical intensity as a function of diffracted angle, grating height, and duty cycle. Experimentally measured diffraction intensities as a function of grating height behaved as predicted. This is important for the analysis of contrast and underlines the importance of process control on grating height. Contrast for a monochromatic laser source on single GLV device has been measured up to 350:1 by properly biasing a dynamic (i.e. movable) GLV device at the proper grating heights. Limiting factors to achieving high contrast for a single pixel are errors in the grating height, the extraneous diffraction effects from neighboring pixels, and scattering from imperfect GLV side-walls.

Black/White or Color contrast are limited by the fact that a finite spectral bandwidth is used and therefore not all light spectra can be nulled. Nevertheless, since the visible spectra is quite narrow, a color pixel is still expected to demonstrate a black and white contrast ratio of 19:1. These color pixels consist of red, green, and blue pitched gratings at only one set of heights optimized for the green.

### Efficiency

Diffraction efficiency was analyzed as a function of the duty-cycle. It was found that if the geometric duty-cycle of the lines and spaces for the GLV was not 50% then some light was lost to even order diffraction modes. Other aspects that will affect the diffraction efficiency are the finite active area of an actual deformable grating. Part of the GLV beams' active length is lost to the immobile supporting frame and to the bent portion of the beam as it comes down to touch the substrate. Thickness errors and optical absorption by the metal layers can adversely affect performance. Shadowing at the edges of a microbridge can effectively superimpose an amplitude grating structure over the

intrinsic phase grating to reduce optical throughput and must be analyzed in the future. Should finer lithographic techniques become available to the GLV process engineer the possibility of blazing the beam elements to a preferred diffraction angle might be pursued as well.

### GLV Display Viewing Systems

Since a grating is a naturally color dispersive device, the GLV can be used as the basis for a color display device without the need for color filters. This is illustrated in Fig 4. A white light source incident on GLV's of three different grating pitches ( $d_{red}$ ,  $d_{green}$ , and  $d_{blue}$ ) will have its component spectral colors diffracted into different angles dependent on the Bragg condition. Thus, if one wants red, green, and blue spectra to diffract into the same angular direction, then defining three GLV grating pitches according to the Bragg condition will provide a color RGB pixel. Placing a spatial filter a focal length away from an intermediate imaging lens will provide color selectivity.

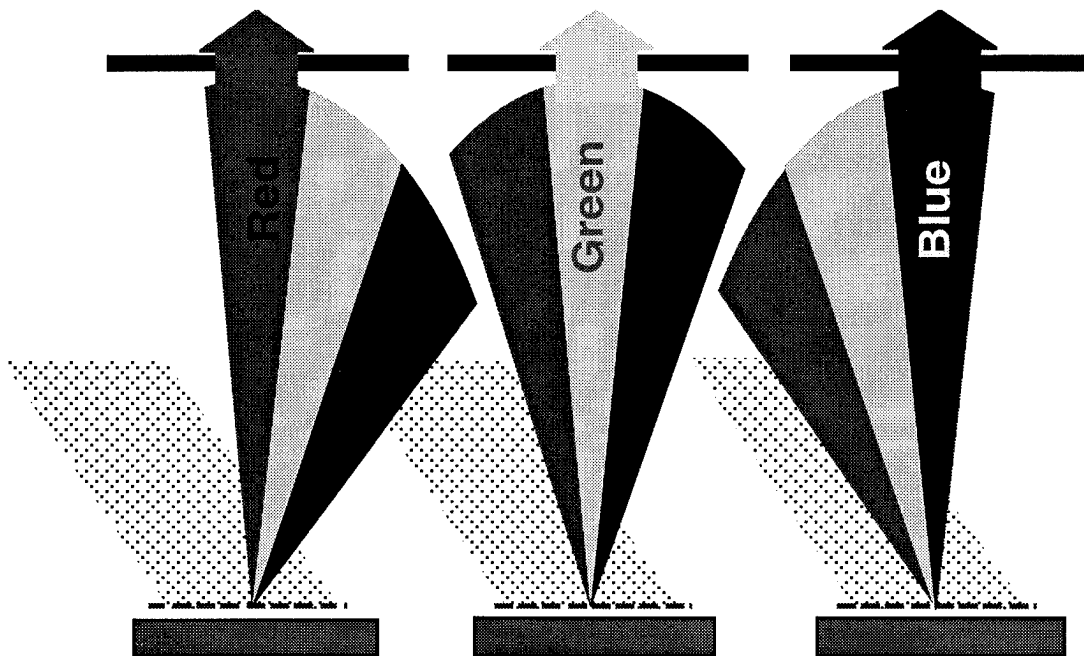


**Figure 4.** Illustration of the application of the GLV to a RGB color pixel element.

For display applications, two simple optical viewing systems are presented in Fig. 5 to illustrate the possible uses of the GLV in heads-up and projection color display systems. System (a) presents an exit pupil to the viewer's eye while system (b) images a

GLV color display to a screen.

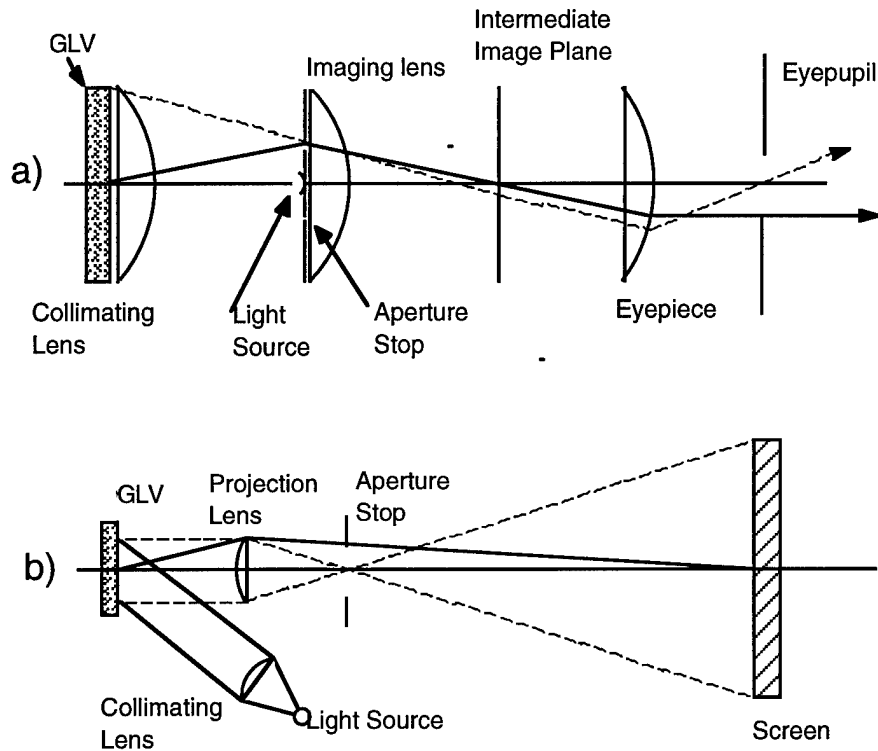


**Figure 5.** Two simple GLV viewing systems. (a) presents an exit pupil to the viewer's eye. (b) images a GLV color display to a screen.

### 3. Beam Mechanics

The GLV mechanical grating elements are doubly-clamped microbridges that are actuated by an electrostatic capacitive force. The beams can be simply modeled as strings with a restoring spring force. The voltages required to switch the beams into contact with the substrate depend on the square-root of the tension and on the inverse of the beam length. Switching speed has the same dependence on tension and beam length, and so there is a trade-off between speed and low-voltage operation. Hysteretic switching has been demonstrated for single pixels. Finally, ringing and its relation to air damping has been observed. Topics not discussed but covered in Apte's or Solgaard's theses are the issues of peak stresses, yield strength, and temperature limits.

The most striking feature of the mechanical operation of the GLV is the hysteresis of the deflection of the microbridges as a function of applied voltage. The reason for the hysteresis is that the electrostatic attraction between the top and bottom electrodes is a

nonlinear function of the deflection while the restoring force caused by the stiffness and tension is linear, as illustrated . 6..

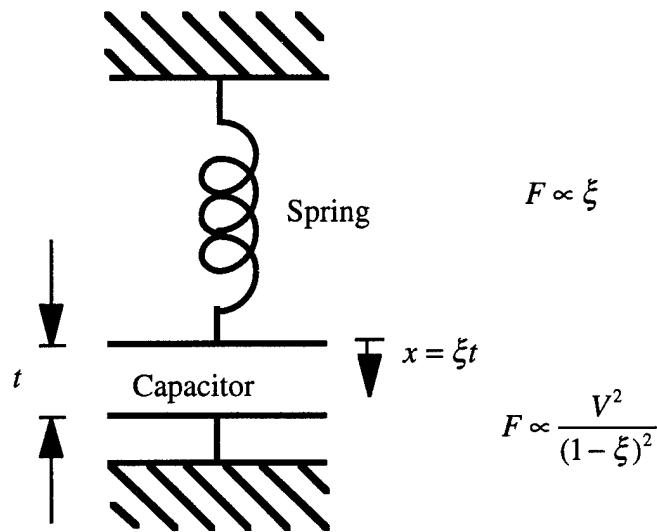


**Figure 6.** The basic model for the GLV beam mechanics. The spring represents the restoring force caused by both beam stiffness and tension. The capacitor represents the electrostatic attraction between the electrodes.

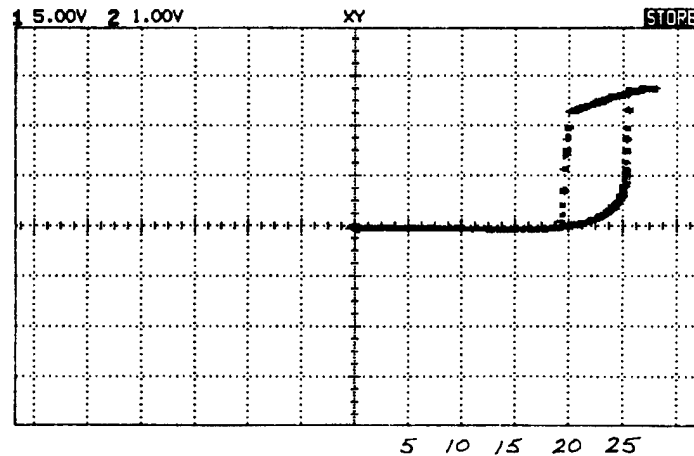


**Figure 7:** GLV optical hysteresis. Plot of optical power in the first diffraction order as voltage is swept from the 0 to 25 V and back to 0V. Horizontal scale is 5V/div.

The hysteresis curve for a single pixel is shown in Fig. 7. To generate this curve, the light diffracted into the +first-order was measured as a function of applied voltage. The switching voltage is approximately 20V and is largely determined by the stress in the nitride microbridge as well as its length.



As the voltage is increased above 20 V, the microbeams start to deflect, causing light to be diffracted into the first orders. At 25 V, the switching point is reached and the beams snap down to the substrate. As the voltage is reduced from above 25 V to 20 V, the beams remain in contact with the substrate but are starting to peel away. Below 20 V, the first instability point, the spring force now overcomes the voltage force and the microbridges spring back up to the undeflected state.

Figure 8 illustrates the hysteretic switching of the GLV. To operate this device digitally, a dc bias of 22.5 volts is applied with a positive or negative-going pulse superimposed on the dc bias. The bias keeps the GLV in the middle of the hysteresis curve of figure 7. A positive-going pulse can bring the voltage level beyond the switching voltage and snap the beams down (GLV light is on), while a negative going pulse will bring the voltage level below the first instability point and allow the beams to come back up (GLV light is off). The top trace of figure 8 is the GLV optical output in the first diffraction order (1 V/div). The bottom trace shows the voltage pulse superimposed on a dc bias level to switch the GLV on and then off (5 V/div). The horizontal scale is 200 ns/div. Since the response time is 30 ns, there was no problem switching the devices at frequencies up to 1 MHz. At higher frequencies, ringing was observed in the output wave form due to insufficient air dampening.

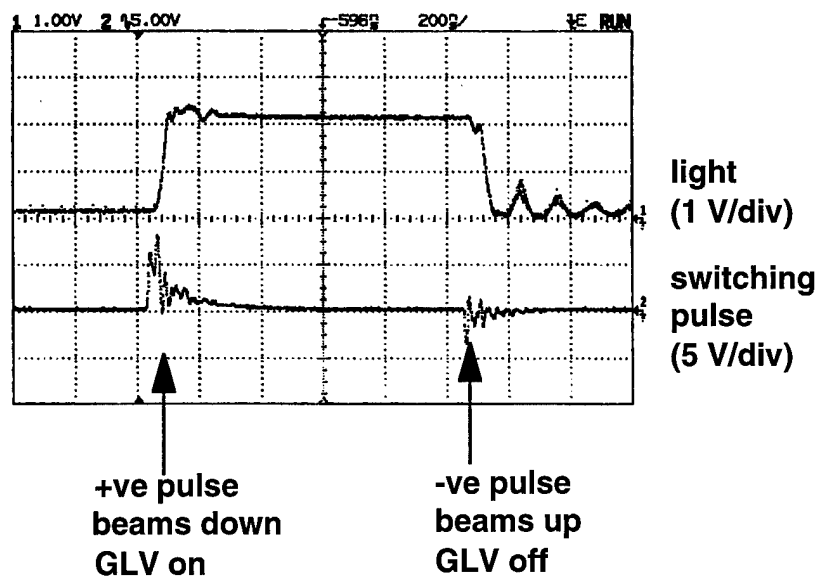


**Figure 8.** GLV hysteretic switching. The top trace is the GLV optical output in the first diffraction order (1 V/div). The bottom trace is the voltage pulse superimposed on a dc bias level to switch the GLV (5 V/div). Horizontal scale is 200 ns/div.

Figure 9 illustrates the trend in switching voltages for two different length pixels versus film stress. Low switching voltages (5V range) are possible with 25  $\mu\text{m}$  long microbridges but at the expense of the restoring force used to overcome stiction.

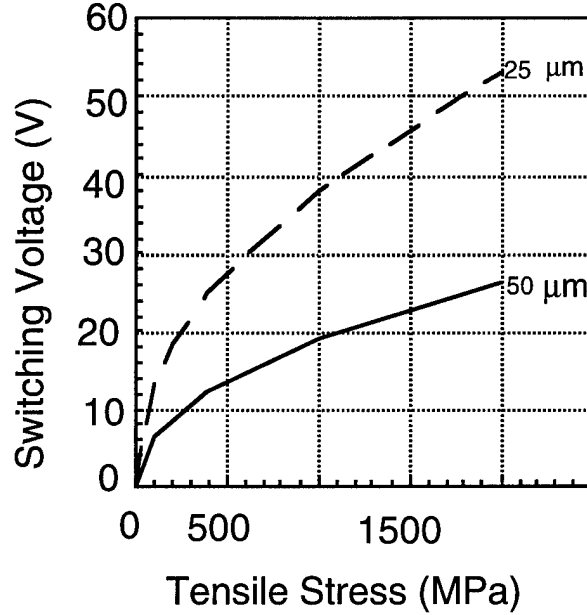


Figure 9. Switching voltage versus tension for 25 $\mu\text{m}$  and 50 $\mu\text{m}$  long microbridges.

The other mechanical property of importance is the resonant frequency of the microbridge. When under tensile stress,<sup>4</sup>

$$f_{res}^{stress} = \frac{1}{2\pi L} \sqrt{10 \frac{\sigma}{\rho}} \quad (1)$$

where  $\rho$  is the density of the silicon nitride (2.1 g/cm<sup>3</sup>),  $\sigma$  is the stress, and  $L$  is the length. This can be compared to the resonant frequency under low or no stress,

$$f_{res}^{nonstress} = \frac{h}{2\pi L^2} \sqrt{10 \frac{E}{\rho}} \quad (2)$$

where  $E$  is Young's modulus (1.2E5 MPa for stoichiometric nitride) and  $h$  is the microbridge thickness ( $h=\lambda_c/4=1325\text{\AA}$ ). The ratio of these two resonant frequencies is

$$\frac{f_{res}^{stress}}{f_{res}^{nonstress}} = \frac{L}{h} \sqrt{\frac{\sigma}{E}} \quad (3)$$

For example, with a stress of  $\sigma = 200$  MPa and a microbridge length of 25  $\mu\text{m}$ , the resonant frequency increases by a factor of 8 over the nonstressed case to a value of 6

MHz. This fast response is important to the operation of the GLV since grayscale operation can be implemented by pulsewidth modulation, i.e. digitally. However, from the preceding discussion, we note that there is a tradeoff between switching voltage and stress: the devices with the highest stress will be the fastest but will also have the largest switching voltages. Our fastest measured switching time to date has been 20ns for pixels with 20  $\mu\text{m}$  long microbridges under 800 MPa of tension.

### **Other Pending Mechanical Issues**

One question will be repeatability and uniformity of the hysteretic curve, not only from one process run to another but even within one wafer area if the device is to be used in a display system. This curve will be used to derive important design parameters for display circuit drivers.

Another important area is that of reliability and long term fatigue of these micromechanical devices. Thin films such as those used for GLV mechanics have not been fully tested for their mechanical properties especially for issues like stress fracture, yield strength, and crack propagation.

## **4. Process and Manufacturing**

### **4.1 Fabrication**

Fabrication of the device illustrated in Fig. 1 began with the deposition of 1325 Å of silicon dioxide followed by 1325 Å of silicon nitride on a silicon wafer. After the nitride was patterned to form the frame and microbridges of the device, an isotropic, selective etch was used to undercut the oxide from beneath the microbridges. In order to free the microbridges, at least 0.75  $\mu\text{m}$  of undercut was needed. This is not enough, however, to completely remove the oxide from beneath the frame. In this way the frame remained supported by the oxide, and the microbridges were supported by the frame. Finally, 400 Å of aluminum was evaporated onto the top of the structure to simultaneously form the top electrode and reflector. These devices suffered from the effects of stiction when released and operated, unless short (15 $\mu\text{m}$ ) microbridges and high tension nitride were used, requiring drive voltages as high as 40V.

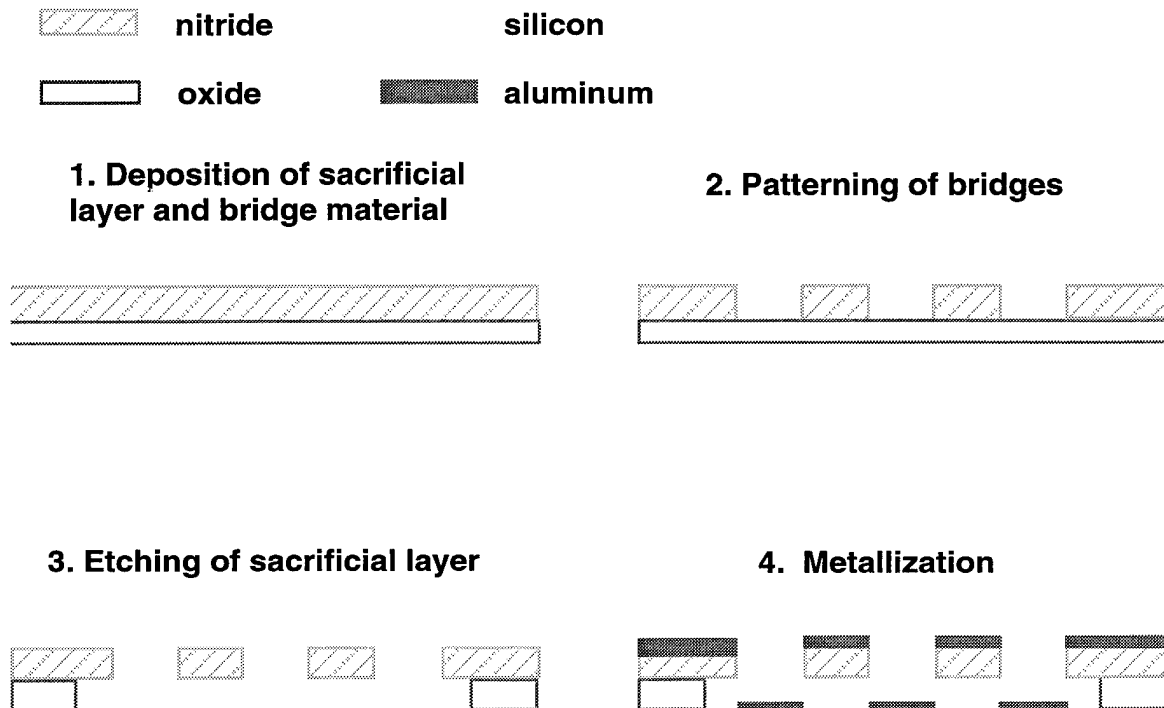


**Figure 10.** Simplest fabrication process of a single GLV pixel with one masking step.

## 4.2 Stiction

We have reviewed the problem of stiction in MEMS devices, identified and modeled various adhesion mechanisms. Like many other MEMS devices, the GLV suffers from hydrogen bonding through liquid bridging and hydroxyl groups. Packaging devices in a dry environment is important to lower the adhesion energy level from the liquid bridging case to the exclusively -OH-based hydrogen bonding case.

The fundamental physical limits to the adhesion problem were determined and for severe stiction problems, as found in the GLV device, engineering solutions are necessary. To lower the effect of the basic adhesion force one can resort to microscopic surface roughening, as with an LPCVD silicon roughening layer. With the optical constraint of a maximum rms roughness of 5 nm, this method was able to reduce the adhesion energy per unit area by at least five times the normal value. Adhesion energies of 10-20 mJ/m<sup>2</sup> were measured for roughened beams.

Further anti-stiction help is provided by macroscopic surface patterning to provide discrete contact points between two surfaces. Table 1 summarizes the results of the various engineering approaches to the stiction problem. The goal was to integrate into the GLV fabrication process a method for the formation of stand-off supports that could reduce the area of contact, avoid shorting, and maintain smooth, optically flat top surfaces.

Process Technique	Mask Steps	Self-Aligned?	Area Reduction	Problems?
Striations	2	No	20 %	Not Flat
Side-Wall Rails	1	Yes	> 90 %	Height Control
T-Structures	1	Yes	> 90 %	Tilting, Shorting
Staggered Si	2	Yes	> 90 %	NONE

**Table 1.** Summary of the engineering approaches to reducing area of surface contact between two contacting, optically-flat surfaces.

Other techniques can be useful for MEMS devices but suffer particular disadvantages that make them incompatible for GLV use. Striation requires an additional masking step, is not self-aligned, provides a limited capacity to reduce contact area, and is not optically flat. Side-wall rails are attractive since they can provide very minimal contact area (demonstrated 98% reduction); they are self-aligned and maintain optical flatness. The drawbacks of this process are that it is hard to control rail dimensions and grating heights; furthermore, it suffers a shorting problem. The T-structure process is almost ideal in that it is a self-aligned, one-mask procedure that can provide more than 90% reduction in surface contact area while still maintaining optical flatness and grating height control. In addition to this, the T-structure process allows the use of a roughening polysilicon layer for the contact areas. Its only problems are tilting and shorting.

The best method of engineering around the adhesion problem is the silicon staggered support structure technique. It has all the advantages of the T-structures, and by adding a non-critical masking step it avoids a tilting and shorting problem. This is the recommended approach to GLV fabrication. In the final integrated GLV process, an insulating layer will be included between the beam and the substrate to prevent shorting as they come in contact, and this might later make the T-structure process more competitive.

### 4.3 Staggered Support Structures

Figure 11 is a schematic that explains the more successful engineering solution, the staggered polysilicon supports. It is a ground view looking up at the bottom of the grating beams. For illustrative purposes the other support end of the beams and the silicon substrate have been cut from the picture. The beams in this case look like diving boards that have support structures protruding from underneath them. These supports are close to the edges and are positioned alternately on the left and the right. This provides support on both edges of the beam and prevents tilting.

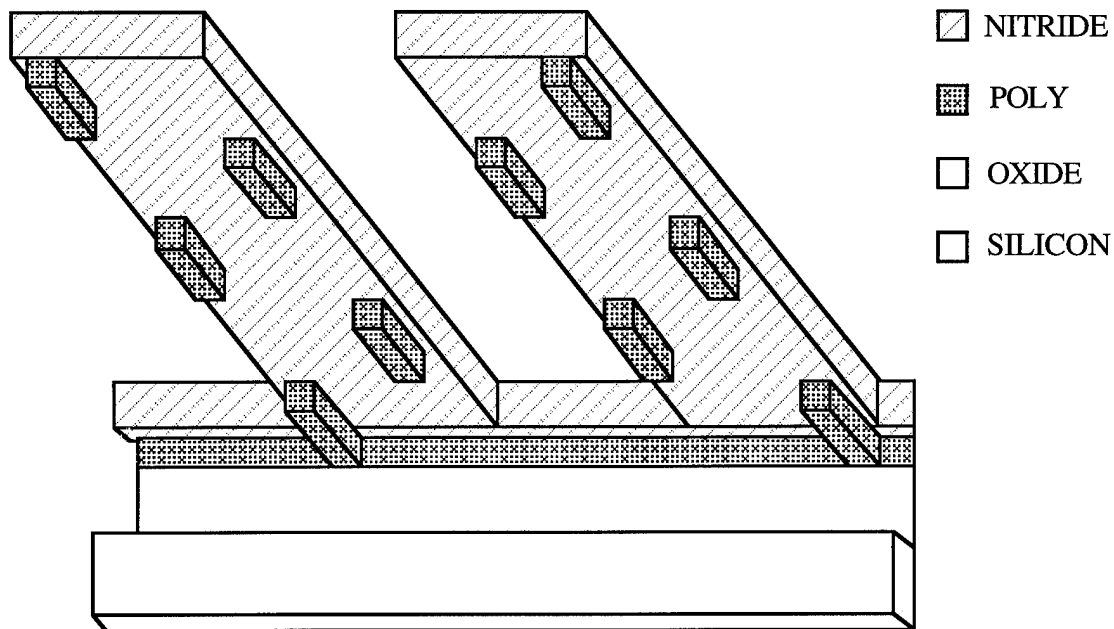
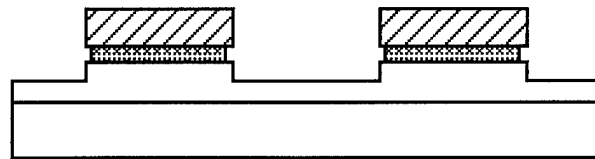


**Figure 11.** Ground view of the bottom of grating beams that have staggered polysilicon support structures at the edges of both sides of the beams.

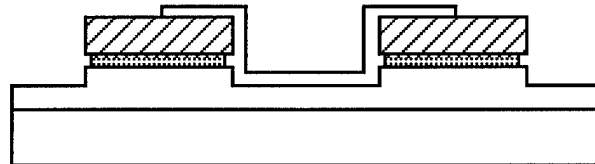
The process for the staggered polysilicon support structures is explained in Fig. 12. The process is identical to our standard process up to the point where the nitride, polysilicon (extra layer added), and oxide are patterned. The oxide layer is only partially etched. Then the polysilicon is etched for one minute in 50°C KOH to undercut the nitride layer by about 0.1  $\mu\text{m}$  on both sides. The cross-section of the beam at this point will look like the top picture in Fig. 12. This break in the step minimizes the shorting of the aluminum layers evaporated later on. After this first polysilicon etch, a 50 nm low temperature silicon oxide (LTO) layer is deposited in an LPCVD furnace. This oxide layer is photolithographically masked and etched in a 6:1 buffered oxide etch for 15 seconds to define a mask for the second KOH etch (see second cross-section in Fig. 12).

From a top-view this mask produces a checkerboard pattern. Rectangular open areas in the pattern are via holes in the oxide mask and will only allow the KOH to attack the polysilicon from alternating sides at different length segments along the beam. This second KOH etch is done in identical conditions as the first, however, the timing is based on the goal of leaving behind a few tenths of a micron of the polysilicon to act as a support structure for the beam when it comes into contact with the substrate. Finally, the whole wafer is placed in 6:1 BOE for about 6 minutes to remove the LTO mask and to release the GLV beams.

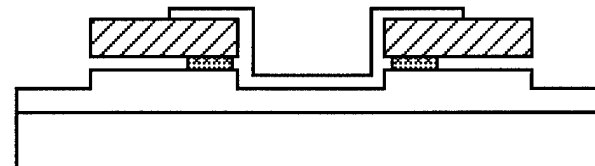
1. Pattern gratings, etching deposited layers.
2. KOH partial undercut of poly layer.



3. Deposit and pattern checkerboard oxide mask.



4. KOH undercut etch from selected sides.



5. BOE release.

**Figure 12.** Process flow for fabricating staggered polysilicon supports under GLV beams.

This process was tested on three different 4-inch  $\langle 100 \rangle$  wafers with identical steps except for the second KOH etch where three wafers were etched for 5, 6, and 7 minutes, respectively. The thermal oxide was 133 nm. The polysilicon layer was about 50 nm, while the nitride thickness was 83 nm. On each wafer, we formed harp structures with beam widths ranging from 1.0  $\mu\text{m}$  to 1.75  $\mu\text{m}$  in steps of 0.25  $\mu\text{m}$ . The polysilicon supports were staggered along the beam length at different periodicities. The checkerboard mask had boxes with varying lengths, from 2  $\mu\text{m}$  to 5  $\mu\text{m}$ . The beams were released in BOE, dump-rinsed in deionized water for six cycles, and spin-dried

The staggered support structures were able to reduce area of surface contact to less than 5% of the beam area and yielded displacement lengths beyond the limit of existing harp test structures (greater than 70  $\mu\text{m}$ ). These were successfully operated in the contact mode.

#### 4.4 Two-Dimensional Addressing

Concurrently with the anti-stiction work, Dr. Apte worked on providing proof-of-principle evidence for two-dimensional addressing of GLV pixels. At the time of these experiments, the anti-stiction approach used utilized rough polysilicon films to overcome the sticking problem. The rough layer effectively reduces the interaction area for van der Waals forces. This was successfully applied to the two dimensional array illustrated in Fig. 13. Processing began with a 5000 Å oxide isolation layer grown on a bare silicon substrate. On top of this layer a 3000-6000 Å undoped polysilicon layer was grown. This layer was probably amorphous initially, but it crystallized during subsequent high temperature processing (the reflow step). The polysilicon was diffusion doped with phosphorous, cleaned, and patterned into a bottom interconnect layer. Next, 1325 Å of low temperature LPCVD oxide was deposited on top of the nonplanar bottom electrode lines. This oxide was doped with 8% phosphorous to reduce the reflow temperature. The oxide was steam reflowed at 1000°C for 20 minutes. 1325 Å of LPCVD nitride was deposited next, then patterned and dry etched. The wafer was cleaned to remove all traces of photoresist. The oxide spacer was removed from under the microbridges with a BOE release. In addition, oxide was removed from under the edges of the frames and the bottom electrode traces. The resulting overhanging polysilicon and nitride provided the necessary isolation between top and bottom electrodes. These devices switched at 11V and did not exhibit stiction problems. However, yields were low due to shorting problems due to stringer material and the surface roughness was severe.



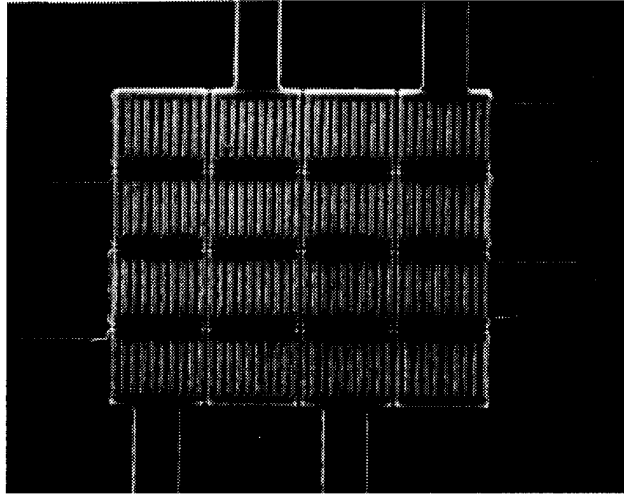


**Figure 13.** 4x4 array with polysilicon bottom electrodes.

#### **4.5 Preliminary Development of a GLV Packaging Technology**

Another major accomplishment was the development of a packaging technology for grating light valve devices. This is crucial for a hand-held prototype which requires an electrically addressable device. Issues involved included the choice of die attach adhesive, protective coating during wire-bonding, and window adhesive. A typical packaging process started with a four-inch wafer with released microbridges. The wafer was coated with an eight micron layer of polyimide acid (OCG Probimide 112) baked for one-half hour at 110°C in a convection oven. This buffer layer was chosen because it could withstand the die-attach temperature and be stripped at a later time. This was then coated with approximately 50  $\mu\text{m}$  of photoresist and sawed into individual dice. The photoresist was stripped removing the saw debris. An individual die was soldered (150°C) into a 32 pin DIP. An ultrasonic, aluminum wirebonder was used to connect the die contacts to the DIP. This instrument was chosen because the die does not have to be heated to 200°C during wirebonding. Finally, a glass window was indium soldered to the top of the DIP in nitrogen ambient. The system has a few problems, but we anticipate that this method can be used in the future for prototyping purposes.

#### **4.6 Conclusion on Process**

The above process development only addresses a part of the total GLV integration problem. Further work is required to incorporate the staggered support structures with a

full GLV process that includes two dimensional addressing and hermetic packaging. The main contribution of this work has been to demonstrate the feasibility of two-dimensional addressing and the engineering approach to the stiction problem, i.e. microscopic roughening and macroscopic surface patterning. And in the general interest of MEMS research, three novel techniques have been developed to form true nano-scale stand-off structures self-aligned underneath 1  $\mu\text{m}$  wide beams whose top surfaces are kept optically flat.

## 5. Conclusion

The GLV research and development project at Stanford has been very successful in many regards. Moving through the invention, engineering, manufacturing, and testing stages, the effort has brought together experience from multiple disciplines: optics, semiconductor process and device physics, mechanical engineering, and surface chemistry. The success of the Grating Light Valve as a device is demonstrated by the commercial interest in this MEMS technology for fiber-telemetry, printer, and display applications. Two companies have licensed the GLV patent from the Office of Technology Licensing of Stanford University.

Certainly, bringing the GLV to market will involve much more beyond this work. The emphasis of this work was in inventing and proving the commercial feasibility of the device. New issues now come to the fore.

Indeed, certain refinements can still be made to the electromechanical and optical models of the grating. And, it would be very interesting to build actual gratings that verify these models as they predict effects due to, for example, shadowing, non-scalar diffraction, duty-cycle errors, surface roughening, and the limited "aperture" or active area of a GLV pixel. However, the most significant issues facing GLV developers have to do with manufacturing: process integration, packaging, uniformity, repeatability, reliability, yields, failure analysis, and lifetime.

Upon the selection of the GLV application of interest, a completely integrated manufacturing process will have to be well designed to incorporate electrical isolation, addressing drive-circuitry (most probably two-dimensional), anti-stiction mechanisms, and a hermetically sealed package.

The desire to integrate the drive circuitry with the GLV device makes it more attractive to consider GLV processes re-designed around low-temperature materials. As in most MEMS systems, the mechanical properties of the chosen ultra-thin film materials have to be better investigated. For each new type of film used, the Young's modulus,

hardness, density, stress, dielectric strength, permittivity, yield strain, life-time, and even pin-hole density have to be experimentally measured.

Stiction is also still an important concern. In the effort to demonstrate the feasibility of the GLV technology, we have developed novel engineering solutions to the stiction problem. These particular solutions may not be directly transferable into a fully integrated GLV system; nevertheless, this work has shown the strength of the engineering approach to the adhesion problem; use surface roughening and self-aligned patterning to circumvent the fundamental limits of the adhesion forces. Moreover, the air damping and stiction problems emphasize the importance of hermetic packaging and sealing of the GLV devices.

Next, the complete manufacturing process and the actual devices will have to be tested for uniformity and repeatability, especially since these affect the GLV electromechanical behavior (e.g. switching voltages and hysteretic behavior), which, in turn, provides important specifications for the driver circuit designers. Finally, the whole process will have to be tested for reliability and life-time. Failure analysis may show strain fracture in the GLV beams, leakage in the package, or stiction, among other things.

## References

1. For a more detailed explanation see Abbe's theory of image formation in M. Born and E. Wolfe, *Principles of Optics* (Pergamon Press, New York, 1959).
2. See pages 61-63 in J. W. Goorman, *Introduction to Fouler Optics* (McGraw-Hill Book Company, San Francisco, 1968).
3. S. A. Gaither, "Two-Dimensional Diffraction from a Surface-Relief Grating," Computer Program, Vers. 26 (May 1988), courtesy of W. Veldkamp, MIT Lincoln Laboratory; W. B. Veldkamp, G. J. Swanson, S. A. Gaither, C.-L. Chen, and T. R. Osborne, "Binary Optics: A Diffraction Analysis," MIT Lincoln Laboratory, ODT-20 (August 23, 1989).
4. O. Solgaard, "Integrated Semiconductor Light Modulators for Fiber-Optic and Display Applications," Ph.D. Thesis, Stanford University (1992).

## **Publications and Technical Reports**

R. B. Apte, F. S. A. Sandejas, W. C. Banyai, and D. M. Bloom, "Deformable Grating Light Valves for High Resolution Displays," *Society for Information Display Symposium Digest of Technical Papers*, vol. 24 (Society for Information Display, Playa del Rey, CA, 1993), pp. 807-808.

Raj B. Apte, Francisco S. A. Sandejas, William C. Banyai, and David M. Bloom, "Deformable Grating Light Valves for High Resolution Displays," *Solid State Sensors and Actuators Workshop*, Hilton Head Island, SC (June 13-16, 1994), pp. 1-6.

Army Research Office - Technical Progress Report for Grant DAAL03-92-G-0232, "High Sped Integrated Light Modulators," (1 January 1994 - 31 December 1994).

## **Scientific Personnel**

B. M. Bloom  
W. Banyai  
B. Paldus  
F. Sandejas (Ph.D. - July 1995)  
D. Terasawa  
R. Apte (Ph.D. - June 1994)  
N. Ulman

## **Inventions**

Method and Apparatus for Modulating a Light Beam

## **APPENDIX A**

**GRATING LIGHT VALVES  
FOR  
HIGH RESOLUTION DISPLAYS**

A DISSERTATION  
SUBMITTED TO THE DEPARTMENT OF  
ELECTRICAL ENGINEERING  
AND THE COMMITTEE ON GRADUATE STUDIES  
OF STANFORD UNIVERSITY  
IN PARTIAL FULFILLMENT OF THE REQUIREMENTS FOR THE  
DEGREE OF  
DOCTOR OF PHILOSOPHY

Raj B. Apte

June 1994

# Abstract

The Grating Light Valve (GLV) is a micromechanical phase grating that can be used for color display applications. Operation is based on electrically controlling the mechanical positions of grating elements to modulate diffraction efficiency. By choosing dimensions of the grating structures carefully, it is possible to produce a digital optical device.

Since gratings are inherently dispersive, the GLV can be used for color displays. Full NTSC-quality colors are available. In addition, the devices are bistable and may be able to operate with a passive matrix of contacts and still achieve the performance of an active matrix light valve. Eight bits of gray scale are possible using time division multiplexing and the fast (20 ns) switching speed of the GLV. The contrast ratio of the device is sensitive to processing errors, and a ratio of 20:1 was measured. With better processing, a color contrast of 200:1 should be achieved. The operating voltage is 20 V, but there is good evidence that 5 V operation is feasible.

One problem in the development of large one-dimensional and two-dimensional arrays of devices was sticking during the final wet processing step. This is a common problem in micromachines. Our solution is to use rough (150 Å-RMS) polysilicon films to reduce the area of contact between the moving parts and the substrate. In the case of two-dimensional arrays, this film could be doped and function as the second dimension of interconnects. Although this structure suffers from some of the difficulties of a non-planar process, it was used to demonstrate two-dimensional arrays of devices.

# Acknowledgments

This work was sponsored by Andy Yang and Ken Gabriel of the Advanced Research Projects Administration under Contracts DAAL03-92-G-0232 and F49620-93-I-0609.

In addition to the sponsors I would like to thank my advisor, Dave Bloom, whose tireless energy and enthusiasm never failed to rouse me from my processing-lab stupor, and my research associate, Bill Banyai, who deconstructed my experiments. I hope that someday I will be worthy of their efforts.



# Contents

Abstract.....	iv
Acknowledgments.....	v
Contents .....	vi
List of Figures .....	ix
List of Tables .....	xii
List of Photographs .....	xiii
Introduction .....	1
1.1 Basic Device Fabrication and Operation .....	1
1.2 Comparison with LCDs and Other Micromechanical Valves.....	2
1.2.1 Limitations of LCDs .....	2
1.2.2 Other Micromechanical Displays .....	3
1.3 This Work .....	6
1.4 Outline .....	6
Optics of the GLV.....	7
2.1 Diffraction Grating Analysis .....	7
2.1.1 Basic Operation of the GLV.....	9
2.1.2 Scalar Diffraction Theory.....	9
2.2 Basic Optical Systems.....	12
2.3 Monochrome Contrast Ratio .....	15

2.3.1	Brightness and Contrast Ratio .....	15
2.3.2	Effect of Etch Anisotropy on Contrast.....	18
2.4	Color Operation.....	18
2.4.1	CIE Color Coordinates .....	20
2.4.2	Color Design.....	22
2.5	Color Contrast Ratio .....	25
2.6	Pixel Size Limits.....	27
Mechanics of the GLV .....		30
3.1	Basics of hysteresis .....	30
3.2	Materials Parameters .....	32
3.3	String Model .....	33
3.4	Beam Model.....	36
3.4.1	Switching Voltage.....	38
3.4.2	Peak Stress.....	39
3.4.3	Hysteresis.....	39
3.5	Row-addressing Method.....	40
3.6	Speed.....	42
3.7	Temperature Limits.....	42
Fabrication of the GLV .....		45
4.1	Basic Process .....	45
4.2	Isolation.....	47
4.3	Interconnect Conductivity and Reflectivity .....	50
4.4	Sticking.....	51
4.4.1	Water.....	52
4.4.2	Beam Peeling Theory.....	53
4.4.3	Stress .....	53
4.4.4	Surface Treatments.....	54
4.4.5	Striations .....	55
4.4.6	Van der Waals Bonding .....	56
4.4.7	Surface Roughness and Contrast.....	60
4.4.8	Progress in Reducing Sticking.....	61
4.5	Two-Dimensional Arrays.....	63
4.5.1	Isolation .....	63
4.5.2	Thermal budget .....	63

4.5.3 Basic Recipe .....	64
4.5.4 Nonplanar Processing .....	64
4.6 Reliability.....	66
4.7 Device Failure.....	67
4.8 Future Process Design.....	67
Conclusion.....	71
5.1 Device Summary.....	71
5.2 Future Work.....	72
Bibliography .....	74
Appendix 1.....	82
A1.1 Standard Process Steps.....	82
A1.2 Current GLV process .....	83
Appendix 2.....	85

# List of Figures

Figure 1.1	
A single GLV pixel.....	2
Figure 2.1	
Diffraction efficiency for several orders of an aluminum reflection phase grating .....	8
Figure 2.2	
Two states of the GLV.....	9
Figure 2.3	
Diffraction efficiency (diffractivity) of the first order as a function of wavelength for a “down” pixel, $S_{down}(\lambda)$ .....	11
Figure 2.4	
Diffraction efficiency (diffractivity) of the first order as a function of wavelength for an “up” pixel, $S_{up}(\lambda)$ .....	11
Figure 2.5a	
Simple monochrome optical system (I).....	13
Figure 2.5b	
Simple optical system (II) for electrical characterization of devices .....	14
Figure 2.6	
BW responsivity of the human eye.....	16
Figure 2.7	
BW contrast ratio vs. wavelength for narrowband sources .....	16
Figure 2.8	
BW contrast ratio vs. film thickness error.....	17
Figure 2.9	
Effect of bad sidewalls on contrast ratio.....	19

Figure 2.10	
Contrast ratio vs. sidewall angle.....	19
Figure 2.11	
Color responsivity of the human eye.....	21
Figure 2.12	
Basic optics of Schlieren system (III).....	24
Figure 2.13	
Measured color coordinates and theoretical values of the GLV with NTSC phosphor standards and the visible gamut.....	26
Figure 2.14	
Color coordinates of green pixel as a function of diffraction angle.....	26
Figure 3.1	
Basic model for the GLV beam mechanics.....	30
Figure 3.2	
Origin of hysteresis .....	31
Figure 3.4	
Results of beam model.....	38
Figure 3.5	
Simulated hysteresis curve .....	40
Figure 3.6	
Measured hysteresis curve of a single pixel.....	41
Figure 3.7	
Pixel switching in 20.5 ns.....	43
Figure 4.1	
Single pixel of the one mask GLV process.....	46
Figure 4.2	
Schematic of single mask process.....	46
Figure 4.3	
Device to device isolation.....	47
Figure 4.4	
Field concentration caused by poor sidewalls.....	50
Figure 4.5	
Control of residual stress in LPCVD nitride .....	54
Figure 4.6	
Beam peel length as a function of residual stress and striations .....	58

Figure 4.7	
Surface roughness and beam sticking.....	59
Figure 4.8	
Contrast ratio versus film thickness.....	59
Figure 4.9	
Schematic of two dimensional array .....	65

# List of Tables

Table 2.1	
Basic values of color parameters .....	22
Table 2.2	
Contrast ratio for unoptimized system .....	27
Table 2.3	
Contrast ratio for optimized system .....	27
Table 3.1	
Basic physical and geometric factors of the GLV .....	33
Table 3.2	
Three different types of nitride in use .....	33
Table 3.3	
Experimental second instability voltages .....	38
Table 3.4	
Materials parameters for thermal expansion .....	44
Table 4.1	
Progress in decreasing sticking .....	62

# List of Photographs

Photograph 2.1	
SEM of color pixels .....	25
Photograph 2.2	
Sideview of stuck beams .....	29
Photograph 4.1	
Grating destroyed by shorting and fusing .....	48
Photograph 4.2	
Closeup of fused beam .....	49
Photograph 4.3	
Harp test structure .....	52
Photograph 4.4	
Atomic force microscope image of harp structure .....	56
Photograph 4.5	
Striations in one dimensional arrays .....	57
Photograph 4.6a	
Rough polysilicon surface.....	60
Photograph 4.6b	
Nitride deformed by rough polysilicon .....	61
Photograph 4.7	
Single pixel in a two-dimensional array .....	62
Photograph 4.8	
4x4 pixel array.....	66
Photograph 4.9	
Four corners of a two dimensional array .....	68
Photograph 4.10	
Four corners point of two-dimensional array, alternate view .....	69



# **Chapter 1**

## **Introduction**

### **1.1 Basic Device Fabrication and Operation**

The Grating Light Valve (hereafter GLV) is a micromechanical light valve intended for display applications. A single pixel is shown in Figure 1.1. The body of the device is a collection of ten beams stretched across a frame. This frame is attached by a spacer to the substrate, leaving the beams suspended in air. By moving the beams electrostatically it is possible to modulate the diffraction efficiency of light incident on the structure. This device, whose fabrication uses only standard Silicon processes, is the subject of this thesis.

As a light valve for display, the GLV has a number of interesting properties. GLV fabrication is fairly simple, requiring only one mask step for basic devices and only three or four for complete array fabrication. This should translate into low production cost. The GLV is capable of either black-and-white (BW) or color operation with white light illumination. The pixels of the GLV are extremely fast, switching in under 25 ns. Furthermore, the pixels are bistable with applied voltage: it may be possible to operate the GLV and achieve active matrix performance with only a passive matrix. The combination of speed and bistability may be used for spatial light modulator applications as well as for simplifying the design of drivers (fast pixels can be addressed by a passive matrix, while slow pixels require the increased complexity of an active matrix structure).

## 1.2 Comparison with LCDs and Other Micromechanical Valves

From the mid-seventies micromechanical display technologies have been under investigation. Commercialization has focused on pivoting or moving mirrors to steer light into or out of collection optics [Sampsel 1992]. An alternative technology uses elastomers as the micromechanical layer in a diffractive configuration [Gerhard-Multhaupt 1990]; this technology is the most similar to the GLV. A comparison of GLV technology with the dominant new display technology, liquid crystal displays (LCDs), and other micromechanical display technologies will serve to explain the motivation for this work.

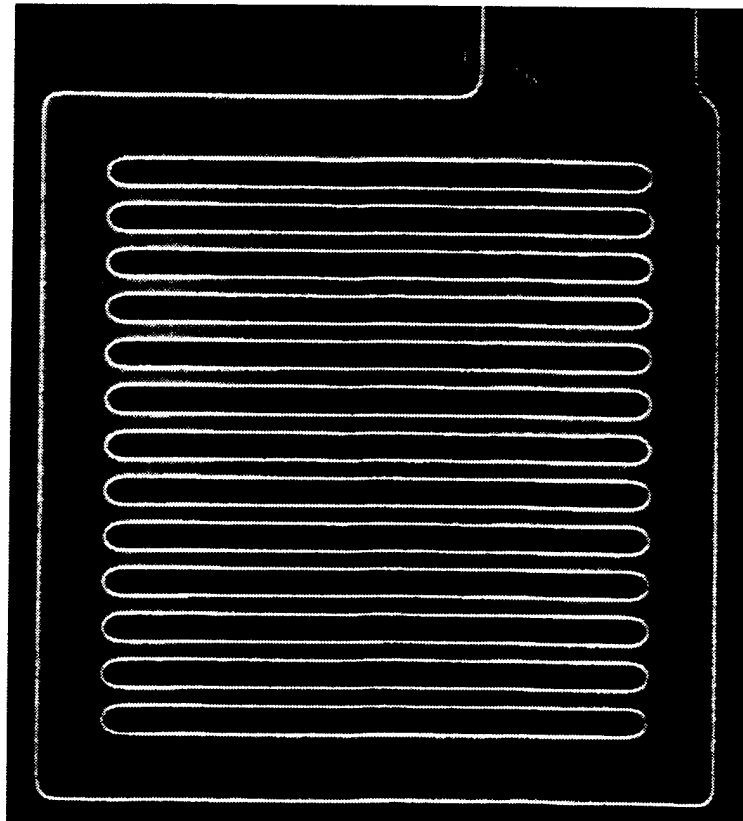


Figure 1.1: A single GLV pixel

### 1.2.1 Limitations of LCDs

The attraction of micromechanical displays is that they do not suffer from the limited speed and efficiency of LCDs. Nematic LCDs switch in milliseconds, and while new, faster liquid crystal technologies are under investigation, commercial LCD pixels operate

at little more than the video frame refresh rate. This complicates the design of device drivers, since simple row-by-row addressing requires devices to respond in a small fraction of the frame rate. LCD panels typically include an active matrix of perhaps a million transistors which can latch quickly. A second problem with LCDs is their limited optical efficiency. Typically around 5% of the light that enters a color LC valve makes it to the screen. This problem is especially acute for projection displays, which require maximum delivery of screen lumens. Micromechanical displays are potentially capable of a 500% improvement in optical throughput over LCDs (i.e., 25% of the incident light reaching the screen). In applications where lamp power is limited, this may be an important factor against LCDs.

If lamp technology is not a limiting factor, then the brightness of a light valve display is governed by the generation of heat in the valve. All the light that is not transmitted through a LC light valve is dissipated in the valve itself as heat, so the low optical throughput translates into device heating. The problem is compounded by the fact that LCDs are very temperature sensitive, with only a 40° C operating range. The GLV is constructed of high temperature ceramic materials and is very insensitive to temperature variations. In addition, micromechanical light valves modulate light by switching it from the collection optics into a beam dump: the energy not transmitted from dark pixels does not heat the device. Only about 8% of the incident light is absorbed by the aluminum reflector on the surface of the chip. These facts combine to make it likely that much larger lamps can be used with micromechanical displays compared to LCDs. Larger lamps and higher efficiencies mean more screen lumens.

The promise solving the problems of LCDs—speed, optical efficiency, and temperature sensitivity/device heating—makes micromechanical displays interesting to a number of companies [Sampsell 1992], including those with LCD manufacturing capability [Yoshida 1993].

### 1.2.2 Other Micromechanical Displays

Pioneers of micromachining first proposed micromechanical displays in the mid-seventies [Petersen 1982]. Commercial development commenced at Texas Instruments soon after and continues to the present [Hornbeck 1991a; Hornbeck 1991b; Sampsell 1990]. Their work is based on electrostatic pivoting or moving mirrors. Since mirrors have to be rigid while beams in the GLV are flexible, mirrors are nearly an order of magnitude thicker than beams. This translates into a larger moment of inertia and slower

accelerations for a given driving torque. Also, mirrors must be deflected by several microns while beams require less than one seventh of a micron deflection. For these reasons GLV is more than two orders of magnitude faster than Texas Instruments' Deformable Mirror Device (DMD).

The difference in speed is sufficient to allow row-addressing of the GLV while limiting the DMD to frame addressing. In row-addressing, each row pixels is selected, one at a time. Simultaneously pixel data is put on the column drivers. Following the write cycle, the current row is de-selected and the next row is selected. If each pixel contains memory, either by the integration of a transistor or some inherent bistability, then this method does not suffer from the limited contrast of passive-matrix addressing [Alt 1973]. Clearly the pixels must respond faster than the frame-rate times the number of rows. For digital pixels (which both DMD and GLV use), the response of the pixel must be faster still by the number of distinct gray levels. For a 1000 row display with 8 bits of grayscale (per color) addressed at 60 Hz, the pixels must be capable of responding at 15 MHz. The GLV is capable of this speed.

For the slower DMD pixels, more cumbersome frame-addressing is needed. A matrix of fast master-slave flip-flops is located beneath the pixels, one flip-flop per pixel. The master is connected to the addressing lines of that pixel, while the slave is connected to the mirror immediately above it. The master flip-flops are row addressed. After the complete frame of master flip-flops has been programmed for the next frame, the data from each master is latched to its slave and the mirror that stands above it. The master to slave latching is done for the entire frame simultaneously. Finally, row-addressing of master flip-flops continues for the next frame.

Frame-addressing achieves the same performance as row-addressing, but requires eight transistors per pixel (four for each flip-flop). Eight million transistors are needed in a megapixel display. Only two-thousand drivers are needed for the GLV, each of which must switch among three logic states. Since tri-state logic requires fewer than 10 transistors per driver, fewer than twenty thousand transistors are needed for a megapixel GLV. The reduced complexity of the GLV should make it less expensive to manufacture than the DMD.

A second advantage of the GLV over the DMD is that the GLV is capable of producing color from a white illumination source without any additional components. Although the

DMD can be used for color, the addition of a large, rotating color wheel or other color selector is needed to illuminate the DMD with red, green, and blue light sequentially. The frame rate is tripled, and the DMD images the red, green, and blue component in succession. The eye integrates the three primary images into one color image. The addition of a color selector is not needed for the GLV: it is converted from BW to color operation simply by narrowing a slit in the projection optics. The intrinsic color generation of the GLV will be very useful for manufacturing compact color displays for pager and head-mounted applications.

Other micromechanical display technologies are based on electron beam, active-matrix Silicon, or CRT/photoconductor addressing of viscoelastic and oil films [Gerhard-Multhaupt 1991]. Electron beams and CRT/photoconductor addressed displays are unlikely to have a major impact because of their high cost and therefore small penetration into the low and middle parts of the market. However, there is promise that research on active-matrix viscoelastic systems may lead to mainstream products in the future because of their simplicity of fabrication and compatibility with CMOS process integration.

Viscoelastic spatial light modulators (VSLMs) [Gerhard-Multhaupt 1990] use a thin viscoelastic layer sandwiched between a flexible layer of metal and a rigid substrate with transistors and metal lines on the other. If a voltage is applied to the lines, which are shaped like gratings, the top metal is attracted and the viscoelastic layer and top metal deform together. This forms a sinusoidal grating on the top metal. Essentially, the GLV and VSLM are based on the same principles of operation, with different implementations of the spacer layer: air vs. plastic. Since the surface deformations are similar in shape, the optical systems are very similar. One advantage of the VSLM is that it does not require any high temperature processing, so integration with driver circuits and active matrices is greatly simplified. Nevertheless, a passive matrix GLV that only requires a few thousand driver transistors may be easier to manufacture than the VSLM with an active matrix of millions of transistors.

## 1.3 This Work

Original contributions of this thesis are the discussions of color, device modeling and the fabrication of two-dimensional arrays of devices. Specifically:

- Generating color using the dispersive properties of gratings and Schlieren optics.
- Modeling the contrast ratio for broadband illumination.
- Modeling the mechanical properties of beams.
- Using striations to reduce sticking of the beams to the substrate.
- Using surface roughness to reduce sticking of the beams to the substrate.
- Fabricating two-dimensional arrays of devices.
- Proposing a two-dimensional addressing scheme.

Other students, Olav Solgaard and Francisco Sandejas, did the initial process design and first mask layout. In addition, Francisco developed other processes to decrease sticking and to obtain critical sidewall (and dimensional) control for higher contrast.

## 1.4 Outline

This chapter presented a sketch of micromechanical entries into display development and a comparison with LCDs. Chapter 2 explains the optical properties of the device, including the principle of operation, color generation, contrast ratio, and scalability. Two models for the electromechanical operation of the device are presented in Chapter 3. These models are used in Chapter 4 to analyze the problem of stiction encountered during fabrication. The process design for two-dimensional arrays is reviewed. Chapter 5 summarizes the research on this device and discusses future research topics. The two appendices give specific process recipe steps for the devices and the details of the numerical beam calculations.

# Chapter 2

## Optics of the GLV

### 2.1 Diffraction Grating Analysis

A diffraction grating is a periodic structure that affects either the amplitude or phase of incident light. Typically the period is several times the wavelength of light. A detailed analysis of diffraction gratings [Born 1980] shows that incident light is diffracted by the grating into several directions which conform to the Bragg condition. Amplitude gratings are formed by alternating stripes of absorbing and transmitting material. Phase gratings modulate the phase rather than the amplitude of light.

The GLV is a microelectromechanical phase diffraction grating. The amplitudes of the diffracted modes of a  $2.00\text{ }\mu\text{m}$  period phase grating with rectangular grooves constructed from aluminum as a function of groove depth are shown in Figure 2.1. The specular mode has a peak reflectivity of 92% when no grooves are present (92% is the reflectivity of aluminum). This value decreases as the light is diffracted rather than reflected. However, when the grooves are  $\lambda/2$  deep, the reflectivity is again maximum. Shadowing effects (caused by reflections from the sidewalls of the grating elements) limit this maximum reflectivity to 82%.

The light that is not reflected into the specular mode is diffracted. For small grating depths there is little diffraction. As the round-trip depth approaches  $\lambda/4$  in phase, the diffraction peaks, with 41% of the light in each of the first order diffraction modes. At a grating depth of  $\lambda/2$  the diffracted light is again nulled. In this case the grating functions like a perfectly flat mirror, for nearly an octave of wavelengths of light. Since each of the

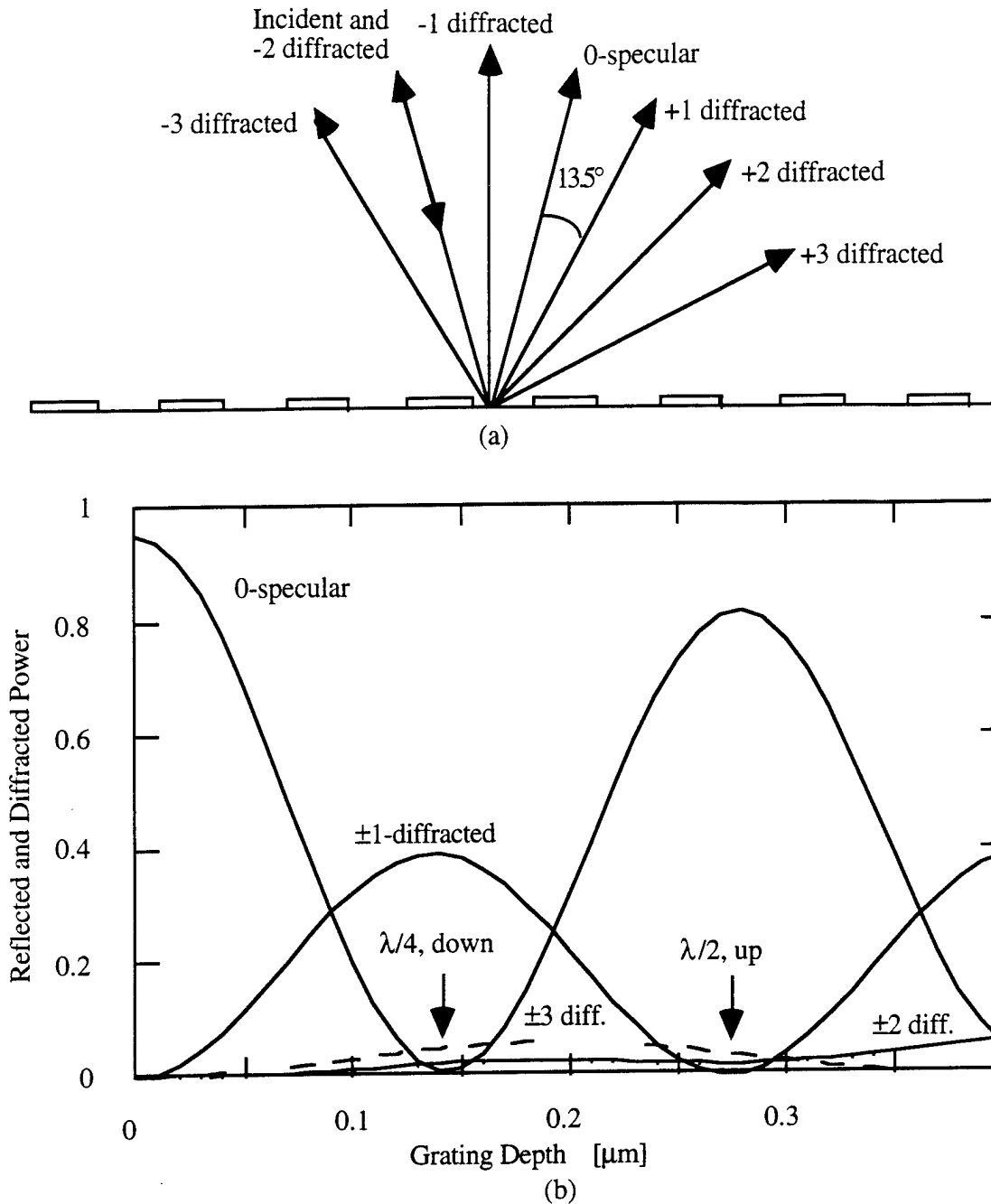


Figure 2.1: Diffraction efficiency for several orders of an aluminum reflection phase grating with a  $2.00\ \mu\text{m}$  period, illuminated at  $13.5^\circ$  incidence at  $550\ \text{nm}$ . (a) shows schematically the diffracted modes. (b) shows the diffracted intensities as a function of grating depth. Note the finite reflectivity of aluminum limits the specular reflection with no grooves to 92%. [Gaither 1988; Veldkamp 1989]



diffracted modes has a different diffraction angle, the component of the wavevector normal to the grating varies with order number. This variation is what causes the higher order modes to null further out than the  $\pm 1$  order. Thus, not all the diffracted modes can be nulled at one grating depth. Fortunately, these higher orders are fairly small in magnitude, so that the total power lost if they are spatially filtered is negligible.

### 2.1.1 Basic Operation of the GLV

The switching of the diffraction efficiency can be used to make devices in a number of ways. The two basic methods depend on whether the reflected or diffracted light is collected by the optical system. These are demonstrated in Figure 2.2. In the undeflected, or “up” case, which corresponds to  $\lambda/2$  the GLV is purely reflecting. In the deflected, or “down” case, the phase delay is  $\lambda/4$  and the diffraction into the  $\pm 1$  diffraction orders is maximized. The key to device operation is that the spacer and beam thicknesses are chosen to be  $\lambda/4$  deep.

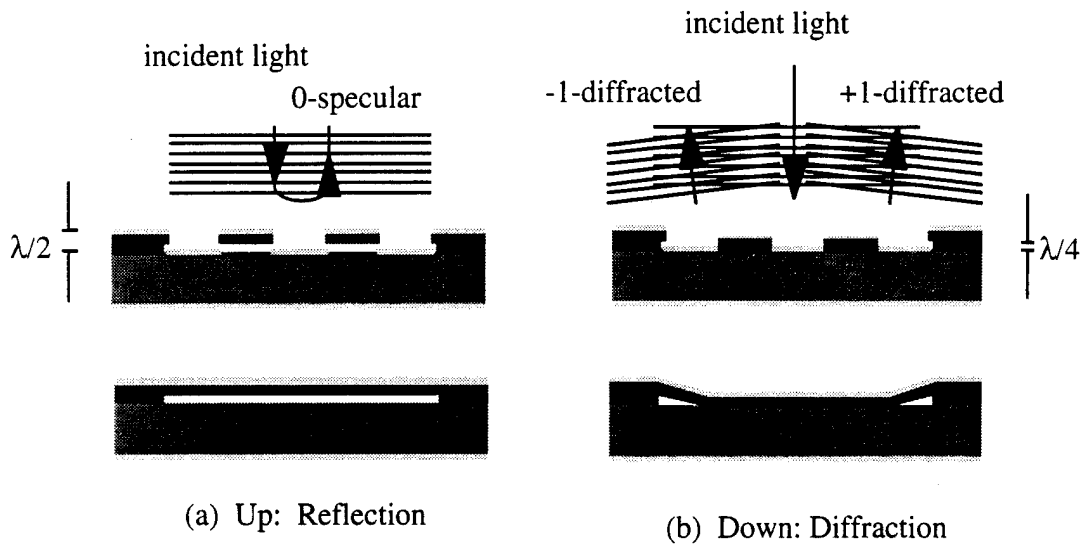


Figure 2.2: Two states of the GLV. In (a), the beams are up and the device reflects the incident light. In (b), when the beams are down, the GLV diffracts all the light. The top two illustrations show the cross section through the beams. The bottom two show a cross section that is parallel to the beams.

### 2.1.2 Scalar Diffraction Theory

Scalar diffraction theory for normal incidence is largely in agreement with Figure 2.1. The scalar theory gives for the  $\pm 1$  diffraction orders [Solgaard 1992]

$$I = \frac{I_0}{2} \text{sinc}^2\left(\frac{\pi}{2}\right) \left[ 1 - \cos \left\{ \frac{2\pi d}{\lambda} \left( 1 + \frac{1}{\sqrt{1 - (\lambda/p)^2}} \right) \right\} \right]$$

where  $I_0$  is the incident light intensity,  $d$  is the grating depth,  $\lambda$  is the wavelength of the incident light, and  $p$  is the periodicity of the grating. For small diffraction angles ( $2 \mu\text{m}$  periodicity gives a diffraction angle of  $15^\circ$  at  $550 \text{ nm}$ ) and a grating designed with  $d = \lambda_0/4$  for a design wavelength of  $\lambda_0$ , the intensity of the  $\pm 1$  diffraction orders for a “down” pixel is

$$S_{\text{down}}(\lambda) = 0.41 \frac{S_0(\lambda)}{2} \left[ 1 - \cos \frac{\pi \lambda_0}{\lambda} \right]$$

For an “up” pixel the corresponding expression is

$$S_{\text{up}}(\lambda) = 0.41 \frac{S_0(\lambda)}{2} \left[ 1 - \cos \frac{2\pi \lambda_0}{\lambda} \right]$$

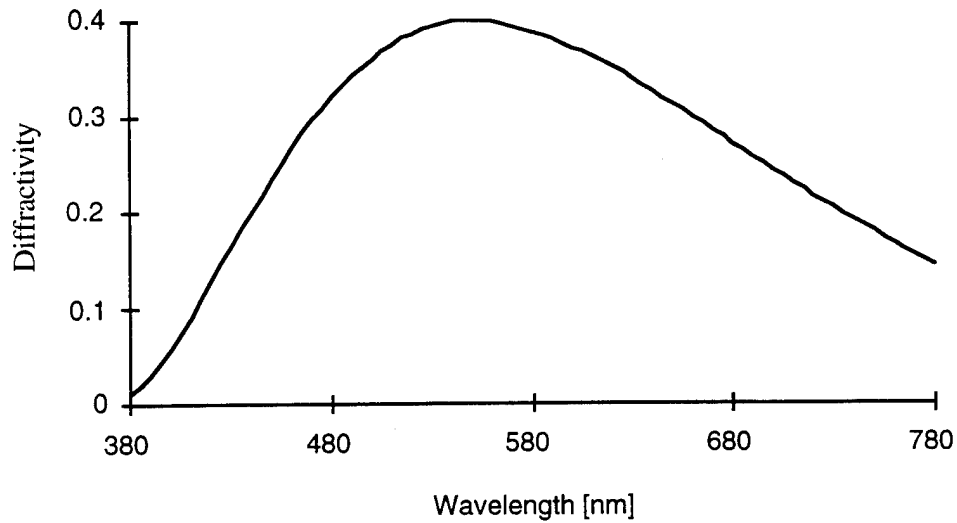


Figure 2.3: Diffraction efficiency (diffractivity) of the first order as a function of wavelength for a “down” pixel,  $S_{down}(\lambda)$ . This grating is designed for 550 nm.

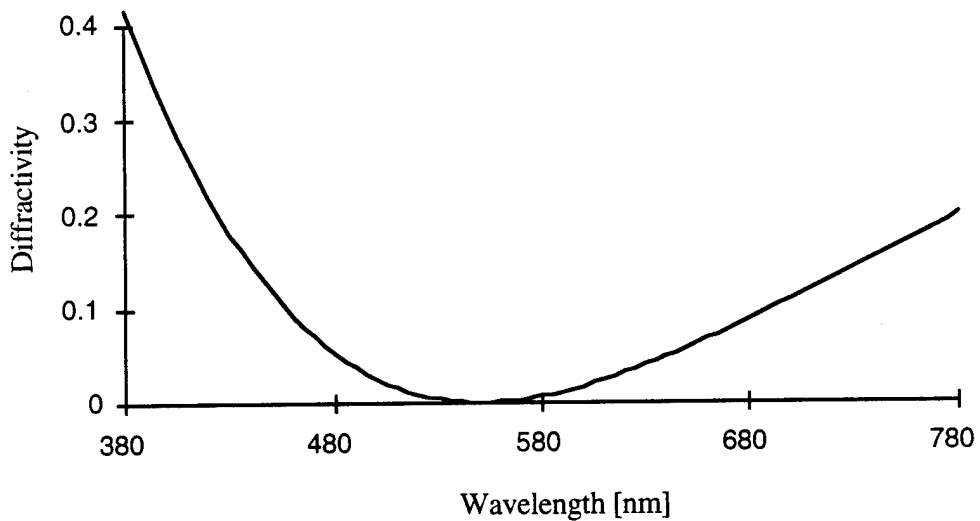


Figure 2.4: Diffraction efficiency (diffractivity) of the first order as a function of wavelength for an “up” pixel,  $S_{up}(\lambda)$ . This grating is designed for 550 nm.

The plots of  $S_{down}(\lambda)$  and  $S_{up}(\lambda)$ , Figures 2.3 and 2.4, respectively, illustrate the basis of the bandwidth and the contrast ratio of the device. It is apparent that the GLV modulates

light over a 200 nm bandwidth. The contrast at any particular wavelength is simply the ratio of  $S_{down}(\lambda)$  to  $S_{up}(\lambda)$ . Because  $S_{up}(\lambda)$  is a null at only a single wavelength (550 nm in this case), the contrast ratio peaks at that point and declines to either side. In Section 2.3 these parameters will be used along with a development of human visual perception to calculate contrast ratios for these devices when used in optical systems described in Section 2.2.

## 2.2 Basic Optical Systems

Optical systems can be constructed to view either the reflected or diffracted light. The latter has two clear advantages. Since the non-diffraction grating portions of the device, including bond pads and other large areas, remain equally reflecting in both the “up” and “down” positions, there will be a problem generating adequate contrast without the use of masking films or spatial filters to remove the unmodulated light. The second advantage to viewing the diffracted light is that the spatial dispersion of the grating, discussed in Section 2.4 and Figure 2.12, can be used to make color pixels.

The basis of BW operation was shown in Figure 2.2. When the beams are “up,” the device is reflective, and the normally incident light is reflected back to the source. If the beams are brought into the “down” position, then the pixel diffracts 82% of the incident light into the  $\pm 1$  diffraction modes. Additional light is diffracted into higher order modes (about 10% of the incident), but the optics used had too small an aperture to collect this light.

The optical systems were used in device testing. The prototypical BW optical system (hereafter, system I), is shown in Figure 2.5. The illumination source was either a 250 W metal halide arc lamp with an integrated reflector or a 40 W tungsten-halogen lamp with dielectric reflector. The light was condensed with f/2.4 optics and imaged without magnification at an intermediate point. At the intermediate point the image was spatially filtered to insure adequate collimation. Since collimation within the plane of Figure 2.5 is essential for good contrast, the arc or filament of the lamp is shown perpendicular to this plane. The source image was then collimated and directed by a turning mirror onto the face of the device. The specular reflection was returned to the lamp, while the diffracted orders were collected by a projection lens placed just over a focal length away. The distance between the device and the projection lens was adjusted to focus the image on a distant screen. In this system the projection lens is used both for projection to the

screen as well as spatial filtering of the diffracted light. A telecentric stop was placed at a distance of one focal length from the projection lens. At this plane, all rays from the device plane with the same angle all pass through the same point, i.e., all the +1 diffraction order rays focus at one point while all the -1 rays focus at another. By placing a stop with slits in it at those two points, all non-diffracted light is blocked from the screen.

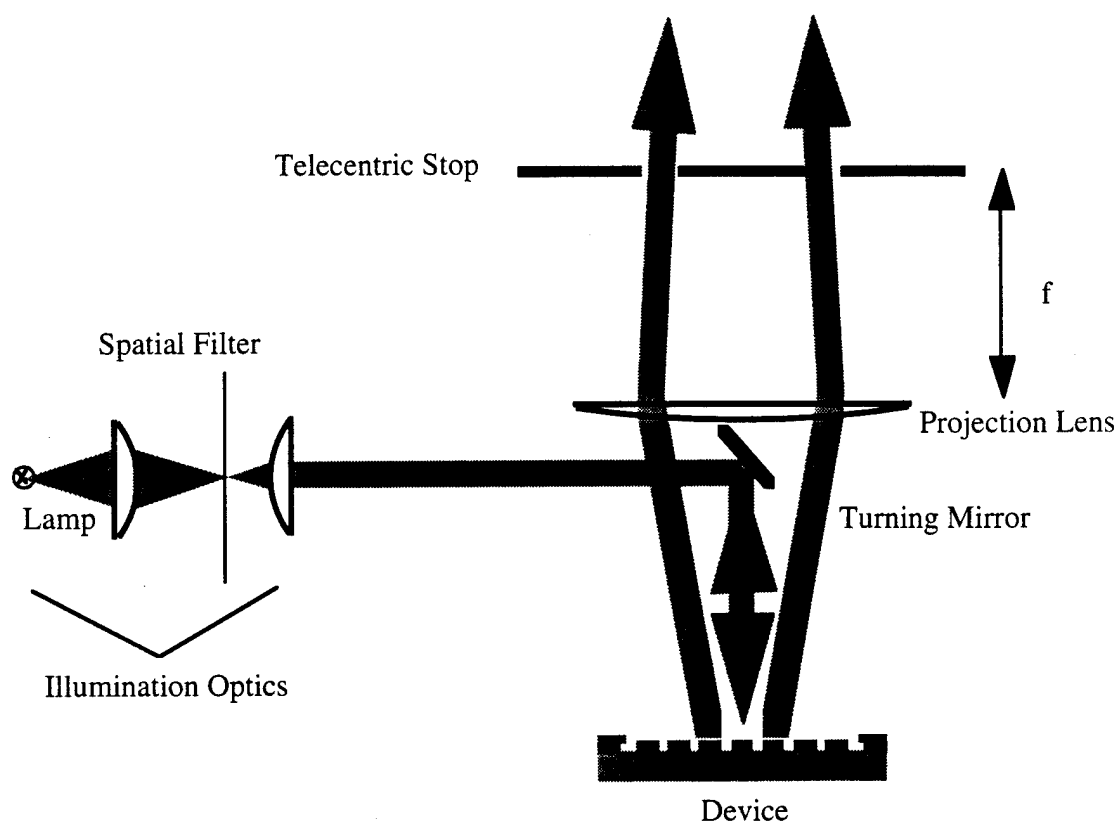


Figure 2.5a: Simple monochrome optical system (I). System I was used as a prototype for a second system, *vide infra*, to do electrical testing (system II) and a third to do optical testing (system III).

System I was used to demonstrate the utility of the GLV for projection and contained a static GLV device. The static GLV device was designed with a fixed, VGA bitmapped image on it. At each pixel of the bitmap, the values for red, green, and blue were quantized to six bits each. At the corresponding location on the static GLV, three pixels

were written, red, green, and blue, and the beam length of each was varied from 0.25 to 16  $\mu\text{m}$  depending on the six bits for each color. A dark pixel was simply left blank. Except for contrast ratio, this static display gives a faithful impression of what a GLV display will look like.

A second system (system II) was constructed for device testing using a microscope/probe station to allow electrical operation of the beams. In this system, the illumination optics were reduced to a tungsten-halogen lamp with integrated collimating reflector. The turning mirror was moved to the side so that the device was illuminated from the diffraction angle. The diffraction angle of the -1 order was then normal to the device. This light was imaged through a microscope objective and eyepiece. The other diffracted modes (+1,  $\pm 2$ ,  $\pm 3$ ) were discarded. At the telecentric point of the objective lens two strips of black tape were used to define a slit. This system was used for most of the electrical device testing (including hysteresis measurements). A third optical system (system III, see Section 2.4.3) was used to measure the color properties of the GLV.

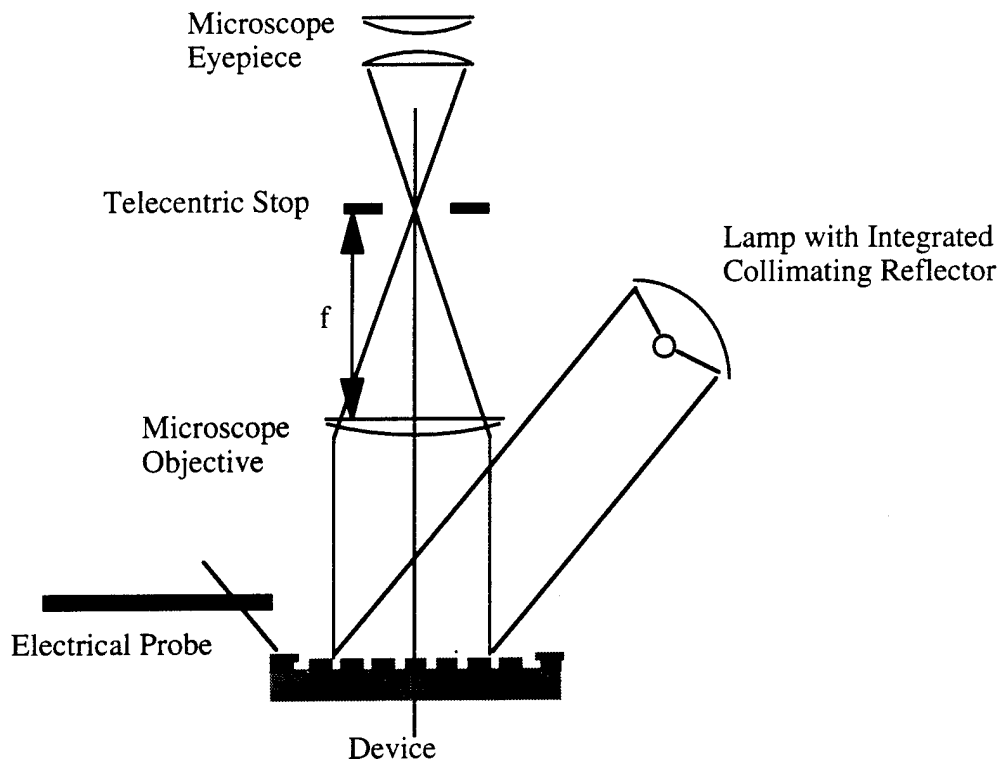


Figure 2.5b: Simple optical system (II) for electrical characterization of devices. This system is constructed on a probe station with microscope.

## 2.3 Monochrome Contrast Ratio

To understand the difference between dynamic range or extinction ratio, terms used in describing optical modulators, and contrast ratio, it is necessary to discuss the responsivity of the human eye [Hunt 1991] and its effect on perceived brightness. Theoretical and experimental values of the BW contrast ratio are discussed, and the difference is explained as a result of process parameters.

### 2.3.1 Brightness and Contrast Ratio

Based on subjective descriptions of comparative brightness for different colors, the *Commission Internationale de l'Éclairage* (hereafter CIE) established in 1931 the CIE standard photometric observer. The basis of this observer is the photopic spectral luminous efficiency function,  $V(\lambda)$ , plotted in Figure 2.6. This function gives the relative brightness of narrowband optical sources of constant optical power over the visible spectrum which peaks at 555 nm. Because of the linearity of the human eye, the apparent brightness,  $Y_x$ , of a source with some spectral distribution,  $S_x(\lambda)$ , is equal to

$$Y_x = \int_{380\text{nm}}^{780\text{nm}} V(\lambda) S_x(\lambda) d\lambda$$

Using the values of  $S_x(\lambda)$  for “up” and “down” pixels in Section 2.1.2, the apparent brightness of “up” and “down” pixels can be calculated for a given illumination spectrum,  $S_0(\lambda)$ . The contrast ratio is defined as  $Y_{\text{down}}/Y_{\text{up}}$ .

To calculate the narrowband contrast ratio of the GLV, i.e. the contrast ratio for a light-emitting diode (LED) or other narrowband illumination, we take  $S_0(\lambda) = \delta(\lambda - \lambda_0)$ , where  $\delta(\lambda - \lambda_0)$  is the delta distribution at  $\lambda_0$ . This contrast ratio is plotted vs.  $\lambda_0$  in Figure 2.7. The narrowband contrast ratio is extremely high at the design wavelength and is still better than 100:1 over nearly 100 nm of spectrum. In the case where the GLV is illuminated with LEDs, contrast ratios of better than  $10^4$  should be expected—perhaps as high as  $10^8$  if the device is grown with perfect dimensions and very smooth aluminum.

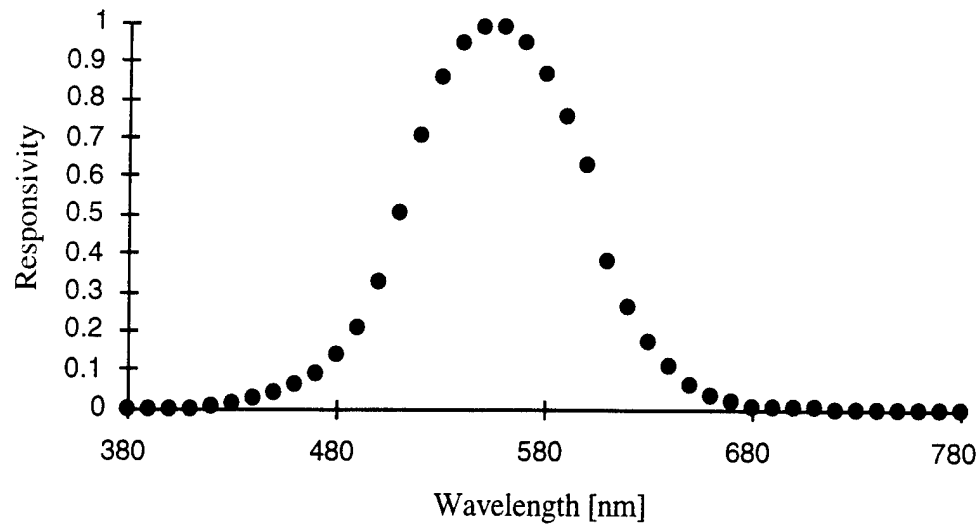


Figure 2.6: BW responsivity of the human eye.[Hunt 1991]

For white light illumination, which is flat over the entire visible spectrum, the contrast ratio is calculated to be 82:1. This value of the contrast ratio is representative of a variety of high-temperature black-body and multiline, white arc sources. It is also representative of contrast ratios seen on existing LCD projectors [Yoshida 1993].

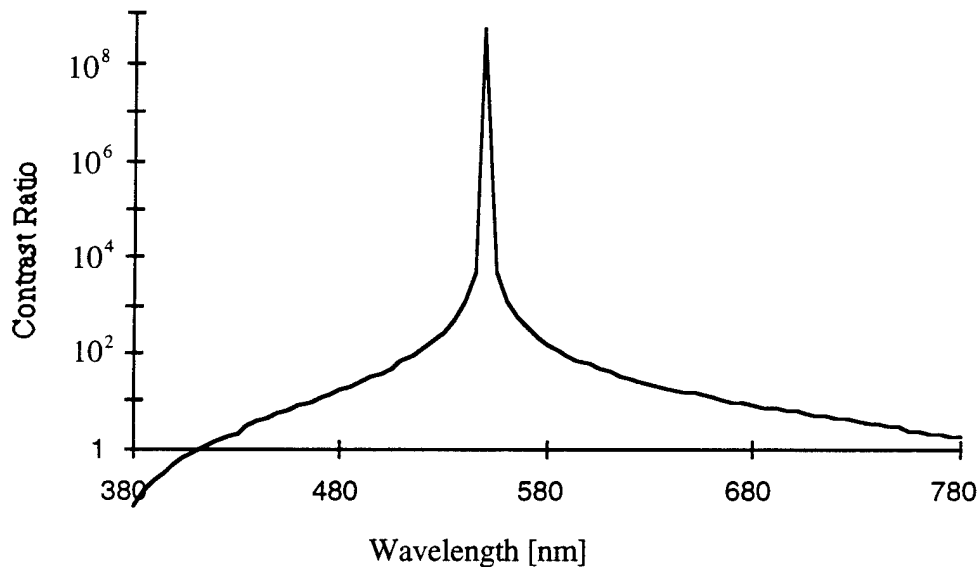


Figure 2.7: BW contrast ratio vs. wavelength for narrowband sources. For narrowband operation, the GLV is capable of operating as an extremely high contrast ratio modulator. For a device optimized for the green the contrast is better than 100:1 from 520 to 580 nm.



Because of the narrowness of the peak of the narrowband contrast ratio, it was feared that the contrast ratio would be a very sensitive function of processing variations, particularly thickness errors that cause wavelength shifts in the optical properties. This hypothesis was tested by recalculating the contrast ratio, as above, but for pixels with design thicknesses other than 555 nm. These contrast ratios are plotted in Figure 2.8 as a function of the change in oxide plus spacer thickness (i.e., a device with design wavelength of 565 nm instead of 555 nm has 10 nm of wavelength error. Since the oxide plus spacer thickness is  $\lambda/2$ , this corresponds to a 5 nm thickness error). This calculation shows that a few percent error in film growth will not destroy the BW contrast ratio of the device.

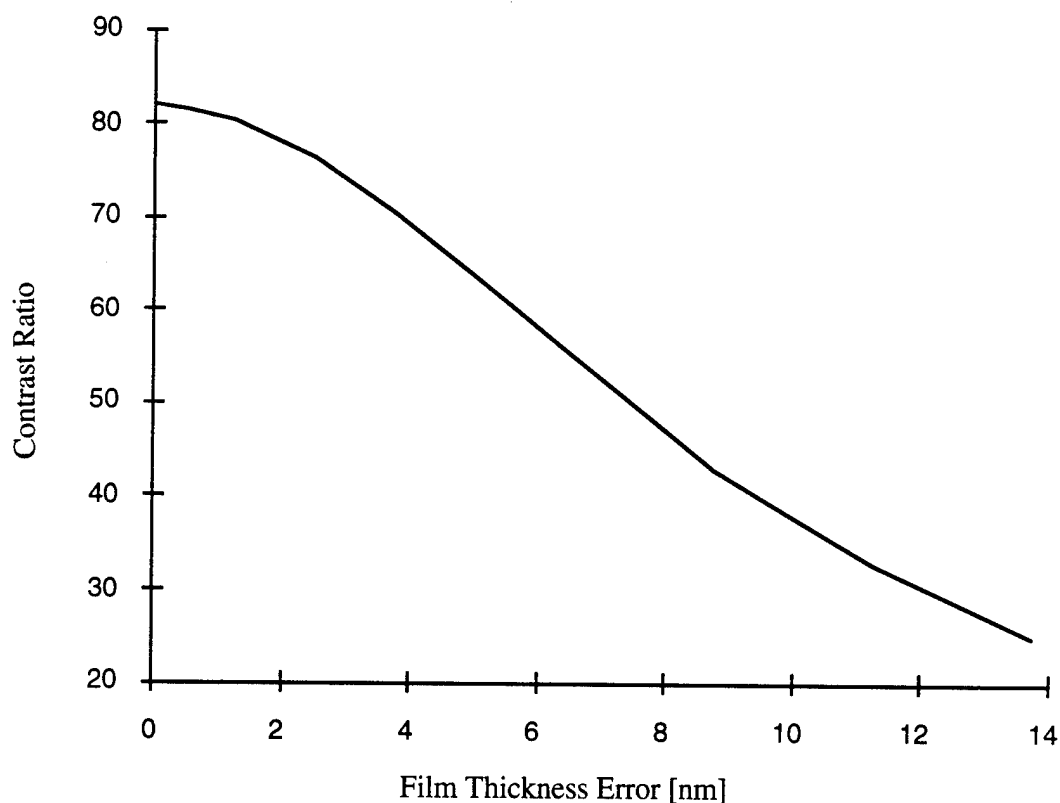


Figure 2.8: BW contrast ratio vs. film thickness error. The contrast ratio is plotted as a function of total film (spacer and beam) thickness error for a pixel with 140 nm total nominal film thickness. Thus, at least 5% control of thicknesses is needed to construct satisfactory contrast ratio devices.

### 2.3.2 Effect of Etch Anisotropy on Contrast

The measured value of the contrast ratio was 20:1 [Apte 1993]. From Figure 2.8, it is apparent that the fourfold discrepancy from theory cannot be explained by film thickness errors (accuracy to within 5 nm was typical). In fact, the error lies in the quality of the sidewalls of the gratings, and thus in the masking and etching process used. Since the diffraction efficiency of the lower part of the sloped sidewall in the “up,” or dark, case is comparable to that of the “down,” or light, case, the contrast is spoiled by the poor quality of the dark state.

To make the effect of poor sidewalls precise is difficult, since a vector diffraction theory will be needed to handle 500 to 1000 Å features [Gaylord 1982]. A simple estimate is possible using the expression for diffraction given in Section 2.1.2. In this expression the intensity of diffraction as a function of grating depth is given. If we average this expression over the range of heights of the beam—including the downward sloping sidewalls—this gives our estimate of the diffraction efficiency of the “up” beams. The substitution of this value for the denominator in the contrast ratio under white light illumination is plotted in Figure 2.10. A contrast ratio of only 11:1 is expected for 45° sidewalls.

The measured value for the sidewall slope for the nitride etch recipe given in Appendix 2 is 25°, which is measured from SEM photomicrographs. This slope gives a contrast ratio of 21:1. Although the method of this calculation neglects the very fine structures of the the sidewalls and their precise effect upon the diffraction, it seems likely that improved sidewall slopes will result in improved contrast ratio. Work on using metal masks instead of photoresist during the etch step are being explored for this reason.

## 2.4 Color Operation

By using the dispersive properties of the grating [Born 1980] the GLV can act both as a light valve and a color filter. For a diffraction grating with normally incident illumination and period,  $p$ , the relationship between diffraction angle,  $\theta$ , wavelength,  $\lambda$ , and order number,  $m$ , is given by

$$\sin \theta = m \frac{\lambda}{p}$$

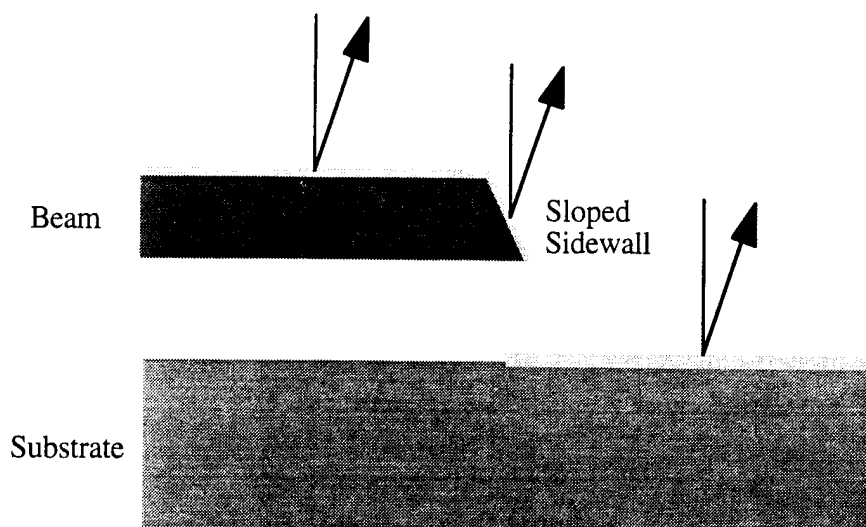


Figure 2.9: Effect of bad sidewalls on contrast ratio. If the sidewalls of the beams are sloped by insufficient anisotropy of the beam etch or unsatisfactory masking, then the lower parts of the slope are at the height for maximum diffraction. Poor contrast results.

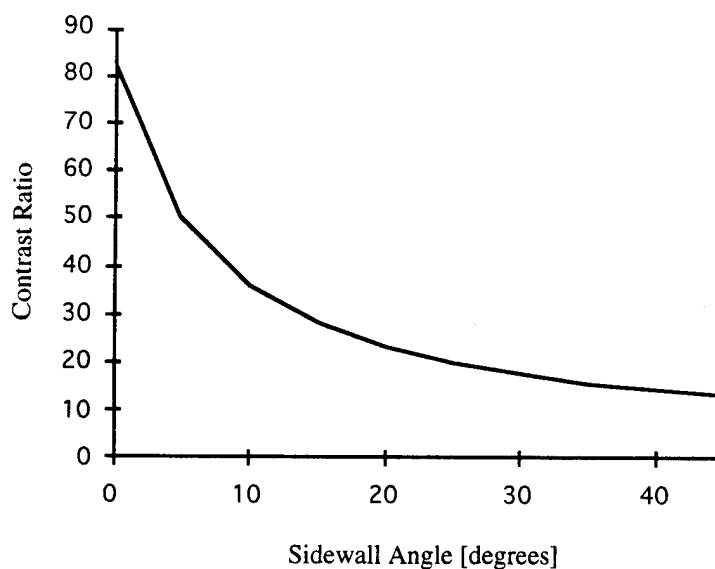


Figure 2.10: Contrast ratio vs. sidewall angle. This figure demonstrates the importance of good anisotropy and masking for the grating beam etch step.

For the first order, in the case of small angles, this reduces to  $\theta = \lambda/p$ . Thus, if an optical system is constructed that accepts diffracted rays from only a narrow set of angles,  $\theta_0 \pm \partial\theta$ , then it will image the GLV only in the spectral range

$$\lambda_0 \pm \partial\lambda = p_0(\theta_0 \pm \partial\theta)$$

In order to image the GLV at  $\lambda_i$  which is not in  $\lambda_0 \pm \partial\lambda$ , we choose another value for the periodicity of the grating,  $p_i$ , so that

$$\theta_0 \pm \partial\theta = \frac{\lambda_i \pm \partial\lambda}{p_i}$$

Thus, it is possible to choose three different grating periodicities such that each one diffracts a different wavelength through the same diffraction angle and thus through the same slit in the telecentric stop. This is a general process that could be used for more sophisticated additive color systems than the usual red-green-blue (RGB) of the National Television Standards Committee (hereafter NTSC). The optics of such a system are shown in Figure 2.12, which shows the third optical system used with the GLV [Hopkins 1992]. The basic innovation of this system is to place the collimating lens onto the face of the grating package. This puts the collimating lens into the optical path of the diffracted light. Before a discussion of the design of color devices, a review of human color perception and colorimetry is presented.

#### 2.4.1 CIE Color Coordinates

The responsivities of the three types of cones in the human eye [Hunt 1991] are plotted in Figure 2.11. If these could be measured accurately for a large number of individuals, then they could form the basis of a color coordinate system. Since this study was not possible, an alternative methodology was arrived at which used color matching experiments. An observer was presented with two illuminated boxes, one with an unknown source, and the other with variable amounts of red, green and blue (which are defined in this case at 700 nm, 546.1 nm, and 435.8 nm and termed R, G and B). The observer then changed the amounts of R, G and B until he matched the unknown source. Assuming that the brightness of the unknown source is such that  $R+G+B$  is constant (ie, brightness is not a factor), then the color of the unknown source could be described by  $(R,G)$ .

This explanation oversimplifies the basis of colorimetry, but gives a flavor of how to interpret CIE color coordinates ( $x,y$ ):  $x$  is the amount of red;  $y$  is the amount of green; and when both decrease the color is blue (since aggregate brightness is constant). Because of complications in the system, the range of visible colors is not described by a simple geometry in the  $x,y$  plane but by a rounded triangle. The edge of the triangle consists of highly saturated colors, like laser or LED illumination. In the center, with equal mixes of red, blue, and green, are shades of white. Thus, moving from the center to the edge of the triangle increases saturation. Moving clockwise increases wavelength. See Figure 2.13.

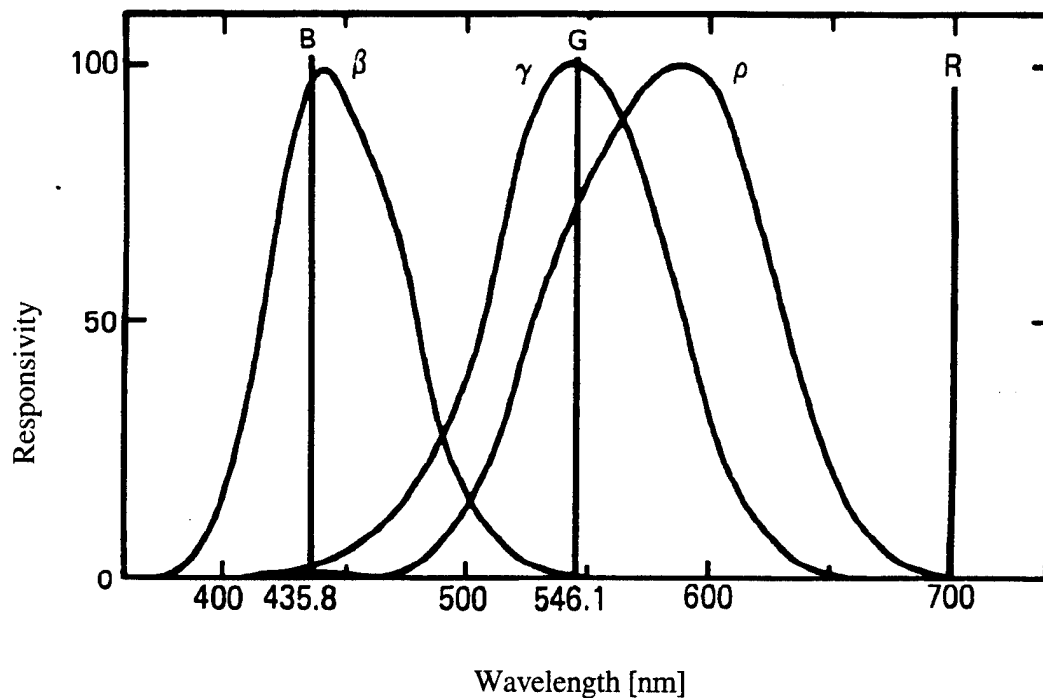


Figure 2.11: Color responsivity of the human eye.  $\beta$ ,  $\gamma$ , and  $\rho$  are the spectral responsivities of the three types of cones in the human eye. B, G, and R are the spectral lines used to define the 1931 CIE Standard Colorimetric Observer. [Hunt 1991]

If a display is constructed with three color sources, such as a color TV with three phosphors, then each color source may be plotted on the  $x,y$  plane. The set of all the perceived colors made by mixing these three sources in varying ratios is called the “gamut” of the colors. Because of the linearity of the human eye and the CIE color coordinate definition, the coordinates of all of the colors in the gamut defined by three

primary sources form the triangle in the  $x,y$  plane defined by the coordinate of the primaries.

### 2.4.2 Color Design

The procedure for designing a color GLV then reduces to the question of how to design the gratings and slits to achieve a desired color gamut. For reasons of compatibility with existing technology, the target gamut is the NTSC phosphor primaries. Since the optical systems we used have a common slit for all three colors to pass through, the key parameters in color design are the choice of center wavelengths, the slit position, and the slit width. Referring again to Figure 2.12, the slit position is given by  $f \frac{\lambda_0}{p_0}$ . The slit

width by  $f \frac{\partial \lambda}{p_0}$ . Thus, the design consists of choosing values for  $p_0$ ,  $\lambda_0$ ,  $\lambda_1$ ,  $\lambda_2$ , and  $\partial \lambda$ .

If  $p_0$  is large, then the diffraction angle is small and it may be difficult to spatially separate the diffracted light from the lamp mechanically. Also, the collimation requirements will be higher (*vide infra*). If  $p_0$  is too small, then the lithography becomes more difficult and the the diffraction angles become very large. In this case, scalar diffraction theory breaks down, and the grating depth for a null in the specular reflection no longer coincides with the peak in first order diffraction. An intermediate value of  $p_0 = 2.25 \mu m$  was chosen to yield high first order diffraction efficiency at a workable angle.

Wavelength [nm]	Periodicity theory [ $\mu m$ ]	Periodicity exp. [ $\mu m$ ]	Diffraction Angle [mrad]	$x, y$ theory	$x, y$ measured	$x, y$ NTSC
$625 \pm 30$	2.65	2.75	$236 \pm 13$	0.66, 0.33	0.54, 0.41	0.67, 0.33
$530 \pm 30$	2.25	2.25	—	0.22, 0.71	0.31, 0.62	0.21, 0.71
$465 \pm 30$	1.97	2.00	—	0.14, 0.05	0.17, 0.04	0.14, 0.08

Table 2.1: Basic values of color parameters.

The choices of  $\lambda_0$ ,  $\lambda_1$ ,  $\lambda_2$ , and  $\partial\lambda$  are governed by colorimetry. A white source spectrum  $S(\lambda)$  was chosen for generality. It is also a good approximation for a blackbody source at 3500°K, such as a tungsten halogen lamp. After the illumination spectrum was chosen, it was chopped into three possibly overlapping segments,  $\lambda_0 \pm \partial\lambda$ ,  $\lambda_1 \pm \partial\lambda$ , and  $\lambda_2 \pm \partial\lambda$ . The color coordinates of each segment were calculated while  $\lambda_0$ ,  $\lambda_1$ ,  $\lambda_2$ , and  $\partial\lambda$  were varied. Since making  $\partial\lambda$  as large as possible would result in a minimum of light being wasted at the telecentric stop,  $\partial\lambda$  was increased from zero until the color coordinates showed signs of decreasing saturation relative to the NTSC standard phosphors; a value of 30 nm matched the saturation of the NTSC phosphors.  $\lambda_0$ ,  $\lambda_1$ , and  $\lambda_2$  were selected by trying to match the wavelengths of green, red, and blue phosphors. The resulting values are summarized in Table 2.1 and plotted in Figure 2.13. A photomicrograph of the pixels themselves is shown in Photograph 2.1.

The color coordinates were measured with a spectra-colorimeter [Photo Research 1992] and are presented in 1931 CIE color coordinates [Hunt 1991]. Figure 2.13 shows the NTSC color gamut along with the theoretical and experimental gamuts. There is a definite loss of saturation of the green and red, although the blue is well-saturated. Figure 2.14 shows the color as a function of diffraction angle. From this plot it is clear that the problem is primarily in the collimation of the incident light: in the absence of good collimation, it is possible to saturate the red and blue by over-tuning, without ever getting a saturated green. For example, if the grating is over-tuned to the blue, then its spectrum will be mostly violet, regardless of the grating pitch. Although there is a loss of brightness (and contrast), it is possible to saturate the color fully. The same is also true of the red, since both red and blue are at the ends of the visible spectrum. The green primary is impossible to over-tune. Thus, the fact that the green coordinate is unsaturated in Figure 2.14 indicates that poor collimation is causing wavelengths outside the  $530 \pm 30$  nm to pass through the slit. To correct this, an angular source size of less than 13 mrad is needed, which corresponds to a linear source dimension of 0.65 mm. A source of approximately 1.0 mm was used.

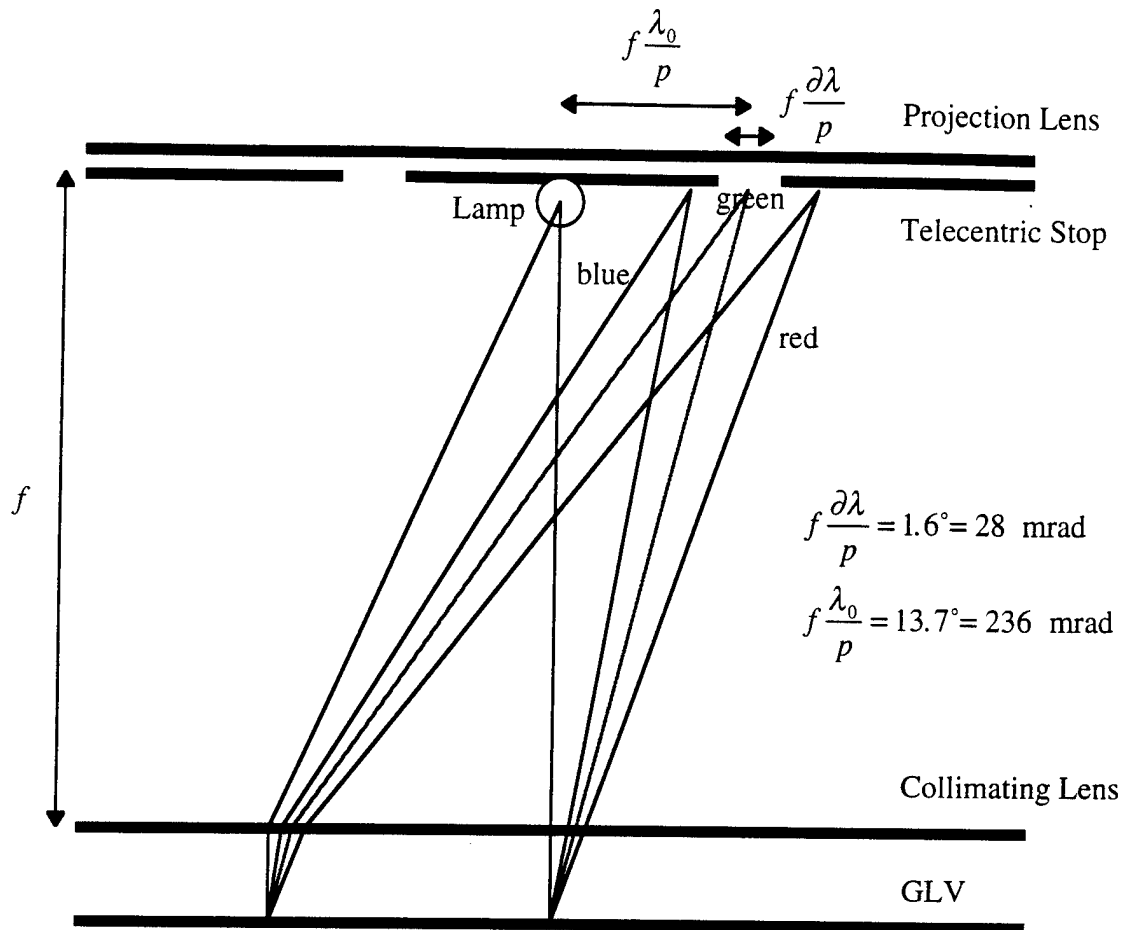
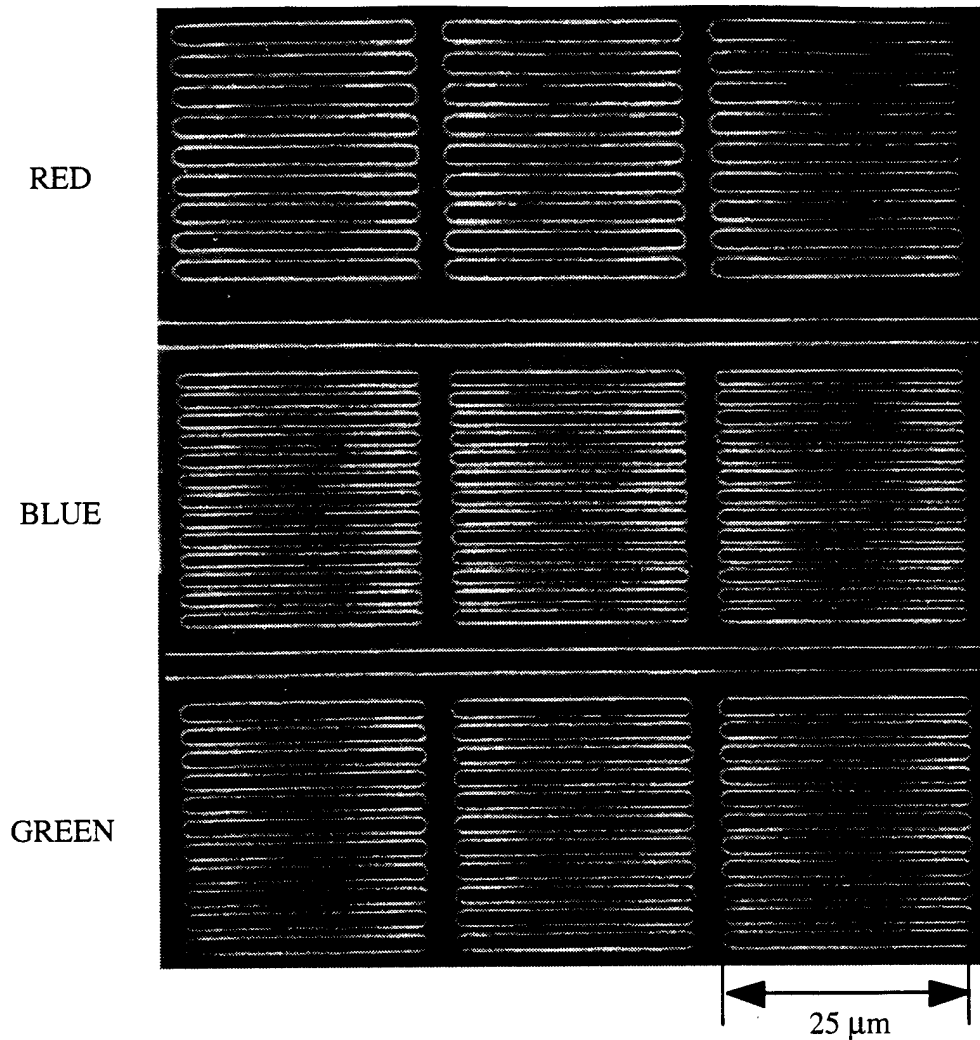


Figure 2.12: Basic optics of Schlieren system (III). This optical system places the lamp collimating lens in the diffracted light path. This innovation produces a very compact, folded optical system. The lamp illumination is collimated at the Collimating Lens. This light strikes the GLV normally, and a diffraction spectrum is produced a focal length away at the Telecentric Stop. Only a portion of the spectrum passes through, depending on the periodicity of the grating. Not shown is an eyepiece or viewer.





Photograph 2.1: SEM of color pixels. The first row corresponds to red, the second blue, and the third green. Each row consists of a series of devices (three are shown) that are electrically connected, which is why each pixel lacks a separate frame.

## 2.5 Color Contrast Ratio

The contrast ratio in the color case is not a simple function of device geometry. Rather, it is a function of the type of system used to project the color, the number of light valves, the number of mask levels, and how the contrast is defined. We will examine two types of systems under two definitions. The unoptimized case has a single light valve with only one beam/spacer thickness. This will ordinarily be optimized for the green. The second case is for a projector with three light valves, each optimized for a single color, or for a projector with a single light valve that has three different beam/spacer thicknesses.

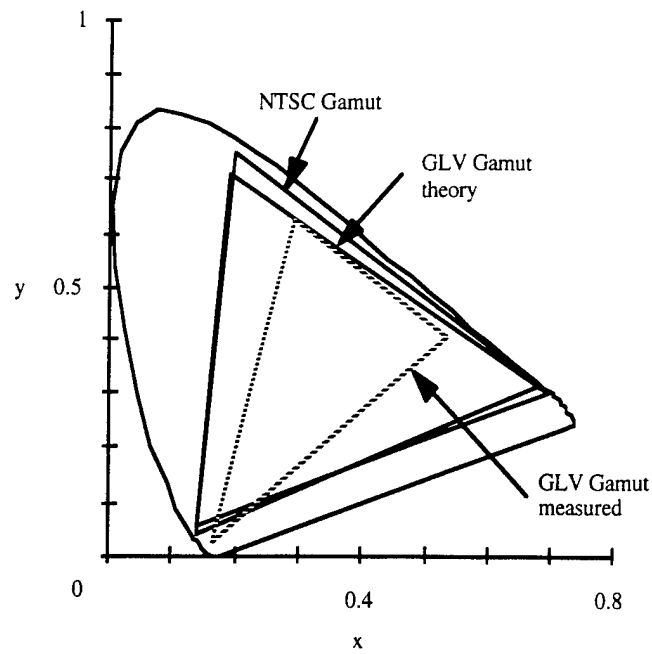


Figure 2.13: Measured color coordinates and theoretical values of the GLV with NTSC phosphor standards and the visible gamut. The outer ring indicates the visible gamut.

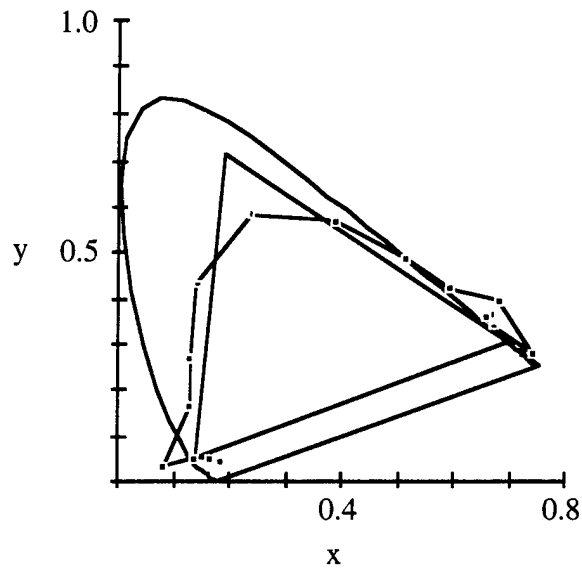


Figure 2.14: Color coordinates of green pixel as a function of diffraction angle. The angle is varied from 160 to 320 mrad. Points outside the edge of the rounded triangle of visible light are noisy.

The unoptimized case is typical of a low cost and weight product, while the optimized case is for higher performance.

The monochrome contrast ratio is the “on” brightness divided by the “off” brightness of a single pixel of a single color. The pixel contrast ratio assumes that each pixel consists of a RGB triad of devices. The pixel contrast ratio is the “on” brightness of a single device divided by the “off” brightness of the whole triad. The values of monochrome and pixel contrast ratios for both unoptimized and optimized systems are given in Tables 2.2 and 2.3. These calculations assume that the devices do not scatter light, have perfect sidewalls and have high beam/spacer thickness uniformity.

Color	Monochrome Contrast Ratio	Pixel Contrast Ratio
red	20	36
green	341	59
blue	22	6

Table 2.2: Contrast ratio for unoptimized system.

Color	Monochrome Contrast Ratio	Pixel Contrast Ratio
red	434	78
green	341	257
blue	375	27

Table 2.3: Contrast ratio for optimized system.

## 2.6 Pixel Size Limits

The GLV exhibits very high pixel densities. Early devices were constructed with 20 x 25  $\mu\text{m}$  frames. The most recent devices, with shorter beams, are 20 x 15  $\mu\text{m}$ . This gives a monochrome pixel density of 0.33 megapixel/ $\text{cm}^2$ , or a color density of 0.11 megapixel/ $\text{cm}^2$ . The question arises, how much further can the pixel size be reduced?

The basic expression for diffraction from a pixel is [Solgaard 1992]

$$I = I_0 (\text{Diff Order Intensities}) \left( \frac{\sin N\alpha}{\alpha} \right)^2,$$

where  $\alpha = \frac{\pi p}{\lambda} \sin \theta$ . The width of the central lobe is given by

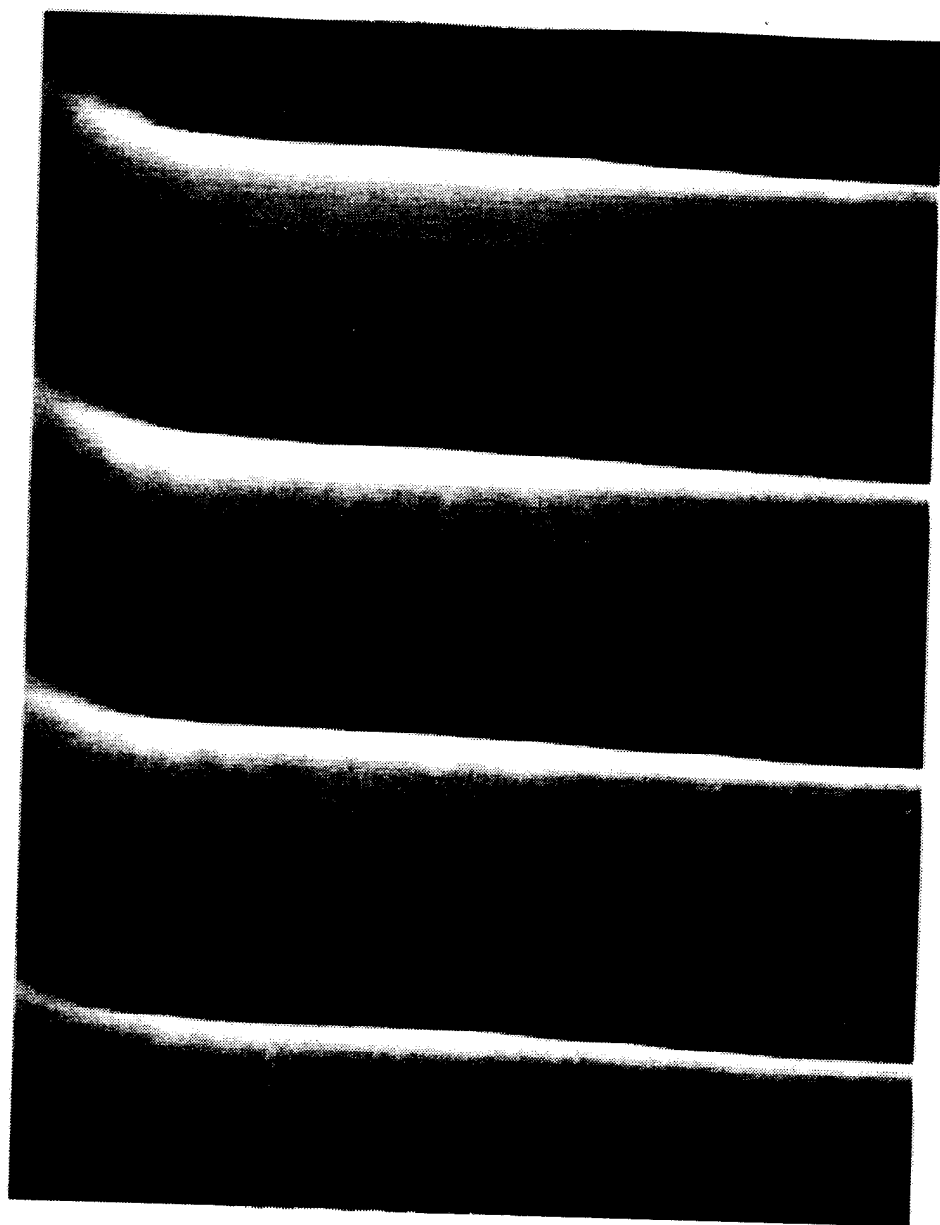
$$\sin \partial \theta = \frac{\lambda}{Np} < \frac{\partial \lambda}{p}$$

so the condition on N, the number of grating lines, for green light,  $\lambda = 530 \text{ nm}$  and  $\partial \lambda = 60 \text{ nm}$ , is

$$N > \frac{\lambda}{\partial \lambda} = 8.8$$

This sets the limit on color pixels as  $8.8 \times 2.25 = 19.9 \mu\text{m}$  across. For BW pixels  $\partial \lambda = 200 \text{ nm}$  and the limit is three times smaller:  $7 \mu\text{m}$ .

In the other direction, along the length of the beams, the limit is given by the aperture ratio. As the beams get shorter both the switching voltage and the amount of undeflectable beam at the ends increase. Since approximately  $3 \mu\text{m}$  of the beam is wasted ( $4 \mu\text{m}$  is more typical, but this includes the  $0.5 \mu\text{m}$  of the frame that is undercut), it is impractical to make a pixel shorter than  $10 \mu\text{m}$ . See Photograph 2.2. The one exception is if singly-supported cantilevers are used instead of doubly-supported beams. In this case pixels might be shortened to  $6 \mu\text{m}$  with a 50% aperture ratio.



Photograph 2.2: Sideview of stuck beams. This micrograph shows the distance over which the beams bend to the substrate.

# Chapter 3

## Mechanics of the GLV

### 3.1 Basics of hysteresis

The most striking feature of the mechanical operation of the GLV is the hysteresis of the deflection of the beams —and hence diffraction efficiency—as a function of applied voltage. Mechanical models of the deflection can provide scaling laws to help design and control the hysteresis. Two models will be presented, one analytical and one numerical. In both cases the reason for the hysteresis is the same, that the electrostatic attraction between the top and bottom electrodes is a nonlinear function of deflection while the mechanical restoring force caused by the beam stiffness and tension is linear. This is shown in Figure 3.1.

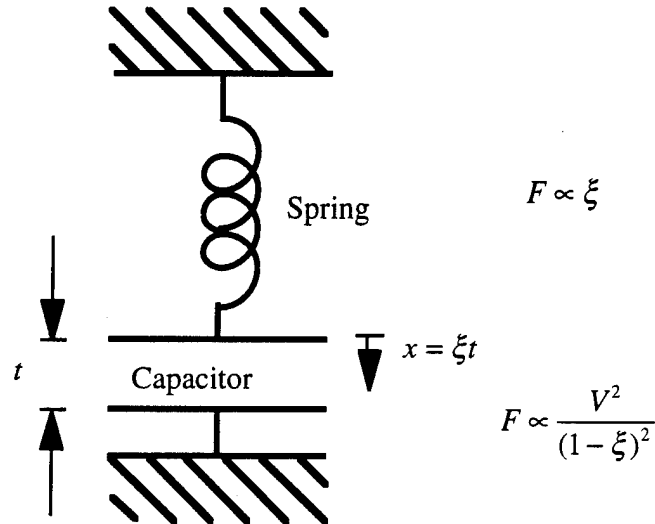


Figure 3.1: Basic model for the GLV beam mechanics. The spring represents the restoring force caused by the beam stiffness and tension. The capacitor represents the electrostatic attraction between the electrodes.

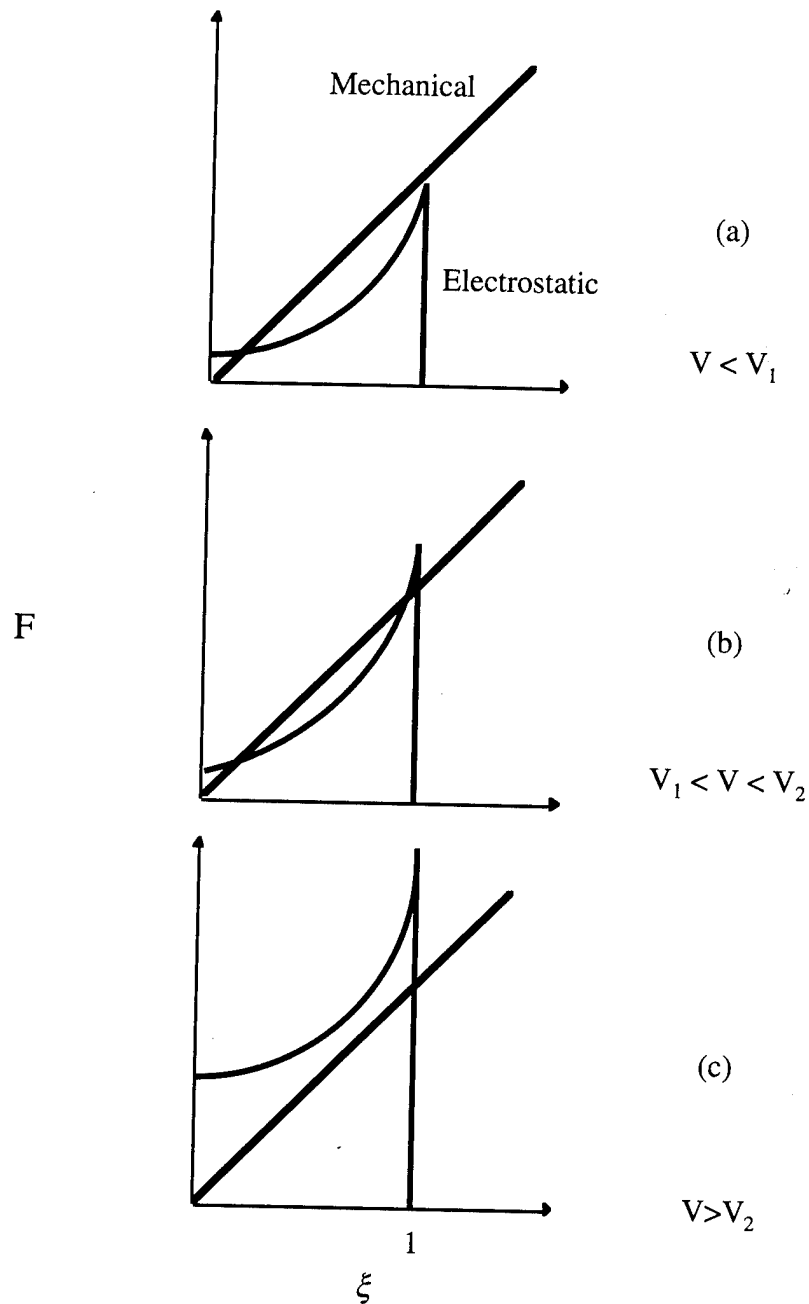


Figure 3.2: Origin of hysteresis. These curves plot electrostatic and mechanical forces as a function of normalized displacement (see Figure 3.1 for equations). When the applied voltage  $V < V_1$ , the first instability voltage, there is one stable solution in which the forces balance (a). If  $V$  is increased past  $V_1$ , then there are two stable solutions, one up and one down (b). For  $V > V_2$ , the second instability voltage, the beam must be in the down position, pinned to the substrate.

The source of the first equation in Figure 3.1 is a linear approximation of the deflection of beams with force. Unless the beam material violates Hooke's law, this approximation is sound. The second equation is the nonlinear force between the plates of a capacitor. The consequence of this nonlinearity of the electrostatic force is shown more clearly in Figure 3.2. The two curves for spring and electrostatic force are plotted vs. normalized displacement of the center of the beam for three voltage ranges. For small voltages, there is only one "load line" solution, in which the beam is slightly deflected. For intermediate voltages there are two solutions, one lightly deflected and the other in full contact with the substrate. For large voltages, the only stable solution is in full contact with the substrate. Thus, the devices shows a hysteresis reminiscent of a magnetic core.

The simplest model for the mechanical operation of the beams of the DGLV neglects the the moment of inertia of the beams. In this case the beam is considered as a string under tension, and the electrostatic force that drives the beam is lumped into the center of the beam. While the first approximation will be shown to be rigorous, the second is a major source of error, since it tends to dramatically underestimate the voltage needed to switch the beams. This fact is mitigated by the utility of the string model in examining scaling laws in analytic form, which is not possible with the numerical simulations that are in agreement with measured switching voltages.

## 3.2 Materials Parameters

The materials parameters and nominal geometry of the beams are given in Table 3.2. In this development we treat the beam and spacer thicknesses as equal. The Young's Modulus of our samples is imperfectly known. Measurements done with samples from the same LPCVD furnace give  $200 \pm 100$  GPa [Hong 1990]. However, other workers have reported inconsistent values for similar growth conditions [Kiesewetter 1992]. The average tension in the beams was determined using a scanning Helium Neon laser deflection system [Flinn 1987] as a function of dichlorosilane to ammonia flows within the furnace [Beck 1990].



Parameter	Symbol	Value
Young's Modulus	E	$200 \pm 100$ GPa
Average Intrinsic Tension	T	100- 800 MPa
Optical Index of Refraction	n	2.0 - 2.39
Relative Permittivity	$\epsilon$	6.45
Top Electrode Thickness		400 Å
Bot. Electrode Thickness		3000 - 6000 Å
Isolation Thickness		5000 Å
Spacer Thickness	t	1325 Å
Beam Thickness	t	1325 Å
Beam Width	w	1.0 - 1.5 $\mu\text{m}$
Beam Length	L	6 - 40 $\mu\text{m}$
Area Moment of Inertia	I	$w t^3/12 = 2.4 \times 10^{-4} \mu\text{m}^4$

Table 3.1: Basic physical and geometric factors of the GLV.

Dichlorosilane/Ammonia Flow	Residual Stress	Index of Refraction
1.0	800 MPa	2.04
3.0	420 MPa	2.19
5.2	80 MPa	2.38

Table 3.2: Three different types of nitride in use.

### 3.3 String Model

The force on a string, for small deflections at a point at the center, is linear. (See Figure 3.3 and Table 3.1 for definitions).  $x$  is the deflection of the beam at the center,  $\xi = x/t$ , and  $K$  is a parameter in units of force.

$$F = \frac{4 T t w}{L} x = K \xi$$

For the case that  $L = 15 \mu\text{m}$  and  $T = 800$  MPa we have  $K = 3.75 \mu\text{N}$ , which is the scale of the restoring force on a single beam element. The electrostatic force [Solgaard 1992] is a function of the applied voltage,  $v$ . The dimensionless parameter  $V$  is defined below.

$$F = \frac{1}{2} \frac{\epsilon_0 L w v^2}{(t-x)^2} = \frac{V^2}{(1-\xi)^2}$$

In this case we have neglected the finite contribution to the capacitance from the dielectric in the beam. When the beam is up, this contribution increases the capacitance by  $\frac{1}{\epsilon_r} \approx 16\%$ . At the inflection point the effect is 10%. The parameters are:

$$K = \frac{4Tt^2w}{L}$$

and

$$V = \sqrt{\frac{\epsilon_0 L w v^2}{t^2}}$$

The condition for the second instability point is that the number of crossing points in Figure 3.2 decreases from three to one. The force and spring constants of the electrostatic attraction and the beam tension must be equal, which is equivalent to saying that the second instability point occurs when the spring line is tangent to the nonlinear electrostatic curve.

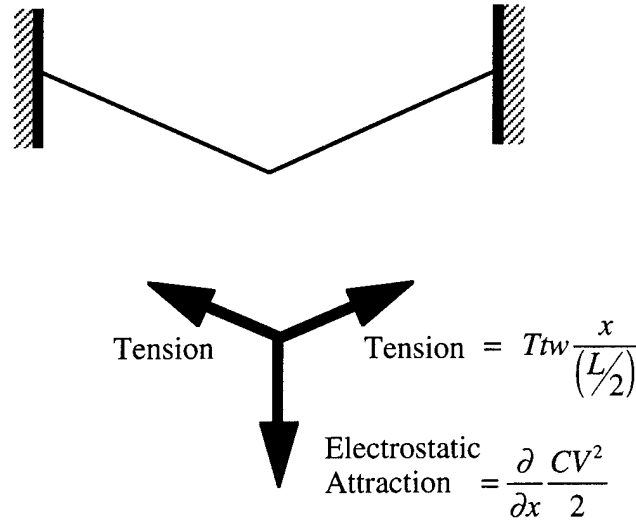


Figure 3.3: Modelling beams as strings. The upward restoring force is caused by tensile stress  $T$  in the beams, while the downward electrostatic attraction is the derivative of the stored energy in the beam capacitance,  $C$ , with deflection  $x$ .

The solution for the second instability point is

$$\xi_2 = \frac{x}{t} = \frac{1}{3}.$$

Thus, the instability point, beyond which the beam collapses with increasing voltage to the substrate, occurs at one-third deflection. As the voltage is retarded, the beam will spring up at the first instability point. This is given by

$$K = \epsilon_r^2 V_1^2.$$

If we now proceed to solve for the second instability voltage, we have

$$V_2 = \sqrt{\frac{32}{27} \frac{T}{\epsilon_0}} \frac{t^2}{L}$$

and

$$V_1 = \sqrt{\frac{27}{4\epsilon_r^2}} V_2 \approx 0.4 V_2$$

Numerically, these expressions underestimate the instability voltages by a factor of 2 compared to experiment. This is because of the assumption that the entire distributed electrostatic attraction is focused at the center of the beam. Nevertheless, the string model accurately predicts the scaling behavior of the switching voltage. Extreme sensitivity to material thickness has been observed, as well as the inverse linear dependence on beam length. Finally, a weak dependence on stress levels has been observed as well. This data will be presented in Section 3.4.1.

There are two major deficiencies with the string model. The first, which is minor, is that the model assumes the beams are long and floppy. An analysis that includes the finite stiffness of the beams gives [Cho 1992]

$$V_2^2 = \frac{8}{27} \frac{t^4 k T}{e_0 L} \frac{1}{\left(\frac{kL}{4} - \text{Tanh} \frac{kL}{4}\right)},$$

where  $k = \sqrt{\frac{Tw}{EI}}$ . For our geometries,  $k = 4 \mu\text{m}^{-1}$ ,  $kL \gg 1$ , and this expression reduces to the previous one. Thus, this error seems minor. However, when predicting the profile

of the beams near the spacer, the beam stiffness becomes important. The second shortcoming is that the deflecting force is lumped into the center of the beam, rather than distributed along the length. To overcome both of these problems, a numerical model was constructed to predict switching voltages more accurately.

### 3.4 Beam Model

The beam model overcomes both failures of the string model and gives accurate results for switching voltages. It is based on solving the 4<sup>th</sup> order beam equation [Hartog 1961]:

$$y^{(4)} - \frac{T}{EI} y^{(2)} - \frac{W}{EI} = 0$$

for the local deflection  $y(l)$ , a function of the position  $l$  along the beam.  $W(y)$  is the one-dimensional electrostatic pressure (N/m) forcing function

$$W(y) = \frac{\epsilon_0 w V^2}{2t^2} \frac{1}{\left(1 - \frac{y}{t(1 + 1/\epsilon_r)}\right)^2}$$

This inhomogeneous, nonlinear equation is best solved by the method of Green's functions with self-consistency. First, the equation is solved assuming that the forcing function is the delta function at position  $a$ . For  $l < a$  the solution is  $\tilde{y}(l; a) = y_1(l)$ , and for  $l > a$  the solution is  $\tilde{y}(l; a) = y_2(l)$ . Then, using an assumed beam displacement function  ${}^0y(l)$  we calculate a trial forcing function  ${}^0W({}^0y(l))$ . A new displacement function is generated by convolving Green's function with the trial forcing function:

$${}^{n+1}y(l) = \tilde{y}(l; a) * {}^nW({}^ny(a))$$

The iterations are performed until  $\|{}^{n+1}y(l) - {}^ny(l)\|$  is small. The algorithm can be made efficient by sampling the beam position at  $n$  grid points. In this case,  $\tilde{y}(l; a)$  is an  $n \times n$  matrix, and the convolution is a matrix multiplication.

To calculate  $y_1(l)$  and  $y_2(l)$  the homogeneous equation must be solved:

$$y^{(4)} - \frac{wtT}{EI} y^{(2)} = 0$$

and the boundary conditions are, for a unity magnitude delta functional at position  $a$  are:

$$\begin{aligned}
 y_1(0) &= 0 \\
 y_2(L) &= 0 \\
 y_1^{(1)}(0) &= 0 \\
 y_2^{(1)}(L) &= 0 \\
 y_1(a) &= y_2(a) \\
 y_1^{(1)}(a) &= y_2^{(1)}(a) \\
 y_1^{(2)}(a) &= y_2^{(2)}(a)
 \end{aligned}$$

and

$$y_1^{(3)}(a) - y_2^{(3)}(a) + 1 = 0$$

These boundary conditions are derived by integrating the delta function-forced beam equation from  $a - \delta$  to  $a + \delta$ . The homogeneous solutions are simple exponentials

$$\begin{aligned}
 y_1(l) &= a_1 + b_1 x + c_1 e^{l\sqrt{\gamma/EI}} + d_1 e^{-l\sqrt{\gamma/EI}} \\
 y_2(l) &= a_2 + b_2 x + c_2 e^{l\sqrt{\gamma/EI}} + d_2 e^{-l\sqrt{\gamma/EI}}
 \end{aligned}$$

Solution of these eight equations in 8 unknowns used a commercial math package [Wolfram 1991].

While many of the details of the solution are straightforward, one subtlety arose during the analysis: how to model the hard contact between the collapsed beam and the substrate. This is not a trivial problem. In this case we assumed that the substrate was springy, i.e. that it responded with a force proportional to the amount it was compressed. Some tuning of this parameter was needed to help keep the deflection iterations from oscillating. While for the present analysis this proved sufficient, any further modeling must include a viscous damping term to keep the solution from vibrating. It must be noted that oscillations in the solution are physical, in the sense that in vacuum the beams do vibrate with high  $Q$  [Solgaard 1992]. The viscous term must then represent the damping of air on the motion of the beam.

### 3.4.1 Switching Voltage

The first question we addressed with the beam model was the prediction of the second instability voltage (switching voltage). The experimental data are given in Table 3.3. The simulation results are in Figure 3.4.

Stress [MPa]	Beam Length[ $\mu\text{m}$ ]	Voltage, $V_2$
800	20	18
800	16	26
400	16	18
100	16	11

Table 3.3: Experimental second instability voltages.

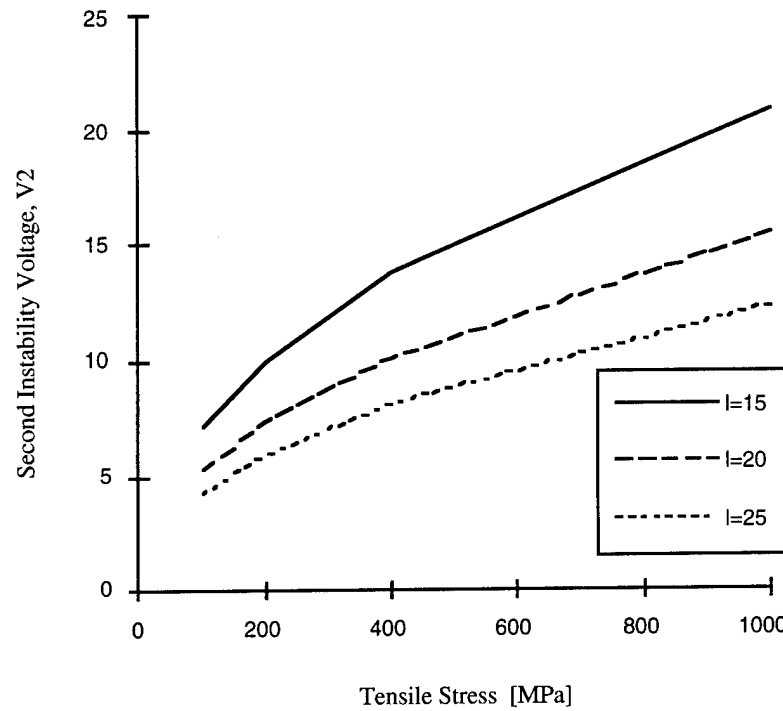


Figure 3.4: Results of beam model. Second instability voltage is plotted as a function of nitride tensile stress for three different length beams, 15  $\mu\text{m}$ , 20  $\mu\text{m}$ , and 25  $\mu\text{m}$ .

The simulated values are approximately 25% lower than the measured values, with no fitting parameters. As can be seen, the results are also consistent with the scaling laws pertaining to length and intrinsic stress. The underestimation of both the string and beam

models may be due to a common error, the use of the semi-infinite parallel plate capacitor model for the beam attraction. Since the gap to width ratio is about 1:10, stray field lines may decrease the capacitance enough to account for part of the 25% error. Two material parameters that are poorly known, Young's modulus and the dielectric constant of nitride, may also contribute. The dominant contribution is probably due to the addition of top electrode aluminum to the beams.

### 3.4.2 Peak Stress

The yield stress of our LPCVD nitride is not well known, so it is not possible to definitively determine how dangerous stress concentrations in the beams will be. According to the bending seen in SEM micrographs and the beam model, it takes a beam from 2 to 4 microns to deform down to the substrate. This means that the increase of peak stress over the average stress[Den Hartog 1949] is less than 400 MPa.

$$s = -\frac{1}{2} Et \frac{\partial \alpha}{\partial z}$$

where  $s$  is peak stress minus the average stress,  $z$  is the direction along the length of the beam, and  $\alpha$  is the angle between the tangent to the beam at  $z$  and the horizontal. The expression can be evaluated in the string model to give an estimate of the peak stress. Thus the maximum stress seen in high-stress devices is 1.2 GPa (400 MPa plus 800 MPa average stress), while the yield stress is nominally 14 GPa [Petersen 1982] (this value was measured for much thicker films and for only one reagent gas ratio). It is likely that stress concentrations due to surface roughness or cracks could produce much large stress concentrations.

### 3.4.3 Hysteresis

A simulation of deflection of the center of a beam in the beam model as a function of voltage is presented in Figure 3.5. The hysteresis width is represented quite well by  $V_1 \approx 0.4V_2$ , which was derived for the string model. The openness of the curve may be useful in passive-matrix addressing. Also, as per the string model, the normalized deflection at the second instability point is less than the 0.33 predicted by the string model.

In Figure 3.6 is a measured hysteresis curve for a single pixel on a striated substrate (as described in Section 4.4.5). Optical system II was used to make the measurement, with a

CCD camera in the microscope frame as the detector. There is a significant dark current in the CCD, so no contrast data can be taken from this curve.

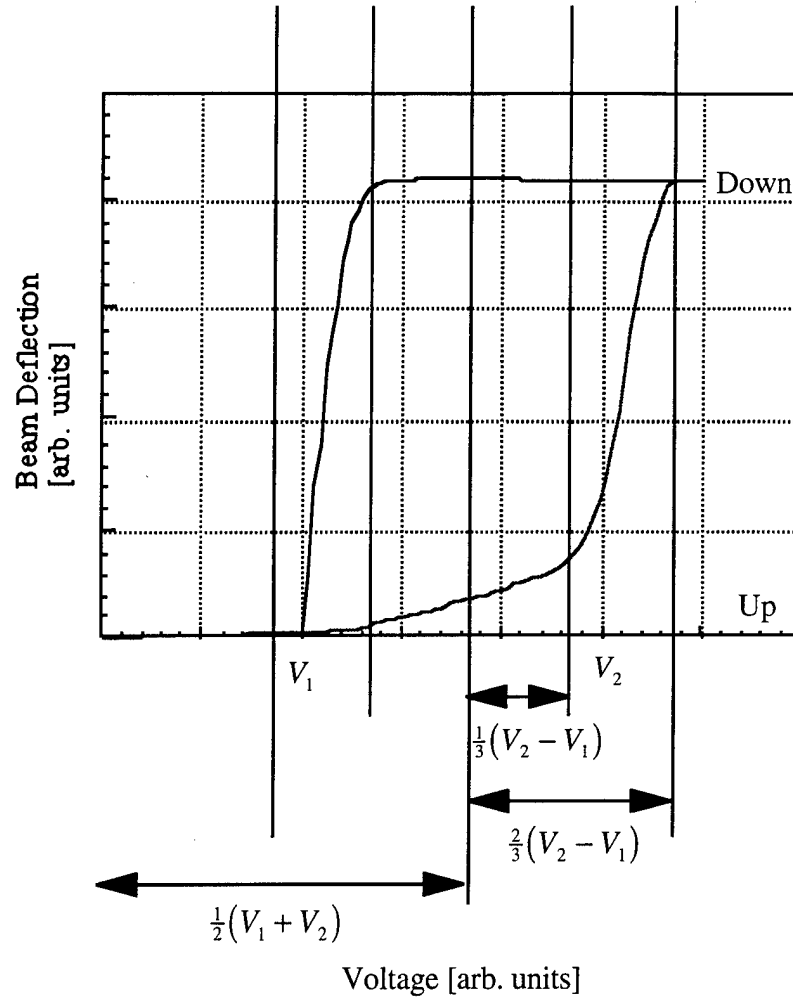


Figure 3.5: Simulated hysteresis curve. Note that  $V_1 \approx 0.4V_2$ , and that the beam is deflected by less than  $1/3$  at  $V_2$ .

### 3.5 Row-addressing Method

The use of inherent device bistability for a passively driven array of devices is a unique feature of micromechanical displays. Passive matrix row-addressing uses three state drivers. Rows are biased at ground, and the columns are biased at  $(V_1 + V_2)/2$ . See Figure 3.5. The frame is addressed twice, once to turn on pixels that are off, and the other to turn off pixels that are on. In the first case, the row is selected by applying  $-(V_2 - V_1)/3$ . Individual columns are turned on by applying  $(V_1 + V_2)/2 + (V_2 - V_1)/3$ . In this case the total voltage across the desired pixel is greater than  $V_2$ , so the pixel turns



on. The voltages on pixels in other rows and columns are all between  $V_1$  and  $V_2$ , so no pixels switch. Similarly, to turn pixels off, the rows are grounded except for one, to which  $+(V_2 - V_1)/3$  is applied. The columns that are to be unchanged remain at  $(V_1 + V_2)/2$ , but to the columns to be switched is applied  $(V_1 + V_2)/2 - (V_2 - V_1)/3$ . The desired pixel then has  $(V_1 + V_2)/2 - 2(V_2 - V_1)/3$ , which is less than  $V_1$ ; so the pixel switches off. Other pixels are left between  $V_1$  and  $V_2$  and do not switch. In this case, at the cost of addressing the frame twice as often, active matrix performance is achieved at passive matrix complexity. Several devices exhibited this behaviour, though they were destroyed in testing.

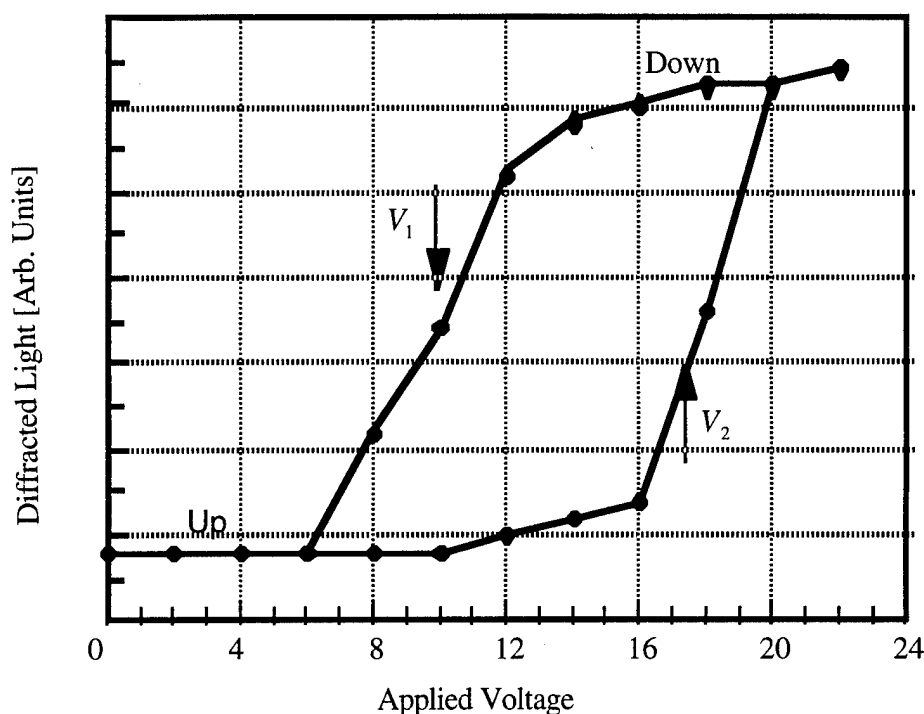


Figure 3.6: Measured hysteresis curve of a single pixel. The finite slope at the instability voltages are due to variation across the pixel of individual beams.

Contrast will be degraded from 80:1 to 40:1 because the beams are partially deflected under a  $(V_1 + V_2)/2$  bias. The way to fix this is to make the spacer thicker, to shift the hysteresis curve down. In this way the thicknesses can be adjusted so that  $(V_1 + V_2)/2$  produces minimal diffraction.

### 3.6 Speed

The resonant frequency of these devices is close to 10 MHz [Solgaard 1992]. They are faster than earlier devices because of smaller dimensions and higher residual stresses. The 10-to-90 switching speed is 20.5 ns (see Figure 3.7). This speed of switching makes the GLV the fastest light valve of which the author is aware, roughly 500 times faster than TI's valve and 500,000 times faster than LCDs on the market. This speed is useful because it allows the device to operate in a row by row fashion. This eliminates the need for a full set of data latches for the entire frame—two orders of magnitude savings in transistor count.

Rate	Events per Frame	Frequency
Frame Rate	1	60 Hz
Frame Address	2	120 Hz
5 bits gray scale	32	3.8 KHz
Line Rate (VGA) noninterlaced	480	1.8 MHz

Table 3.4: Time budget for row by row addressing. A 1.8 MHz line rate is used to address a non-interlaced VGA display with 15 bits (i.e., 5 bits per color).

### 3.7 Temperature Limits

If the GLV is used in a projection system, it is likely that an extremely bright and high power source will be used. About 5% of the incident light will be absorbed by the aluminum top reflector, and this light will heat the device. Since the materials used are fairly stable with respect to temperature up to 400°C, the melting point of aluminum, it is expected that the GLV will be robust with temperature. However, it is important for the driver design that the instability voltages not change too much with temperature.

Using the values in Table 3.4, the average stress in beams composed of 1325 Å of nitride and 400 Å of aluminum decreases by 0.25 MPa/°C. Therefore, at 400°C the average tensile stress in the beams decreases by only 100 MPa, which results in approximately a 25% shift in instability voltages for low residual stress devices. The change is correspondingly smaller for higher stress devices.

Another problem is the fact that the aluminum, which becomes compressed by the smaller thermal expansion coefficient of silicon, may force the beam to deflect up past the plane of the spacer. Because of the dependency of the materials parameters on deposition technique, this possibility should be explored experimentally. Since only 5% of the incident illumination is absorbed, it is extremely unlikely that any lamp could heat a GLV past 150 or 200 °C.

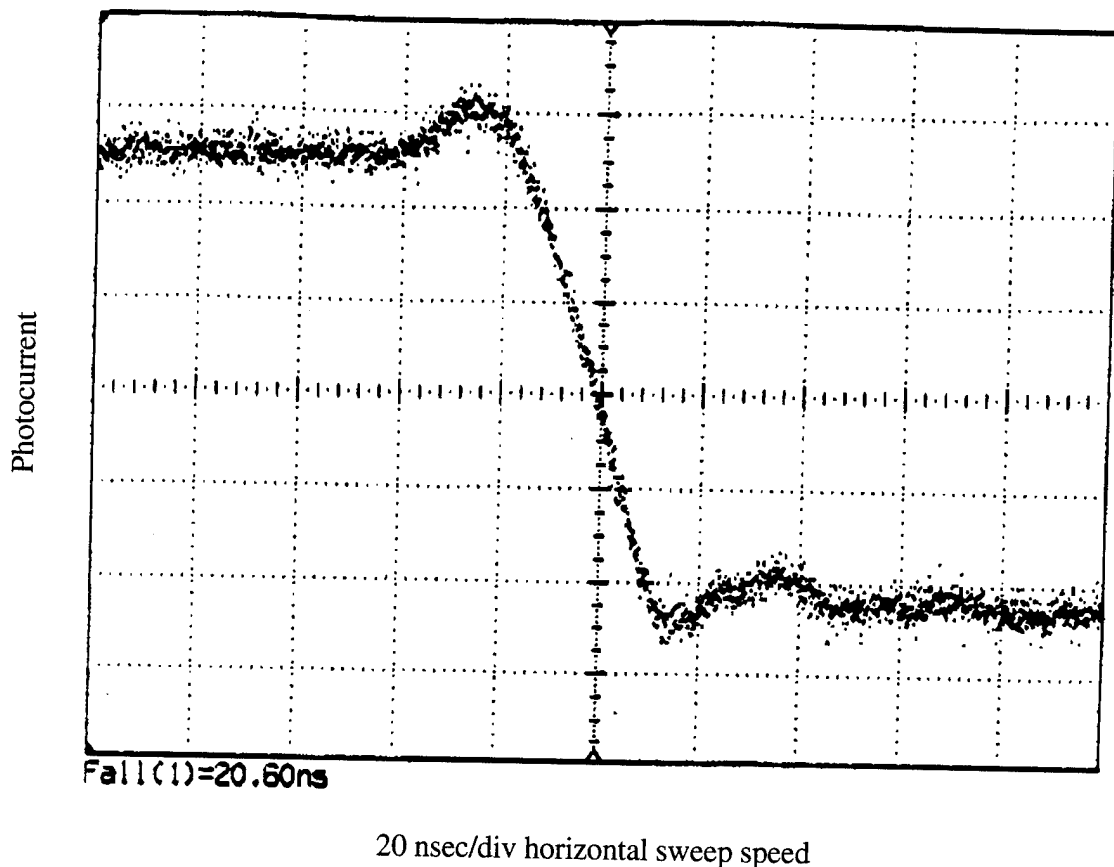


Figure 3.7: Pixel switching in 20.5 ns. The photocurrent from a single 25 x 25  $\mu\text{m}$  pixel is shown as measured on a silicon photodetector on optical system I. The pixel switches from the up to the down position. The rise before the transition is thought to be an artifact of the measurement.

Material	Youngs Modulus [GPa]	Thermal Expansion [ $10^{-6}/^{\circ}\text{C}$ ]
Al	70	25.0
Si	73	2.33
Si <sub>3</sub> N <sub>4</sub>	200	0.8

Table 3.4: Materials parameters for thermal expansion. [Petersen 1982]

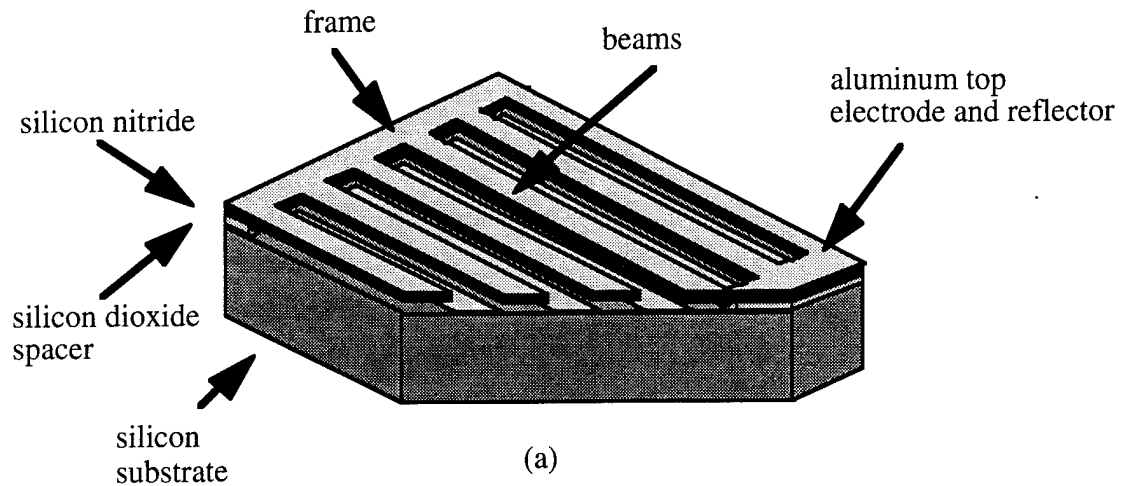
# Chapter 4

## Fabrication of the GLV

### 4.1 Basic Process

The GLV can be fabricated in its simplest form with only a single mask. The morphology of a single pixel is shown in Figure 4.1. The pixel is defined by a frame which extends along the front and back edges. Connecting the two pieces of the frame are several beams, which are the moving parts of the device. Beneath the frame is a spacer layer, which supports the frame away from the substrate. An air gap separates the beams from the substrate, which is conducting. On top of the beams, the frame, and the exposed areas of the substrate is a thin layer of metal, which enhances the reflectivity of the structure and serves as the top electrode.

Fabrication of linear arrays of these devices is diagrammed in Figure 4.2. The first step is to deposit on an prime silicon wafer a 1325 Å thick layer of silicon dioxide (hereafter abbreviated "oxide") followed by 1325 Å of silicon nitride ("nitride"). The nitride is patterned to form the frame and beams of the device. Then an isotropic, selective etch is used to undercut the oxide from beneath the beams. In order to free the beams, at least 0.75 μm of undercut is needed. However, this is not enough to completely undercut the oxide from beneath the frame. In this way the frame remains supported by the oxide, and the beams are free but supported at their ends. Since a silicon rich LPCVD nitride is used, the beams are under tension. Finally, 400 Å of aluminum are evaporated onto the top of the structure to form the top electrode and reflector. The wafers are then diced.



beams held up  
by tensile stress

(b)



beam pulled down  
electrostatically

(c)

Figure 4.1: Single pixel of the one mask GLV process (a). Beams in the undeflected position (b). Beams pulled against the substrate (c). Not to scale.

1: Deposition of sacrificial layer and bridge material



2: Patterning of bridges



3: Etching of sacrificial layer



4: Metallization

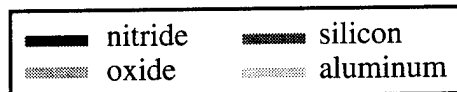


Figure 4.2: Schematic of single mask process.

## 4.2 Isolation

Device to device isolation is essential for device operation. Although electrical devices typically rely on reverse-biased junctions or mesas, only mesas are suited to micromechanical devices.

The problem with reverse-biased junctions arises from the fact that the 10:1 width-to-thickness ratio makes it difficult to clean contaminants from under the beams. For this reason, it is undesirable to use photoresist on the GLV after the top electrode/reflector layer has been evaporated. Without a patterning, the electrode material will short the isolation junctions. Another problem is that the large operating voltages of the GLV, up to 30 V, can cause avalanche breakdown of the isolation junctions.

In order to design a mesa isolation process that requires no masking steps after the metal deposition, overhanging features are needed. Fortunately, the nitride layer of the GLV overhangs the oxide spacer by over half a micron in all directions, providing maskless device isolation. This overhang is an artifact from the release-etch process, which has to undercut by at least one half of the width of the widest beam. In color devices this means at least 0.75  $\mu\text{m}$  of nitride overhang the oxide.

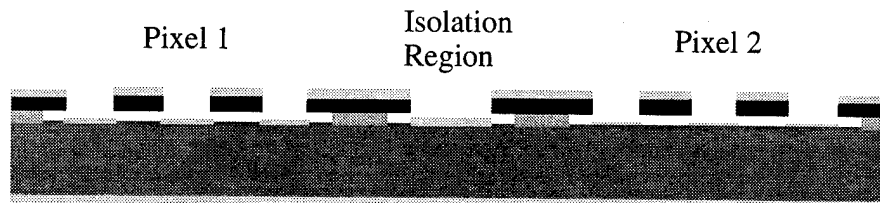
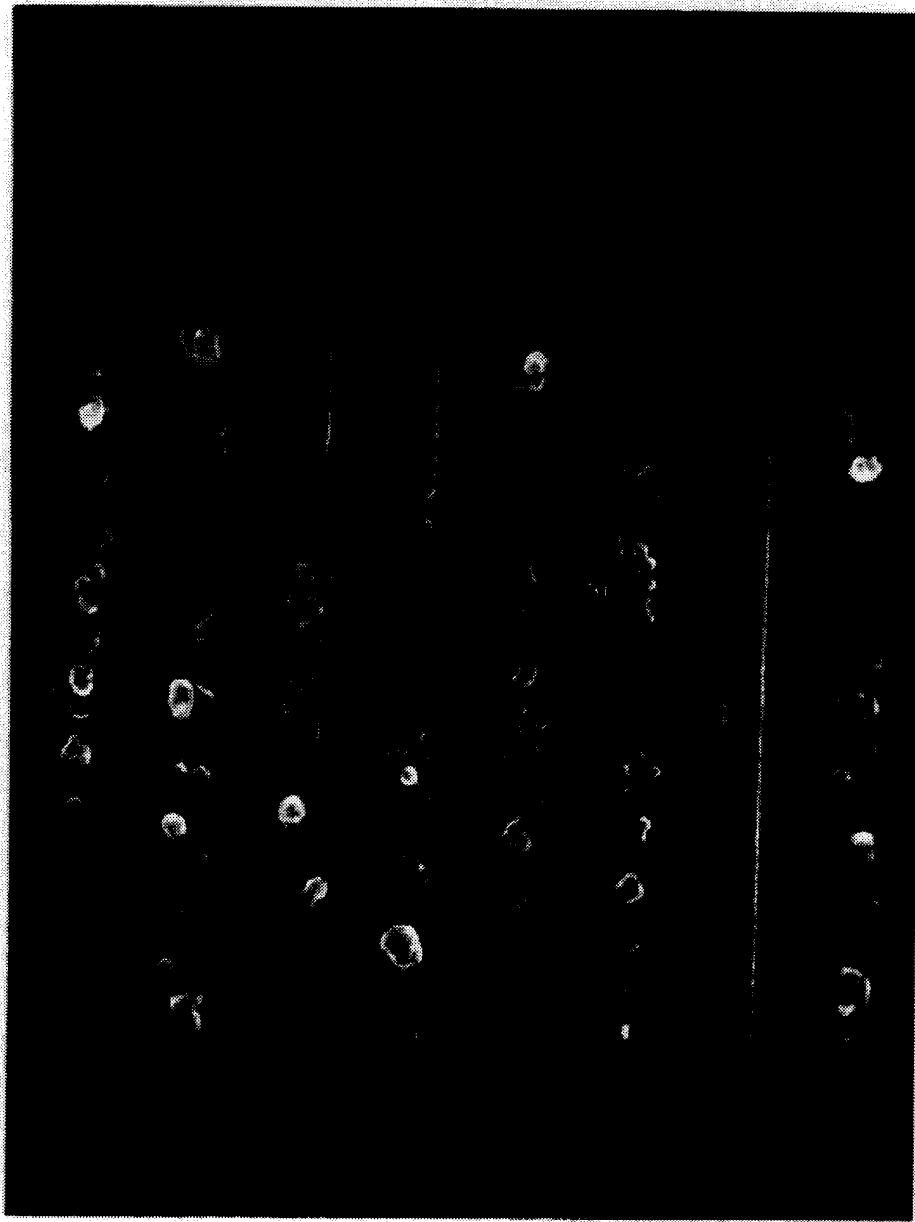


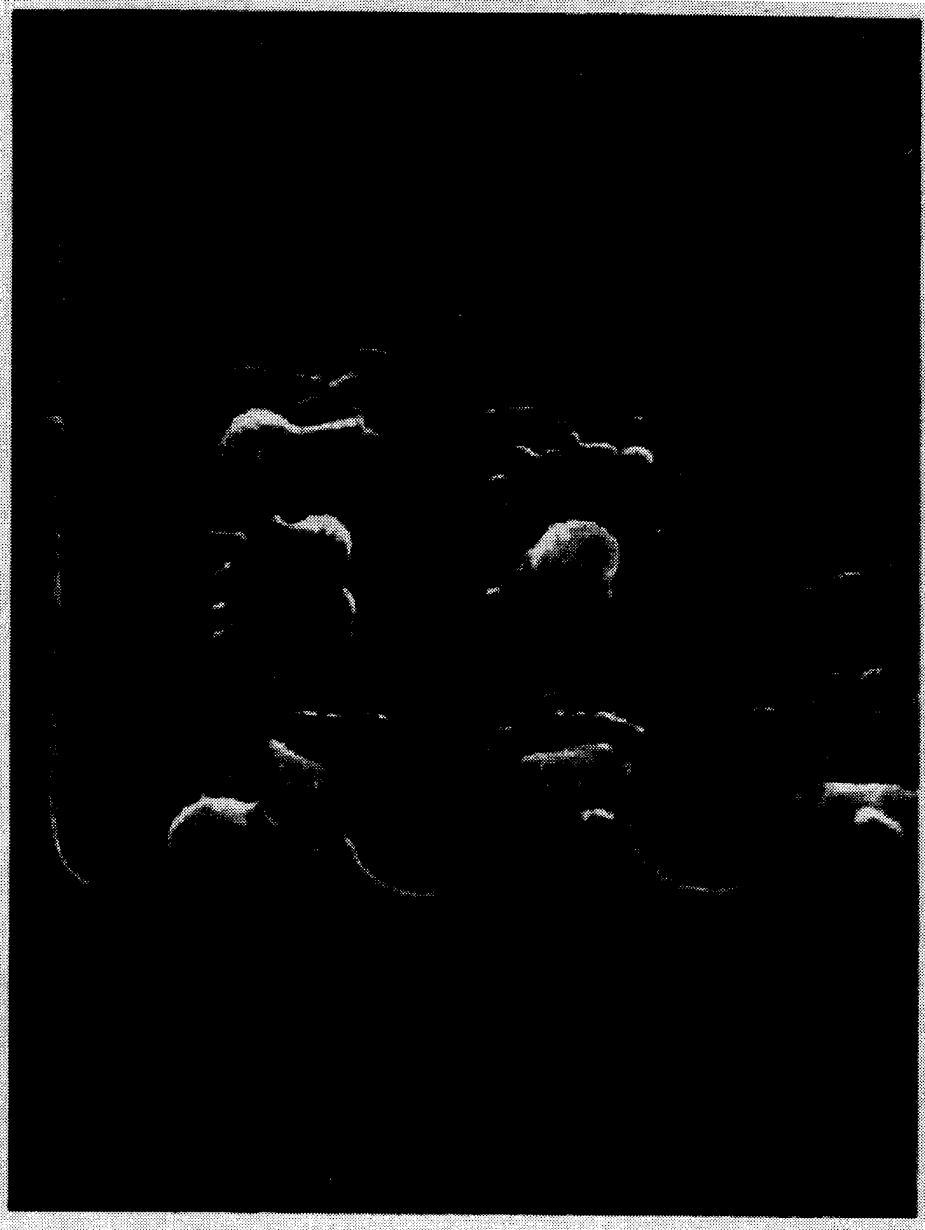
Figure 4.3: Device to device isolation.

In the case of an ideal device with a perfectly evaporated top-electrode, the thickness of the metal could approach that of the oxide spacer, over 1000 Å. However, if the quality of the sidewalls is poor, then it becomes apparent that thick metal can increase the likelihood of shorting when the beams are brought into contact with the substrate as in Figure 4.4. Peak fields in air and nitride can approach 200 V/ $\mu\text{m}$  for an ideal device. If the sidewalls are imperfect, the fields can increase several-fold, to perhaps 1 KV/ $\mu\text{m}$ . These fields are dangerously close to the dielectric breakdown fields. For this reason thinner aluminum was used, with some loss in conductivity and reflectivity. Photographs 4.1 and 4.2 show devices that may have been destroyed by shorting (see Section 4.7).



Photograph 4.1: Grating destroyed by shorting and fusing. The failure of these beams is attributed to poorly insulating nitride and electrostatic break down. This hypothesis is supported by the fact that single beams have not been observed to fail in this way: this process either affects an entire wafer or is absent. The destruction of gratings is far less common than sticking as a failure mode. Fusing occurs at low voltages, typically less than 20 V.





Photograph 4.2: Closeup of fused beam.

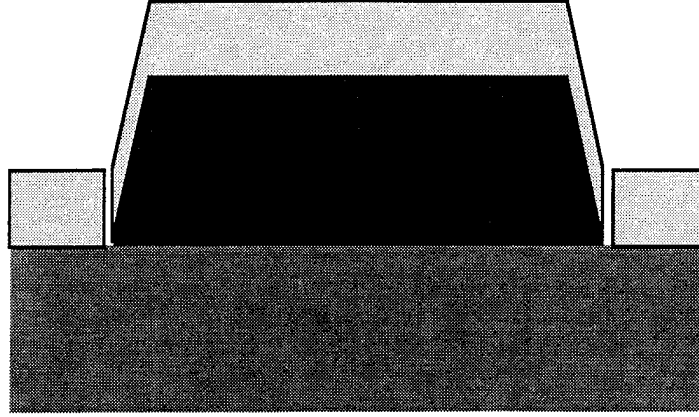


Figure 4.4: Field concentration caused by poor sidewalls.

### 4.3 Interconnect Conductivity and Reflectivity

To enable simple line-by-line addressing of the GLV in a megapixel display requires an RC charging time for a row (or column) of 100 ns or better. This in turn requires a sheet conductivity of  $0.5 \Omega$  (per square). This is achievable with a variety of metal interconnects including aluminum, silver, and common group VIII metals. Of these, aluminum and silver are the two with good reflectivity. Silver suffers from corrosion problems compared to aluminum, so aluminum was chosen for the top electrode (and the top surface of the bottom electrode, since the deposition isn't masked or etched). The thickness of aluminum needed for  $0.5 \Omega$ , which is  $750\text{\AA}$ , is too thick given the slope in the nitride sidewalls as discussed above. Therefore, a thinner aluminum layer was used. The sheet conductivity of  $400\text{\AA}$  of aluminum is  $1 \Omega$ . The decrease in conductivity will be problem for large arrays but is not an issue for the smaller arrays tested here.

The reflectivity of a thin layer of aluminum on top of nitride is given as [Ramo 1984]:

$$R = \left\| \frac{Z - Z_0}{Z + Z_0} \right\|^2$$

where

$$Z = Z_{Al} \frac{Z_{SiN} \cos \beta L + j Z_{Al} \sin \beta L}{Z_{Al} \cos \beta L - j Z_{SiN} \sin \beta L}$$

and  $Z_{SiN} = 154\Omega$ ,  $Z_{Al} = 5.3 + 53j\Omega$  [Palik 1985],  $Z_0 = 377\Omega$ , and  $\beta = 2\pi/\lambda$ . The reflectivity  $R$  is 0.33 for  $L=200\text{\AA}$  of aluminum, and 0.75 for  $400\text{\AA}$ . The same result

holds for silicon, with  $Z_{Si} = 108\Omega$  and reflectivities of .38 and .84 for 200 and 400Å, respectively. Although 400 Å is not desirable from either reflectivity or conductivity considerations, it is a fair compromise with minimizing the thickness. With improved sidewall formation, 750Å of aluminum will satisfy reflectivity and conductivity requirements for the top electrode.

Mechanically, the main effect of the aluminum is to add mass and stiffness to the cantilevers. Young's modulus of aluminum is 70 GPa, but the increase in beam stiffness is primarily due to the increase in beam thickness. For normal operation of the devices, the elastic limit of aluminum is exceeded, so Hooke's law is no longer valid. For this reason the aluminum was neglected in the modelling in Chapter 3, with a resulting underestimate of switching voltages.

Other possibilities for the bottom electrode include metal silicides and polysilicon. The bottom electrode will generally be covered with a layer of materials from the top electrode deposition: the only optical requirement of the bottom electrode is smoothness. But silicides and polysilicon suffer from unsatisfactory conductivities. The advantage, however, is that both are stable at much higher temperatures than simple metals [Murarka 1993]. In particular, polysilicon is stable at 785 °C, the temperature for LPCVD nitride deposition. In this work polysilicon is used for the bottom electrode. Ultimately a more conductive bottom electrode will be required.

## 4.4 Sticking

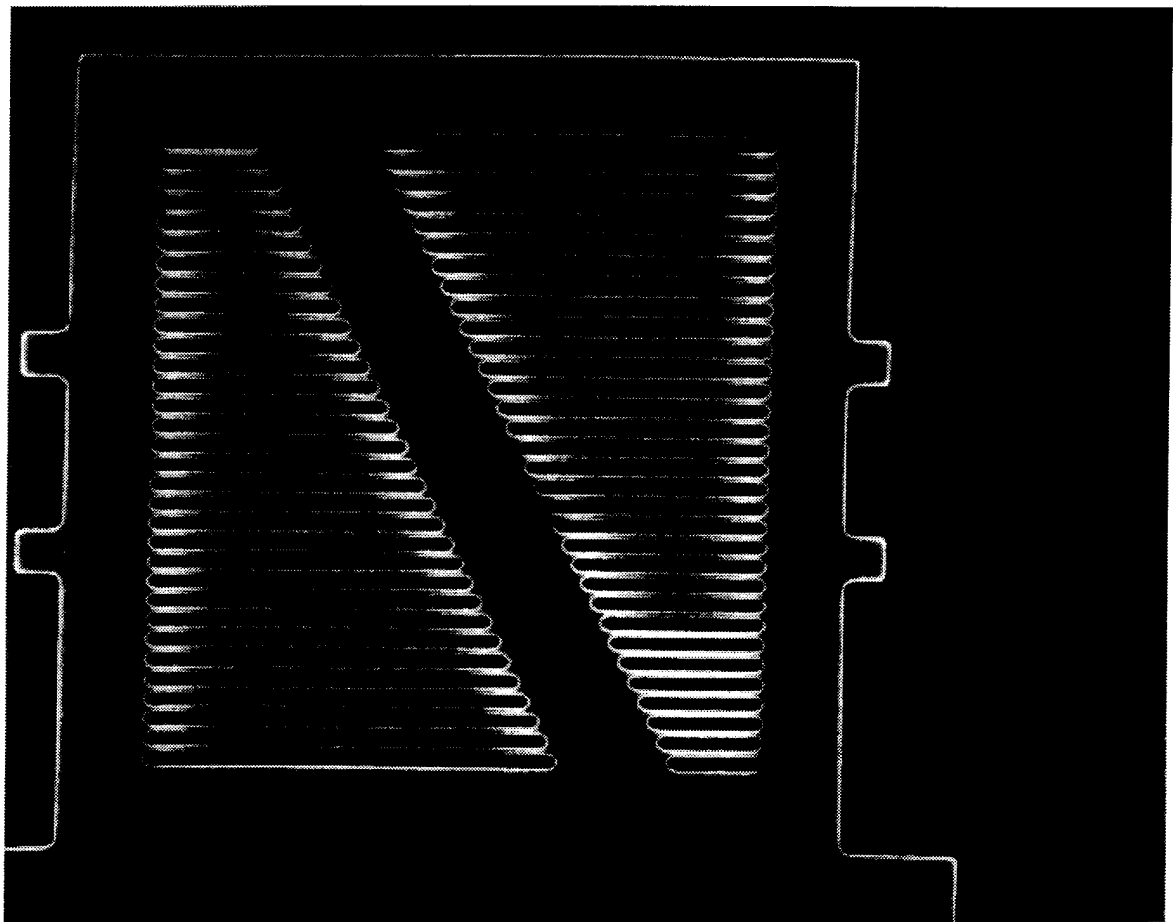
Whenever the beams of the GLV are brought into contact with the substrate (or underlying interconnect) there is a possibility of sticking. Sticking generally occurs either during the drying step after the oxide release etch or when the beams are switched down into substrate contact by a voltage exceeding  $V_2$ . In the absence of a third electrode, which could supply an upward electrostatic attraction to raise stuck beams, sticking must be regarded as a device failure. As a failure mode, it is not catastrophic, since sticking usually is not accompanied by short- or open-circuiting (which then destroys a row or column).

The basic mechanism of sticking depends on when it occurs. During fabrication, as the water that fills the volume beneath the beams evaporates, surface tension of the fluid pulls the beams into contact with the substrate. It was postulated [Alley 1992b] that

solutes in the evaporating fluid that remain behind can covalently bond the beams to the substrate. Since beams that have been stuck in this way take several hours to become unstuck when re-immersed in water, it is assumed that the binding energy is large.

#### 4.4.1 Water

If the beams become stuck during operation, the likely culprit is hydrogen bonding mediated by moisture between hydrogenated and hydroxylated surfaces [Scheeper 1992]. In the GLV the beams are made of nitride, which can hydroxylate, and the substrate of silicon, which can oxidize. The test of the applicability of this theory to the GLV is quite simple: much higher device yields and longer device operation are seen for light valves operated in a flowing dry nitrogen ambient. Also, device failure from sticking during operation is reduced for wafers that are stored in a dry vacuum chamber. In order to quantify these results, beam peeling theory will be reviewed in the next section.



Photograph 4.3: Harp structure.

Sensitivity to water vapour is not unique to GLVs, and when manufactured they can be baked and hermetically sealed in packages.

#### 4.4.2 Beam Peeling Theory

An excellent theory that analyzes the dynamics of beam sticking has recently been published by Mastrangelo [Mastrangelo 1992; Mastrangelo 1993a; Mastrangelo 1993b]. The applicable formula for  $L_h$ , the minimum beam length that will be stuck, is given as a function of the average stress in the beam,  $\sigma_R$ , the specific binding energy,  $\gamma_s$ , and the ratio of surface contact area to total area under the beam,  $\delta$ :

$$L_h^4 = \left( \frac{128Et^5}{5\gamma_s\delta} \right) \left( 1 + \frac{4\sigma_R L_h^2}{21Et^2} \right)$$

The equation can be solved numerically; the elastic modulus term that comes from the stiffness of the beam and the residual stress term are both significant—neither beam stiffness nor beam stress dominates. Mastrangelo finds  $\gamma_s = 270 \text{ mJ/m}^2$  for hydrophilic (water attracting) and  $\gamma_s = 100 \text{ mJ/m}^2$  for hydrophobic (water repelling) surfaces; our data (see Figure 4.6) agrees with the hydrophilic finding. The reason hydrophilic surfaces have a higher binding energy than hydrophobic is that hydrophilic surfaces have hydroxyl groups that can hydrogen bond, while hydrophobic surfaces use the weaker Van der Waal's bond.

The basic means of testing the specific binding energy is through the use of a test structure that has a number of different length beams, from 10 to 40  $\mu\text{m}$ . This “harp” structure is shown in Photograph 4.3. Generally, all the beams longer than a certain length,  $L_h$ , will be stuck, while all the shorter beams will be up. This is shown on an atomic force micrograph in Photograph 4.4. To have high yield, a GLV device should be designed with  $L < L_h$ . As discussed in Section 2.6, it is desirable to make  $L$  between 10 and 20  $\mu\text{m}$ . This requires that  $L_h$  be at least 20  $\mu\text{m}$  if not 30. Initial values were  $9 \pm 2 \mu\text{m}$ . The resulting value of  $L_h$  for each process variation will be given, and the results are summarized in Section 4.4.8.

#### 4.4.3 Stress

The simplest way to decrease sticking is to increase the residual stress in the film. This can be accomplished by varying the ratio of dichlorosilane to ammonia in the nitride LPCVD reactor [Beck 1990]. Stresses from 100 MPa to 800 MPa are possible without

compromising the stability and breakdown characteristics of the film. The first step in decreasing sticking was to move from using 100 MPa films to 400 and 800 MPa. This resulted in  $L_h$  increasing from less than 10  $\mu\text{m}$  to 12 or 13  $\mu\text{m}$ , in agreement with Mastrangelo's equation. The tradeoff for decreased sticking is increased operating voltage.

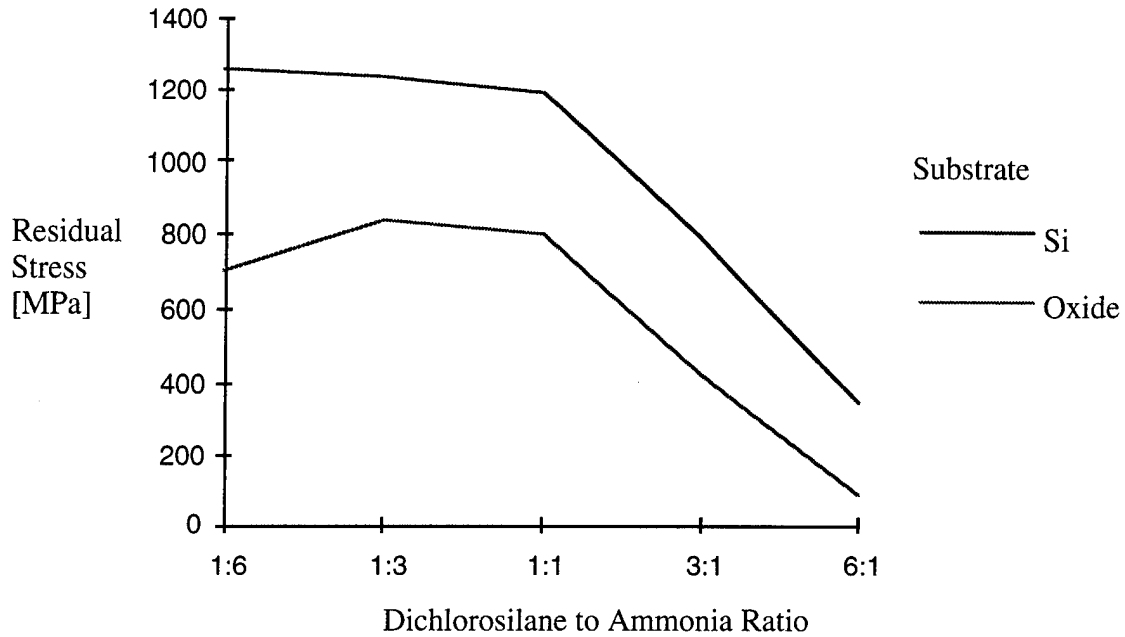


Figure 4.5: Control of residual stress in LPCVD nitride. From [Beck 1990].

#### 4.4.4 Surface Treatments

After increasing the residual stress, the next approach to increasing  $L_h$  was to decrease  $\gamma_s$ , the specific binding energy. Mastrangelo reported a decrease of  $\gamma_s$  to 100 mJ/m<sup>2</sup> when the binding surfaces were changed from hydrophilic to hydrophobic. This is consistent with [Scheeper 1992]. Bare silicon is hydrophobic, but its oxide is hydrophilic. So while a freshly released wafer may have a hydrophobic surface, within hours that surface becomes hydrophilic.

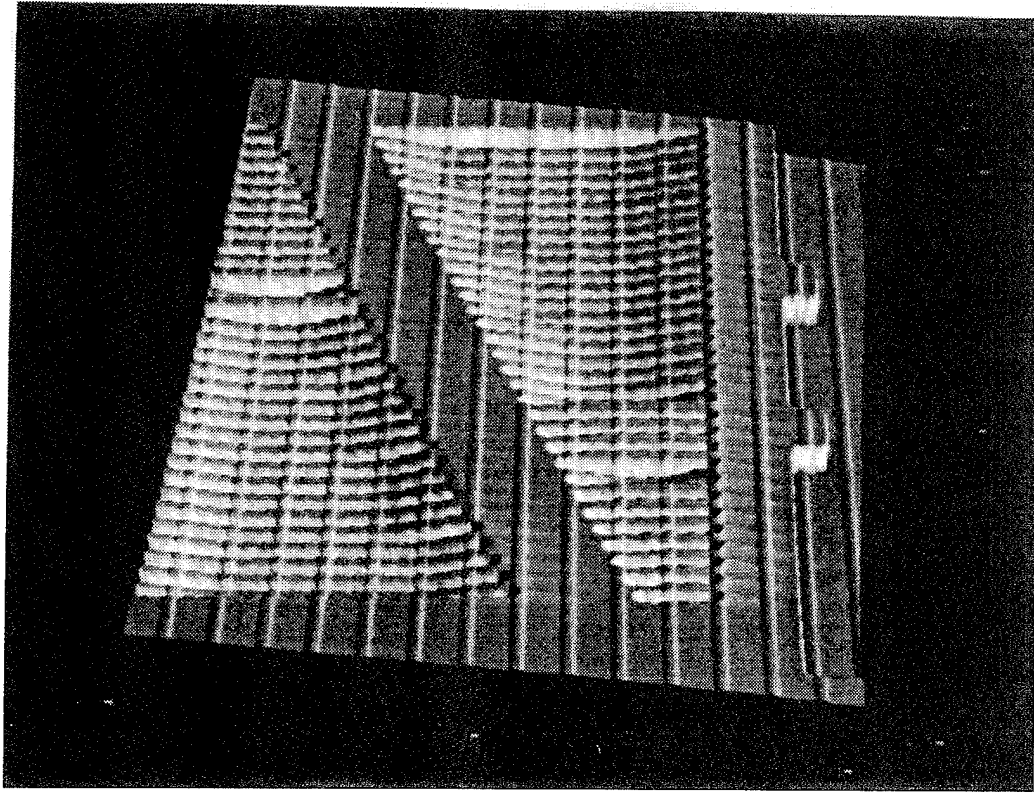
One strategy for solving this problem is to bond a hydrophobic monolayer over the oxidized surface, since preventing the formation of a surface oxide is difficult in a packaged device [Alley 1992a; Alley 1992b]. Alley's octadecyltrichlorosilane method was tried on the GLV with no success. The beam sticking became worse than before; all

beams in the harp structure stuck to the substrate. Since the chemistry of the surface treatment required anhydrous conditions, wafers were transferred from the release-etch bath to dry, organic solvents. If the large aspect ratio of the areas under the beams impeded diffusion of water from these regions, then the silating agent would bond to the water rather than the oxidized surface. This produced a hydrated polymeric material beneath the beams that ruined the devices. It is thought that this process should be able to be developed for the GLV to avoid this problem, but it promises only a two fold improvement in  $\gamma_s$ . Since  $L_h$  depends on the product of  $\delta$ , and  $\gamma_s$ , another approach is to reduce the effective area of contact between the bottom of the beam and the substrate, which is discussed in the next section. Other work has been done to reduce the contact area which is not discussed here [Sandejas 1993].

#### 4.4.5 Striations

If the substrate beneath the beams is corrugated, then  $\delta$  is reduced by the ratio of the change in surface contact area. For example, if the substrate is etched to produce 100 Å tall lines, 1 μm wide, spaced every 5 μm, then the total contact area is reduced by a factor of five. The lines, hereafter referred to as "striations," are in the direction perpendicular to the beams. This assumes that when the beams are brought into contact with the substrate, they only hit the tops of the lines, not the spaces in between. In order to insure this, the switching voltage for 5 μm long beams with 100 Å gaps was calculated using the beam model and found to be larger than that needed to switch 15 μm beams with .1325 μm gaps. See Photographs 4.4 and 4.5.

This method of reducing  $\delta$  has three variables, the height of the striations, the width of the striations and the line-to-line spacing. Increasing the height of the striations is desirable because it allows the line-to-line spacing to increase. The height of the striations is limited by it's effect on contrast ratio. Heights of 100 Å do not reduce contrast appreciably (see Figure 4.8 and the fact that the striation only occupies 0.2 or less of the surface). With 100 Å high striations, the line-to-line spacing can be several microns, at least 5 if not 10. The striation width is limited by lithography or processing techniques. Since we used lithographically defined striations with no etch-stop (which would uncouple the striation width and height), we were limited to 1 μm wide striations. This gives a total  $\delta = 5$ . This geometry increased  $L_h$  from 13 to 22 μm, which again agrees with Mastrangelo's equation.



Photograph 4.4: Atomic force microscope image of harp structure. Striations are clearly evident on both substrate and nitride. In this case the reflow smoothing process failed to provide a flat surface for nitride deposition.

#### 4.4.6 Van der Waals Bonding

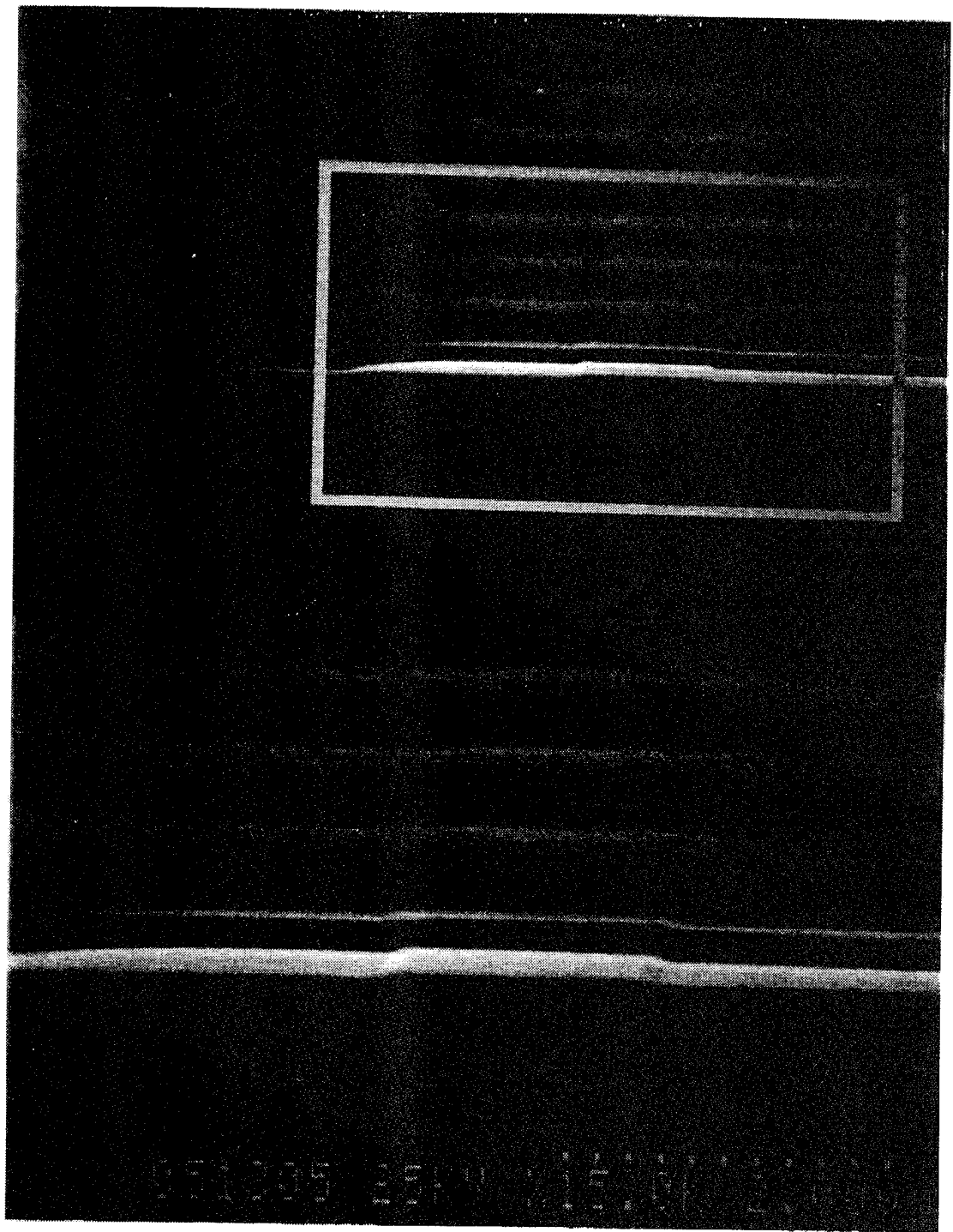
Although water undoubtedly plays an important role in the sticking forces, in a dry ambient sticking still remains a problem. In this case the culprit is not a surface chemistry problem but a fundamental limitation, the Van der Waal's attraction between two insulators [Scheeper 1992]. The pressure of the attraction is given by

$$P = \frac{A}{6\pi D^3}$$

where  $A$  is the Hamaker constant and  $D$  is the separation between the two materials. For  $D > 30\text{nm}$  the long-range attraction is given by

$$P = \frac{B}{D^4}$$





Photograph 4.5: Striations in one dimensional arrays. Note the slight striation in the nitride beams and the 1  $\mu\text{m}$  undercut of the frame.

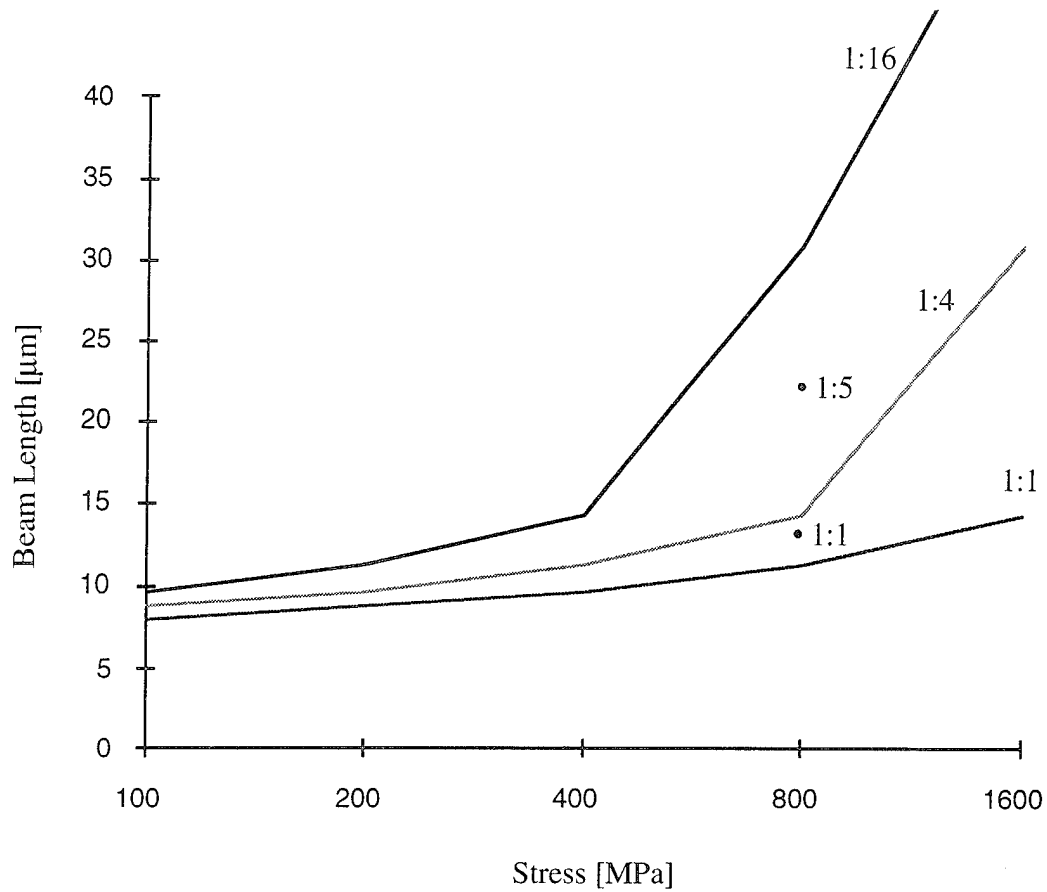


Figure 4.6: Beam peel length as a function of residual stress and striations. The three curves are for  $\delta = 1:1$  (i.e., no striations), 1:4, and 1:16. The two data points are experimental for  $\delta = 1:1$  and 1:5 with 800 MPa residual stress.

The expressions for Van der Waals bonding and the string model of chapter 3 can be combined to plot  $L_h$  as a function of the striation ratio,  $\delta$ , and residual stress,  $\sigma$ . See Figure 4.6. The results show an encouraging trend. For lithographically defined striations, with a maximum  $\delta$  of 1:10, there are modest gains possible. But through the use of an etch stop layer, which would allow timed etching to narrow the striations,  $\delta = 1:100$  is possible. This should exhibit an extremely long  $L_h$ . Although this approach is appealing, using surface roughness is simpler.

When  $D$  is approximately 2 nm, which may not be a bad guess for the surface roughness on the bottom side of the nitride beams, then this expression gives a good estimate for the observed value of  $\gamma_s$  for a substrate exposed to moisture. This suggests that increasing

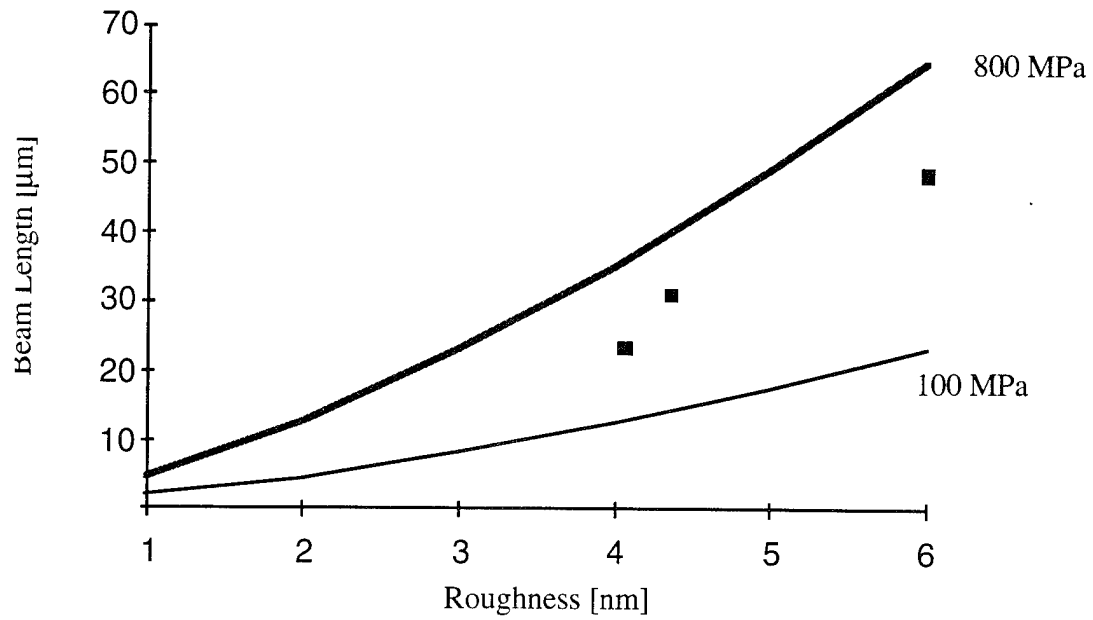


Figure 4.7: Surface roughness and beam sticking. The three dots show data for 800 MPa and RMS surface roughness measured by AFM.

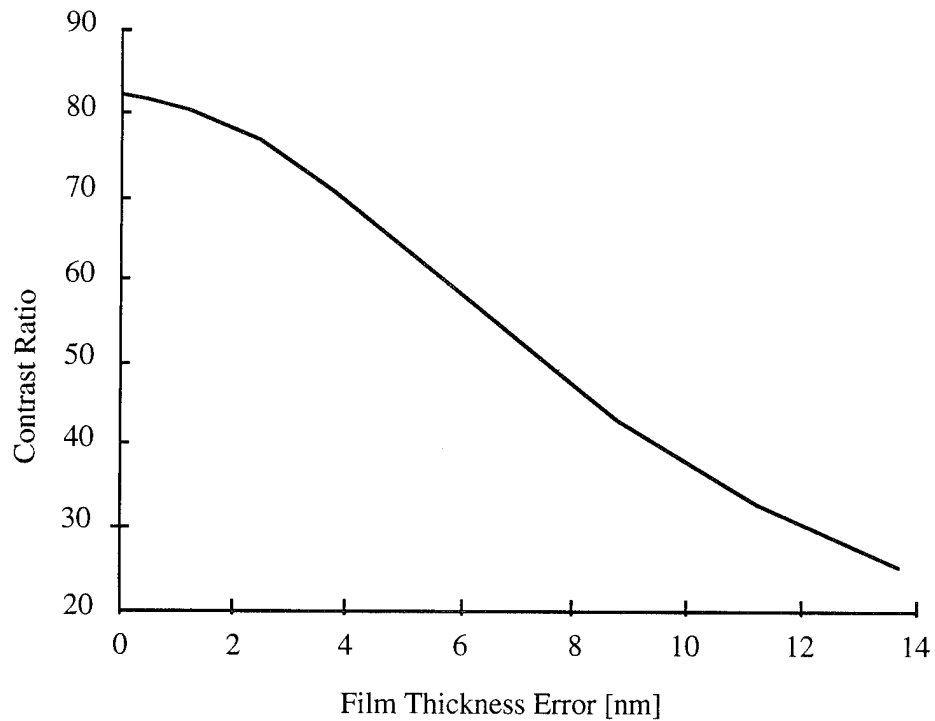
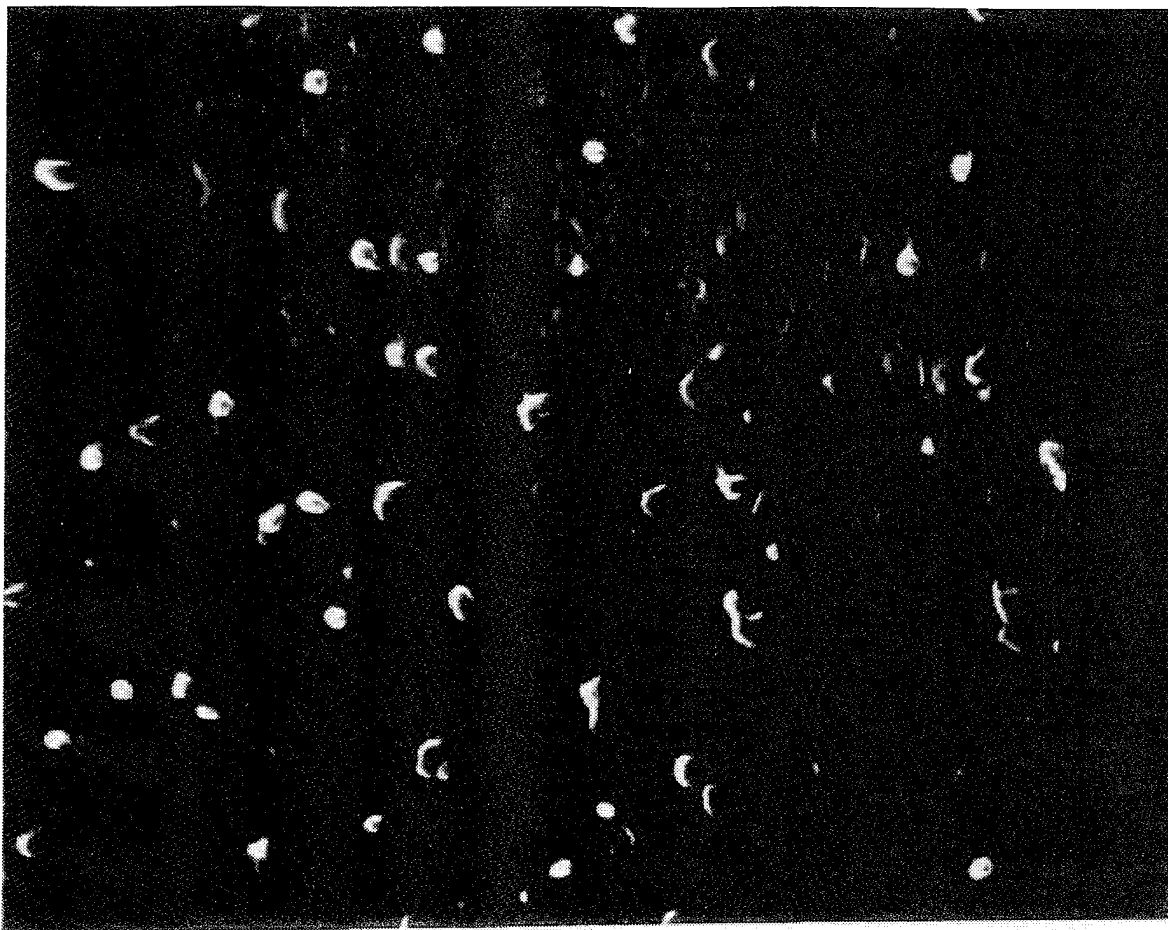


Figure 4.8: Contrast ratio versus film thickness. Although thickness error and roughness are not the same, this figure, repeated from Chapter 2, shows that only a few nanometers of roughness are acceptable before the contrast ratio decreases precipitously.

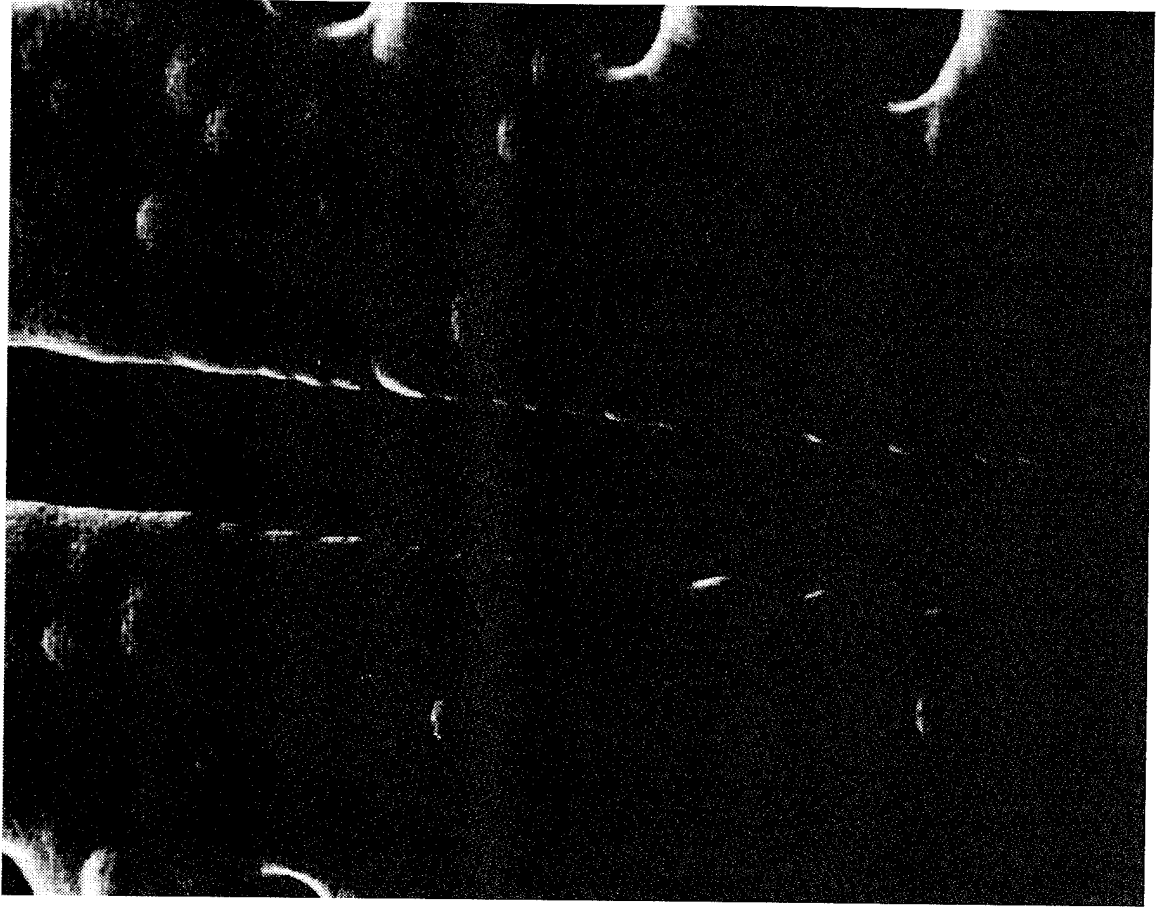


Photograph 4.6a: Rough polysilicon surface.

the roughness of the substrate or the bottom side of the beams will be useful in controlling stiction.

#### 4.4.7 Surface Roughness and Contrast

One semiconductor material that has controllable roughness is LPCVD silicon, which may be amorphous or polycrystalline [Bawolek 1993; Dana 1993; Voutsas 1993]. By controlling growth temperature, film thickness, and substrate surface quality a very large range of surface roughness is possible [Ibok, 1993 #64]. If we make the identity that  $D$ , the distance between the beam and the substrate in the down position, is equal to the surface roughness, then using the string model and the Van Der Waals force gives Figure 4.7, in which  $L_h$  is plotted as a function of residual stress and surface roughness. Three data points are added for 800 MPa devices with various polysilicon roughnesses (measured by atomic force microscopy). Photographs 4.6a and 4.6b show the rough polysilicon surface and the nitride that is grown over it.



Photograph 4.6b: Nitride deformed by rough polysilicon. The reflow process smooths the oxide surface, but some roughness remains.

It is clear from Figure 4.7 that increased roughness, although not as effective as striations at increasing  $L_h$ , is still very effective. The tradeoff is with contrast ratio. Although we do not have a theory for contrast that includes sub-wavelength scale roughness, Figure 4.8 gives some idea of the decrease in contrast ratio in this circumstance.

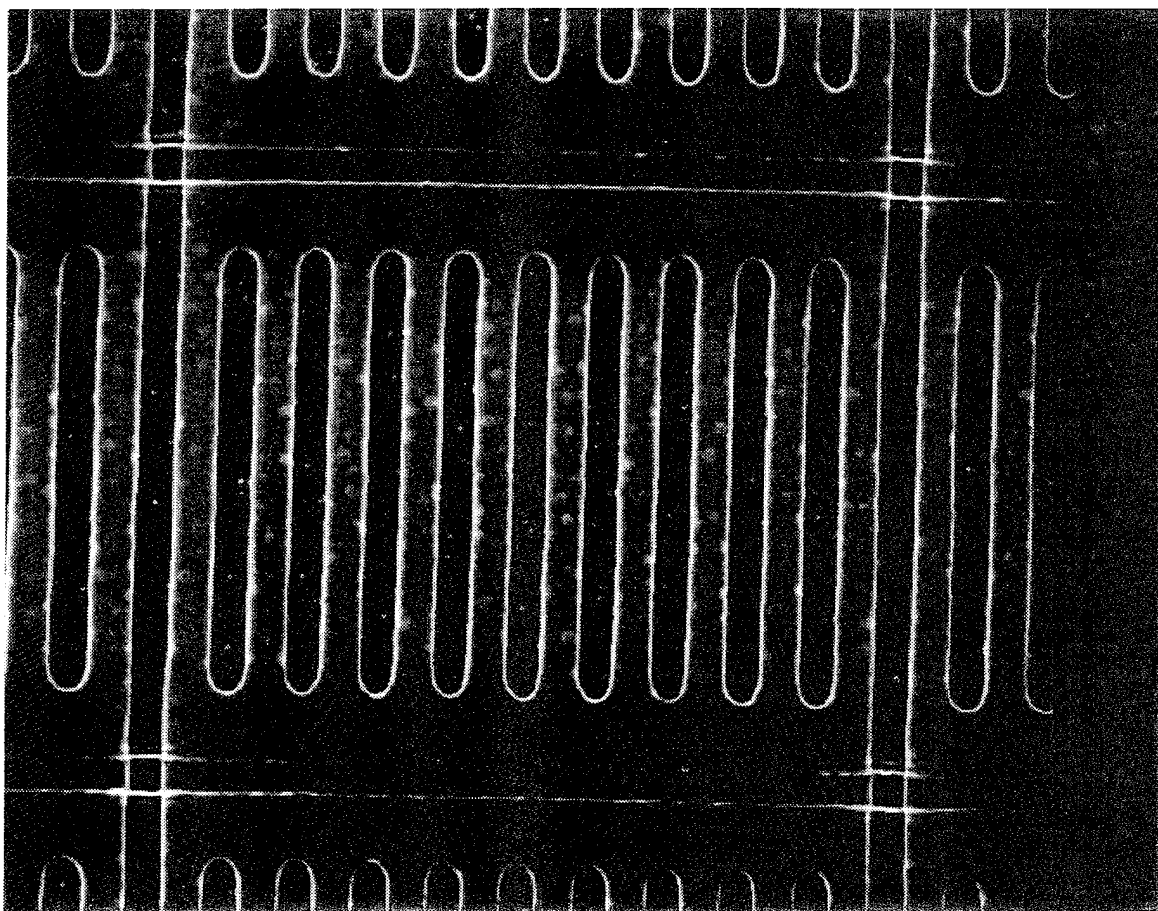
#### 4.4.8 Progress in Reducing Sticking

The progress in solving the sticking problem is summarized in Table 4.1, in which  $L_h$  is given for each process variant. Short beams have very high switching voltages. An observed practical limit was that above 40V electromigration of the aluminum resulted in the devices shorting to ground. If the test circuit had significant source impedance, then the beams simply do not move (although they are up). If a low-impedance source is used,

the device explodes, scattering debris from the beams, frame, and bondpads. In order to keep operating voltages to 35 V or less, the minimum usable beam length is 15  $\mu\text{m}$ . To insure >99% yield of usable devices, an  $L_h$  of 25  $\mu\text{m}$  is desired:

Process	$L_h$ [ $\mu\text{m}$ ]
Desired	>25
Initial (low stress)	10
High stress	13
Surface treated	8
Striated	22
p-Si roughened	>40

Table 4.1: Progress in decreasing sticking.



Photograph 4.7: Single pixel in a two-dimensional array. Roughness in the nitride results in less than optimal lithography.

## 4.5 Two-Dimensional Arrays

The problems with building two-dimensional arrays of pixels are important because solving them is the first step in integrating the processes of light valve construction and driver circuit integration and fabrication. Regardless of whether an active or passive matrix is used, the interconnection of the drivers and the pixels will require an interconnect step, and the development of two-dimensional arrays exhibits significant difficulties.

The primary difficulties with adding an interconnect layer are twofold: the interconnects must remain isolated from one another, the substrate, and the top electrodes; and the interconnect layer must be thermally compatible with subsequent processing. The first of these problems we have solved, the second is a source of continuing concern.

### 4.5.1 Isolation

The interconnect layer presents special problems because of the fact that the present process does not have a masking step after the top electrode deposition. Because of the large aspect ratio of the beams and the small thickness of the spacer, it is difficult to remove photoresist residue from beneath the released beams following lithography. Therefore, the basic process includes no wet processing after the release etch. Since the top electrode deposition follows the release, there is no patterning of the top electrode metal. In the basic process, isolation between top electrodes depends on the overhang of the nitride over the spacer to prevent shorting. The same mesa isolation strategy is used to isolate the bottom electrodes. The use of mesa isolation requires the use of a very non-planar structure, with the concomitant problems. (See Photographs 4.8 and 4.9).

### 4.5.2 Thermal budget

The reasons given for choosing aluminum for the top electrode are equally valid for the bottom electrode. The difficulty is that subsequent layers, especially the LPCVD nitride deposition at 785 °C, exceed the thermal budget of the aluminum (<400 °C). For this reason polysilicon interconnects are used instead of aluminum. Although the conductivity of polysilicon will make arrays larger than 200x200 be RC limited rather than device limited, polysilicon has the advantages that its roughness can be controlled by processing and it is stable at the nitride deposition temperature (provided it is capped with oxide).

### 4.5.3 Basic Recipe

Processing begins with a 5000 Å oxide isolation layer being grown on a bare silicon substrate. This isolation layer can be grown by any available technique. On top of this layer is grown a 3000-6000 Å undoped polysilicon layer. The temperature of this growth may be varied to control surface roughness. The layer is probably amorphous initially, but it crystallizes during subsequent high temperature processing (the reflow step). The polysilicon is pre-dep diffusion doped with phosphorous, cleaned, and patterned into the bottom interconnect layer. 1325 Å of low temperature LPCVD oxide are deposited on top of the nonplanar bottom electrode traces. This oxide is doped with 8% Phosphorous to reduce the reflow temperature. The oxide is steam reflowed at 1000 °C for 20 minutes. 1325 Å of LPCVD nitride are deposited next, then patterned and dry etched. The wafer is then cleaned to remove all traces of photoresist and released. The oxide spacer is removed from under the beams. In addition, oxide is removed from under the edges of the frames and the bottom electrode traces. The overhanging polysilicon and nitride provide the isolation. This process is depicted in Figure 4.9, and complete details are given in Appendix 1.

### 4.5.4 Nonplanar Processing

The difficulties in the development of this process are best shown in Photographs 4.9 and 4.10, which are two views of the corner regions of the 4x4 array in Photograph 4.8. Photograph 4.9 is in the same orientation as Photograph 4.8, with the top electrode making connections vertically and the polysilicon lines underneath running horizontally. Photograph 4.10 is from the the other orientation. The nonplanar structure used to isolate the bottom electrodes creates the possibility of nitride stringers shorting between adjacent top electrodes. These stringers are evident at the bright horizontal line in Photograph 4.9 and on the right side of Photograph 4.10. Second, step coverage along the edges of the polysilicon makes it possible for the top electrode to be open-circuited if the reflow is not sufficient. This can be seen in the top part of Photographs 4.10, where the nitride/top electrode runs horizontally over the polysilicon, down to the isolation oxide between the polysilicon lines, and then back up the next polysilicon line. Careful tuning of the reflow process was used to solve both problems by smoothing out the edges of the nonplanar structures.



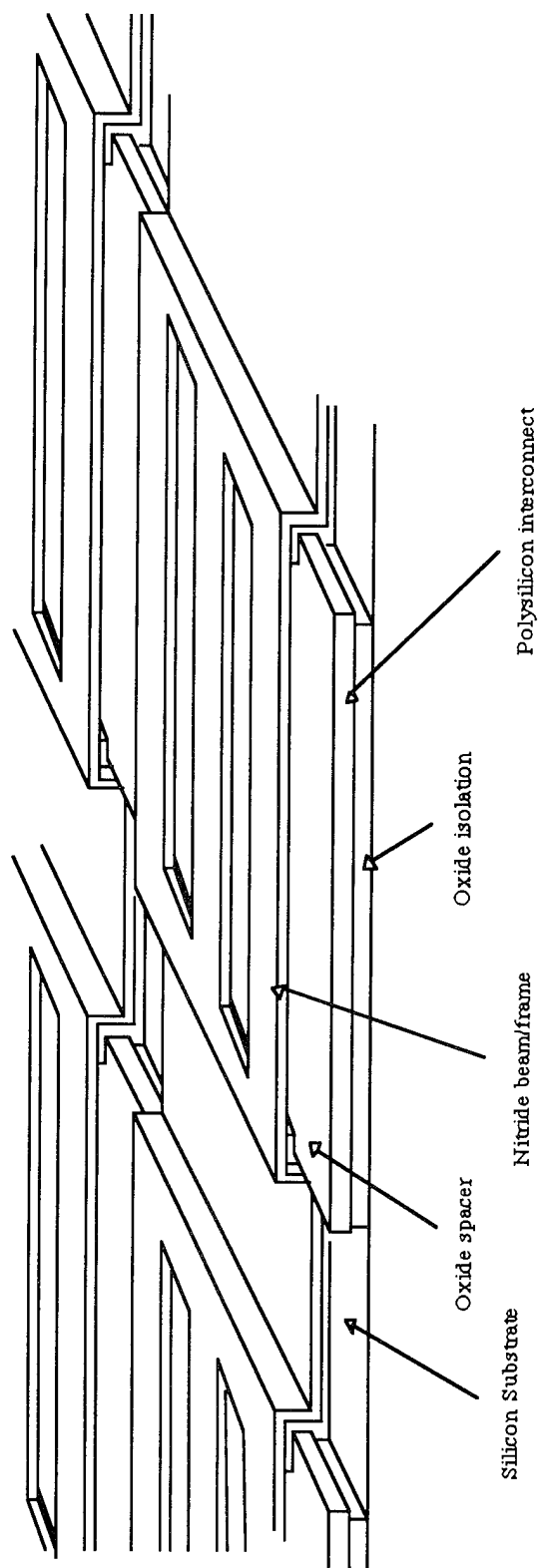
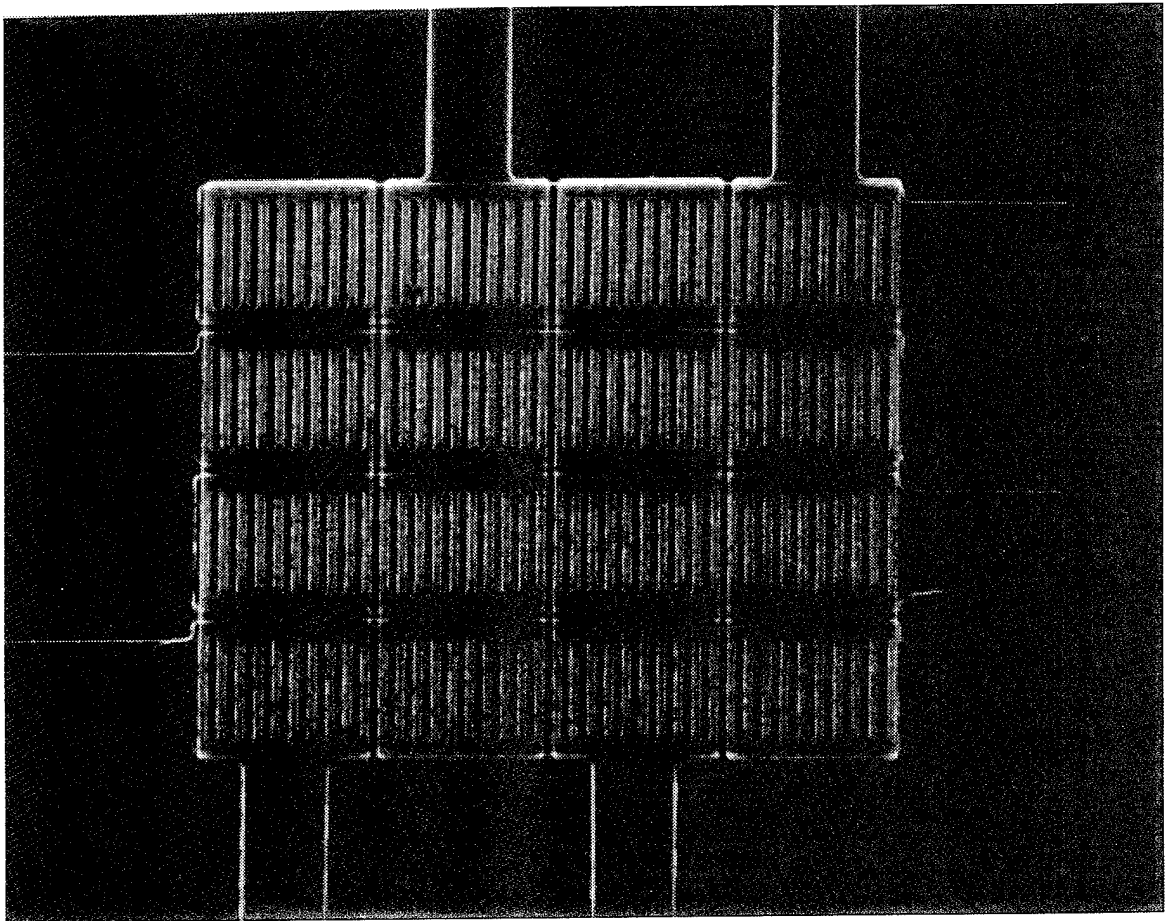


Figure 4.9: Schematic of two dimensional array. This figure shows pixels with only three beams rather than the usual ten for clarity.

## 4.6 Reliability

Adequate data for reliability does not exist for the GLV. An initial experiment was done that cycled pixels over 300 billion cycles at an accelerated rate (1 MHz for 100 hours), which corresponds to ten years of television use for a color GLV with eight bits of gray scale. The devices were operated with a 25 V square wave in ambient conditions. No pixel damage (in the form of sticking or fusing) was observed. However, recent work [Pryputniewicz 1994] suggests that accelerated lifetime testing is not valid, since it doesn't give the material time to deform plastically or for cracks to grow. A second limitation is that this testing was done on striated devices. It is not known whether the use of surface roughness rather than striations will increase beam cracking or not.



Photograph 4.8: 4x4 pixel array.

## 4.7 Device Failure

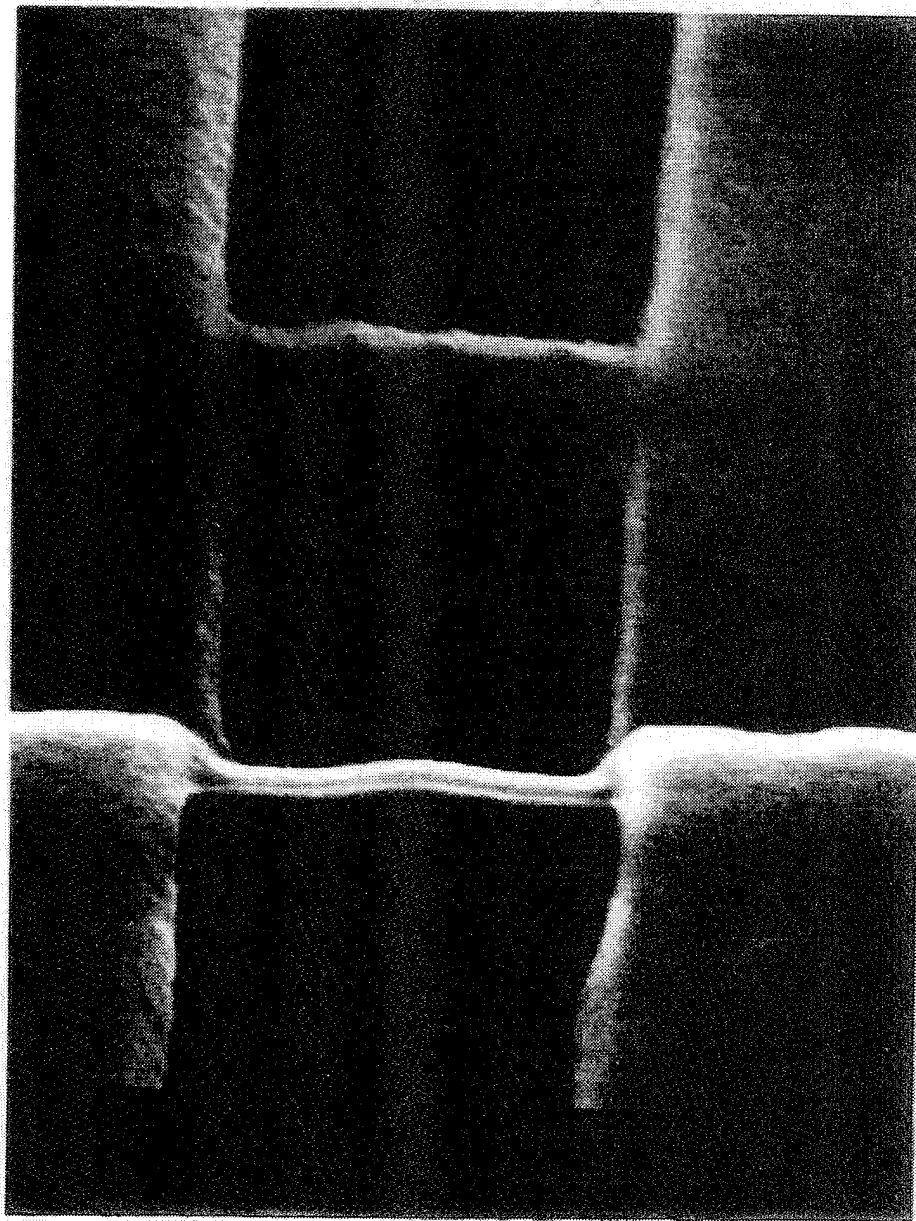
Three types of device failure have been observed. Low voltage fusing is a process that is related to a failure in wafer processing. It first appeared to be correlated to particular LPCVD nitride depositions, although measurement of thickness and refractive index did not reveal anything unusual. A later hypothesis was that the use of thicker (1  $\mu\text{m}$ ) aluminum bondpad metalizations caused leaching of silicon from the nitride into the aluminum. This process degrades the nitride and is known as the Kirkendall Effect [Wolf 1990]. The solution to this problem is to use an aluminum sputter target with 4% silicon. Subsequent wafers have confirmed this phenomenologically, although no measurements have been performed to establish causality. Wafers coated with aluminum/silicon did not exhibit fusing.

The second type of device failure is high voltage shorting. When  $> 40$  V is applied to devices arcing causes large currents to flow and device heating. Usually the device is destroyed catastrophically. It is thought that the large field concentrations described in Section 4.2 are responsible.

Sticking of the beams to the substrate is the third and most common form of device failure. In initial experiments, the beams stuck to the substrate during the drying process following the release-etch. Previous work established that freeze-drying the devices resulted in un-stuck devices [Solgaard 1992]. However, when operated into contact with the substrate these devices would stick. After the development of the high stress nitride process, the freeze-drying technique was abandoned in favor of standard spin-drying. For all subsequent work, if a certain beam did not stick during spin-drying, it generally would not stick during subsequent operation. For this reason the figure of merit for yield,  $L_h$ , was recorded for devices that had been recently released. Some degradation of  $L_h$  over time was observed in devices that had been left in air for months, so later devices were stored in vacuum and tested in dry nitrogen. The standard deviation for  $L_h$  on a wafer was between 2 and 3  $\mu\text{m}$ , so making  $L_h$  10  $\mu\text{m}$  larger than the design length resulted in yields of greater than 90%.

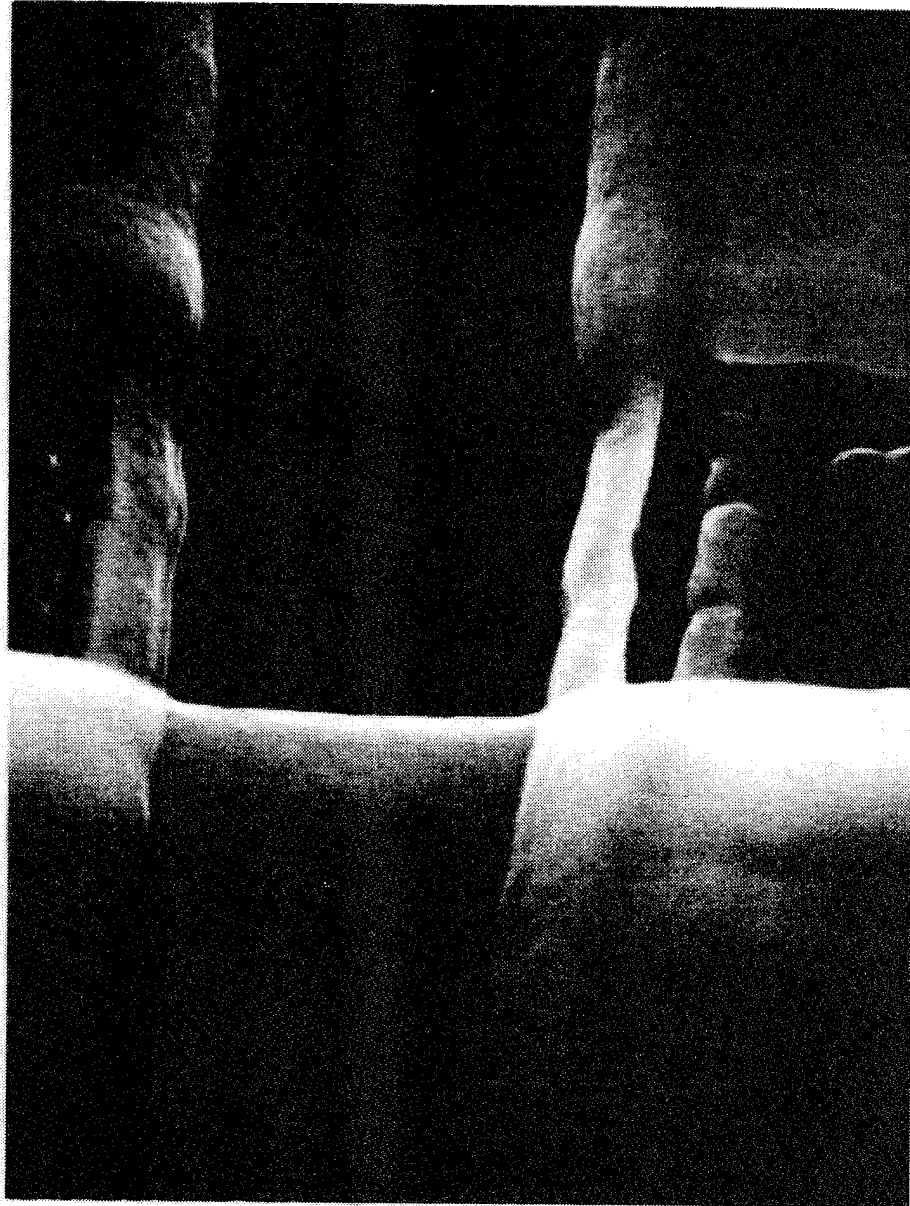
## 4.8 Future Process Design

The present work lessened the sticking problem and the interconnect problem through the use of the surface roughness and doping of polysilicon. It is very likely that stress concentration when the beams strike a roughened substrate will increase damage rates.



Photograph 4.9: Four corners of a two dimensional array. The nitride runs vertically, and the middle shows the isolation region. A nitride stringer is apparent in the bottom half of the picture.

Also, it is possible to redesign the striations so that they are not visible from the top surface. This modification would prevent the contrast ratio from being degraded. Thus, it is likely that future processes will make use of smooth materials and etched striations.



Photograph 4.10: Four corners point of two-dimensional array, alternate view. Nitride/top electrodes run horizontally and must be continuous over the step formed by the polysilicon lines, which run vertically. In the right half of the picture the nitride, spacer, and polysilicon can be clearly seen. A nitride stringer shorts two adjacent top electrodes together.

Another weakness of the present process is the very high thermal budget, which is 785 °C for the nitride and 1000 °C for the reflow. While clever etching might eliminate the need for reflow, the nitride is a serious problem. One alternative is to use a lower temperature nitride, say PECVD. PECVD nitride is deposited at 200 °C and through the use of a two-frequency system has controllable residual stress. Since such systems can also deposit oxide, PECVD appears to solve the thermal budget problem. Aluminum could be used for the bottom electrode as well as the top. The problem is that the release etch should have a good differential rate between oxide and nitride. For LPCVD it is well over 100:1, which is necessary for etching 10:1 aspect ratios. For PECVD, the best differential etch rate we found was 10:1. If another etch could be found, then the PECVD option becomes an excellent solution.

# Chapter 5

## Conclusion

### 5.1 Device Summary

The grating light valve is a relatively new display technology. It is based on reflection phase gratings of electrically controllable depth. When the beams are suspended "up" from the substrate the device has a minimum of diffraction, and normally incident light is reflected. If a potential is applied to bring the beams into contact with the substrate, then the device diffracts 80% of the light into the first order diffraction modes, which are then collected by a Schlieren optical system. The contrast ratio was measured to be 20:1 for black-and-white displays. A contrast of 80:1 should be achievable with improved processing techniques. A color gamut a little smaller than that of television phosphors was measured. Improved lamp collimation should improve the saturation of the colors. Contrast ratios for optimized color devices should exceed 200. Pixels as small as  $6 \times 20 \mu\text{m}$  are possible.

The position of the beams is bistable for intermediate voltages. For a qualitative understanding, the beams can be modelled as strings under tension. To get better quantitative results, a full integration of the fourth order beam equation was used. The validity of the model was limited because the contribution of top electrode aluminum to the beam stiffness was neglected. Switching voltages between 5 and 10 V should be obtainable. The lowest measured in this work is 11 V. The combination of bistability and speed—the devices switch in 20.5 ns—might be used for passive matrix addressing in a row-by-row fashion. The device operation should not be significantly affected by temperatures in excess of 200 °C.

Simple fabrication requires only a single mask. To make devices with two-dimensional arrays of contacts two masks are needed. Through the use of the overhang of the frame

material the devices are isolated from each other without an additional masking step. Aluminum is used for the top layer of interconnects and the reflective layer on the beams and spaces. Sticking of the beams to the substrate is caused by hydration of the surface and/or Van der Waals bonding. The two methods of reducing this problem, corrugating the substrate with striations and using a naturally rough substrate material like polysilicon, both are extremely successful at reducing sticking. However, both have deleterious effects on the optical performance of the device if overdone. Two-dimensional arrays were constructed with a highly non-planar process. Despite problems with shorts and opens in the top conductor, this method was used to demonstrate working two-dimensional arrays.

## 5.2 Future Work

There are four major areas of development needed for these devices, presented in order of increasing importance.

In order to use the bistability of the devices for switching, it is necessary to insure that the hysteresis loop is made as open as possible. This might be achieved by using conducting beams or beams with higher permittivities. Conducting beams would have the effect of decreasing the gap between the top and bottom electrodes when the beams are down. This increase in capacitance would cause a substantial decrease in the first instability voltage.

A second area of research is to determine the effect of surface roughness on contrast ratio. This will help determine whether roughness or striations should be used to reduce sticking. A new process for striations should be designed that is self-aligned and produces quarter micron striations. This might have a minimal effect on contrast while decreasing sticking. Ultimately, a self-aligned striation that would not affect contrast would be ideal.

Third, the devices of this thesis were all produced with LPCVD. This process requires too high temperatures to be compatible with driver circuit fabrication. Either a move to PECVD or to alternate materials must be considered. Possibilities for alternate materials include spin-on glasses, polymers, metals, and other types of oxynitrides. This process redesign is absolutely necessary for reliable operation, since the high temperatures of the current process make it necessary to bond the drivers to the display rather than integrate them monolithically.

Finally, the aging characteristics of micromechanical displays are not at present well understood. Texas Instruments' deformable mirror device uses metal flexures, while the



grating light valve uses silicon nitride. The latter is expected to have much better ageing characteristics than the metal flexures. Although this problem is speculative, it may prove to be a critical deciding factor. In addition, it is not clear what sort of packaging is necessary to insure long life of these devices, i.e. whether full hermeticity is needed.

These four areas of research highlight the limitations of this work and the present state of the grating light valve. With additional work in these areas it is possible that the grating light valve will someday be commercially produced.

# Bibliography

- [Alley 1992a] R. Alley, "Recipe for OTS Silating," Personal Communication, Nov. 11, 1992 .
- [Alley 1992b] R. L. Alley, G. J. Cuan, R. T. Howe, and K. Komvopoulos, "The Effect of Release-Etch Processing on Surface Microstructure Stiction." In *IEEE Solid-State Sensor and Actuator Workshop*, Hilton Head, SC, IEEE, pp. 202-207, 1992b.
- [Alt 1973] P. M. Alt and P. Pleshko, "Scanning Limitations of Liquid-Crystal Displays," *IEEE Transactions on Electron Devices*, vol. ED-21, no. 2, pp. 146-155, 1973.
- [Apte 1993] R. B. Apte, F. S. A. Sandejas, W. C. Banyai, and D. M. Bloom, "Deformable Grating Light Valves for High Resolution Displays." In *Society for Information Display Symposium*, Seattle, WA, 1993.
- [Aratani 1993] K. Aratani, P. J. French, P. M. Sarro, R. F. Wolffenbuttel, and S. Middelhoek, "Process and Design Considerations for Surface Micromachined Beams for a Tuneable Interferometer Array in Silicon." In *Solid-State Sensors and Actuators: TRANSDUCERS '93*, Yokohama, pp. 230-235, 1993.
- [Backlund 1992] Y. Backlund, K. Hermansson, and L. Smith, "Bond-Strength Measurements Related to Silicon Surface Hydrophilicity," *Journal*

of the *Electrochemical Society*, vol. 139, no. 8, pp. 2299-2301, 1992.

- [Bawolek 1993] E. J. Bawolek, J. B. Bohr, E. D. Hirleman, and A. Majumdar, "Light scatter from polysilicon and aluminum surfaces and comparison with surface-roughness statistics by atomic force microscopy," *Applied Optics*, vol. 32, no. 19, pp. 3377-3400, 1993.
- [Beck 1990] P. A. Beck, S. M. Taylor, J. P. McVittie, and S. T. Ahn, "Low Stress Silicon Nitride and Polysilicon Films for Micromachining Applications." In *Proceedings of the Materials Research Symposium*, vol. 182, pp. 207-212, 1990.
- [Bloom 1992] D. M. Bloom, F. S. A. Sandejas, and O. Solgaard, "Method and Apparatus for Modulating a Light Beam," *United States Patent*, Number Serial Number 07/876,078. Issued: Filed April 28, 1992.
- [Born 1980] M. Born and E. Wolf, *Principles of Optics*. Sixth Edition (Corrected) ed., Pergamon Press, 1980.
- [Bowling 1985] R. A. Bowling, "An Analysis of Particle Adhesion on Semiconductor Surfaces," *Journal of the Electrochemical Society: Solid State Science and Technology*, vol. no. September 1985, pp. 2208-2214, 1985.
- [Boysel 1989] R. M. Boyssel, J. M. Florence, and W.-R. Wu, "Deformable Mirror Light Modulators for Image Processing." In *Optical Information Processing Systems and Architectures*, vol. SPIE 1151, pp. 183-194, 1989.
- [Burns 1990] D. W. Burns and H. Guckel, "Thin Films for Micromechanical Sensors," *Journal of Vacuum Science and Technology A*, vol. 8, no. 4, pp. 3606-3613, 1990.

- [Cho 1992] S. T. Cho, K. Najafi, and K. D. Wise, "Internal Stress Compensation and Scaling in Ultrasensitive Silicon Pressure Sensors," *IEEE Transactions on Electron Devices*, vol. 39, no. 4, pp. 836-842, 1992.
- [Dana 1993] S. S. Dana, M. Anderle, G. W. Rubiloff, and A. Acovic, "Chemical vapor deposition of rough-morphology silicon films over a broad temperature range," *Applied Physics Letters*, vol. 63, no. 10, pp. 1387-9, 1993.
- [Den Hartog 1949] J. P. Den Hartog, *Strength of Materials*. New York: Dover Publications, 1949.
- [Flinn 1987] P. A. Flinn, D. S. Gardner, and W. Nix, "Measurement and Interpretation of Stress in Aluminum-Based Metallizaion as a Function of Thermal History," *IEEE Transactions on Electron Devices*, vol. ED-34, no. 3, pp. 689-699, 1987.
- [Gaither 1988] S. A. Gaither, "Two-Dimensional Diffraction from a Surface-Relief Grating," Computer Program, Vers. 26 May 1988, courtesy of W. VeldKamp, MIT Lincoln Laboratory .
- [Gaylord 1982] T. K. Gaylord and M. G. Moharam, "Planar Dielectric Grating Diffraction Theories," *Applied Physics B*, vol. 28, no. pp. 1-14, 1982.
- [Gerhard-Multhaupt 1991] R. Gerhard-Multhaupt, "Light-valve technologies for high-definition television projection systems," *Displays*, vol. 12, no. 3/4, pp. 116-129, 1991.
- [Gerhard-Multhaupt 1990] R. Gerhard-Multhaupt, W. Brinker, H.-J. Ehrke, W.-D. Molzow, H. Roeder, T. Rosin, and R. Tepe, "Viscoelastic Spatial Light Modulators and Schlieren-Optical Systems for HDTV Projection Displays," *SPIE Large-Screen Projection Displays II*, vol. 1255, no. pp. 69-78, 1990.

- [Guckel 1989] H. Guckel, J. J. Sniegowski, and T. R. Christenson, "Fabrication of Micromechanical Devices from Polysilicon Films with Smooth Surfaces," *Sensors and Actuators*, vol. 20, no. 1989, pp. 117-122, 1989.
- [Guckel 1990] H. Guckel, J. J. Sniegowski, T. R. Christenson, and F. Raissi, "The Application of Fine-grained, Tensile Polysilicon to Mechanically Resonant Transducers," *Sensors and Actuators*, vol. A21-A23, no. 1990, pp. 346-351, 1990.
- [Hartog 1961] J. P. D. Hartog, *Strength of Materials*. New York: Dover, 1961.
- [Heath 1978] J. W. Heath and E. V. Jull, "Perfectly Blazed Reflection Gratings with Rectangular Grooves," *Journal of the Optical Society of America*, vol. 68, no. 9, pp. 1211-1217, 1978.
- [Hermansson 1991] K. Hermansson, U. Lindberg, B. Hok, and G. Palmkog, "Wetting Properties of Silicon Surfaces," vol. no. pp. 193-196, 1991.
- [Hong 1990] S. Hong, T. P. Weihs, J. C. Bravman, and W. D. Nix, "Measuring Stiffnesses and Residual Stresses of Silicon Nitride Thin Films," *Journal of Electronic Materials*, vol. 19, no. 9, pp. 903-909, 1990.
- [Hopkins 1992] G. W. Hopkins, "Light Valve Viewer," George W. Hopkins, Consultant, Nov. 1, 1992.
- [Hornbeck 1987] L. J. Hornbeck, "Spatial Light Modulator and Method," *United States Patent*, Number 4,710,732. Issued: Dec. 1, 1987.
- [Hornbeck 1989] L. J. Hornbeck, "Deformable-Mirror Spatial Light Modulators." In *Spatial Light Modulators and Applications III*, San Diego, California, Proceedings of the SPIE, vol. 1150, 1989.

- [Hornbeck 1990] L. J. Hornbeck, "Spatial Light Modulator," *United States Patent*, Number 4,956,619. Issued: Sep. 11, 1990.
- [Hornbeck 1991a] L. J. Hornbeck, "Spatial Light Modulator and Method," *United States Patent*, Number 5,061,049. Issued: Oct. 29, 1991.
- [Hornbeck 1991b] L. J. Hornbeck and W. E. Nelson, "Spatial Light Modulator System," *United States Patent*, Number 5,028,939. Issued: Jul. 2, 1991.
- [Hunt 1991] R. W. G. Hunt, *Measuring Colour*. 2nd ed., New York: E. Horwood, 1991.
- [Ibok 1993] E. Ibok and S. Garg, "A Characterization of the Effect of Deposition Temperature on Polysilicon Properties," *Journal of the Electrochemical Society*, vol. 140, no. 10, pp. 2927-37, 1993.
- [Kiesewetter 1992] L. Kiesewetter, J.-M. Zhang, D. Houdeau, and A. Steckenborn, "Determination of Young's Moduli of Micromechanical Thin Films Using the Resonance Method," *Sensors and Actuators A*, vol. 35, no. 1992, pp. 153-159, 1992.
- [Mastrangelo 1992] C. H. Mastrangelo and C. H. Hsu, "A Simple Experimental Technique for the Measurement of the Work of Adhesion of Microstructures." In *IEEE Solid-State Sensor and Actuator Workshop*, Hilton Head Island, SC, pp. 208-212, 1992.
- [Mastrangelo 1993a] C. H. Mastrangelo and C. H. Hsu, "Mechanical Stability and Adhesion of Microstructures under Capillary Forces—Part I: Basic Theory," *Journal of Microelectromechanical Systems*, vol. 2, no. 1, pp. 33-43, 1993a.
- [Mastrangelo 1993b] C. H. Mastrangelo and C. H. Hsu, "Mechanical Stability and Adhesion of Microstructures Under Capillary Forces—Part II: Experiments," *Journal of Microelectromechanical Systems*, vol. 2, no. 1, pp. 44-62, 1993b.

- [Matson 1989] D. W. Matson and R. D. Smith, "Supercritical Fluid Technologies for Ceramic-Processing Applications," *Journal of the American Ceramic Society*, vol. 72, no. 6, 871-81, 1989.
- [Murarka 1993] S. P. Murarka, *Metallization: Theory and Practice for VLSI and ULSI*. Boston: Butterworth-Heinemann, 1993.
- [Osram 1988] Osram Corporation, "HTI Metal Halide Short Arc Lamps," Sep. 1988. OCN-1007.
- [Osterberg 1994] P. M. Osterberg, R. K. Gupta, and S. D. Senturia, "A Quantitative Model for the Measurement of Residual Stress Using Electrostatic Pull-in of Beams." In *IEEE Solid-State Sensor and Actuator Workshop*, Hilton Head, SC, submitted for presentation, 1994.
- [Palik 1985] E. D. Palik, ed. *Handbook of Optical Constants of Solids*. Academic Press, 1985.
- [Petersen 1982] K. E. Petersen, "Silicon as a Mechanical Material," *Proceedings of the IEEE*, vol. 70, no. 5, pp. 420-457, 1982.
- [Photo Research 1992] Photo Research, "PR-650 SpectraColorimeter," vol. no. 1992.
- [Pryputniewicz 1994] R. J. Pryputniewicz, "Accelerated lifetime testing," Personal Communication, March, 1994 .
- [Ramo 1984] S. Ramo, J. Whinnery, and T. V. Duzer, *Fields and Waves in Communication Electronics, Second Edition*. John Wiley and Sons, 1984.
- [Sampsell 1990] J. B. Sampsell, "Spatial Light Modulator," *United States Patent*, Number 4,954,789. Issued: Sep. 4, 1990.

- [Sampsell 1992] J. B. Sampsell, "An Overview of the Digital Micromirror Device (DMD) and Its Application to Projection Displays." In *Society for Information Display Symposium*, Seattle, WA, vol. XXIV, pp. 1012-1015, 1992.
- [Sandejas 1993] F. S. A. Sandejas, R. B. Apte, W. C. Banyai, and D. M. Bloom, "Surface Microfabrication of Deformable Grating Light Valves for High Resolution Displays." In *Solid-State Sensors and Actuators: TRANSDUCERS '93*, Yokohama, Late News Digest, 1993.
- [Scheeper 1992] P. R. Scheeper, J. A. Voorthuyzen, W. Othuis, and P. Bergveld, "Investigation of Attractive Forces Between PECVD Silicon Nitride Microstructures and an Oxidized Silicon Substrate," *Sensors and Actuators A*, vol. 30, no. 1992, pp. 231-239, 1992.
- [Shimbo 1986] M. Shimbo, K. Furukawa, K. Fukuda, and K. Tanzawa, "Silicon-to-Silicon Direct Bonding Method," *Journal of Applied Physics*, vol. 60, no. 8, pp. 2987-2989, 1986.
- [Solgaard 1992a] O. Solgaard, "Integrated Semiconductor Light Modulators for Fiber-Optic and Display Applications", Ph.D. Dissertation, Stanford University, 1992a.
- [Solgaard 1992b] O. Solgaard, F. S. A. Sandejas, and D. M. Bloom, "A Deformable Grating Optical Modulator," *Optics Letters*, vol. 17, no. 9, p. 688, 1992b.
- [Stengl 1989] R. Stengl, T. Tan, and U. Gosele, "A Model for the Silicon Wafer Bonding Process," *Japanese Journal of Applied Physics*, vol. 28, no. 10, 1735-1741, 1989.
- [Veldkamp 1989] W. B. Veldkamp, G. J. Swanson, S. A. Gaither, C.-L. Chen, and T. R. Osborne, "Binary Optics: A Diffraction Analysis," MIT Lincoln Laboratory, Aug. 23, 1989. ODT-20.



- [Voutsas 1993] A. T. Voutsas and M. K. Hatalis, "Surface treatment effect on the grain size and surface roughness of as-deposited LPCVD polysilicon films," *Journal of the Electrochemical Society*, vol. 140, no. 1, pp. 282-288, 1993.
- [Wiszniewski 1993] W. R. Wiszniewski, R. E. Collins, and B. E. Pailthorpe, "Mechanical Light Modulator Fabricated on a Silicon Chip Using SIMOX Technology." In *Solid-State Sensors and Actuators: TRANSDUCERS '93*, Yokohama, pp. 1027, 1993.
- [Wolfram 1991] S. Wolfram, "Mathematica 2.0," Computer Program, Wolfram Research, Inc. .
- [Yoshida 1993] M. Yoshida, "Visit to Ultrafast Electronics Laboratory by Representatives of Sharp Electronics Corporation," Personal Communication, 1993 .

# Appendix 1

## Process Recipe

The recipe for two-dimensional arrays of GLVs is given in this appendix. The recipe is specific to the processes and equipment of the Center for Integrated Systems (CIS), Stanford University, during the latter part of 1993.

### A1.1 Standard Process Steps

There are two standard cleaning steps that are part of any CIS process.

Organic Clean.

- a.  $\text{H}_2\text{SO}_4:\text{H}_2\text{O}_2$ , 9:1, 120C, for 00:20:00.
- b. Dump rinse and spin dry (hereafter, DRSD).

Diffusion Clean

- a. Organic Clean.
- b.  $\text{H}_2\text{SO}_4:\text{H}_2\text{O}_2$ , 3:1, 90C, for 00:10:00.
- c. DR.
- d.  $\text{HF}:\text{H}_2\text{O}$ , 1:50, for 00:00:15.
- e. DR.
- f.  $\text{H}_2\text{O}_2:\text{H}_2\text{O}:\text{HCl}$ , 1:5:1, 70C for 00:10:00.
- g. DRSD.

The standard lithography process includes:

- a. Singe, 150C, 00:30:00.

- b. SVGCoat recipe 1 (includes adhesion promoter and pre-bake).
- c. Expose 110mJ/cm<sup>2</sup>, Ultratech stepper.
- d. SVGDev recipe 1 (includes development and post-bake).

## A1.2 Current GLV process

### 1. SCRIBE

Buy L-Prime wafers.

Scribe.

DRSD.

### 2. WET THERMAL OXIDATION

Diffusion Clean.

Furnace Tylan 1,3, or 4. Program WET1000, process time 02:15:00.

### 3a. POLYSILICON DEPOSITION (option 1)

Furnace Tylanpoly. Program AMOR4006, process time 01:41:00.  
target 0.32  $\mu\text{m}$ .

T=560°C. SiH<sub>4</sub>=136 sccm. H<sub>2</sub>=110 sccm.

### 3b. POLYSILICON DEPOSITION (option 2)

Furnace Tylanpoly. Program AMOR550, process time 01:41:00.  
target 0.26  $\mu\text{m}$ .

T=550°C. SiH<sub>4</sub>=136 sccm. H<sub>2</sub>=110 sccm.

### 4. POLYSILICON DOPING

Furnace Tylan 6. Program POCL3900, process time 00:40:00.

Predep diffusion in POCl<sub>3</sub> ambient. T=900°C.

HF:H<sub>2</sub>O, 1:50, for 00:00:30.

DRSD.

### 5. POLYSILICON LITHOGRAPHY

Standard lithography, field "POLY," reticle TWOLEVELS—clearfield.

Etcher Drytek2, Standard Poly Etch (SF<sub>6</sub>:C<sub>2</sub>ClF<sub>5</sub>), 00:01:15 per wafer.

## 6. LOW TEMPERATURE OXIDE DEPOSITION

Diffusion Clean.

Furnace Tylanbpg. Program PSG400, T = 400°C, SiH<sub>4</sub>=14 sccm, PH<sub>3</sub>=86 sccm, process time 00:05:10. target 1225 Å—oxide will densify AND thicken during the reflow step by 100 Å.

## 7. OXIDE REFLOW

Furnace Tylan 1,3, or 4. Program REFLOW.

T = 950°C. Steam ambient. 00:10:00.

## 8a. NITRIDE DEPOSITION (option 1)

Furnace Tylannitride. Program SIN5.2, process time 00:37:45.  
target 1325 Å.

T = 785°C. NH<sub>3</sub>=32 sccm. DCS=165 sccm.

## 8b. NITRIDE DEPOSITION (option 2)

Furnace Tylannitride. Program SIN3.0, process time 00:33:45.  
target 1325 Å.

T = 785°C. NH<sub>3</sub>=50 sccm. DCS=150 sccm.

## 8c. NITRIDE DEPOSITION (option 3)

Furnace Tylannitride. Program SIN1.0, process time 00:28:00.  
target 1325 Å.

T = 785°C. NH<sub>3</sub>=100 sccm. DCS=100 sccm.

## 9. NITRIDE LITHOGRAPHY

Standard lithography, field "NITRIDE," reticle TWOLEVELS—clearfield.

Etcher Drytek2, Standard Nitride Etch (SF<sub>6</sub>:CF<sub>3</sub>Br), 00:04:30 per wafer.

NB: this is too short to clear up stringers; should be 00:08:00.

## 10. RELEASE ETCH

Organic clean.

Etch BOE 6:1, 00:02:50.

DRDRSD.

## Appendix 2

### Beam Model

The following Mathematica script was typical of those used in modelling the GLV mechanics. The first step is to assume Green's function for the beam equation is of a particular form. Then this solution with undetermined constants is constrained by the homogeneous beam equation, the boundary conditions for rigid supports, and the integral of the beam equation across an arbitrary impulse forcing function. Numerical values are substituted and Green's function  $g[p, q]$  is evaluated as a 50x50 matrix. The function `deform[p, v, z]` returns the convolution of Green's function and the nonlinear capacitor forcing function as evaluated for deflections  $p$ , with voltage  $v$ .  $z$  is a viscosity or step-size parameter to damp oscillations of the solution. `iter[v, k]` is a routine that calculates the self consistent beam deflection for voltage  $v$ , with  $k$  as a limit on the number of iterations. The remainder of the appendix shows the details of a calculation of a hysteresis loop.

```

y1= a1 + b1 x + c1 E^(T x) + d1 E^(- T x);
y2= a2 + b2 x + c2 E^(T x) + d2 E^(- T x);

boundaryValues = Solve[ {
    y1==0 /. x->0,
    y2==0 /. x->1,
    D[y1,{x,1}]==0 /. x->0,
    D[y2,{x,1}]==0 /. x->1,
    y1==y2 /. x -> a,
    D[y1,{x,1}]==D[y2,{x,1}] /. x -> a,
    D[y1,{x,2}]==D[y2,{x,2}] /. x -> a,
    D[y1,{x,3}] - D[y2,{x,3}] + W ==0 /. x -> a},
    {a1,b1,c1,d1,a2,b2,c2,d2}];

s1= y1 /. boundaryValues;
s2= y2 /. boundaryValues;

ee = 1.2 10^11;      Young's Modulus [Pa]
ep0 = 8.85 10^-12;   Permittivity of Free Space [F/m]
tt = .13 10^-6;      Beam Thickness [m]
dd = 1 10^-6;        Beam Width [m]
ll = 25 10^-6;       Beam Length [m]
ii = dd tt^3 / 12;   Beam Moment of Inertia
t0 = .13 10^-6;      Spacer Thickness [m]
ten = 400 10^6;       Residual Beam Stress [Pa]
ww = 10^-12 ep0 ll dd / (2 t0^2 ee ii)
    Normalized electrostatic attraction (equal to W)
tt = 10^-6 (ten tt dd/ (ee ii))^5
    Normalized restoring force (equal to T)

p1 = First[Simplify[ s1 /.
    {T -> .070 1.414, W -> 8.2 10^(-6), l -> 50}]];
p2 = First[Simplify[ s2 /.
    {T -> .070 1.414, W -> 8.2 10^(-6), l -> 50}]];
g[p_,q_] := If[p>q, p2 /. {x -> p, a ->q}, p1/.
    {x -> p, a ->q}]      Green's Function at q

bounds[i_] := {i,1,49,1}

deflectionTable = Table[g[x,a],Evaluate
    [bounds[a]], Evaluate[bounds[x]]];
    Numerical evaluation of g

forcingFunction[d_] := If[d<.10,((1 - d/.13)^(-2)),
    58 - 6 10^3 (d-.2)] +
    If[d>.135,5 10^3 (d - .135),0]

limitFunction[c_] := Max[Min[.135,c],0]

```

```

middleMask = Table[If[(x>15 && x<35),1,0],
  Evaluate[bounds[x]]]

{0, 0, 0, 0, 0, 0, 0, 0, 0, 0, 0, 0, 0, 0, 0, 1, 1, 1, 1, 1
  1, 1, 1, 1, 1, 0, 0, 0, 0, 0, 0, 0, 0, 0, 0, 0, 0, 0, 0, 0,
errorFunc[a_,b_] := Apply[Plus,Abs[(a-b)middleMask]]/49
yFull = clearY[.2];
yZero = clearY[0];

viter[start_,stop_,increment_,iterations_] :=
  Module [{i,out,v},
    out = {};

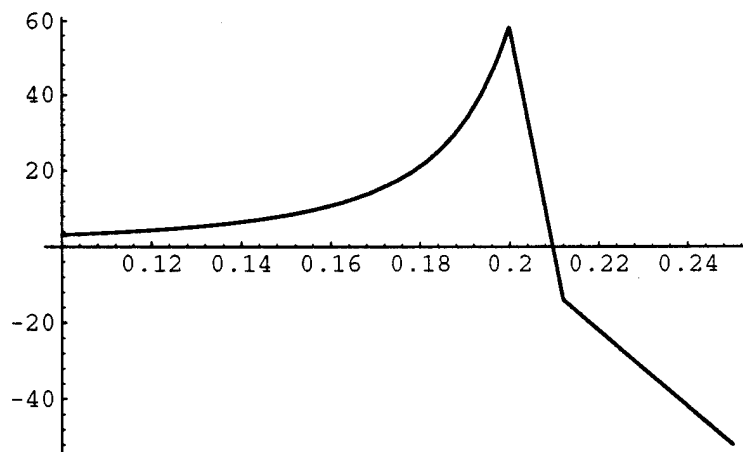
    Do[(
      iter[v,iterations];
      out = Append[out,{v,y[[25]]}];
    ),{v,start,stop,increment}];
    ListPlot[out,PlotJoined -> True];
    out
  ] This module calculates the deflection for voltages

clearY[s_] := Evaluate[Table[s,Evaluate[bounds[x]]]]

showY := Show[Table[ListPlot[m[[i]], PlotJoined -> True,
  DisplayFunction -> Identity],{i,Length[m]}],
  DisplayFunction -> $DisplayFunction,PlotRange -> All]

showF := ListPlot[forceVector,PlotJoined->True]
Plot[forcingFunction[w],{w,.1,.25}]

```



-Graphics-

```
deform[p_,v_,z_] := Module [{i},
  forceVector = Map[forcingFunction,p];
  qC = (v^2)/49 deflectionTable . forceVector;
  qC = Map[limitFunction,qC];
  p + z (qC-p)
]      This module performs one iteration of the self-
      consistent algorithm
```

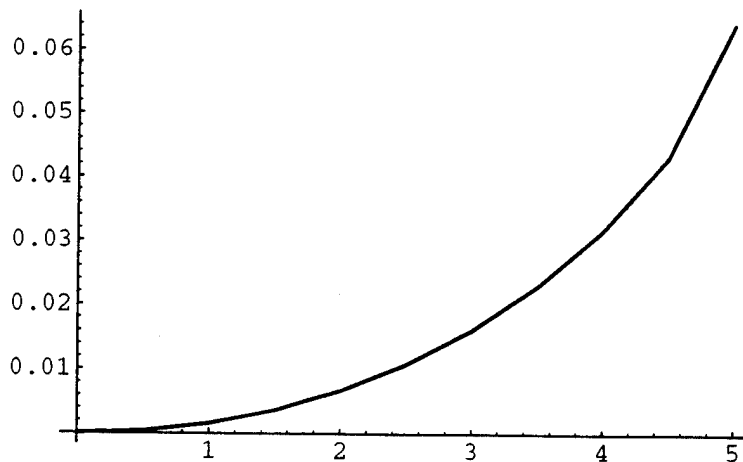
```
iter[v_,k_] := Module [{i},
  For[m={},error={};
  oldY=y;e1=1;e2=errorFunc[yFull,y];step=
    Min[10 e2,.9];i=1,
  ((i<=k) && (e1 > 10^-5) && (e2 > 10^-4)), i++,
  newY = deform [y,v,step];
  m = Append[m,newY];
  e1 = errorFunc[y,newY];
  e2 = errorFunc[yFull,newY];
  error = Append[error,{e1,e2,step}];
  step = If[ 200 e1 < step,step/2,step];
  step = If[ 10^2 e2 < step,step/3,step];
  oldY = y;
  y = newY;
];
showY
]      This module calculates the deformation at voltage v_
```

y = yZero

```
{0, 0, 0, 0, 0, 0, 0, 0, 0, 0, 0, 0, 0, 0, 0, 0, 0, 0, 0, 0, 0, 0
  0, 0, 0, 0, 0, 0, 0, 0, 0, 0, 0, 0, 0, 0, 0, 0, 0, 0, 0, 0,
```

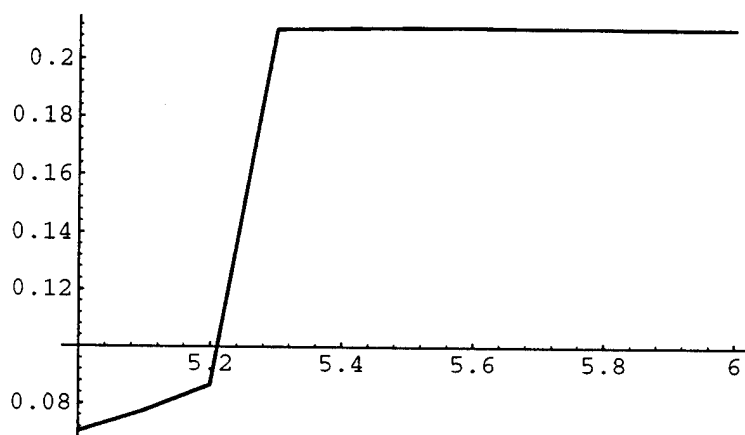
viter[0,5,.5,50]





```
{ {0, 0}, {0.5, 0.000377021}, {1., 0.00157196}, {1.5, 0.0036
  {2.5, 0.0107871}, {3., 0.0161082}, {3.5, 0.0229396}, {4.,
    {4.5, 0.0431862}, {5., 0.0641659}}
```

**viter[5,6,.1,100]**

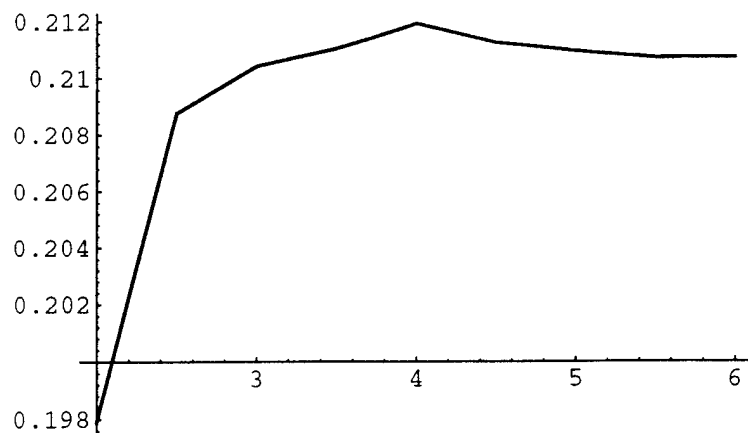


```
{ {5, 0.0703352}, {5.1, 0.0775739}, {5.2, 0.0866328}, {5.3,
  {5.5, 0.211044}, {5.6, 0.211131}, {5.7, 0.210948}, {5.8,
    {6., 0.210744}}
```

**Join[%75,%76]**

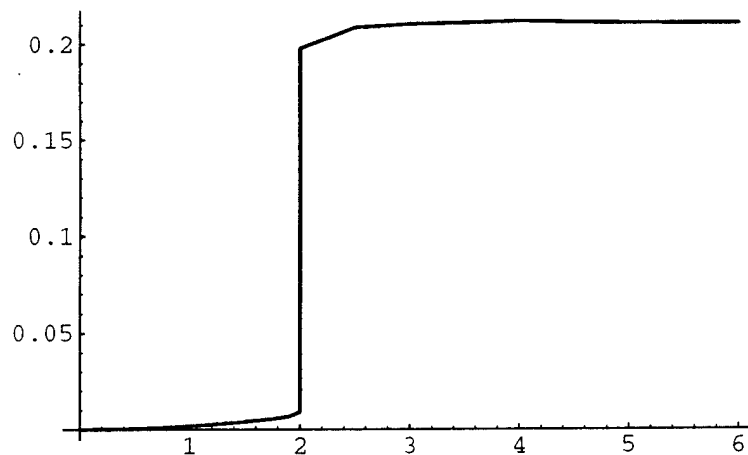
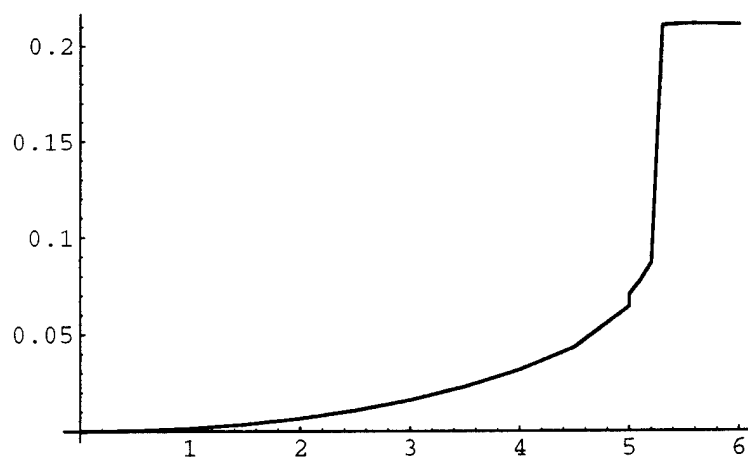
```
{ {0, 0}, {0.5, 0.000377021}, {1., 0.00157196}, {1.5, 0.0036
  {2.5, 0.0107871}, {3., 0.0161082}, {3.5, 0.0229396}, {4.,
    {4.5, 0.0431862}, {5., 0.0641659}, {5, 0.0703352}, {5.1,
      {5.3, 0.210394}, {5.4, 0.210773}, {5.5, 0.211044}, {5.6,
        {5.8, 0.210906}, {5.9, 0.210802}, {6., 0.210744}}
```

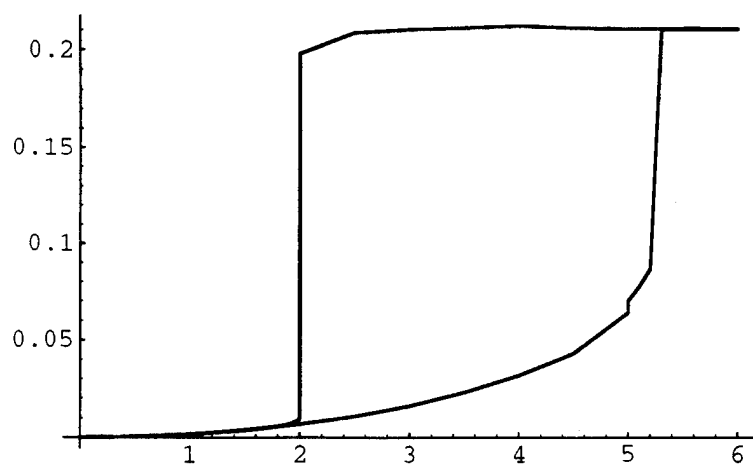
**viter[6,2,-.5,30]**



```
{ {6, 0.210758}, {5.5, 0.210734}, {5., 0.210985}, {4.5, 0.210734},
  {3.5, 0.211063}, {3., 0.210419}, {2.5, 0.208765}, {2., 0.198} }
```

```
Show[ ListPlot[%79, PlotJoined -> True],
ListPlot[%83, PlotJoined -> True] ]
```





-Graphics-

t=2000 A, T = 400 MPa, v = voltage \* 2, L = 50 $\mu$ m

## **APPENDIX B**

**SILICON MICROFABRICATION  
OF GRATING LIGHT VALVES**

by

Francisco S. A. Sandejas

G. L. Report No. 5324

Internal Memorandum

Edward L. Ginzton Laboratory  
Stanford University  
Stanford, California 94305

July 1995

## Abstract

We have invented the Grating Light Valve (GLV) which is a deformable grating structure fabricated by silicon surface micromachining. Essentially a reflection phase grating, optical modulation is achieved by electromechanically controlling the grating amplitude. Light modulation occurs by transferring optical power from the specular or zeroth diffraction order into the higher diffraction orders. The GLV is a promising light valve technology for spatial-light-modulator and display applications, particularly for projection and head-mounted displays.

We have demonstrated bistable switching at speeds as fast as 20 ns. Single-pixel contrast ratios of 200:1 have been measured. The GLV is inherently capable of color selection and, with the proper optical system, produces a full NTSC color gamut. Since the device is reflective it is capable of handling high-brightness levels, is efficient, and has a large temperature range of operation. Finally, arrays of 150-by-192 pixels have been fabricated and operated to demonstrate the GLV's color display potential.

The basic device fabrication process for the GLV is simple and compatible with CMOS processing. However, more than other microelectromechanical devices, the GLV suffers a pronounced surface adhesion problem (stiction), since it consists of optically-flat, compliant structures separated by sub-micron air gaps. Our solution is the combination of beam stiffening, surface modification, and the development of self-aligned processes to build sub-micron nanostructures underneath 1- $\mu$ m-wide deformable microbridges.

# Acknowledgements

Many people have contributed valuable assistance to this effort. I especially wish to thank:

- Prof. David Bloom for his support and guidance.
- Prof. Pierre Khuri-Yakub and Prof. Krishna Saraswat for being members of my orals and reading committees. Prof. Jim Plummer for chairing my orals committee.
- Prof. Bert Auld and Prof. Bill Spicer for their initial guidance and help.
- Jim Mcvittie, Prof. Greg Kovacs, and Prof. Simon Wong for their advise on processing issues.
- Bill Banyai, Olav Solgaard, Raj Apte, Daisuke Terasawa, and Tien Sng for their collaboration in my experiments on the GLV.
- Dave Arnone, Ike Chuang, Barb Paldus, Andy Huibers, and Ben St. John for their help in the GLV project.
- Gladys Sarmiento, Nancy Latta, Margaret Prisbe, Marnel King, Robin King, Steve Taylor, and all the other unsung heroes of CIS for all the processing help.
- Tom Carver and Lance Goddard for their help in physical vapor depositions.
- Patti Beck, Shinya Akamine, Marco Tortonese, and Matt Haller for their useful insights into micromachining.
- All former Bloom group members for making the lab a neat place in which to work.
- The Ginzton Lab and CIS Staff for making research possible.

- The Stanford University Office of Technology Licensing and the Advanced Research Projects Administration for their financial support.
- I especially want to acknowledge the encouragement and support of my wonderful family, especially my parents. Also, there are numerous friends in Opus Dei, the BGN, Stanford Students for Life and lots of other places whose friendship made this process much easier. They are too many to list and thank here, but they know who they are.



# Contents

Abstract.....	v
Acknowledgements .....	vi
Contents .....	viii
List of Figures .....	ix
List of Tables .....	xiv
List of Photographs .....	xv
Introduction and General Operating Principles .....	1
1.1. Micromachining and Optical Devices.....	1
1.2. Basic Principle of the Grating Light Valve (GLV).....	2
1.3. GLV Applications.....	5
1.3.1. GLV as a Light Valve.....	5
1.3.2. GLV as a Spatial Light Modulator.....	6
1.4. Simple Fabrication Process.....	6
1.5. This Work .....	6
Optics of the GLV.....	8
2.1. Introduction.....	8
2.2. Phase Grating Diffraction.....	9
2.2.1. General Treatment of the Diffraction Problem .....	9
2.2.2. Fraunhofer Diffraction of a Generalized Periodic Grating Structure.....	11
2.2.3. GLV: A Periodic Phase Grating .....	13
2.3. Discussion of GLV Characteristics .....	17
2.3.1. Contrast, Intensity, and Thickness.....	17

2.3.2. Duty-Cycle.....	19
2.4. Experimental Results.....	21
2.4.1. Optical Measurement System.....	21
2.4.2. Intensity and Grating Height .....	21
2.4.3. Diffraction Efficiency.....	23
2.5. GLV Color Selection.....	24
2.6. GLV Display Viewing Systems .....	24
2.7. Discussion of Results.....	25
2.7.1. Contrast .....	25
2.7.2. Efficiency .....	26
GLV Electromechanics.....	27
3.1. Introduction .....	27
3.2. Materials Parameters .....	28
3.3. Actuation .....	29
3.4. Bistability.....	32
3.5. Switching Voltage, Stress, and Beam Geometry.....	34
3.6. Hysteresis of the GLV.....	37
3.7. Resonant Frequency and Switching Speed.....	38
3.8. Ringing and Air Damping.....	40
3.9. Conclusion .....	41
The GLV Manufacturing Process and Stiction .....	42
4.1. Basic GLV Fabrication .....	42
4.2. Causes of Stiction .....	44
4.2.1. Capillary Forces.....	45
4.2.1.1. Nature of the Capillary Force or Laplace Pressure .....	45
4.2.1.2. Lowering the Capillary Force.....	47
4.2.1.3. Eliminating the Capillary Force.....	49
4.2.2. Surface Adhesion Forces .....	49
4.2.2.1. Mechanical Internal Bending Moments .....	50
4.2.2.2. Electrostatic Forces.....	50
4.2.2.3. Solid Bridging .....	51
4.2.2.4. Water Bridging and Hydrogen Bonding .....	52
4.2.2.5. Hydrogen Bonding.....	56
4.2.2.6. Van der Waals Forces and London Dispersion Forces .....	57
4.2.2.7. Conclusion: Adhesion Mechanisms and the GLV .....	58

4.3. Adhesion Energy and the Peel Condition.....	60
4.3.1 Measurement of Solid-Adhesion Energy.....	60
4.3.2 Range of Values for Various Polysilicon-Silicon Systems .....	64
4.3.3 Dependence on Roughness .....	65
4.3.4 Roughening Experiments .....	67
4.4. Stiction and the GLV.....	70
4.5. Engineering Solution to Stiction: Lessen Area of Contact.....	72
4.5.1. Incorporating the Surface Reduction Parameter into the Mastrangelo Model. ....	72
4.5.2. Limits to the Surface Patterning Technique.....	74
4.5.3. Striations.....	75
4.5.4. Self-aligned Side-wall Rails .....	78
4.5.5. Polysilicon T-Structures .....	81
4.5.6. Staggered Polysilicon Supports.....	84
4.6. Summary and Conclusion.....	89
Conclusion and Future Work.....	91
Appendix A: Definition of Terms .....	99
Appendix B: Sample CIS Process Sheet for Staggered Support Structures .....	101

# List of Figures

Figure 1.1	
Cut-out view of a GLV Pixel .....	3
Figure 1.2	
Cross-sectional cut along the length of a GLV .....	4
Figure 1.3	
Cross-section perpendicular to the length of a GLV pixel .....	4
Figure 2.1	
Diagram of a reflection phase grating.....	9
Figure 2.2:	
Close-up of one GLV diffraction element.....	10
Figure 2.3	
Diffraction intensity versus Angle .....	15
Figure 2.4	
Various components of the intensity function .....	16
Figure 2.5	
Normalized optical power in the first diffraction order versus grating height .....	18
Figure 2.6	
Diffraction versus angle for various duty-cycles.....	20
Figure 2.7	
Schematic diagram of the GLV measurement system. ....	21
Figure 2.8	
Static GLV devices fabricated to perform the contrast measurement. ....	22

Figure 2.9	
Measured optical power in the first diffraction order versus grating height.....	22
Figure 2.10	
Diffracted optical power in the different orders .....	23
Figure 2.11	
Illustration of the application of the GLV to a RGB color pixel element. ....	24
Figure 2.12:	
Two simple GLV viewing systems.....	25
Figure 3.1	
Mechanical force diagram of the GLV beam with an applied electrostatic force and a restoring tensile force.....	29
Figure 3.2	
Modeling beams as strings.....	30
Figure 3.3	
Basic GLV mechanical model .....	31
Figure 3.4	
Origin of bistability .....	33
Figure 3.5	
Apte's numerical model of switching voltage versus stress and beam length .....	35
Figure 3.6	
Plot of switching voltage as a function of beam length.....	36
Figure 3.7	
GLV optical hysteresis .....	37
Figure 3.8	
GLV hysteretic switching.....	38
Figure 3.9	
GLV 30 ns switching speed .....	39
Figure 3.10	
Ringing and air damping .....	40
Figure 4.1	
Simplest fabrication process of a single GLV pixel with one masking step .....	43
Figure 4.2	
Capillary forces. ....	46
Figure 4.3	
Two SiO <sub>2</sub> surfaces kept together by hydrogen bonding .....	54

Figure 4.4	Diagram of a doubly-clamped beam brought into contact with the substrate .....	62
Figure 4.5a	Illustration of the physical significance of roughness/variance.....	66
Figure 4.5b, c	Kurtosis and Skewness .....	67
Figure 4.6	Test-structure to measure adhesion energies of various material systems.....	68
Figure 4.7	Measured adhesion energies for various material systems.....	69
Figure 4.8	Surface adhesion energy as a function of GLV beam displacement lengths .....	73
Figure 4.9	Process flow for the striated substrate technique.....	76
Figure 4.10	Process flow for the dimpled GLV beams.....	77
Figure 4.11	Process flow for the side-wall rails process. ....	79
Figure 4.12	Process flow for fabricating polysilicon T-structure GLV beams.....	82
Figure 4.13	Ground view of staggered polysilicon support structures .....	84
Figure 4.14	Process flow for fabricating staggered polysilicon supports under GLV beams.....	85
Figure 4.15	Beam displacement length as a function of percentage contact area of the polysilicon staggered supports. ....	88
Figure 4.16	A segment of a GLV beam. Illustration of the KOH undercut etch process. ....	88

# List of Tables

Table 3.1	
Basic physical and geometric factors of the GLV .....	28
Table 3.2	
Measured properties of LPCVD nitride .....	28
Table 3.3	
Some other useful film properties of LPCVD nitride.....	28
Table 3.4	
Experimental switching voltages.....	36
Table 4.1	
Adhesion energy values for silicon-to-silicon interfaces with varying rinse treatments based on references. ....	65
Table 4.2	
Beam displacement lengths as a function of the periodicity of the staggered support structures and of the KOH undercut etch length.....	86
Table 4.3	
Summary of the engineering approaches to reducing area of surface contact between two contacting, optically-flat surfaces. ....	89

# List of Photographs

Photo 1.1	
SEM of a GLV pixel.....	2
Photo 4.1	
A close-up SEM of two 2 $\mu\text{m}$ wide-beams .....	44
Photo 4.2	
Two harp test structures.....	61
Photo 4.3	
Silicon nitride cantilevers curled upward due to stress gradients .....	62
Photo 4.4	
TEM picture of a smooth polysilicon/oxide interface.....	70
Photo 4.5	
SEM photograph of a successful striated substrate .....	75
Photo 4.6	
SEM of side-wall rails with sloped side-walls. ....	78
Photo 4.7	
SEM of side-wall rails with more vertical side-walls and more controllable rail heights .....	80
Photo 4.8	
Cross-section SEM of polysilicon T-structures. ....	81
Photo 4.9	
SEM of a transverse cross-section of two GLV beams fabricated using the T-process. ....	83



**Photo 4.10**

**Harp test structure with a checkerboard oxide mask pattern for the formation  
of staggered silicon supports in a KOH etch .....86**

**Photo 4.11**

**Harp structures showing the effectiveness of this process.....87**

# **Chapter 1**

## **Introduction and General Operating Principles**

### **1.1. Micromachining and Optical Devices**

Silicon micromachining has been described by some critics as a field full of solutions looking for a problem. This comment is understandable from an applications-oriented point of view. However, the relatively young area of microelectromechanical systems (MEMS) has been quickly coming of age as fabrication technologies are better understood and engineers are becoming more adept at using them to build devices that have never before been possible.

A research area that stands to benefit from this technology is that of optical light modulators. Some examples of MEMS optical applications are the Fabry-Perot cavity filter [Herman, 1991], infra-red shutters [Tabata, 1993], and the micromirror light valve [Petersen, 1982], which is being commercialized by Texas Instruments [Hornbeck, 1991a; Hornbeck, 1991b; Sampsell, 1993]. Micromachining provides an added attraction to optical engineers because it is an adaptation of microelectronic manufacturing processes and typically the techniques involved provide very tight control on layer thicknesses, on the order of optical wavelengths. This allows the engineers to exploit interference and diffraction phenomena. An example of a diffractive device is the viscoelastic spatial light modulator [Gerhard-Multhaupt, 1990]. Another such device is the Grating Light Valve (henceforth to be simply called "GLV").

## 1.2. Basic Principle of the Grating Light Valve (GLV)

The GLV is a microelectromechanical light valve. Particularly, it is a programmable mechanical reflection phase grating. The GLV modulates light by electrostatically adjusting the grating amplitude of the phase grating. Photo 1.1 is a scanning electron microscope (SEM) photograph of an actual GLV pixel. This particular pixel consists of 12 nitride beams stretched across a nitride frame. The beams are  $25\text{ }\mu\text{m}$  long,  $1\text{ }\mu\text{m}$  wide, and spaced with a  $2.25\text{ }\mu\text{m}$  period. The frames are  $2.5\text{ }\mu\text{m}$  wide.

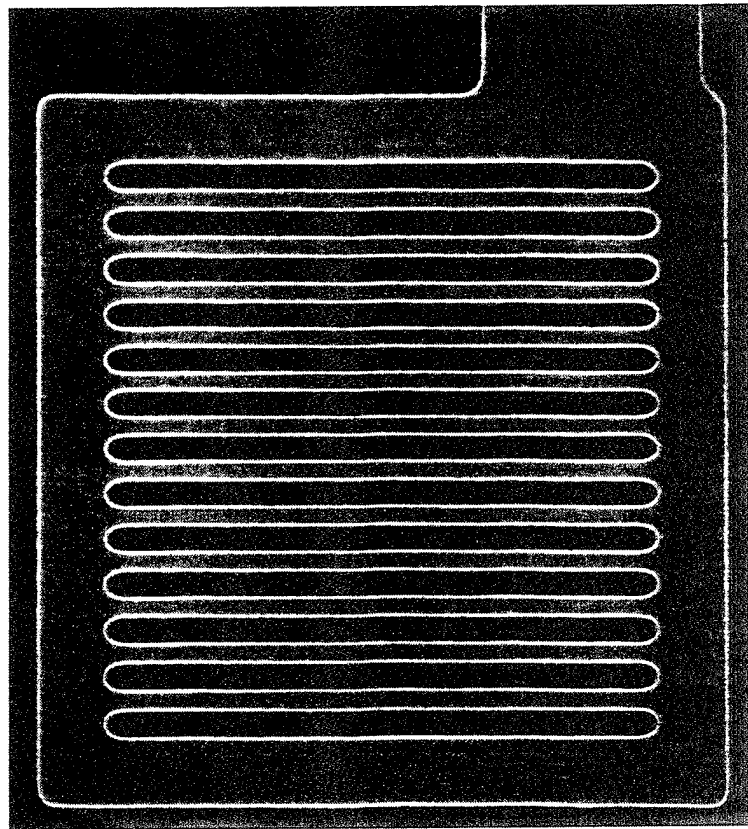
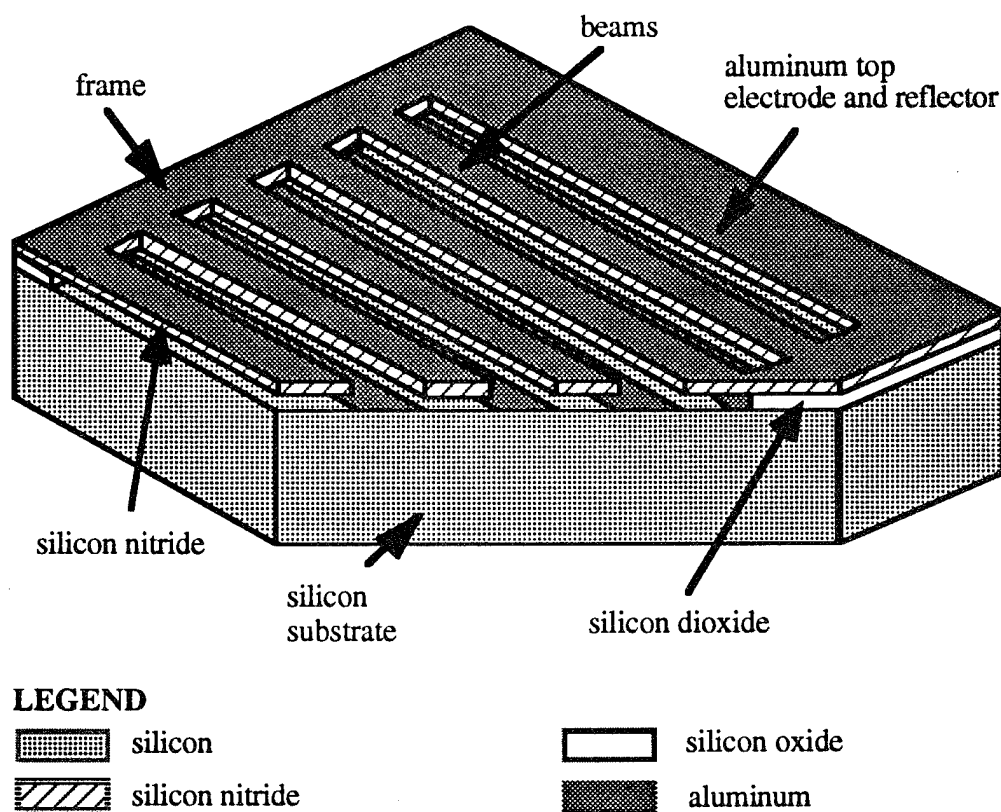


Photo 1.1: SEM of a GLV pixel with beams that are  $25\text{ }\mu\text{m}$  long,  $1\text{ }\mu\text{m}$  wide, and spaced with a  $2.25\text{ }\mu\text{m}$  period.

Figure 1.1, is a representation of the GLV with a portion of one corner cut out to show the different underlying layers. For ease of illustration, the picture is exaggerated in the vertical dimension and only four grating beam elements are drawn. We describe the drawing starting from the bottom going up. A silicon substrate supports the whole structure. On top of the substrate, a  $132\text{ nm}$  thick oxide layer forms an O-ring that

supports the nitride frame. Spanning the length of the nitride frame are the 132 nm thick beams which are stretched across the substrate. A thin aluminum layer is evaporated on top of all the vertically exposed surfaces, i.e. on the beams and on the surfaces of the spaces between the beams. This serves as a reflection layer and also as the top and bottom electrodes. There is no oxide underneath the beam area, so if a cross-section is taken along the length of the pixel then the picture will look like figure 1.2. The beams form microbridges supported and raised above the substrate by the oxide at their ends. Tension in the nitride film keeps the beam from collapsing into the substrate area. Figure 1.2b demonstrates what happens if a voltage force is applied between the top electrode and the substrate electrode. This electrostatic load pulls the beams to the substrate. If the force is removed then the tension in the beams will provide a restoring force that pulls them back up.



**Figure 1.1:** Illustration of an aerial view of a Grating Light Valve pixel with a corner cut-out to expose its underlying elements.

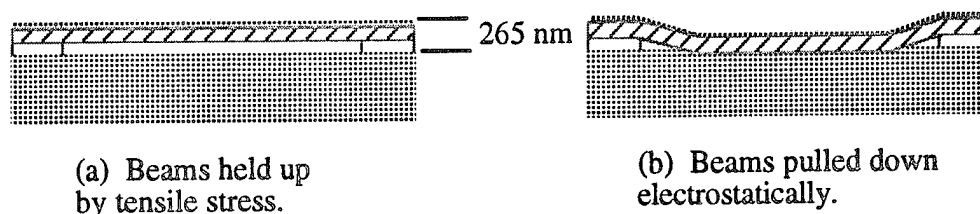


Figure 1.2: Cross-sectional cut along the length of a GLV beam structure. On the left, the beam is up; on the right, down.

Silicon micromachining is the technology that has enabled the fabrication of such a grating structure. The manufacturing process for the GLV is simple but tricky; we will therefore leave its discussion for later. For now, we will assume that such a micromechanical device can be made and will perform as described above.

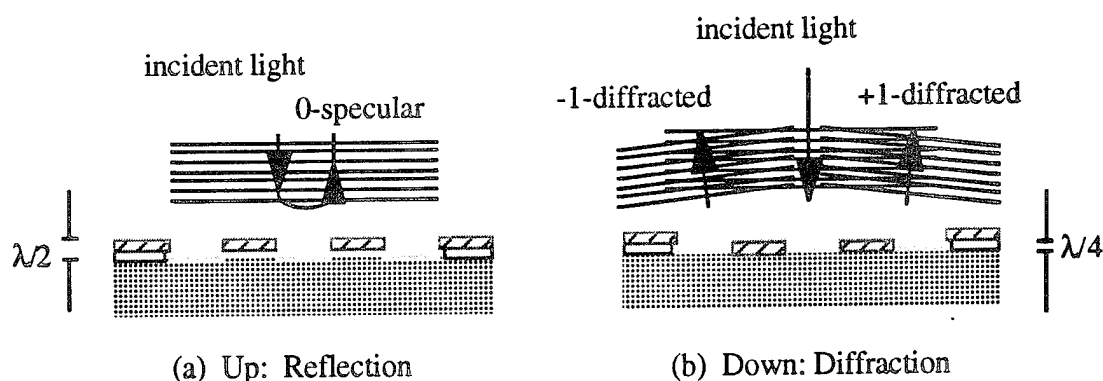


Figure 1.3: Cross-section perpendicular to the length of a GLV pixel. The device forms a reflection phase grating with two sets of diffraction elements, one of which is movable allowing control of the grating amplitude. In (a) the beams are up and the GLV reflects light; while in (b) the beams are down and diffract the light.

Typical thicknesses of the air gap and the nitride beams are 132 nm, which corresponds to a fourth of the visible green wavelength (530 nm). The mechanical deflection of the beam is also equal to this quarter-wave distance. This tiny mechanical motion allows the grating to modulate reflected light. Taking a cross-section perpendicular to the length of the beam reveals a picture as in figure 1.3. The left side corresponds to the up-state and the right side corresponds to the down-state. Optically, the structure is a reflection phase grating with a grating amplitude that can be controlled via the electromechanical motion of the beams. The grating amplitude is defined as the height difference between the two sets

of diffraction elements. The GLV's two sets of diffraction elements are the tops of the beams and the reflective metal in the spaces between the beams. A very simple way of analyzing this diffraction case starts by considering a source of monochromatic light normally incident on the GLV pixel. With no voltage applied between the bridges and the substrate, the grating amplitude is one half of the wavelength of the incoming light. Since the round-trip path difference between the light reflected from the top and bottom of the grating is one wavelength, the reflected light adds in-phase and constructive interference occurs. The grating acts like a flat mirror. However, when a voltage is applied between the bridges and the substrate, the electrostatic force pulls the bridges down. The grating amplitude is now one quarter of the wavelength; the round-trip path difference is half a wavelength; and, diffraction from the bridges and the substrate add destructively. Light power is not sent into the specular direction but is instead diffracted into the odd diffraction modes. If the detection system for the reflected light has a numerical aperture which accepts only the zero-order light, a mechanical motion of only one quarter of a wavelength is sufficient to modulate the reflected light with high contrast. This is the most basic way of analyzing the diffraction condition for the grating light valve. Chapter 2 will discuss the optics of the GLV in more detail.

## 1.3. GLV Applications

### 1.3.1. GLV as a Light Valve

The invention of the grating modulator was made possible by silicon microfabrication enabling technologies. In actuality, the GLV was the result of the merger of previous Stanford expertise in micromachining and in the area of programmable reflection phase gratings. The Silicon Modulator (SIMOD) [Hemenway, 1990] is a phase grating that exploits the charge plasma effect in silicon to change its effective index of refraction. The envisioned application for the SIMOD was fiber telemetry or remote sensing via a fiber-optic network. Granting that most sensor applications do not require large bandwidths and prefer cheap, robust transducers, the GLV was initially developed with the same motivation [Solgaard, 1992a; Solgaard, 1992b; Sandejas, 1992].

As a light valve, the GLV offers a number of attractive features. The obvious distinction is that it is a silicon micromachined device that is simple to fabricate. It can be made cheaply and integrated with CMOS circuitry. Mechanically, the device is fast and bistable: we have demonstrated high-speed switching as fast as 20 ns and have also demonstrated hysteretic behavior. This type of latching behavior simplifies system

integration and possible drive circuitry since active transistors will not be necessary to maintain either the on or off states. Depending on the device geometry and material properties, the voltage levels required to switch the GLV ranges from 5 to 30 V, well within the range of display drivers today. Finally, the optical device is relatively polarization insensitive, efficient, capable of high-brightness levels, and gives contrast ratios of up to 350:1 using laser illumination.

### 1.3.2. GLV as a Spatial Light Modulator

There are also large-array applications for the grating light valve. Single columns of the GLV can be used in printers. GLV-based two-dimensional spatial light modulators (SLM's) can be used for optical computing or display applications. Of course, the display application area is the most commercially attractive and, thus, became a major focus of this research effort.

Beyond the strong points of the GLV as an individual light valve, it possesses attractive features for display systems. The grating device is inherently color dispersive and has demonstrated a full-NTSC color gamut without the use color filters. Its bistability could enable a high-image-quality GLV display without active matrix addressing; while, the short switching times will allow 8 bits of gray-scale with time-division multiplexing schemes. Since it is efficient and reflective, the GLV can tolerate very high optical power levels, leading to brighter projection systems. Finally, high-density arrays of these valves can be fabricated using existing silicon technology.

## 1.4. Simple Fabrication Process

The GLV in its most basic form requires only one-masking step and uses standard CMOS processes. A severe problem encountered in the manufacturing of the GLV is that of surface adhesion. Some additional process techniques were investigated to overcome stiction. Nevertheless, the integrated manufacturing process will potentially be completely compatible with integrated drive circuitry and provide a lower-cost, higher-quality solution to projection display systems.

## 1.5. This Work

Original contributions of this author's research effort have been the following:

- co-invention of the GLV
- fabrication and testing of the first GLV devices

- calibration and measurement of basic light valve properties
- process design and development with an emphasis on solving the stiction problem
- dynamic switching demonstration of a 150 x 168 array of 20 x 20  $\mu\text{m}^2$  RGB pixels in a color bar display configuration

This document will mainly focus on GLV fabrication process development (Chapter 4). It will only present the very basic design concepts for device optics (Chapter 2) and electromechanics (Chapter 3), particularly as they relate to process constraints. Thus, the focus is on the GLV as a simple light valve element rather than as a display device, even if that is probably its most commercially attractive application. Finally, it must be added that theory and data for the calibration measurements of intensity versus film thickness and duty-cycle, and the experimental verification of GLV hysteretic switching are presented here for the first time.

Other interesting aspects of the GLV opus have been reported by Olav Solgaard and Raj Apte [Solgaard, 1992a; Apte, 1994b], two other collaborators at different stages in this work. Olav is a co-inventor of the GLV, while Raj joined later to assist in much of the theoretical modeling and in the development of 2-dimensional addressing. Their theses include sections on mechanical fracture, stress limits, and beam modeling by numerical methods. Electronic and optical issues discussed are modeling of GLV color operation, contrast for broadband illumination, and 2-dimensional addressing.



## Chapter 2

# Optics of the GLV

### 2.1. Introduction

Regardless of the intended application of a particular light valve, a high contrast ratio and an efficient optical throughput are always desired. Contrast ratio is defined as the difference between the bright and dark-state luminance over the luminance of the pixel in its dark-state (see equation 2.17). For displays this is often considered as the most important visual characteristic. For power, brightness, and thermal issues, optical efficiency is also a strong concern. Optical efficiency is defined as the luminance of useful light out over the luminance of light used to illuminate a device. In the case of the GLV, this is mainly determined by the diffraction efficiency of the grating. In this chapter, we will only be considering the GLV device by itself without any spatial or color filters, which would further decrease efficiency in optical systems.

There are other optical characteristics that are of interest, especially for display engineers. For completeness, the end of this chapter will briefly discuss the application of the GLV to optical display systems. However, this chapter will mainly focus on characteristics of the GLV as a general light valve device and not particularly as a device for display applications. For more detail on the GLV as a display component see [Apte, 1994b].

From chapter one, it was understood that the basis of the grating light valve operation is the electromechanical control of the grating depth of a reflection phase grating. However,

to experiment with the optical characteristics of the GLV it was simpler to work with static phase grating devices. While Chapter 4 will show how the GLV manufacturing process had to be carefully developed, working with fixed, immobile gratings allowed simultaneous investigation of the GLV optical characteristics, even when it was difficult to yield working mechanical devices that did not stick. Furthermore, since it is easy to know the geometric dimensions of the static grating, they can also be used as calibration standards for the moving gratings.

## 2.2. Phase Grating Diffraction

### 2.2.1. General Treatment of the Diffraction Problem

As an optical device, the GLV is basically a reflection phase grating whose grating depth or amplitude can be mechanically controlled. The GLV's grating depth is determined by the height difference between two sets of reflective, diffraction elements. The first set consists of the top surfaces of the microbeams and the second set is formed by the reflective metal on the exposed spaces between the microbeams.

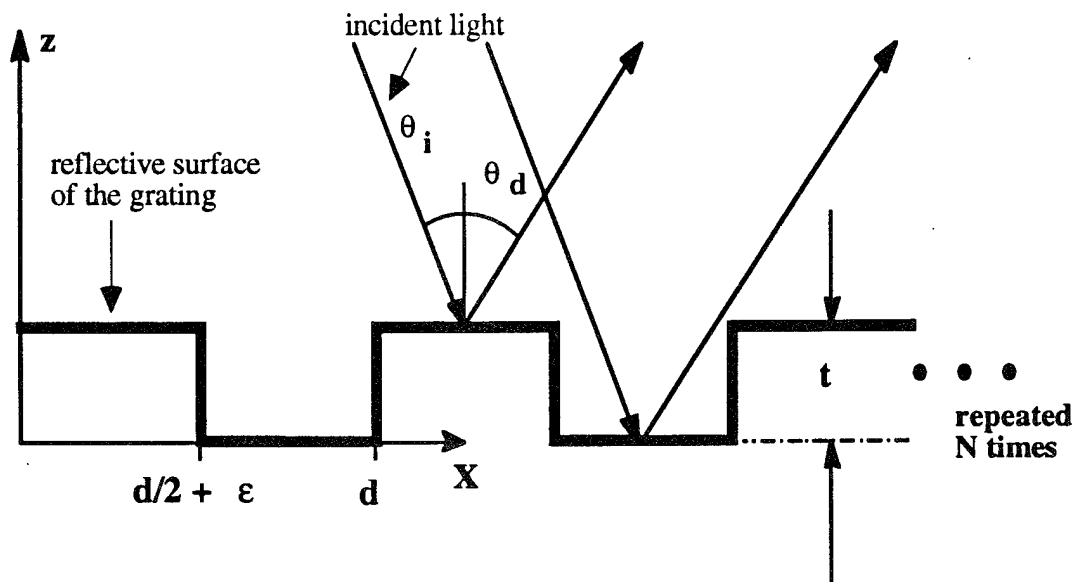


**Figure 2.1:** Diagram of variables for diffraction from a reflection phase grating (vertical dimensions are exaggerated for illustrative purposes). Two light rays are shown reflecting off the grating's diffractive elements.

If we take a cross-section of the GLV along the beams' transverse direction and consider only the important optical surfaces of the device, we are left with a general grating structure as pictured in figure 2.1. This analysis will neglect the effect of shadowing and the absence of metal on the side-walls of the grating.

Figure 2.1 illustrates the important parameters of consideration in the GLV reflection phase grating. The grating consists of repeated diffraction elements, each of which is a couple of flat mirror surfaces at two different height levels, separated by a distance,  $t$ , in the  $z$ -direction. The grating pitch or periodicity is determined by the horizontal separation distance,  $d$ , between two adjacent periods or line-pairs.  $N$  is the number of diffraction line-pair elements in the GLV pixel. Finally, the duty cycle of the grating is defined as the ratio of the width of the higher surface compared to the grating period. Figure 2.2 is a close-up of one diffraction element drawn to show the dimensional elements that affect the duty-cycle. The diffraction element has a width of  $d$ , starting from  $x = -d/2$  to  $x = d/2$ . The top surface continues from  $x = -d/2$  to  $x = \epsilon$ . While the bottom surface runs from  $x = \epsilon$  to  $x = d/2$ . The offset value,  $\epsilon$ , is limited to an absolute value of  $d/2$  by the geometry of the device. Thus, the duty-cycle is defined as:

$$\text{Duty Cycle} = \left( \frac{1}{2} + \frac{\epsilon}{d} \right) \times 100\% \quad (2.1)$$

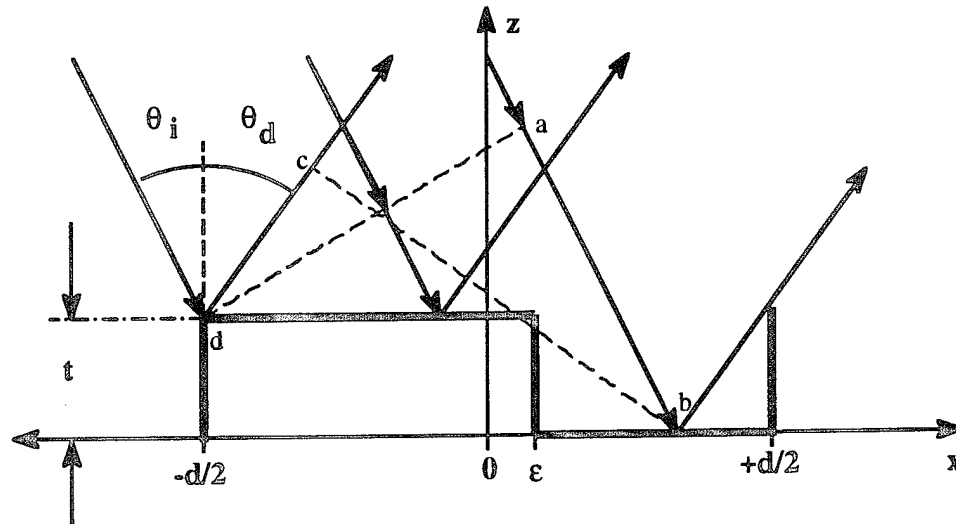


Figure 2.2: Close-up of one GLV diffraction element.

Figure 2.2 also shows light rays bouncing off the reflective surfaces to illustrate how we derived the added phase due to varied optical paths. A simple analysis of the above

geometry shows us how we should add and subtract segments of the optical paths. From looking at the geometry above and subtracting path differences, it can be shown that for optical rays incident upon a surface at the same height but separated by a certain distance  $x$  in the horizontal direction, the magnitude of the total path difference, PD, is given by:

$$\text{Path Difference} = PD = x(\sin \theta_i - \sin \theta_d) \quad (2.2)$$

where  $\theta_i$  is the angle of incidence and  $\theta_d$  is the diffraction angle. However if there is an added height difference,  $t$ , to the path delay, as is the case of light bouncing off the right side, then the path difference for a the third ray relative to the first ray is given by the difference between the line segments  $ab$  and  $cd$  (i.e.  $\overline{ab} - \overline{cd}$ ):

$$\begin{aligned} \text{Path Difference} = PD &= \overline{ab} - \overline{cd} \\ &= x(\sin \theta_i - \sin \theta_d) + t(\cos \theta_i + \cos \theta_d) \end{aligned} \quad (2.3)$$

At this point, we define

$$p = \sin \theta_i - \sin \theta_d \quad (2.4)$$

$$q = \cos \theta_i + \cos \theta_d \quad (2.5)$$

such that the phase delay,  $\Delta\phi$  is defined as:

$$\Delta\phi = k \times PD = \begin{cases} kpx & -\frac{d}{2} \leq x < \varepsilon \\ kpx + kqt & \varepsilon \leq x < \frac{d}{2} \end{cases} \quad (2.6)$$

where  $k$  is the wavenumber and is equal to  $2\pi/\lambda$ .

### 2.2.2. Fraunhofer Diffraction of a Generalized Periodic Grating Structure

Before delving into the diffraction problem for the particular case of the GLV, it is useful to understand the general case of diffraction from a periodic grating structure, be it a phase or amplitude grating.

Born & Wolf's [Born, 1989] Fraunhofer analysis of a simple periodic grating with  $N$  diffraction elements gives us the following value for the optical intensity as a function of  $p$ , which is dependent on the incident and diffracted angles.

$$I(p) = I_o(p) \times H\left(N, \frac{kdp}{2}\right) \quad (2.7)$$

The above relation expresses the optical intensity,  $I(p)$ , as the product of two functions:  $I_o(p)$  is the intensity contribution of a single grating period on the optical intensity; and,  $H(N, kdp/2)$ , represents the effect of the interference of light from different periods.  $H(N, x)$  is defined as:

$$H(N, x) = \left( \frac{\sin Nx}{\sin x} \right)^2 \quad (2.8)$$

This interference function acts like a sampling function with strong, principal peaks of value  $N^2$  whenever  $x$  is zero or an integral multiple of  $\pi$ . It also has minor maxima points, depending on the value of  $N$ , in between these peaks. As  $N$  approaches infinity, the function  $H(N, x)$  becomes a comb function with delta functions positioned at the major peak positions. The interference function determines the angles of the various diffraction modes of the grating. To better understand the function  $H(N, x)$  we proceed to analyze the periodic grating case. In this case  $x = kdp/2$ . Solving for the values of  $x$  that are integral multiples of  $\pi$  and that lead to those very strong peaks in intensity, one derives the famous Bragg diffraction condition.

$$p = \sin \theta_i - \sin \theta_d = \frac{m\lambda}{d} \quad (m = 0, \pm 1, \pm 2, \dots) \quad (2.9)$$

It says that, at various angular orientations, the optical intensity will peak when there is constructive interference. The integer  $m$  represents the path difference in wavelengths between light diffracted into particular diffraction angles from corresponding points in two adjacent grating elements. The integer  $m$  is called the diffraction order number.

The interference function above is modulated by an envelope function  $I_o(p)$  which is based on the effect of a single period and determines the relative intensities of the optical power in the different diffraction orders.  $I_o(p)$  is found by solving the following relation and integral :

$$I_o(p) = |E_o(p)|^2 = E_o^*(p) E_o(p) \quad (2.10)$$

$$E_o(p) = C \int_A F(x) e^{-jkpx} dx \quad (2.11)$$

where  $C$  is a normalizing constant, and the subscript  $A$  for the integral means that

integration is taken over the aperture area of one diffraction period.  $F(x)$  is the aperture function of the diffraction element. It is through this aperture function that we are able to distinguish the effects of particular periodic grating types.

### 2.2.3. GLV: A Periodic Phase Grating

Thus far, we have analyzed the general case of a periodic grating structure. Now, we consider the particular case of a grating whose periodic elements are phase objects.

The above analysis of the GLV phase grating and of the phase delays based on path differences due to geometrical path delays shows us that  $F(x)$  is given by the following function,

$$F(x) = \begin{cases} e^{-jkqt} & -\frac{d}{2} \leq x < \epsilon \\ 1 & \epsilon \leq x < \frac{d}{2} \end{cases} \quad (2.12)$$

Since, the GLV's diffraction elements are only phase objects and do not attenuate the incident light, the absolute value of  $F(x)$  is always unity but includes an added phase term,  $e^{-jkqt}$ , to the incident wave. The other  $e^{-jkpx}$  term from the path difference analysis is not included in the aperture function because this term arises from the x-position variation and Born and Wolf's generalized analysis already includes this term in the integral as seen in equation (2.11). Thus, to find the diffraction intensity from the GLV grating, we start by evaluating the integral for  $E_o(p)$  based on the aperture function given in (2.12). Then relation (2.10) will give the intensity and its angular dependence. The final result is:

$$I_o(p) = E_o(p)E_o^*(p) \\ = \frac{CC^*}{(kp)^2} \left\{ \cos^2\left(\frac{kqt}{2} - \frac{kpd}{4}\right) \sin^2\left(\frac{kpd}{4}\right) \cos^2\left(\frac{kp\epsilon}{2}\right) + \right. \\ \left. \sin^2\left(\frac{kqt}{2} - \frac{kpd}{4}\right) \cos^2\left(\frac{kpd}{4}\right) \sin^2\left(\frac{kp\epsilon}{2}\right) \right\} \quad (2.13)$$

Plugging this value for  $I_o(p)$  into Equation (2.7) and normalizing the resultant function, we finally have the expression for total diffracted intensity from a GLV pixel of N periodic grating elements:

$$I(p) = \frac{H(N, \frac{kpd}{2})}{N^2} \frac{I(p=0)}{\left(\frac{kpd}{4}\right)^2} \left\{ \begin{array}{l} \cos^2\left(\frac{kqt}{2} - \frac{kpd}{4}\right) \sin^2\left(\frac{kpd}{4}\right) \cos^2\left(\frac{kpe}{2}\right) + \\ \sin^2\left(\frac{kqt}{2} - \frac{kpd}{4}\right) \cos^2\left(\frac{kpd}{4}\right) \sin^2\left(\frac{kpe}{2}\right) \end{array} \right\} \quad (2.14)$$

Equation (2.14) is the governing relation that best describes the principle behind the GLV. It is used in the following sections to derive various operational parameters of this optical device.

$I(p)$  was normalized such that  $I(p=0)$  is the optical intensity measured in the zero or specular order from an aperture of width  $(Nd)$ .  $H(N, kpd/2)$  determines the diffraction order angles. Within the brackets of the third factor are two terms, each comprised of three more factors, which are out-of-phase trigonometric functions with the same arguments. Looking at these two terms within the brackets, we start by focusing on their second factors which contain the argument  $kpd/4$ . The  $\sin^2(kpd/4)$  term zeroes at all the even diffraction modes of  $H(N, kpd/2)$  and is equal to unity at the odd modes. The reverse is true of the  $\cos^2(kpd/4)$  term. Hence, the first term determines the existence of odd modes while the second term contributes even modes. The relative intensities of the light in these modes is determined by the two other factors within terms. The third factor contains the duty-cycle parameter,  $\epsilon$  in  $(kpe/2)$ , and determines whether or not any even orders will exist. A perfect 50% duty cycle will set  $\epsilon = 0$  and zero the contribution of the even-order second term, meaning all the even modes will be nulled. This situation will reduce equation (2.14) to (2.15).

$$I(p) = \frac{H(N, \frac{kpd}{2})}{N^2} I(p=0) \left\{ \cos^2\left(\frac{kqt}{2} - \frac{kpd}{4}\right) \frac{\sin^2\left(\frac{kpd}{4}\right)}{\left(\frac{kpd}{4}\right)^2} \right\} \quad (2.15)$$

The odd order modes are dominant in the GLV system. Finally, the first factor whose argument is  $(kqt/2 - kpd/4)$  demonstrates how the GLV actually modulates the intensity in the different diffraction orders. It shows us how by changing the grating height,  $t$ , we can either cancel or maximize the intensity in particular diffraction orders.

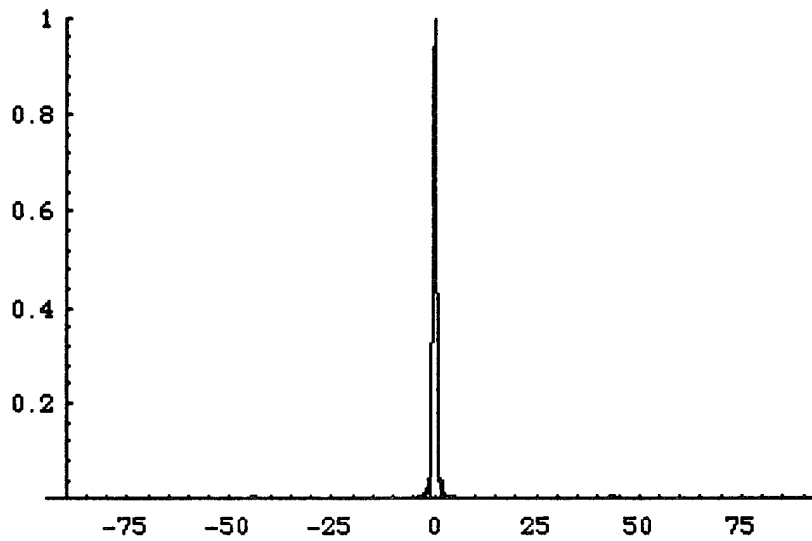


**Figure 2.3a:** Intensity versus angle in degrees for HeNe light (633 nm) normally incident on a "red" pixel ( $d = 2.75 \mu\text{m}$ ) with a grating depth of  $t = 316 \text{ nm}$ .

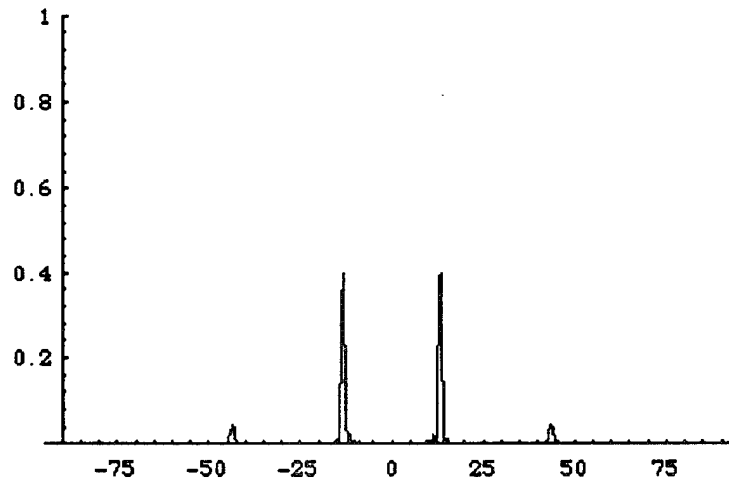


**Figure 2.3b:** Intensity versus angle in degrees for HeNe light (633 nm) normally incident on a "red" pixel ( $d = 2.75 \mu\text{m}$ ) with a grating depth of  $t = 158 \text{ nm}$ .

Continuing our analysis of the ideal GLV (with a 50 % duty-cycle and only odd-order modes), we further simplify the situation by assuming that our incident light source is coming in from a normal direction to the grating, making  $\sin \theta_i = 0$ . Thus  $p = -\sin \theta_d$ . We take as an example the particular case of red light from a HeNe laser (632.8 nm wavelength) incident upon a "red" grating with a period of  $d = 2.75 \mu\text{m}$ . A plot of the intensity versus the angle of diffraction at two particular heights ( $t = 316 \text{ nm}$  for the up-state and  $t = 158 \text{ nm}$  for the down-state) is shown in figure 2.3. The top plot is for the case



of the up position and shows us how all the optical power is diffracted into the zero order. However, the second plot shows us how by moving the grating height to half this distance will extinguish this order and send the optical power into the odd order modes, with the  $\pm 1$  modes getting about 40.5 % each.

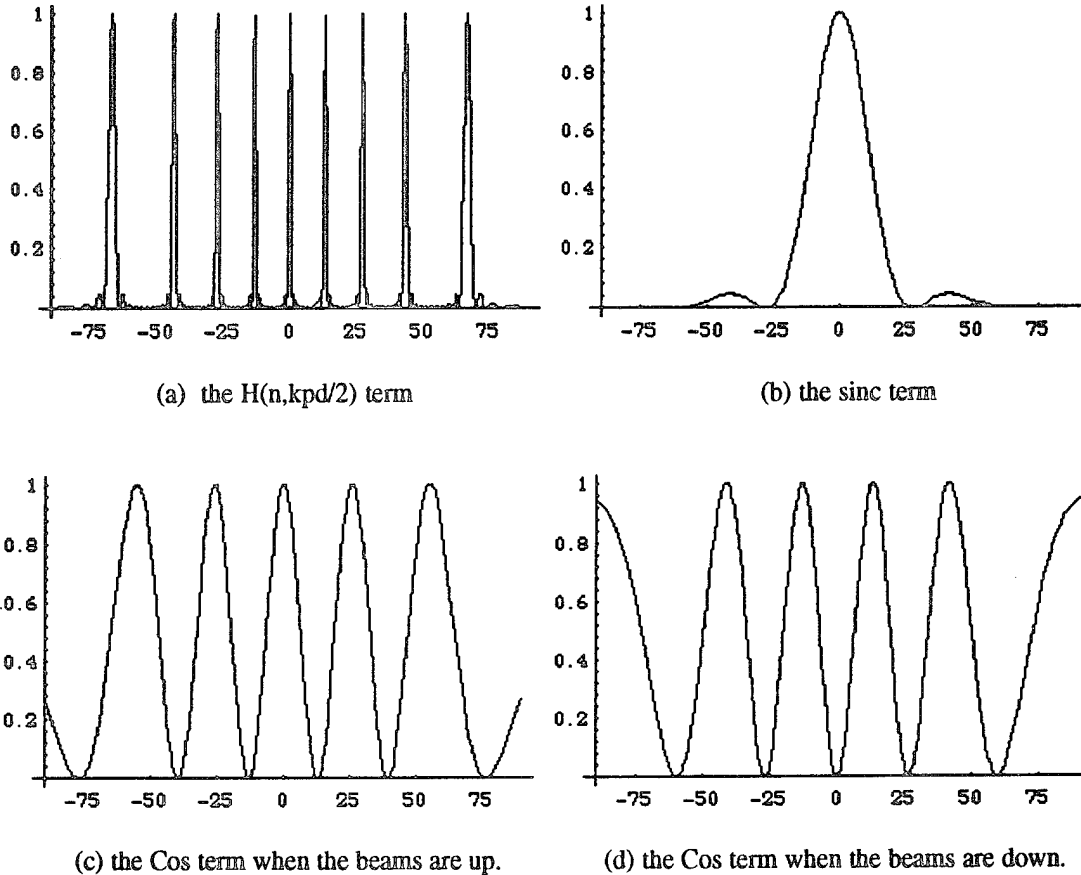


Figure 2.4: Various components of the intensity function in figure 2.3. The plots show the values of the 3 factors for normalized intensity as a function of angle (in degrees) for HeNe light (633 nm) normally incident on a “red” pixel ( $d = 2.75 \mu\text{m}$ ) with grating depths of  $t = 316 \text{ nm}$  (Figure c, beams are up) and  $t = 158 \text{ nm}$  (Figure d, beams are down).

It is very instructive at this point to evaluate the individual terms that go into the total diffraction intensity value. See figure 2.4. Independent of the height, the first term  $H(N, kpd/2)$  will give the diffraction orders at angles where  $p = \pm m\lambda/d$ . For example, the first diffraction angle ( $m = 1$ ) is at  $\theta_d = \sin^{-1}(m\lambda/d) = 16.33^\circ$ . The third term is essentially the square of a sinc function with nulls in the even mode angles. Its magnitude in the odd order modes determines the maximum optical power output in these angles. This is

depicted in plot (b) and is also independent of the grating height,  $t$ . For the  $\pm m$  order modes, the maximum intensity will be given by:

$$I_{\max}(p = m\lambda / d) = I(p = 0) \frac{\sin^2(m\pi / 2)}{(m\pi / 2)^2} \quad (2.16)$$

At  $m = 1$ ,  $I_{\max} = 40.5\%$  of  $I(p=0)$ ; and at  $m = 3$ ,  $I_{\max} = 4.5\%$  of  $I(p=0)$ .

Plots (c) and (d) are the plots of the second term  $\cos^2(kqt/2 - kpd/4)$  and depending on the grating height, will determine whether or not a particular odd order or the specular order are completely extinguished. Plot (c) is for a grating height of  $t = 316$  nm where the zero order is at its peak and the odd orders are extinguished; on the other hand plot (d) is for the case of  $t = 158$  nm and here the  $\pm 1$  orders are at their peak while the zero order is extinguished.

## 2.3. Discussion of GLV Characteristics

### 2.3.1. Contrast, Intensity, and Thickness

In the GLV case, good contrast at a particular diffraction angle is determined by the ability to null out that order and bring it to its maximum intensity (see equation 2.16). Since contrast is defined as:

$$Contrast = \frac{I_{\max} - I_{\min}}{I_{\min}} \quad (2.17)$$

it is highly dependent on the ability of the GLV to null the particular diffraction order being detected. From the analysis below, this means controlling the grating height well.

In practical applications, optical efficiency is a major concern. Since most power is transferred between the specular order and the first diffraction modes, the first order is chosen as the active modulated order. With this in mind, the diffraction efficiency in the first diffraction order will be analyzed as a function of grating height.

To simplify our analysis of the GLV, first assume the ideal grating case with a 50% duty-cycle, i.e.  $\epsilon = 0$ . We take the simple case of normal incidence ( $\theta_i = 0$ ) and consider two types of helium-neon (HeNe) lasers, one emitting light at the red (632.8 nm) and the other, at the green (543.5 nm). The red light is normally incident on a GLV pixel with a pitch of  $2.75 \mu\text{m}$  while the green light strikes a  $2.25 \mu\text{m}$  pitch GLV pixel. The expression for the intensity in the first diffraction orders reduces to:

$$I(p = \lambda / d) = I(p = 0) \cos^2 \left( \frac{kqt}{2} - \frac{\pi}{2} \right) \frac{\sin^2(\pi / 2)}{(\pi / 2)^2} \quad (2.18)$$

Figure 2.5 plots, for both cases, the optical intensity as a function of grating height which is evaluated from 100 nm to 310 nm. Extrema are located at the thicknesses where the arguments of the cosine term go from  $\pi$  to  $\pi/2$ . The leftmost curve represents the green light on the 2.25  $\mu\text{m}$  pixel. The null for this case is at 276 nm, and the peak is at 138 nm. While for the red case it is at 320 nm. and 160 nm, respectively. Maximum values for the intensity are 40.5 % of the maximum in the specular order.

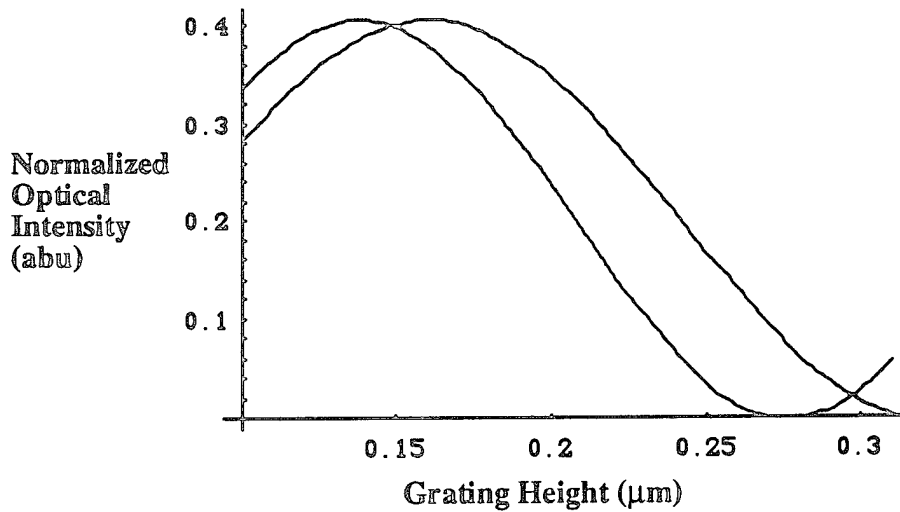


Figure 2.5: Normalized optical power in the first diffraction order versus grating height (in  $\mu\text{m}$ ) as a fraction of  $I(p=0)$ . The left most plot is for green (543.5 nm) light normally incident on a 2.25  $\mu\text{m}$  pixel. The second curve is for red (632.8 nm) normally incident on a 2.75  $\mu\text{m}$  pixel.

### 2.3.2. Duty-Cycle

For efficiency reasons, the chosen method of light modulation would be to transfer optical power between the specular and the first diffraction orders. And, for the particular case of a color selective light valve, the first diffraction order has to be used, since the wavelengths are not dispersed in the specular order.

However, from equation 2.14, if the duty-cycle wavers from 50 %, then the even modes start to appear and the coupling efficiency to the first orders is lowered. The power that would otherwise go to these orders now show up in the even order modes, which would not exist if the duty-cycle was 50 %. To simulate this effect, we consider the same GLV system with duty-cycles of 50, 40, and 30 % ( $\varepsilon = 0, 0.225$ , and  $0.450 \mu\text{m}$ , respectively). The system has similar parameters as the examples above:  $d = 2.25 \mu\text{m}$ ,  $\lambda = 632.8 \text{ nm}$ , and a normal angle of incidence ( $\theta_i = 0^\circ$ ). Figure 2.6 plots normalized optical intensity as a function of diffraction angle (only positive angles are plotted since the system is symmetric around the normal). There are two traces in each plot corresponding to two grating heights,  $t = 316 \text{ nm}$  (lighter traces) and  $t = 158 \text{ nm}$  (darker traces). The three different plots correspond to the values of duty-cycle.

These two plots clearly demonstrate how the power is indeed lost from the odd order modes to the even order modes if the duty-cycle is not 50 %. The second order's maximum intensity as a percentage of  $I(p=0)$  is given by the following relation:

$$\frac{I_{\max}(p = 2\lambda / d)}{I(p = 0)} = \left( \frac{\sin(2\pi\varepsilon / d)}{\pi} \right)^2 \quad (2.19)$$

The second plot is for a 40 % duty-cycle, and at its peak  $I_{\max}(m=2) = 3.5 \%$  of  $I(p=0)$  while  $I_{\max}(m=1)$  is reduced to 36.6 % of  $I(p=0)$ . For 30 % duty-cycle,  $I_{\max}(m=2) = 9.2 \%$  while  $I_{\max}(m=1)$  is reduced to 26.5 %.

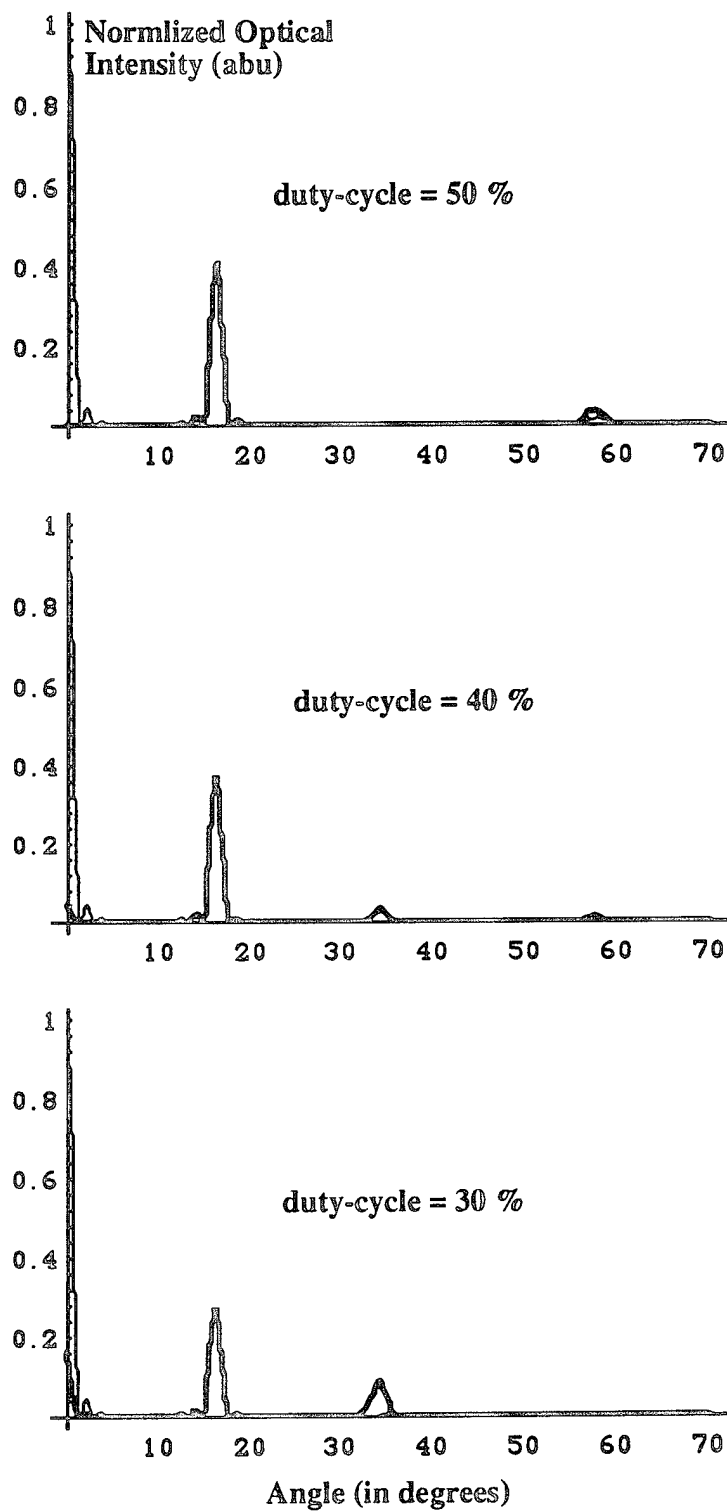


Figure 2.6: Diffraction versus angle for duty-cycles of 50% , 40%, and 30 % at two different grating heights. The dark traces are calculated at  $t = 158$  nm and the lighter traces are for  $t = 316$  nm.

## 2.4. Experimental Results

### 2.4.1. Optical Measurement System

To experimentally verify the predictions for the GLV optical characteristics, a simple measurement system was used and is schematically depicted in figure 2.7. It consists of a collimated laser source focused onto a GLV pixel element through some simple optics. A photodetector circuit is positioned at the proper angles to measure the optical intensity at the corresponding diffraction orders. Typically, the focus spot size was  $20\text{ }\mu\text{m}$  to fit within a  $25\text{ }\mu\text{m}$  or  $50\text{ }\mu\text{m}$  pixel and was observed to have a flat phase front.

This simple system was used to measure optical intensity as a function of grating height, the diffraction efficiency, and other electromechanical properties to be later discussed in Chapter 3.

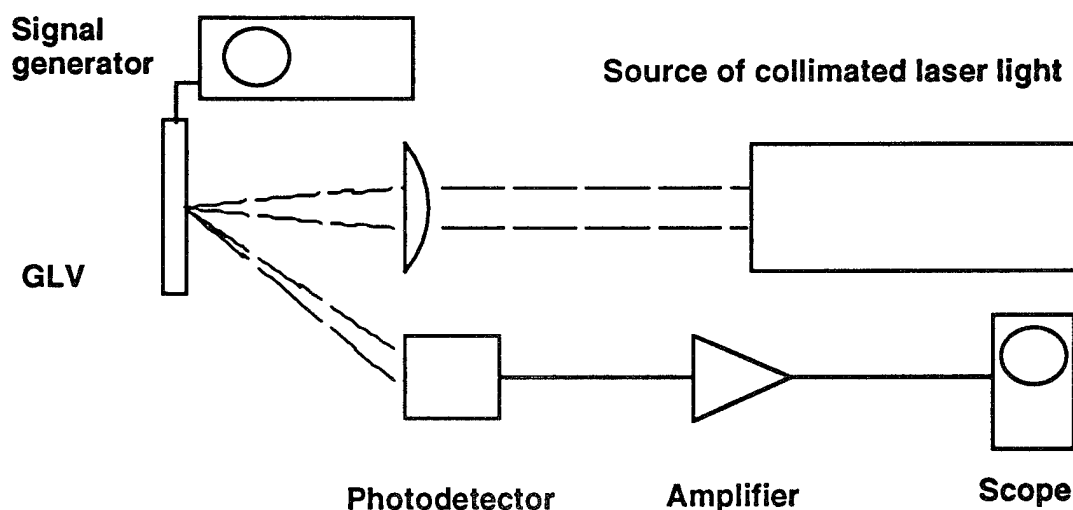


Figure 2.7: Schematic diagram of the GLV measurement system.

### 2.4.2. Intensity and Grating Height

To accurately measure the relation of intensity to the grating height, it was easiest to build static GLV's with known layer thicknesses. Figure 2.8 shows the simple structures used for this purpose. They consist of bi-layer T-structures where the bottom layer is an oxide spacer layer of a variable thickness ranging from  $27\text{ nm}$  to  $270\text{ nm}$ , and the second layer is the GLV beam of a fixed nitride thickness of about  $50\text{ nm}$ . These structures were built on

the same four-inch silicon wafer by dipping parts of the wafer for variable etch times. Having these structures all on one wafer guarantees similar duty-cycles (same photolithography process), same metal layer deposition thickness, and the same angle of incidence in the optical set-up

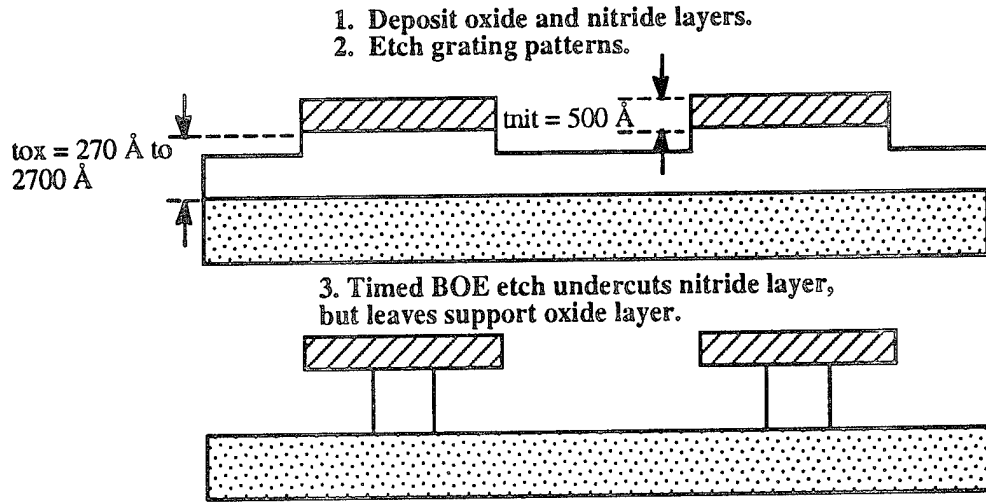


Figure 2.8: Diagram of the static GLV devices fabricated to perform the contrast measurement. The important parameter is the fixed oxide spacer thickness which was etched back to different values on the same wafer.

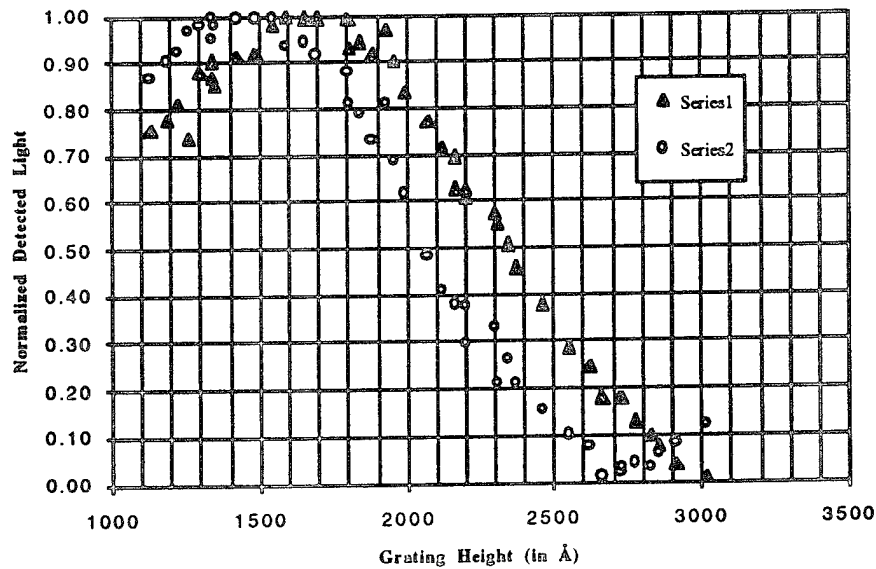
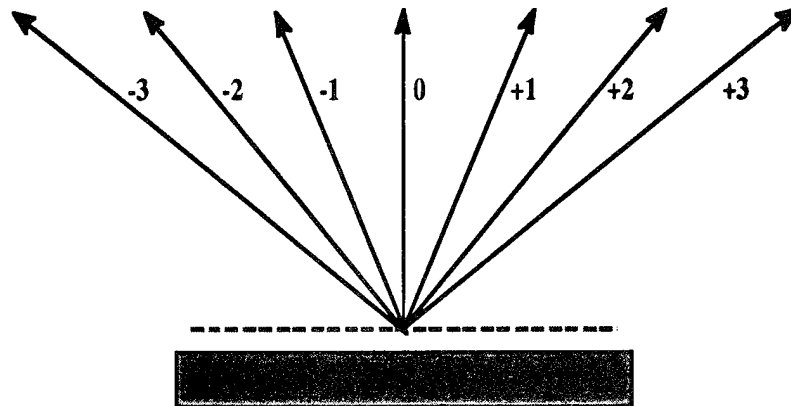


Figure 2.9: Plot of normalized optical power in the first diffraction order versus grating height. The measurement was carried out using both red (632.8 nm, Series 1) and green (543.5 nm, Series 2) helium-neon lasers.

The results of these measurements are charted in figure 2.9 where first order diffraction intensity is shown for different thicknesses at red and green wavelengths. The 632.8 nm light peaked around 166 nm and the minimum was not reached with the manufactured grating heights, but was expected to be slightly beyond 310 nm. The 543.5 nm wavelength peaked at 134 nm and nulled at 266 nm, in good agreement with our calculated maxima of figure 2.5, considering a thickness uncertainty of about 5 nm.

#### 2.4.3. Diffraction Efficiency

STATE	m = -3	m = -2	m = -1	m = 0	m = 1	m = 2	m = 3	Voltage
UP	6 %	6 %	1 %	74 %	1 %	6 %	6 %	0 V
DOWN	5 %	2 %	34 %	18 %	34 %	2 %	5 %	25 V



**Figure 2.10:** Diagram of optical power diffracted by a GLV pixel into the different orders. The illustration indicates the change in optical power as the pixel goes from the off/up state to the on/down state. Note the presence of the even order modes.

Finally, figure 2.10 tabulates the relative diffraction intensity of a GLV device with a duty-cycle that is around 35-40 % in its up and down state. It was taken from a GLV pixel with a periodicity of 2.25  $\mu\text{m}$ , a mechanical beam length of 25  $\mu\text{m}$ , and a beam thickness of about 200 nm and a spacer thickness of 190 nm.

The percentage numbers are normalized such that the sum of all measured intensities in the diffraction orders is equal to 100 %. Furthermore, the specular order is not effectively nulled due to the error in the layer thicknesses. The point of the graph is not to measure the exact value of the intensity but to show how the offset in the duty-cycle can cause the even diffraction orders to appear and lower the diffraction efficiency in the odd diffraction orders.



## 2.5. GLV Color Selection

Since a grating is a naturally color dispersive device, the GLV can be used as the basis for a color display device without the need for color filters. This is illustrated in figure 2.11. A white light source incident on GLV's of three different grating pitches ( $d_{red}$ ,  $d_{green}$ , and  $d_{blue}$ ) will have its component spectral colors diffracted into different angles dependent on the Bragg condition, equation (2.9). Thus, if one wants red, green, and blue spectra to diffract into the same angular direction, then defining three GLV grating pitches according to the Bragg condition will provide a color RGB pixel. Placing a spatial filter a focal length away from an intermediate imaging lens will provide color selectivity.

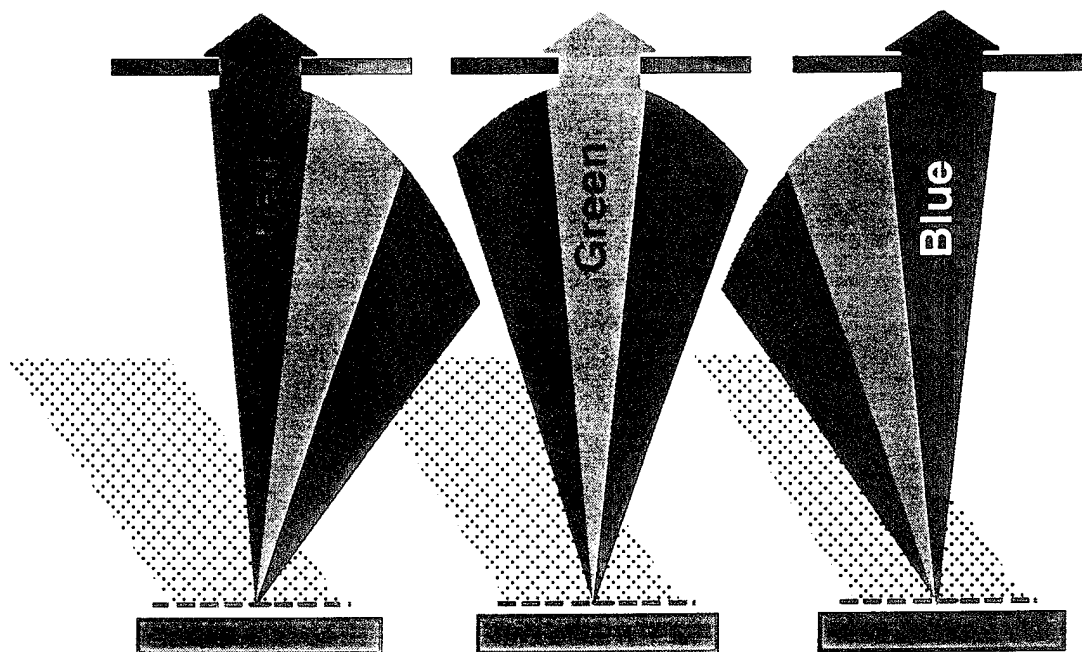
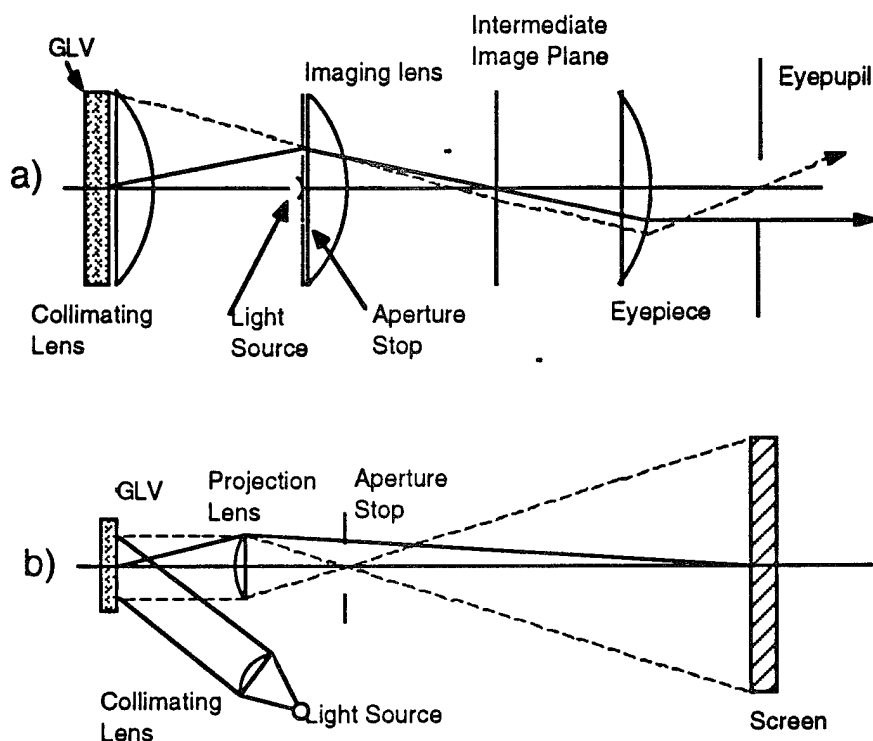


Figure 2.11: Illustration of the application of the GLV to a RGB color pixel element.

## 2.6. GLV Display Viewing Systems

For display applications, two simple optical viewing systems are presented in figure 2.12 to illustrate the possible uses of the GLV in heads-up and projection color display systems. System (a) presents an exit pupil to the viewer's eye while system (b) images a GLV color display to a screen.



**Figure 2.12:** Two simple GLV viewing systems. (a) presents an exit pupil to the viewer's eye. (b) images a GLV color display to a screen.

## 2.7. Discussion of Results

### 2.7.1. Contrast

So far, we have developed analytical expressions for the optical intensity as a function of diffracted angle, grating height, and duty cycle. Experimentally measured diffraction intensities as a function of grating height behaved as predicted. This is important for the analysis of contrast and underlines the importance of process control on grating height. Using the simple optical system in figure 2.7, contrast for a monochromatic laser source on single GLV device has been measured up to 350:1 by properly biasing a dynamic (i.e. movable) GLV device at the proper grating heights. Limiting factors to achieving high contrast for a single pixel are errors in the grating height, the extraneous diffraction effects

from neighboring pixels, and scattering from imperfect GLV side-walls [Apte, 1994b].

Color contrast is limited by the fact that a finite spectral bandwidth is used and therefore not all light spectra can be nulled. Nevertheless, since the visible spectra is quite narrow, a color pixel is still expected to demonstrate a black and white contrast ratio of 19:1 [Staker, 1995]. These color pixels consist of red, green, and blue pitched gratings at only one set of heights optimized for the green.

### 2.7.2. Efficiency

This chapter analyzed the diffraction efficiency as a function of the duty-cycle. Other aspects that will affect the diffraction efficiency are the finite active area of an actual deformable grating. Part of the GLV beams' active length is lost to the immobile supporting frame and to the bent portion of the beam as it comes down to touch the substrate. Thickness errors and optical absorption by the metal layers can adversely affect performance. Shadowing at the edges of a microbridge can effectively superimpose an amplitude grating structure over the intrinsic phase grating to reduce optical throughput and must be analyzed in the future. Should finer lithographic techniques become available to the GLV process engineer the possibility of blazing the beam elements to a preferred diffraction angle might be pursued as well [Bloom, 1994].

## Chapter 3

# GLV Electromechanics

### 3.1. Introduction

Thus far, it has been shown that a phase grating with an adjustable grating height serves as a very useful light valve technology. The concept of the GLV is truly simple but has only been made feasible by the advent of planar microfabrication technology and, in this particular case, of silicon surface micromachining. Microfabrication enabled the manufacture of tiny movable motors, sensors, and actuators. It has also enabled the fabrication of miniature smooth and flat movable beams and diaphragms, which are also very useful devices, particularly for optical applications.

This chapter will focus on the GLV electromechanics, with the assumption that the tiny GLV microbeams or microbridges are manufacturable and that they can be moved up and down repeatedly. The next chapter will talk about the concrete manufacturing process.

The GLV relies on a capacitive electrostatic actuation force to move its beam elements. This is a commonly studied MEMS actuation mechanism [Benecke, 1991]. Here we will cite the simple theoretical framework and quickly enter the specifics of the GLV electromechanical system. The first experimental observation of a hysteretic, memory-like behavior will also be presented. A more detailed mechanical model can be found in the Ph.D. dissertation of Apte [Apte, 1994b].

### 3.2. Materials Parameters

For any microelectromechanical system to be characterized and analyzed particular material properties have to be known. Geometry is, of course, very important: thicknesses of the deposited etched films have to be measured; while the widths and lengths are determined by the accuracy of the photolithographic process. Other film parameters that must be known are the stress, Young's modulus, Poisson's ratio, yield strength, density, hardness and coefficient of thermal expansion. Since, the films are also used electrically and optically, the dielectric permittivity, the optical index of refraction, flatness, and conductivity are also needed.

Parameter	Symbol	Value
Top Electrode Thickness		400 Å
Spacer Thickness	$h$	1325 Å
Beam Thickness	$t$	1325 Å
Beam Width	$w$	1.0 - 1.5 $\mu\text{m}$
Beam Length	$l$	6 - 75 $\mu\text{m}$
Area Moment of Inertia	$I$	$w^3/12 = 2.4 \times 10^{-4} \mu\text{m}^4$
RMS Surface Roughness		7-50 Å

Table 3.1: Basic physical and geometric factors of the GLV

CIS Recipe Name	DCS:NH3 Gas Flow Ratio	Residual Stress (MPa)	Index of Refraction	Young's Modulus E (GPa)	Average Hardness (GPa)
SIN1.0	1:1	950	2.07	236	23.2
SIN3.0	3:1	500	2.19	217	21.9
SIN5.2	5:1	160	2.38	222	21.3

Table 3.2: Measured properties of LPCVD nitride deposited using three different recipes at Stanford's CIS. Mechanical measurements assumed a Poisson's Ratio of 0.28 [English, 1994; Vlassak, 1992].

Parameter	Value	Reference
Dielectric Constant	6-7	[Sze, 1988]
Density	2.9-3.1 g/cm <sup>3</sup>	[Sze, 1988]
Poisson's Ratio	0.28	[Vlassak, 1992]
Resistivity	10 <sup>16</sup> ohm-cm	[Sze, 1988]
Dielectric Strength	10 <sup>7</sup> V/cm	[Sze, 1988]
Thermal Oxide's Dielectric Strength	1.1 x 10 <sup>7</sup> V/cm	[Sze, 1988]

Table 3.3: Some other useful film properties of LPCVD nitride assumed based on references, including thermal oxide's dielectric strength.

Materials used in the MEMS area are various but still somewhat limited by practical processing issues. In practice, they are further limited by the micromachining foundry capabilities available to the process engineers. For GLV process development within Stanford's Center for Integrated Systems (CIS) clean room, the selected materials and their parameters are tabulated in Tables 3.1 to 3.3. The three kinds of LPCVD silicon nitride were selected particularly for stress reasons, a very important control parameter for GLV mechanical design.

### 3.3. Actuation

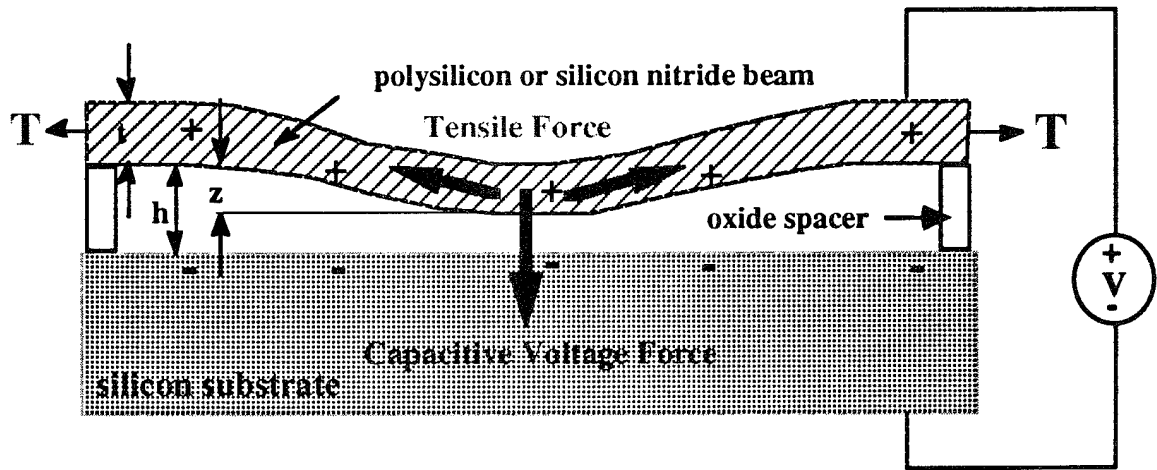


**Figure 3.1:** Diagram of the GLV Beam with an applied electrostatic force and a restoring tensile force.

Figure 3.1 is a diagram of a GLV cross-section taken along the longitudinal direction, i.e. parallel to the length of the beam. The beam is considered clamped at both ends by virtue of the silicon oxide supports. In its natural unbent state, the beam is already under some level of tension due to a built-in stress in the nitride film. Applying a voltage between the metal on top of this beam and the substrate electrode sets up an electrostatic capacitive force between the two surfaces which tends to pull them together. If we model the structure as a bi-layered capacitor (one dielectric being the air and the other being the nitride) then the capacitive electrostatic force per unit area is given by:

$$\frac{F_{el}}{A} = \frac{\epsilon_o V^2}{2(h - z + t / \epsilon_{nit})^2} \quad (3.1)$$

Where,  $\epsilon_0$  is the permittivity of air;  $\epsilon_{nit}$ , the relative permittivity of silicon nitride;  $h$ , the oxide spacer thickness;  $t$ , the beam thickness; and,  $z$ , the beam's downward displacement (downwards being the positive direction). Given a particular displacement shape of the beam, one can know the height of each distributed element along the  $x$ -direction and thus calculate the distributed load at those points. It is important to note that there is a non-linear relation between this electrostatic force with respect to the  $z$ -displacement. That is, as the beam is pulled down by a particular voltage level, the air gap ( $h-z$ ) decreases and the force increases non-linearly as  $1/(h-z+t/\epsilon_{nit})^2$ .

On the other hand the restoring force of the GLV beam is due to two mechanical contributions: the tension and the intrinsic force due to beam stiffness [Hartog, 1961]. Under most GLV experimental conditions, the tension force is dominant and this allows the beam to be modeled as a string under tension. See figure 3.2.

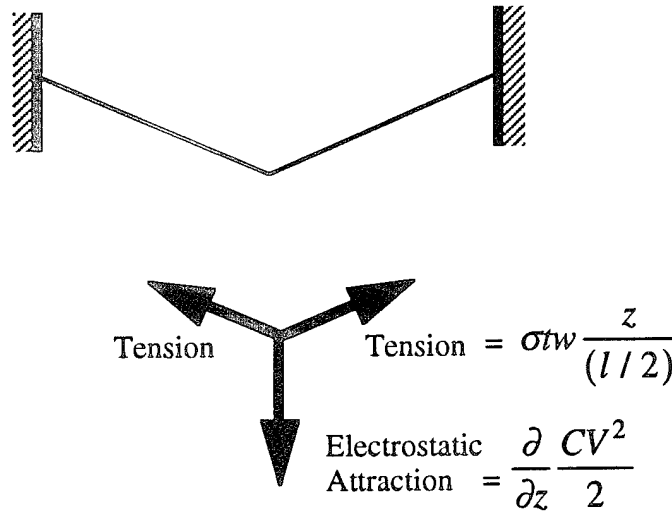


Figure 3.2: Modeling beams as strings. The upward restoring force is caused by tensile stress  $\sigma$  in the beams, while the downward electrostatic attraction is the derivative of the stored energy in the beam capacitance,  $C$ , with deflection  $z$ .

Referring to figure 3.2, it can be seen that the spring restoring force on the center element of beam is given by the expression:

$$F_{spring} = -\frac{4 \sigma t w}{l} z \quad (3.2)$$

Where  $\sigma$  is the stress in the nitride film;  $t$  is the beam thickness;  $w$  is the beam width, and  $l$  is the beam length. The negative sign means the force counters an increasing  $z$ -displacement and points upwards if  $z$  is positive.

The switching voltage of the GLV is defined as that voltage required to bring the beam to the substrate, i.e. to switch from the up-state to the down-state. The GLV system is a slightly complex mechanical system since the applied voltage force is a non-linear function of position. To gather accurate values for the switching voltages, numerical methods have to be used. These were carried out by Apte [Apte, 1994b] and the results are presented later on in the chapter. However, to gather an analytical understanding for the GLV actuation system and to derive simple analytical expressions for the relationships between the GLV parameters of interest (switching voltage, stress, and beam geometry), it is very useful to carry out a simpler first-order analysis.

Figure 3.3 shows the simple model of the GLV system in figure 3.1. The GLV beam is a parallel plate capacitor with a lumped force at its center position. This force is equal to the electric force per unit area (equation 3.1) multiplied by the area of the beam ( $wl$ ). The assumption made is that we can lump the electrostatic force of the beam at the center and equate it to the force value for a plate of the beam's area ( $wl$ ) at the height  $z$ . This analysis will underestimate the switching voltages by close to a factor of two but is nevertheless still very useful. The restoring force is a spring force from the beam tension and is given by equation (3.2).

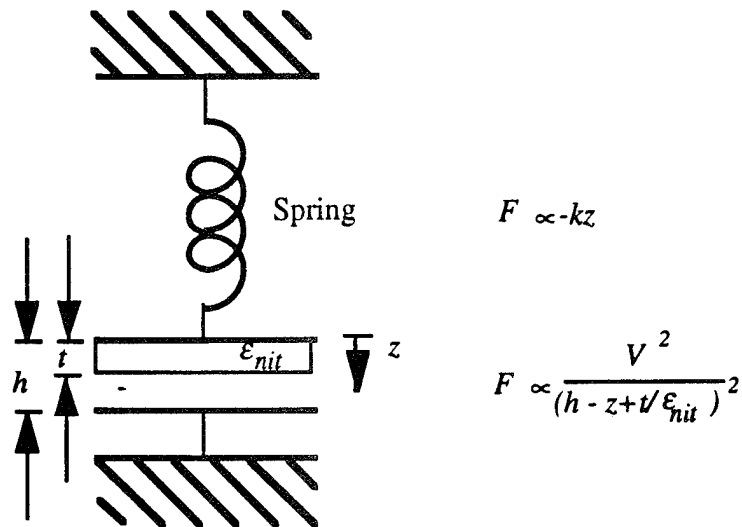


**Figure 3.3:** Basic model for the GLV beam mechanics. The spring represents the restoring force caused by beam stiffness and tension. The capacitor represents the electrostatic attraction between the electrodes.



### 3.4. Bistability

Figure 3.4 is a set of three plots of the beam forces as a function of the beam displacement,  $z$ . A beam displacement of  $z = h$  means that the beam has come into contact with the substrate. The three plots are for each possible range of applied voltages. For each plot, the linear restoring force is the same diagonal line. On the other hand, the voltage force is non-linearly dependent on  $z$  by the relation  $F_{el} \propto V^2/(h - z + t/\epsilon_{nit})^2$  and also includes a variable voltage term which acts to move this curve upwards and increase its slope as the voltage increases. The linear spring force acts as a restoring force that tends to pull the beam system upwards; on this plot, this means that if it dominates over the electrostatic force it will move the system to the left,  $z \rightarrow 0$ . The non-linear voltage force is a pull-down force so it pulls the beam towards  $z = h$ , where the beam hits the substrate. A stable point occurs at a point  $z$  where the force lines intersect and to its left the voltage force dominates and to its right the spring force dominates.

We trace the path for a beam with a sweeping voltage in figure 3.4. The first plot shows that for a voltage below  $V_1$ , the first instability voltage, only one point of stability exists at an intermediary displacement,  $z$ , which increases as  $V$  increases. If the voltage rises to a level between  $V_1$  and  $V_2$  (figure 3.4b), there are two stable points one at a still increasing displacement  $z$  and the other at  $z = h$  - the beam is in contact with the substrate (the second point of intersection is not a stable point, for the reasons stated in the previous paragraph). Above the second instability voltage  $V_2$ , there is only one stable point and that is the contact state (see figure 3.4c).  $V_2$  is also called the switching voltage,  $V_{switch}$ , and occurs at the point where the force curves intersect and are also tangent to each other.

On the downward path, switching between the free-state and the contact-state occurs only at the point where  $V$  rises to  $V_2$ , because before that point, the intermediary height  $z$  is stable and so the beam will remain at that point. However, on the upward path, the beams will not switch back up as  $V$  is reduced to  $V_2$  since the electrostatic force is now stronger given the same voltage level but a larger capacitance. The beams will return to their up-state only as the voltage is lowered below  $V_1$ , which is the voltage where the electrostatic force is equal to the spring restoring force at the displacement  $z = h$ .

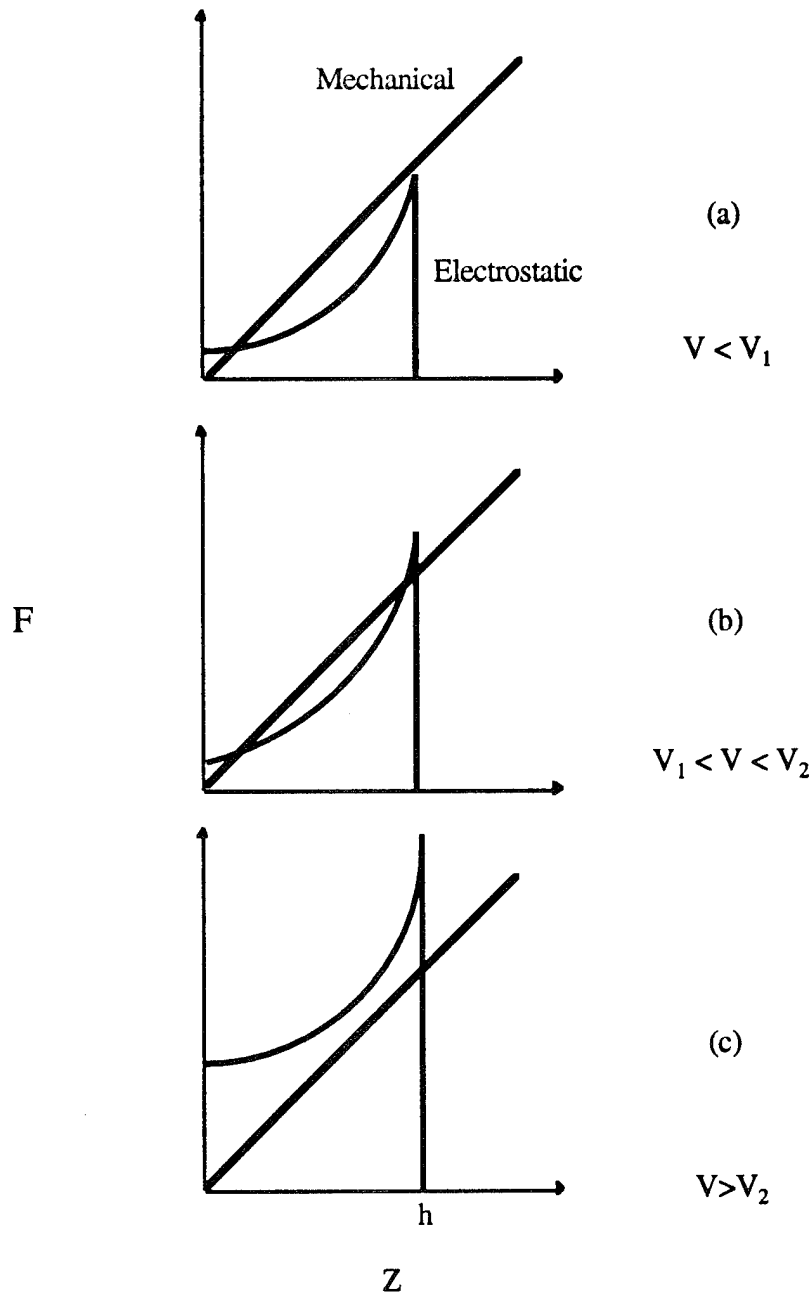


**Figure 3.4:** Origin of bistability. These curves plot electrostatic and mechanical forces as a function of displacement. When the applied voltage  $V < V_1$ , the first instability voltage, there is one stable solution in which the forces balance (a). If  $V$  is increased past  $V_1$ , then there are two stable solutions, one up and one down (b). For  $V > V_2$ , the second instability voltage, the beam must be in the down position, pinned to the substrate.

We use the following equations to solve for the switching voltage,  $V_2$ , and the displacement point of instability,  $z_{switch}$ :

$$F_{el}(z_{switch}, V_{switch}) = F_{spr}(z_{switch}) \quad (3.3)$$

$$\left. \frac{\partial}{\partial z} F_{el} \right|_{z=z_{switch}, V=V_{switch}} = \left. \frac{\partial}{\partial z} F_{spring} \right|_{z=z_{switch}} \quad (3.4)$$

$$z_{switch} = z_2 = \frac{(h + t / \epsilon_{nit})}{3} \quad (3.5)$$

$$V_{switch} = V_2 = \sqrt{\frac{32t}{27\epsilon_o} \left( h + \frac{t}{\epsilon_{nit}} \right)^{3/2} \frac{\sqrt{\sigma}}{l}} \quad (3.6)$$

And to solve for  $V_1$ , we recall the condition that

$$F_{el}(z = h, V_1) = F_{spr}(z = h) \quad (3.7)$$

$$V_1 = \sqrt{\frac{8h}{\epsilon_o \epsilon_{nit}^2} t^{3/2} \frac{\sqrt{\sigma}}{l}} \quad (3.8)$$

Equation (3.5) tells us that using a constant voltage as the beam actuation mechanism will allow the beam to travel only the first third of the total air gap between the beam and the substrate. After traveling a third of the way down, the beam hits the instability point and snaps to the substrate.

### 3.5. Switching Voltage, Stress, and Beam Geometry

It is also useful to note the relation between the instability voltage levels,  $V_1$  and  $V_2$ , and the stress and beam length. Beam thicknesses and air gaps are determined by the optical wavelengths and are not as easy to vary. Both  $V_1$  and  $V_2$  are proportional to the square-root of the stress and inversely proportional to the beam length. Therefore, it is possible to lower the switching voltage by lowering the tensile stress in the beam or by lengthening the beam.

An example calculation using the above relations can be done for a 20  $\mu\text{m}$  long beam, with an oxide spacer and beam thickness of 132 nm, a tensile stress of 800 MPa. This

would give  $V_1 = 3.6$  V and  $V_2 = 11.3$  V (using a  $\epsilon_{nit} = 6.45$  and  $h = 8.854 \times 10^{-12}$  C<sup>2</sup>/J<sup>2</sup>m). Experimental results and a numerical solution show that these values are off by at least a factor of two but nevertheless relations (3.5) to (3.8) give a good understanding of the parametric space and scaling relations of the GLV system.

The experimental data are given in table 3.4. The simulation results of Apte are in figure 3.5. The numerically simulated values are approximately 25% lower than the measured values, with no fitting parameters. Apte attributes the error to neglect of fringing fields in the electrical model, neglect of the metal on the beam top surfaces, and the uncertainty in the values of the nitride's Young's Modulus and dielectric constant. Figure 3.6 is an experimental verification of the dependence of the switching voltage on the inverse of the beam length. Exact magnitudes of the switching voltages in this case were not predicted by Apte's model because this data was taken from GLV beams of a slightly more complex geometry (see the T-structure process in section 4.5.5.).

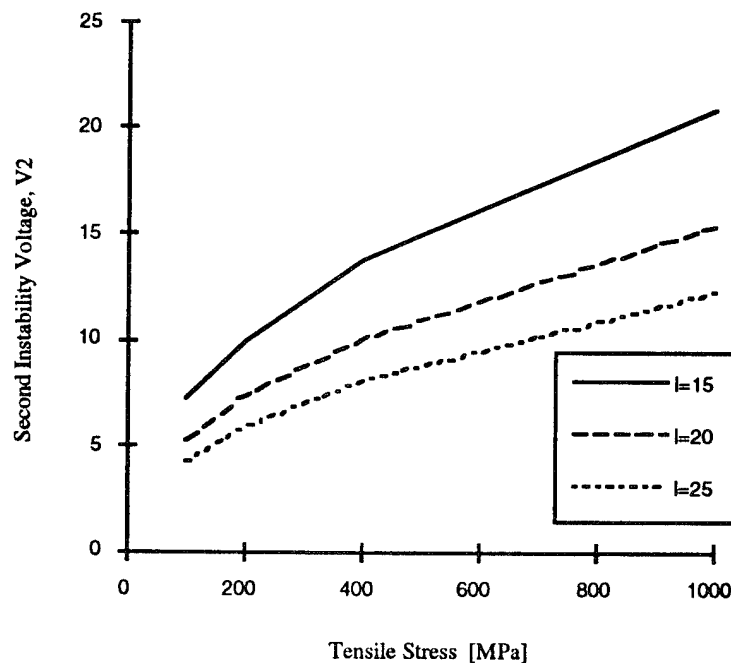


**Figure 3.5:** Results of Apte's numerical model of beam electromechanics. Second instability (switching) voltage is plotted as a function of nitride tensile stress for three different length beams, 15  $\mu$ m, 20  $\mu$ m, and 25  $\mu$ m.

Stress [MPa]	Beam Length[ $\mu\text{m}$ ]	Voltage, V2
800	20	18
800	16	26
400	16	18
100	16	11

Table 3.4: Experimental switching voltages.

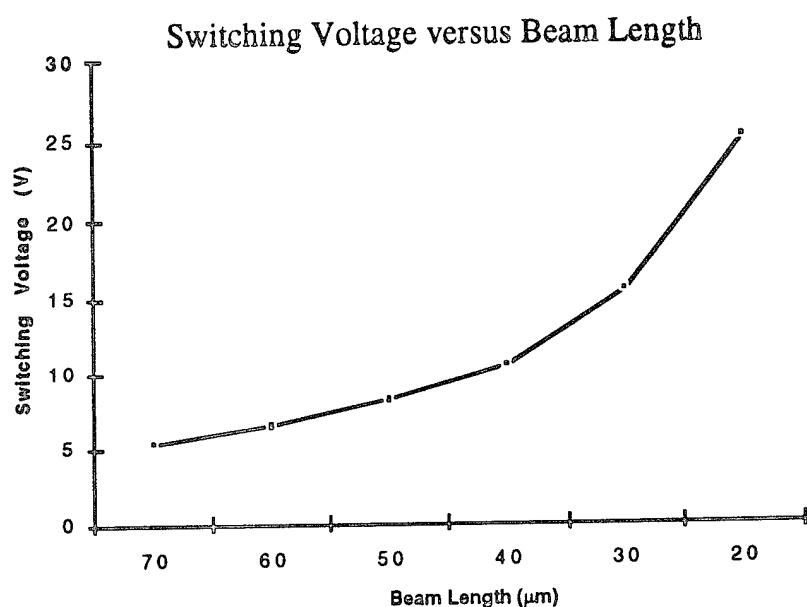
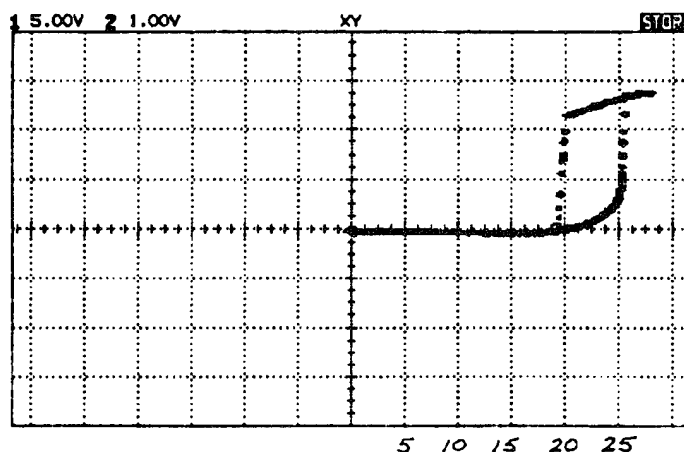


Figure 3.6: Plot of switching voltage as a function of beam length. The beams are  $1\ \mu\text{m}$  wide,  $132\ \text{nm}$  thick and have a built-in tensile stress of  $800\ \text{MPa}$ . These values were taken from a harp device manufactured with polysilicon T-Structure supports (process is described in Chapter 4).

### 3.6. Hysteresis of the GLV

A very attractive characteristic of the GLV is its hysteresis. From the discussion of the GLV bistability above, it is obvious that this optical device can switch with a memory-like behavior. This is desirable to display engineers since it allows the possibility of an active-matrix-quality display without the use of transistor switches for each pixel. The GLV acts as its own switch.



**Figure 3.7:** GLV optical hysteresis. Plot of optical power in the first diffraction order as voltage is swept from the 0 to 25 V and back to 0V. Horizontal scale is 5V/div.

Using the optical measurement system described in figure 2.7 to look at diffracted light in the first diffraction order of the GLV, optical hysteresis was demonstrated. Figure 3.7 is a trace of the light detected in the first diffraction order as a function of applied voltage.

As the voltage is increased above 20 V, the microbeams start to deflect, causing light to be diffracted into the first orders. At 25 V, the switching point is reached and the beams snap down to the substrate. As the voltage is reduced from above 25 V to 20 V, the beams remain in contact with the substrate but are starting to peel away. Below 20 V, the first instability point, the spring force now overcomes the voltage force and the microbridges spring back up to the undeflected state.

Figure 3.8 illustrates the hysteretic switching of the GLV. To operate this device digitally, a dc bias of 22.5 volts is applied with a positive or negative-going pulse superimposed on the dc bias. The bias keeps the GLV in the middle of the hysteresis curve of figure 3.7. A positive-going pulse can bring the voltage level beyond the

switching voltage and snap the beams down (GLV light is on), while a negative going pulse will bring the voltage level below the first instability point and allow the beams to come back up (GLV light is off). The top trace of figure 3.8 is the GLV optical output in the first diffraction order (1 V/div). The bottom trace shows the voltage pulse superimposed on a dc bias level to switch the GLV on and then off (5 V/div). Horizontal scale is 200 ns/div. Since the response time is 30 ns, there was no problem switching the devices at frequencies up to 1 MHz. At higher frequencies, ringing was observed in the output wave form for reasons to be discussed below.

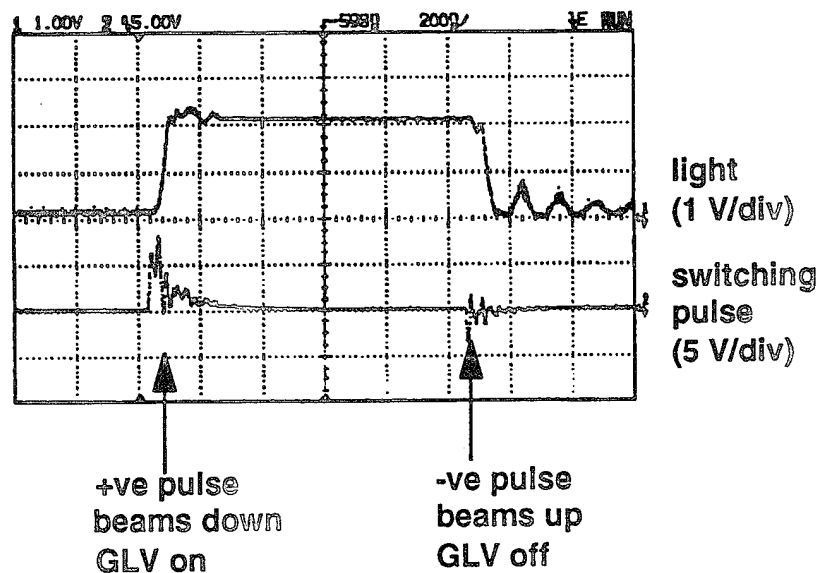


Figure 3.8: GLV hysteretic switching. The top trace is the GLV optical output in the first diffraction order (1 V/div). The bottom trace is the voltage pulse superimposed on a dc bias level to switch the GLV (5 V/div). Horizontal scale is 200 ns/div.

### 3.7. Resonant Frequency and Switching Speed

The GLV can switch at relatively fast speeds. It is 500 times faster than TI's micromirror and about 500,000 times faster than liquid crystal light valves. The speed limitation for switching the GLV is determined by its mechanical resonance frequency. The GLV resonance frequency is determined by its spring constant and its mass. An analysis of the GLV as a resonant doubly-clamped microbridge with high tensile stress [Howe, 1987]

can be simplified to a simple relation for the fundamental resonant frequency [Solgaard, 1992a]

$$f_{res} \approx \sqrt{\frac{\sigma}{4\rho}} \frac{1}{l} \quad (3.9)$$

where  $\rho$  is the density of the beam material,  $l$  is the beam length. This simple relation comes from assuming a particular deformation shape and neglecting the effects of the beam stiffness due to the Young's modulus. The stress term dominates the stiffness of the GLV. Experimental values of the GLV resonance have been measured to range from 1 MHz to 15 MHz.

The trade-off between switching speed and voltage now becomes obvious. Both values have the same functional dependence on stress and beam length. To obtain faster speeds we want a stiffer beam, i.e., higher tensile stress and shorter lengths. However, this increases the required switching voltage.

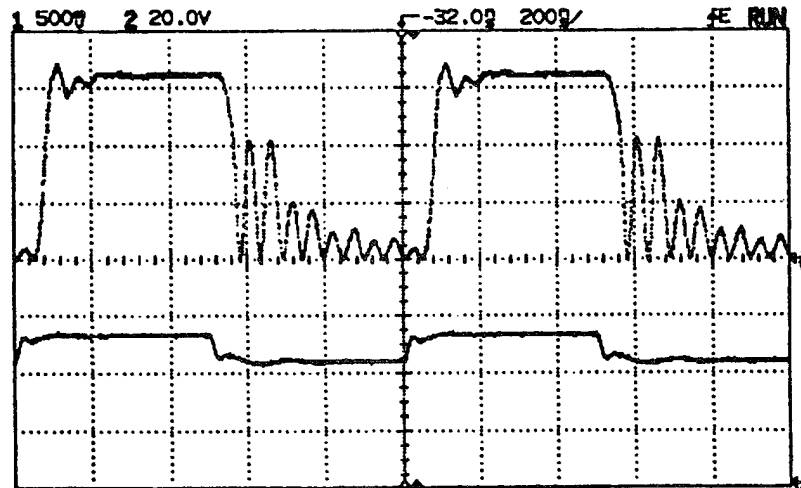


**Figure 3.9:** GLV 30 ns switching speed. The top trace is the optical output in the first diffraction order. The bottom trace is a 1 MHz square-wave (with a dc bias) to switch the GLV pixel. The horizontal scale 200 ns/div. Note the ringing when the microbridges are in the up-state (GLV is off).

Figure 3.9 is a trace of brightness in the first diffraction order of an actively switching GLV pixel and demonstrates its ability to switch at high speeds. In this case, the 10-90% switching speed is about 30 ns. The top trace is the optical output in the first diffraction order. The bottom trace is a 1 MHz square-wave (with a dc bias) to switch the GLV pixel. Ringing is observed in the off-state (beams are up and vibrating). The mechanical ringing is transformed into an optical output that is rectified with a frequency twice that



of the mechanical resonance. The reason is that the GLV pixel diffracts light both when it overshoots its off/up-state going upwards and when going downwards.

### 3.8. Ringing and Air Damping

Looking at figure 3.9, some ringing is observed when the beams return to their relaxed state. This is due to the beam resonance and can be dampened by the air around it. This is illustrated in figure 3.10, where the influence of increasing the air pressure lowers the ringing phenomenon to a critically damped situation. It is a photograph of an oscilloscope trace of GLV diffracted power showing ringing and air damping. The top trace is 1 V p-p negative pulse exciting a GLV device in non-contact mode. Below are traces of optical output showing GLV ringing at 1/6 atm and 1/2 atm.  $f_{res} = 1.3$  MHz. The bottom-most trace corresponds to the 1/2 atm case and indicates that for this particular system ringing can be close to being critically damping (stress was about 100 MPa, length = 120  $\mu\text{m}$ , width = 2  $\mu\text{m}$ , and the thicknesses of the beam and spacer were 0.2  $\mu\text{m}$ ).

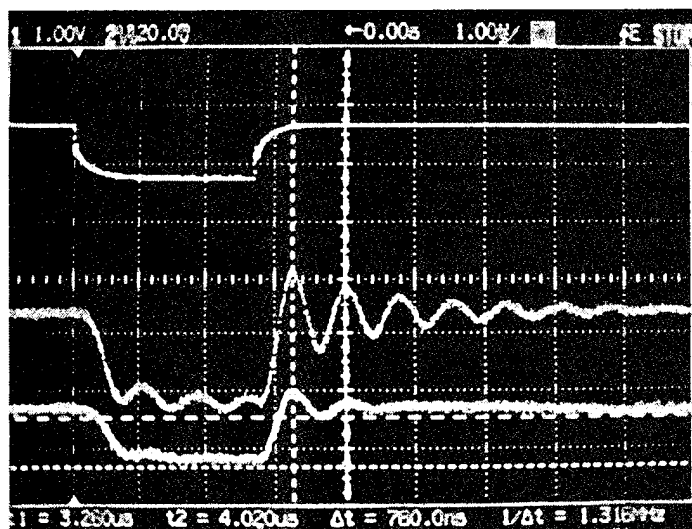


**Figure 3.10:** Photo of an oscilloscope trace of GLV diffracted power showing ringing and air damping. The top trace is 1 V p-p negative pulse exciting a GLV device in non-contact mode. Below are traces of optical output showing GLV ringing at 1/6 atm and 1/2 atm.  $f_{res} = 1.3$  MHz.

### 3.9. Conclusion

The GLV mechanical grating elements are doubly-clamped microbridges that are actuated by an electrostatic capacitive force. The beams are simply modeled as strings with a restoring spring force. The voltages required to switch the beams into contact with the substrate depend on the square-root of the tension and on the inverse of the beam length. Switching speed has the exact same dependence on tension and beam length, and so there is a trade-off between speed and low-voltage operation. Hysteretic switching has been demonstrated for single pixels. Finally, ringing and its relation on air damping has been observed. Topics not discussed but covered in Apte's or Solgaard's theses are the issues of peak stresses, yield strength, and temperature limits. Other pending issues that have still to be investigated are numerous.

One of the biggest questions will be repeatability and uniformity of the hysteretic curve, not only from one process run to another but even within one wafer area, if the device is to be used in a display system. This curve will be used to derive important design parameters for display circuit drivers.

Another important and very uncertain area is that of reliability and long term fatigue of these micromechanical devices. Thin films such as those used for GLV mechanics have not been fully tested for their mechanical properties especially for issues like stress fracture, yield strength, crack propagation, among many others. In general, the material science of MEMS is still developing.

## Chapter 4

# The GLV Manufacturing Process and Stiction

### 4.1. Basic GLV Fabrication

The basic process for GLV fabrication essentially has a single masking step and is summarized in figure 4.1. Starting with a boron-doped, 4 inch, <100> wafer, 132 nm of silicon dioxide is thermally grown or deposited. This is followed by deposition of 132 nm of silicon nitride. The tensile stress in the LPCVD nitride ranges from 40 to 1000 MPa, depending on the flow ratio of the dichlorosilane and ammonia gases. A photoresist etch mask is patterned, then the nitride is dry-etched to the oxide layer. The oxide layer is also partially dry-etched in this step. The photoresist is stripped. After photoresist removal, the wafers are placed in a buffered oxide etch (BOE) which is isotropic and undercuts the nitride layer. This step releases the GLV beams; it also undercuts the frame area partially. We design the frame area to be wider than the thickest beams such that a timed oxide etch will fully release the beams but not the frame, where the remaining oxide acts as the support and spacing layer for the grating structure. Next, the wafer is rinsed and spin-dried in water. Finally, a thin layer of aluminum is evaporated to form the reflection layer, which also serves as the top and bottom electrodes.

The above process is appealing in its simplicity but suffers from the problem of surface adhesion. This problem is illustrated in the photograph 4.1 where portions of two

GLV beams are shown. The top beam is released from the substrate while the lower beam is stuck.

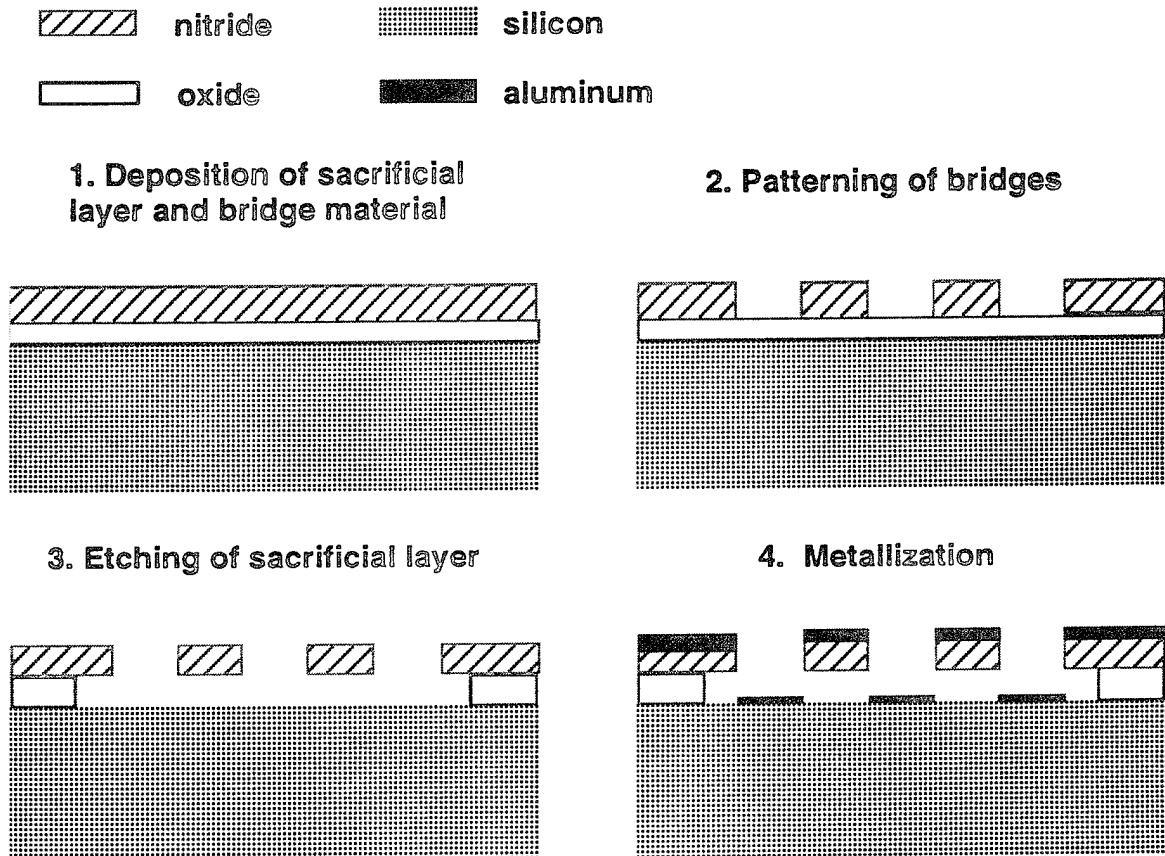
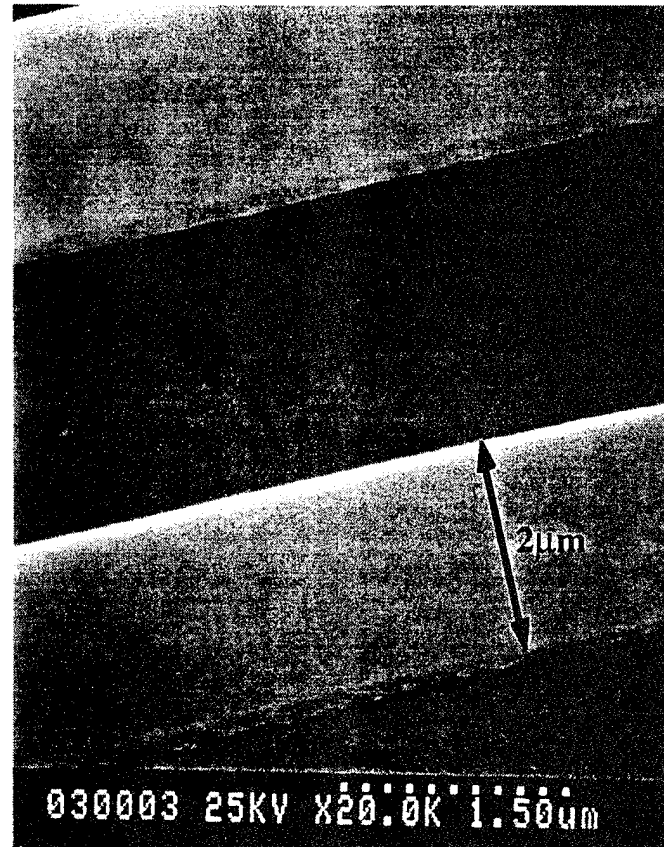


Figure 4.1: Simplest fabrication process of a single GLV pixel with one masking step.



**Photo 4.1:** A close-up SEM of two 2  $\mu\text{m}$  wide-beams. The beam in the foreground is stuck to the substrate by surface forces; while, the beam in the back is free-standing over the substrate.

## 4.2. Causes of Stiction

One of the most challenging issues of the Grating Light Valve technology is stiction or the adhesion of the very smooth surfaces that come into contact. In the case of the GLV, the contacting surfaces are the top of the substrate and the bottom of the grating beam elements. For display applications, this mechanical contact is the desired method of controlling the height difference between the top and bottom reflection surfaces. This difference is simply determined by the well-controlled film thickness of the deposited layers, e.g. oxide and nitride.

Before going into the details of the GLV system, it is useful to enter a general review of the stiction problem which is present in most MEMS devices. Surface contact obviously precedes adhesion and this contact can occur at two different stages of the life of a MEMS device. Contact can occur during wet processing due to elastocapillary forces, or it can occur during device operation. If contact during device operation can be avoided, then the stiction problem can be solved by eliminating the capillary force during the drying process.

Unfortunately, mechanical shock or vibrations can accidentally cause contact in some MEMS systems that have compliant structures or very tight tolerances. Or, as in the case of the GLV, some systems require surface contact for proper device operation.

This chapter starts off by reviewing the capillary force that initiates surface contact during sacrificial etch processing. This force can be avoided. However, adhesion only occurs if, after the liquids are removed, the surface adhesion forces overcome the mechanical spring restoring force in the microstructures. These adhesion forces are reviewed and modeled to derive approximate adhesion energy values. Because of the approximate nature of these models and the closeness of their magnitudes, it is then admitted that there are uncertainties in knowing the exact nature of the stiction force when it comes to particular MEMS systems. A simple technique for measuring the surface adhesion energy (which is the work required to peel the surfaces apart and is simply the separating force integrated over the distance traveled) is discussed and claimed to be of more significance when it comes to practical fabrication. Finally, in an effort to reduce the stiction force, surface roughening and patterning are presented as engineering solutions.

#### 4.2.1. Capillary Forces

##### 4.2.1.1. *Nature of the Capillary Force or Laplace Pressure*

Guckel first noted that in a sacrificial etch process (normally used to release free-standing microstructures like bridges, cantilevers, and diaphragms), liquid drying involves a capillary force due to surface tension forces in the liquid [Guckel, 1989]. As the rinsing liquid dries from the space between compliant surfaces, it generates a capillary force which is normally sufficient to pull them together (see figure 4.2); once in intimate contact a number of surface adhesion forces contribute to cause the permanent adhesion of the surfaces even after the final rinse liquid has completely evaporated.

Mastrangelo and Hsu have published a very good reference on the mechanical stability and adhesion of MEMS devices [Mastrangelo, 1993a]. In the first part of their

paper, they focus their analysis on the case of liquid drying away from underneath a flexible microstructure and on whether the resulting capillary force will be sufficient to initiate contact. They assume that a single point of contact will automatically lead to adhesion. They derive a term called the elastocapillary bound,  $N_{EC}$ , which is indicative of the ability of the capillary force to overcome the beam stiffness and cause the microstructure to contact the substrate. They analyze the cases of cantilevers, doubly-clamped beams, and diaphragms of various shapes. For the GLV case of doubly-clamped beams under tension, they derive the following elastocapillary number:

$$N_{EC} = \frac{128 E h^2 t^3}{15 \gamma_l \cos \theta_c l^4 (1 + t/w)} \left(1 + \frac{2 \sigma_R l^2}{7 E t^2}\right) \quad (4.1)$$

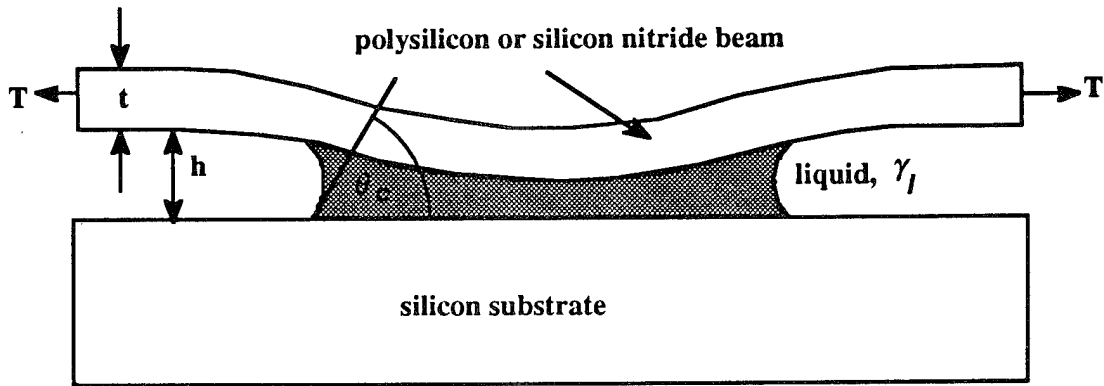


**Figure 4.2:** Side-view along the transverse direction of a doubly-clamped beam being deflected by capillary forces.

$N_{EC}$  is the elastocapillary bound (if  $N_{EC} > 1$  then the beam will not come into contact with the substrate; but if  $N_{EC} < 1$  then contact will occur);  $h$  is the thickness of the air gap;  $E$ ,  $\sigma$ ,  $t$ ,  $w$  and  $l$  are the Young's modulus, tensile stress, thickness, width, and length of the beam material, respectively;  $\theta_c$  is the contact angle the liquid makes with the silicon material (if the top layer were not silicon,  $\cos \theta_c$  would be replaced by  $(\cos \theta_{top} + \cos \theta_{bottom})/2$ ); and  $\gamma_l$  is the surface tension or energy of the liquid.

To give an example of how this bound can be used, we take the case of a GLV beam drying in water with  $E = 225$  GPa,  $h = t = 132$  nm,  $w = 1$   $\mu$ m, and  $\sigma = 800$  MPa. Using the water surface tension value of  $73$  mJ/m<sup>2</sup> [Israelachvili, 1992] and an assumed contact

angle of  $5^\circ$  for hydrophilic silicon, we find that  $N_{EC} > 1$  if  $l < 8.3 \mu\text{m}$ . This means that all doubly-clamped beams of length greater than  $8.3 \mu\text{m}$  will be pulled into contact with the substrate by the capillary force.

In essence, the elastocapillary number tells us about the balance of the mechanical stiffness of the beam and the capillary force. The beam stiffness gives a countering force to that of the liquid and is dependent on the geometry of the structure, the tensile stress, and the Young's modulus. An obvious way to ensure that  $N_{EC} > 1$  is to make the beam stiffer by using a material with more tensile stress and a higher Young's modulus, and by designing the structure to be thicker, shorter, and farther away from the other surface. On the other hand, the capillary force being a characteristic of the drying liquid, contact can be prevented by using liquids of lower surface tension and that have a large contact angle with the materials of the MEMS device.

#### 4.2.1.2. Lowering the Capillary Force

Obviously, process techniques that prevent the initial contact during sacrificial etch processing will solve the adhesion problem for devices whose surfaces can be kept from contacting during operation. Furthermore, even devices that operate in contact-mode, such as the GLV, stand to benefit from these techniques since they allow the process engineer flexibility in designing a post-process step that could treat the surfaces which would otherwise be stuck, unexposed, and untreatable. These techniques also avoid the possibility of the capillary force exerting a straining force beyond the microstructures' elastic limit.

Scheeper *et al.* have confirmed that drying in non-polar solvents reduced the capillary effect [Scheeper, 1992]. They observed that non-polar solvents exerted less force to pull down the shorter beams, resulting in longer unstuck cantilevers. Deionized water gave them their worst results; ethanol was slightly better; and, n-hexane gave the very best results for PECVD nitride cantilevers over an oxidized silicon substrate.

Aside from moving to less polar liquids with lower surface tension, another parameter that can be modified is the wetting or contact angle. If the liquid has less of a tendency to wet the surface, the capillary force is weakened. In the relation for  $N_{EC}$ , this is indicated by larger contact angles, hence a lower  $\cos(\theta_c)$  term in the denominator. It is noted that if the wetting contact angle,  $\theta_c$ , approaches  $90^\circ$  this means that the liquid is non-wetting and will not pull the surfaces together, hence  $N_{EC}$  goes to infinity. In the extreme case where  $\theta_c$  is greater than  $90^\circ$ , the elastocapillary bound does not hold any longer (since a negative bound is meaningless); however, one note to make from this is that a non-



wetting film if trapped between the two surfaces will tend to push the two apart rather than together, at least until it can escape from that space.

Since water is often the final rinsing liquid, it is highly desirable in the majority of systems to convert the naturally oxidizing and, thus, hydrophilic silicon surfaces into stable hydrophobic ones. This procedure will also minimize the problem of permanent adhesion due to liquid bridging which we will discuss in the section on adhesion forces. To gather a stronger grasp of the effect of hydrophobicity on the capillary force, we again take a look at the example above for the GLV beam drying in water, but this time we assume that the wetting contact angle is changed from  $5^\circ$  (for an RCA cleaned wafer) to  $70^\circ$  for a hydrophobic wafer water rinsed an HF etch [Backlund, 1992a; Hermansson, 1991]. If we calculate the length of the doubly clamped beam that satisfies the elastocapillary bound, we find that beams shorter than  $13.2\text{ }\mu\text{m}$  should not be pulled down by the water. Surface treatments have been developed that can engineer this contact angle to vary from  $5^\circ$  to about  $110^\circ$  [Alley, 1992]. We will briefly reference here, three published procedures for surface modification.

Scheeper *et al.* used an hexamethyldisilazane (HMDS) surface modification technique, which replaces the hydroxyl groups (-OH) with  $-\text{O}-\text{Si}(\text{CH}_3)_3$  groups. Secondly, Alley reported the successful use of octadecyltrichlorosilane (OTS),  $\text{C}_{18}\text{H}_{37}\text{SiCl}_3$ , as a self-assembled coating monolayer over a hydroxylated silicon surface [Alley, 1992]. However, it was our experience that OTS monolayer formation is a very tricky process. Alley says that extensive rinsing with methanol and  $\text{CCl}_4$  is required to remove all the water between the microstructure surfaces prior to the monolayer formation because the OTS will react with the water to form a solid polymer which will impede the desired motion of the GLV microstructures. In systems similar to the GLV, where structure geometries only allow sub-micron crack vias for the chemical diffusion, such a thorough rinsing process is made more difficult.

Another hydrophobic monolayer procedure has been developed at Stanford by Linford and Chidsey [Linford, 1993]. In this procedure, the Si-H bonds of a freshly HF etched silicon wafer are replaced by alkyl monolayers by the pyrolysis of diacyl peroxides ( $[\text{CH}_3(\text{CH}_2)_n\text{C}(\text{O})\text{O}]_2$ ,  $n = 10$  or  $16$ ). This process yields good, robust hydrophobic surfaces and is simpler than that of trichlorosilanes since it does not require the complete removal of water from the solution and neither does it require the hydroxylation of the silicon surface for the monolayer formation.

Applied to the MEMS area, the three monolayer processes mentioned are still in an experimental development stage. And if the process engineer decides to incorporate any

of them in the MEMS fabrication process, it will have to be insured that it will be compatible with and survive in the steps that follow the monolayer formation.

#### 4.2.1.3. *Eliminating the Capillary Force*

There are a number of ways to completely eliminate the capillary force. Essentially, these approaches entail the replacement of the liquid with a solid or a gel which are directly brought into the gaseous phase or dry etched. Guckel first proposed this approach by demonstrating water freeze-drying [Guckel, 1989]. Orpana *et al.* introduced the technique of replacing the rinse liquid with a mixture of photoresist/acetone and consequently ashing off the resist in an isotropic O<sub>2</sub> plasma etch [Orpana, 1991]. Yet another alternative is that of drying in supercritical carbon dioxide which has been developed for MEMS by researchers at U.C. Berkeley [Mullhern, 1993] and at AT&T Bell Labs [Ho, 1990]. This process has been used by biologists for SEM sample preparation. It involves bringing pressurized, liquid CO<sub>2</sub> above a critical temperature and pressure, which is called the supercritical phase, wherein the fluid enters the gaseous state without ever having a liquid-gas interface.

#### 4.2.2. Surface Adhesion Forces

The capillary force observed during the drying process is essentially an actuation mechanism that brings surfaces into contact and by itself is not the cause of stiction, unless, of course, some amount of liquid remains and acts as an adhesion bridge between the two surfaces. Irrespective of the actuation mechanism, be it capillary forces, electrostatic voltage forces or any other means, once the surfaces are brought into contact, surface forces determine whether or not adhesion will occur.

Numerous papers have been presented recently about the nature of surface adhesion forces. In this section we will review a number of these papers and present our best consolidated view of all the possible sources of stiction forces. Qualitatively, it is simple to explain the various possible adhesion phenomena. It is even possible to experimentally identify the cause of stiction in many of the systems studied. This can be done by varying experimental parameters to isolate particular adhesion mechanisms and observe the effect on the fabrication yield. However, because of the inaccuracy of the physical modeling and the large experimental variation in measured adhesion energies it is normally not so simple to identify the culprit for stiction based on the process yield. Nevertheless, presented below will be what we think to be the best physical models of the

various adhesion mechanisms with the disclaimer that they are still very rough and that experimental verification will always give the best and clearest answer.

Before proceeding, it is necessary to define a few terms. The surface adhesion forces are those attractive forces that tend to pull two surfaces together. The work of adhesion or adhesion energy, normally represented by  $\gamma_s$  (some books use  $W$ ), is the amount of energy or work required to separate two surfaces, each of unit area, from contact to an infinite separation distance. Therefore, the surface adhesion energy per unit area is given by the equation:

$$\gamma_s = W = \int_{z=\text{contact}}^{\infty} F_{\text{adhesion}}(z) dz \quad (4.2)$$

Of course, taking the derivative of this energy or work function with respect to the separation distance,  $z$ , will return the stiction force as a function of  $z$ .

For practical purposes, the separation distance when in contact is determined by the average roughness of the surfaces. Unfortunately, many of the papers referenced below neglect to mention the average roughness of the surfaces used for their experiments. This is another source of uncertainty in the measurements or calculations of adhesion energies. Later in the chapter, we will present an energy-based analysis of stiction and, in this case, the condition for beam peeling will be used to obtain an estimate of the surface adhesion energy.

#### 4.2.2.1. Mechanical Internal Bending Moments

Mechanically, non-uniform stresses can lead to internal bending moments that bias a microstructure to bend in one direction [Scheeper, 1992]. Secondly, compressive strains in bounded structures can lead to buckling toward the substrate. Strictly speaking these are not adhesion forces but they are still means by which a released microstructure can get stuck to another boundary surface. They can be avoided by proper control of the deposition process. In the particular case of the GLV, the beams are normally doubly clamped and under tension, so these issues are not significant.

#### 4.2.2.2. Electrostatic Forces

Electrostatic forces can arise either from induced charge transfer in materials of different work functions or from trapped charges in an insulator material.

Electrostatic pressure due to the work function differences of two different materials are determined by the following relation:

$$P_{el} = \frac{F_{el}}{Area} = \frac{\epsilon_0 U^2}{2h^2} \quad (4.3)$$

where  $\epsilon_0$  is the permittivity of free space,  $U$  is the potential difference, and  $h$  is the separation distance. For most materials, the work function difference will never exceed a potential of 1 V under equilibrium conditions. And in the case of the GLV and many MEMS devices, the materials have very similar work functions. For completeness, the electrostatic adhesion energy is given by

$$\gamma_{s,el} = \frac{\epsilon_0 U^2}{2h} \quad (4.4)$$

Assuming the worst case of  $U = 1$  V, a separation of  $h = 10$  Å (based on a typical rms roughness value for the GLV system), equation 4.4 says that the electrostatic adhesion energy per unit area is about 4.4 mJ/m<sup>2</sup> which is quite small as we shall see later.

On the other hand, if the surfaces are electrically well-isolated insulators and charge trapping occurs, then we can model the surfaces as a parallel plate capacitor with a fixed stored charge. The energy required to pull unit areas of the plates from contact to a distance  $h$ , is

$$\gamma_{s,tc} = \frac{\rho^2 h}{2\epsilon_0} \quad (4.5)$$

where  $\rho$  is the surface charge density which is normally kept below  $10^{10}$  charges per cm<sup>2</sup> by proper processing. Assuming this worst case, the work of adhesion due to the trapped charges should be about  $1.9 \times 10^{-6}$  J/m<sup>2</sup>, a very weak energy value compared to the values due to the phenomena below. Even if trapped charges on the order of  $2 \times 10^{12}$  charges/cm<sup>2</sup> are deliberately implanted into the microstructure films, the adhesion energy will only equal 76 mJ/m<sup>2</sup>.

In summary, it is highly unlikely that electrostatic forces will be significant in the stiction problem for most MEMS systems.

#### 4.2.2.3. Solid Bridging

Solid bridging was observed by Alley at U.C. Berkeley [Alley, 1992]. This phenomenon involves the cementing of silicon surfaces by silicon oxide residue which is dissolved in water that covers bare silicon surfaces. Silicon oxide residues or "watermarks" were independently studied by Watanabe who showed that if oxygen gas is available it will

dissolve into a water drop on the silicon surface, the silicon surface then forms a chemical oxide which is in turn dissolved, probably in silicic acid ( $\text{H}_2\text{SiO}_3$ ) form [Watanabe, 1989]. As the liquid dries it deposits the residual  $\text{H}_2\text{SiO}_3$  which can cement to surfaces around it.

Alley found that this residue could be minimized by following a few extra procedures: (1) thorough rinsing to remove the silicon oxide residue just prior to the drying step; (2) using a spin dryer which has a nitrogen environment and gets the water out more quickly before the oxidation chemistry takes place (Watanabe noted that the completion of the hydrophilization process of a silicon wafer in  $\text{O}_2$  takes about 22 minutes); (3) doing the final drying step with an isopropanol or methanol solvent since these chemistries do not form the oxide that water, air and a silicon wafer do; or, (4) one can form a silicon oxide barrier on the silicon surface which avoids the formation of the chemical silicon oxide residue altogether. The last procedure may be done by taking the wafer with released microstructures, keeping it wet, and replacing it into an oxidizing chemical bath, such as Piranha, RCA1, RCA2 or  $\text{H}_2\text{O}_2$ . The drawback is that this oxide layer is now hydrophilic and is susceptible to water bridging. However, this problem can possibly be addressed by perfecting the hydrophobic monolayer surface modification techniques discussed in section 4.2.1.2.

On a final note, Guckel has also observed stiction due to a fluorocarbon residue left after HF etching of oxide. This residue chemically bonds two silicon surfaces [Guckel, 1989]. Alley says that this can be prevented by rinsing with  $\text{NH}_4\text{OH}$  [Alley, 1992].

As a way of conclusion, solid bridging is a cementing adhesion mechanism, a source of total device failure, and must be avoided using the methods discussed above. If it could be measured, the expected adhesion force would correspond to the yield strength of the solid and lead to very high adhesion energy values close to atomic bond energies.

#### 4.2.2.4. Water Bridging and Hydrogen Bonding

The capillary force discussed in section 4.2.1 was described as an actuation mechanism by which a body of liquid drying from between two surfaces is able to exert an attractive force between the two. This so-called Laplace pressure is given by

$$P_{lb} = \frac{F_{lb}}{\text{Area}} = \frac{\gamma_l (\cos \theta_1 + \cos \theta_2)}{h} \quad (4.6)$$

where  $\theta_1$  and  $\theta_2$  are the contact angles of the liquid with surfaces 1 and 2,  $\gamma_l$  is the surface tension of the liquid (73 mJ/m<sup>2</sup> for water),  $h$  is the air gap, and the area is that of

the two surfaces covered by liquid. In section 4.2.1, Mastrangelo and Hsu used this pressure to derive the elastocapillary bound for the special case of  $\theta_1$  and  $\theta_2$  both being equal to  $\theta_c$  ( $\theta_c = 5^\circ$  for water on hydroxylated chemical oxide).

It was mentioned that if the liquid did not completely dry from the two surfaces then it could act as a glue. Israelachvili points out that liquids that wet surfaces will spontaneously condense from vapor into cracks and pores as liquid and that, at equilibrium, the meniscus curvature ( $1/r_1 + 1/r_2$ ) is related to the vapor pressure (relative humidity for water)  $p/p_{sat}$  by the Kelvin equation:

$$\left( \frac{1}{r_1} + \frac{1}{r_2} \right)^{-1} = r_k = \frac{\gamma V}{RT \log(p / p_{sat})} \quad (4.7)$$

where  $r_k$  is the Kelvin radius and  $V$ , in this case, is the molar volume ( $\gamma V / RT = 0.54$  nm for water at  $20^\circ$  C) [Israelachvili, 1992, p. 330]. For a spherical concave water meniscus with  $r_1 = r_2 = r$ , he calculates that  $r$  is about -10 nm, -1.6 nm and -0.5 nm for relative humidities of 90%, 50% and 10%, respectively. Since, real surfaces are rough and full of asperities, the condensed liquid (water in many cases) will only exert its full strength when the Kelvin radius is greater than the asperity size. In dry environments, if the water meniscus radius is smaller than the asperities then there will be no liquid bridging. This has been confirmed experimentally for adhesion of cantilevered heads to rotating disks [Tian, 1993]. Similarly, running the GLV beams in a dry nitrogen environment enabled continuous operation of the GLV without stiction. When the dry nitrogen source was exhausted and moist air entered the system, stiction was observed. Unfortunately, the exact correlation between humidity and adhesion energy was not measured. This would be a very interesting experiment to carry out in the future.

Qualitatively, water bridging is easily described as hydrogen bonding of water molecules physisorbed to the hydroxylated silicon surface. P.R. Scheeper noted that the main reason for stiction of PECVD nitride films to oxidized silicon substrates is the water bridging of adsorbed water molecules on the two surfaces [Scheeper, 1992]. In the case of silicon surfaces, rinsing a clean silicon surface with water leads to chemisorption (chemical bonding) of hydroxyl (-OH) groups, which in turn attract physisorbed (hydrogen bonded) water molecules. Stengl *et al.* have described a model for silicon wafer bonding via this mechanism and this model is illustrated in figure 4.3 [Stengl, 1989].

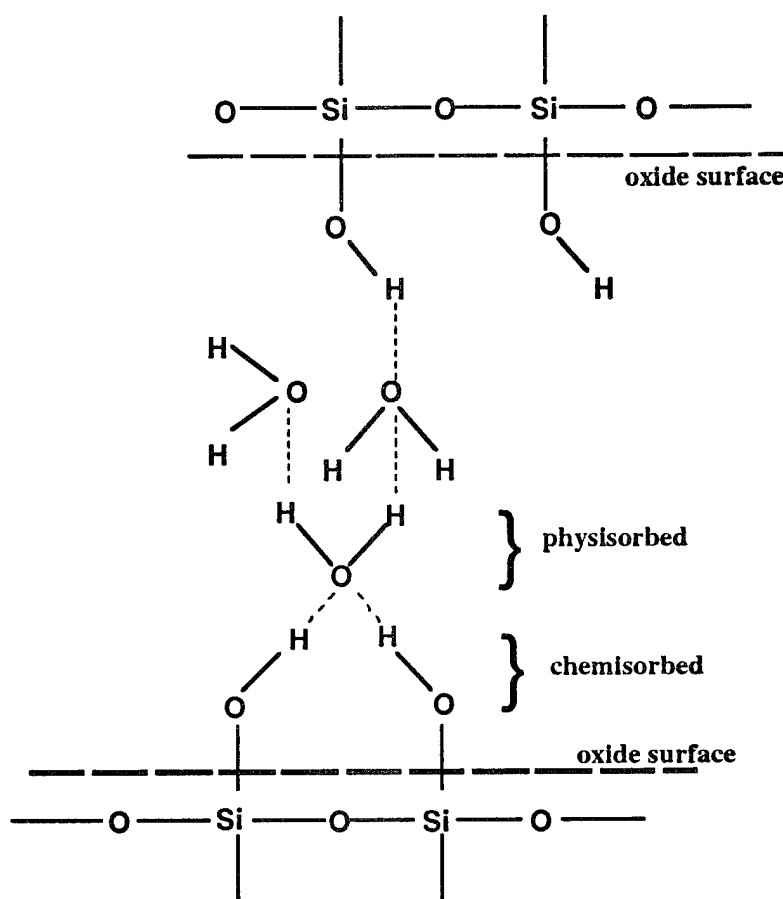


**Figure 4.3:** Two  $\text{SiO}_2$  surfaces kept together by hydrogen bonding between physisorbed water molecules as proposed by Stengl, *et al.*

Scheeper did not talk about the exact mechanism of chemical bonding to  $\text{Si}_x\text{N}_y$  but we can assume that a very similar process takes place, since the low-stress nitride used in the GLV system is silicon-rich and oxidizes as well.

It is quite difficult to derive a quantitative model of the work of adhesion for the liquid bridging case. We will present here two methods of analysis and point out their drawbacks and uncertainties.

Stengl estimated the adhesion energy due to the liquid bridge by multiplying the strength of the hydrogen bond by the surface density of the water hydrogen bonds in his model above [Stengl, 1989]. This evaluation resulted in the value of  $102 \text{ mJ/m}^2$ , which is pretty close to some of the values ( $136 \text{ mJ/m}^2$  and  $140 \text{ mJ/m}^2$ ) measured for smooth silicon oxide surfaces claimed to be suffering from liquid bridging [Backlund, 1992a; Mastrangelo, 1992]. He assumed that the hydrogen bonds had a bond strength of  $43.3 \text{ meV/bond}$ , the bond surface density on each of the two surfaces was one site every  $13.3$

Å<sup>2</sup>, and that 100% of the surface area contributes to the liquid bridging. This may not be true for real surfaces with a finite roughness unless the adsorbed water has a meniscus radius that is greater than the roughness. In which case, the water overflows the spaces and 100% of the area is covered with water.

An alternative method of finding the adhesion energy is carried out by Legtenberg using the Laplace pressure. This entails taking the derivative of the pressure over distance. Two questions arise if this is to be done. What limits are to be used for the integration, i.e. over what distance does this pressure hold since the body of water cannot be stretched to an infinite distance? Legtenberg seems to indicate that a good approximation would be to use twice the meniscus radius as the upper bound of separation. However, his choice of 2 µm is confusing because it is an unreasonable value for normal environments. The Kelvin radii numbers of Israelachvili are probably better limits for this calculation. The other question is: over what area does this pressure act? If we assume a constant volume of water then the “active” area is reciprocally related to the separation height ( $Area = V/h$ ), hence the force exerted is given by the expression:

$$F_{lb} = \frac{2\gamma_l \cos \theta_c Area}{h} = \frac{2\gamma_l \cos \theta_c V}{h^2} \quad (4.8)$$

where  $Area$  is the area covered by liquid and  $V$  is the constant volume of the liquid, which is equal to the initial height of the air gap filled with water times the initial area covered by that liquid at that separation height, ( $Area_o h_o$ ). If we integrate this force from initial contact to the final separation distance ( $h_{final}$ ) and normalize for the area of concern,  $Area_o$ , we arrive at the work of adhesion.

$$\gamma_{s,lb} = \frac{W}{Area_o} = 2\gamma_l \cos \theta_c \left( 1 - \frac{h_o}{h_{final}} \right) \quad (4.9)$$

An interesting note is that if we take  $h_{final}$  to be at infinity, then the work of adhesion is simply  $2\gamma_l$ , which corresponds to the simple case of splitting a body of water and increasing its surface area by two. For a practical case of hydrophilic surfaces with contact angles of 5°, an initial separation of 10 Å and a final separation distance of 32 Å (twice the Kelvin radius at 50% relative humidity), we calculate a work of adhesion per unit area of 100 mJ/m<sup>2</sup>.

Once again, we point out the fact that OTS or alkyl monolayers lower the liquid bridging force since these films are hydrophobic and lead to smaller contact angles.



However, these monolayers are still under development and process engineers will work hard to ensure that these films will survive the full microfabrication process.

Finally, a note of caution. We have derived two values of the adhesion energies due to the liquid bridging effect, both of which give numbers on the same order of magnitude as what researchers have measured for what they claim to be liquid bridging. However, much more work has yet to be put into this model. The references cited do not indicate the relative humidity nor the surface roughness in their experiments so it is truly difficult to say how accurate the above models are and how valid the assumptions are. At the very least the models give us an order of magnitude approximation of the liquid bridging effect and provide the engineer with some parameters to play with in developing a process for MEMS fabrication. One main conclusion is that humidity should be kept low enough such that the water meniscus radius is significantly less than the rms roughness of the surfaces. This indicates that packaging is an important issue to prevent stiction in MEMS devices.

#### 4.2.2.5. Hydrogen Bonding

If the silicon surfaces are hydroxylated but in a dry environment, hydrogen bonding can still take place. M. Schmidt of MIT in his review of silicon wafer bonding processes says that the most commonly held assumption for silicon wafer bonding at room temperature is that -OH groups are responsible for the attractive forces [Schmidt, 1994]. Backlund *et al.* have also discussed the direct bonding of silicon wafers [Backlund, 1992a, b] and agree that at room temperature the bonding of water-rinsed, freshly-HF-etched silicon wafers may be carried out through the hydrogen bonding of the hydroxyl groups which are present after water rinsing. But they do not clearly present any measurements of this type of bonding in a dry environment where liquid bridging is clearly eliminated from consideration. [Legtenberg, 1993] calculated the adhesion energy per unit area to be within the range of 100 to 300 mJ/m<sup>2</sup> by multiplying the hydrogen bond strength of 10-40 kJ/mol and the hydrogen bonding site surface density of 5 bonds per nm<sup>2</sup> for fully hydrated silica surfaces. Since, the hydrogen bond has such a short range, it is difficult to write an analytical relation for the hydrogen bonding force as a function of distance and it is guessed that it has the same dependence on the separation distance as the van der Waals forces discussed below. The difference between Legtenberg's and Stengl's values for adhesion energy is due to the discrepancy of the hydrogen bond energy.

Since both are hydrogen bond dependent, the adhesion energy per unit area of dry hydroxylated surfaces is on the same order as that of the liquid bridging case. Then why

did operating GLV beams in a dry nitrogen environment not demonstrate the same level of stiction as in a humid environment? The reason is that the surface adhesion energy due to the -OH-based hydrogen bonds must be multiplied by a factor corresponding to the percentage of actual contact area between the two surfaces. Since the surfaces have a finite roughness and no water is present to flood every available surface area then contact only occurs at the asperity heights (see section 4.3.3 on roughness). The hydrogen bond is very short ranged. This indicates that in the case of very smooth surfaces, the improvement due to keeping moisture out of the system is no longer effective because hydrogen bonding will still take place due to the hydroxyl groups.

For future work it is noted that if the wafers are not rinsed in water then the free silicon bonds will be mostly terminated by hydrogen atoms. And in this case, the hydrogen atoms will not cause hydrogen bonding since more electronegative atoms than Si are required to cause hydrogen bonding. The remaining binding force is the van der Waals force.

It is also interesting to note that silicon wafers can be dehydrated of the -OH groups by raising the temperature to leave mostly -H terminations. This could offer a method of getting down to the van der Waals limit for some MEMS systems after a successful freeze drying step. Researchers [Grunder, 1986; Stengl, 1989] found that water is released in the temperature range of 30 to 200°C depending on pressure and atmospheric conditions; however, -OH bonds are harder to break and progressively dissociate in the range above 200°C, with 40% surviving at 400° C, and some groups surviving up to 1000°C.

#### 4.2.2.6. Van der Waals Forces and London Dispersion Forces

Van der Waals forces serve as the fundamental limit for the problem of surface adhesion, i.e. the lowest adhesion energy value practically attainable. They can be classified into induction, orientation and dispersion forces, with the first two being present in systems involving polar molecules [Israelachvili, 1992]. Even if non-polar molecules or atoms are considered and all other forces are eliminated, we will still have London dispersion forces due to induced-dipole-to-induced-dipole interactions. Israelachvili says that the pressure force exerted by this force can be described by the following equation [Israelachvili, 1972a]:

$$P_{vdw} = \frac{F_{vdw}}{Area} = \frac{A}{6\pi h^3} \quad (4.10)$$

where  $A$  is the short range Hamaker constant,  $d$  is the distance between the two ideally flat surfaces, and  $P$  is the pressure or force per unit area. This equation is valid for short range forces where  $h < 10$  nm. If  $h > 10$  nm then the expression for the van der Waals pressure is

$$P_{vdw} = \frac{F_{vdw}}{Area} = \frac{B}{h^4} \quad (4.11)$$

where  $B$  is the long-range Hamaker constant. Most cases we will be dealing with have surface roughness values that place the separation distance within the short range regime of  $h < 10$  nm. Scheeper uses the following numbers  $A = 5.4 \times 10^{-20}$  J, and  $B = 10^{-28}$ . Alley and Torii *et al.* [Torii, 1993] use the same expression for van der Waals pressure but a Hamaker constant of  $A = 2.723 \times 10^{-19}$  J. Israelachvili [Israelachvili, 1992] notes that the Hamaker constants of most condensed phases are found to lie in the range  $(0.4-4) \times 10^{-19}$  J.

To get the adhesion energy per unit area, the above force terms are used in the integral over the distance from the initial separation  $h_0$  to infinity. Legtenberg *et al.* simplify all this by only using expression (4.7) and assuming that the errors will be small since the force is so short-ranged. Using this simplification the adhesion energy turns out to be:

$$\gamma_{s,vdw} = \frac{A}{12\pi h^2} \quad (4.12)$$

For the case of  $A = 4 \times 10^{-19}$  J and  $h = 10$  Å, the adhesion energy will be about 10 mJ/m<sup>2</sup>. Backlund *et al.* [Backlund, 1992b] claim to have also measured adhesion energies of about 26 mJ/m<sup>2</sup> on smoother wafers believed to be dominated only by van der Waals forces. The discrepancies in the energy values come from uncertainties in the separation height and in the Hamaker constant.

#### 4.2.2.7. Conclusion: Adhesion Mechanisms and the GLV

In this section, we have discussed the forces that contribute to the bonding or adhesion of two semiconductor surfaces. Ranked in decreasing order of magnitude, they are the solid bridging force, the liquid bridging force, the -OH-based hydrogen bonding force, and the van der Waals force. The electrostatic force can be a strong if artificially created, but under normal circumstances it is lower than the van der Waals force. All these forces are

short-ranged and can be minimized or engineered around, except the van der Waals forces which will always exist between any two surfaces.

Typically, the GLV system uses silicon nitride beams and an oxidized silicon substrate. Very similar to the omnipresent and well-studied polysilicon and silicon substrate system, the adhesion mechanisms are alike. If the devices are operated in air, the main culprit for GLV stiction is liquid bridging. This was demonstrated by successfully operating some devices in a dry nitrogen environment for two weeks. Stiction occurred when humid air replaced nitrogen as the dry nitrogen supply ran out. In dry nitrogen, it is believed that the more roughness-dependent and weaker hydrogen bonding of hydroxyl groups dominates. Therefore, it is desirable to develop a good packaging process as well for the GLV. Ideally, this package will be provide a hermetic seal. No processing scheme has yet been developed to reach the van der Waals limit by avoiding the hydroxylation of the silicon surface.

### 4.3. Adhesion Energy and the Peel Condition

#### 4.3.1 Measurement of Solid-Adhesion Energy

In the previous section, we have discussed the mechanisms for surface stiction. However, in actual practice, engineers are normally forced to work within the constraints of certain material systems. It becomes important to monitor the range of the stiction force and observe its value as various procedures and treatments are altered. Besides providing a clue to the possible causes of stiction, this procedure, more importantly, calibrates a process' adhesion limits, around which engineering solutions can be developed.

Torii *et al.* [Torii, 1993] have proposed and demonstrated measuring the adhesive force by using an atomic force microscope (AFM). However, a simpler empirical approach and one that is more practical from a processing point of view is that proposed by Mastrangelo and Hsu [Mastrangelo, 1992 and 1993b]. They have made a thorough analysis of beam peeling theory and have demonstrated a simple procedure for determining the adhesion energy of MEMS systems (N.B. this measure of adhesion energy per unit area does not really give an indication of the exact force versus distance relation at the interface).

The Mastrangelo procedure entails the fabrication of cantilevers and microbridges of various lengths and noting the critical lengths of the structures beyond which stiction is observed and below which the cantilevers or bridges are released. In the latter case, the restoring force of the beams is sufficient to peel the beams away from the substrate; hence, the term "peel condition". Photograph 4.2 is a picture of the harp test structure used in GLV development work. Typical cantilevers and doubly-clamped beams fabricated ranged from 3-25  $\mu\text{m}$  and from 11-65  $\mu\text{m}$ , respectively, in steps of 1  $\mu\text{m}$ .

In the case of cantilevers, peeling occurs if:

$$N_P = \frac{3Eh^2t^3}{8\gamma_s l^4} > 1 \quad (4.13)$$

where  $N_P$  is the peel number, which, if greater than unity, indicates that there is enough strain energy stored in the bent beam to overcome the adhesion energy. In the above relationship,  $\gamma_s$  is the adhesion energy per unit area (or work of adhesion);  $E$ , the Young's Modulus;  $t$ , thickness of the beam;  $h$ , the air gap and maximum beam displacement; and  $l$  is the length of the cantilever beam. This relation can give us the adhesion energy per unit area, since the harp structure indicates the beam displacement length,  $l = l_d$ , at which

stiction begins to occur and at this point  $N_p = 1$ . Using this information, Mastrangelo derived the expression for the adhesion energy per unit area using the observed displacement length:

$$\delta_s = \frac{3}{8} \frac{Eh^2 t^3}{l_d^4} \quad (4.14)$$

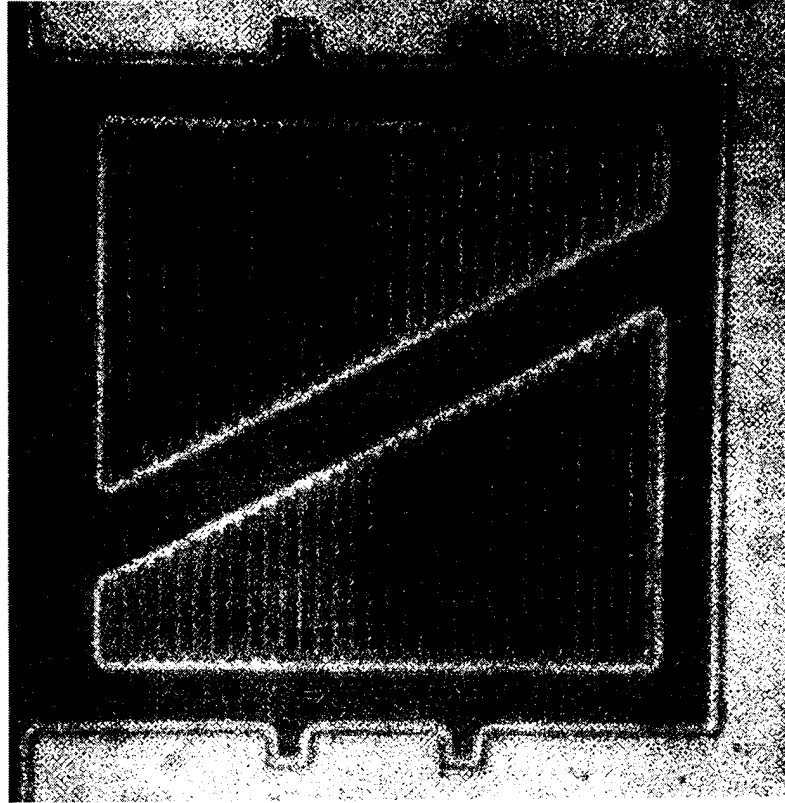


**Photo 4.2.:** Two harp test structures consisting of doubly clamped beams varying in length from 11 to 40  $\mu\text{m}$ . The bottom harp shows that the left-side beams shorter than 25  $\mu\text{m}$  are free, while the beams to the right of the 25  $\mu\text{m}$  displacement length are stuck down (indicated by the color changes due to interference effects).

The above analysis tells us that given an adhesion energy for a particular material system ( $\gamma_s$  and  $E$ ) and geometry ( $h$  and  $t$ ), cantilevers longer than the displacement length ( $l_d$ ) will be stuck and those shorter will peel from the substrate.

It should be noted that the calculated values for  $\gamma_s$  will be independent of the widths of the beams. Also, these equations include the mechanical analysis of shear deformation at the very tip of the cantilever. However, it does assume that there are no stress gradients in the mechanical films that can contribute a built-in bending moment. In fact,

we found that for the GLV process, stress gradients in the vertical direction (the direction of film growth) were so pronounced that the cantilever test structure could not be used as a measure of the adhesion energy. Photograph 4.3 shows silicon nitride cantilevers about 130 nm in thickness that are curled upward due to these stress gradients.

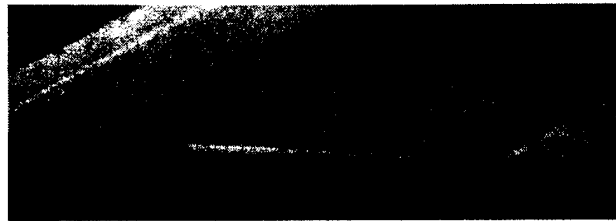


**Photo 4.3.:** 6  $\mu\text{m}$ -long silicon nitride cantilevers about 130 nm in thickness that are curled upward due to stress gradients in the nitride material.

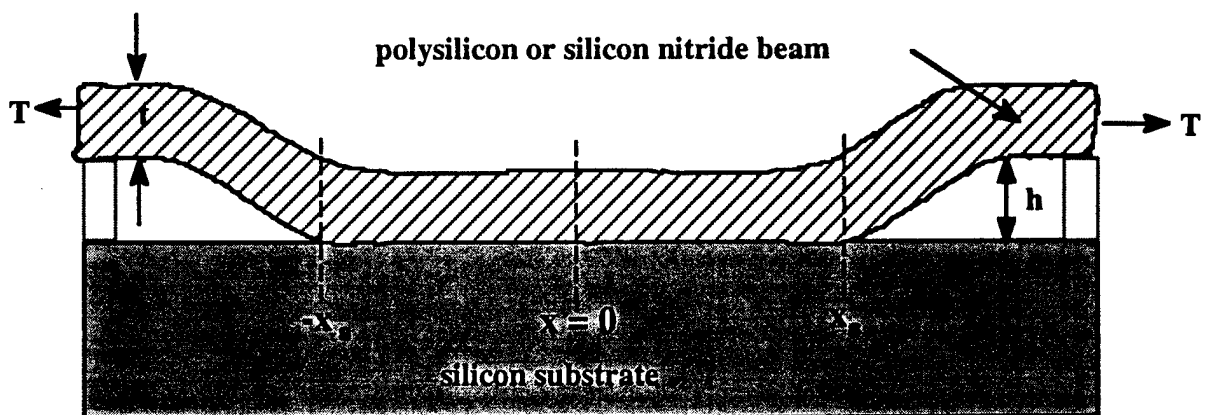


**Figure 4.4.** Diagram of a doubly-clamped beam brought into contact with the substrate. Two energy terms are involved in the analysis: surface adhesion energy and the elastic strain energy (due to bending and the tensile stretching).

For this reason, GLV development relied more on doubly-clamped harp test structures. In a follow-up paper, Mastrangelo and Hsu [Mastrangelo, 1993b] generalized the above analysis for arbitrary shapes and defined a peel bound condition in a very similar way to the elastocapillary number  $N_{EC}$ . For the case of microstructures deflected to a substrate, they defined a peel number  $N_P$  such that if this number is greater than unity then the deflected structure will peel back and not stick. A method of energy analysis was used to derive the peel number, which is a statement of whether or not the energy

equilibrium state is one in which there is surface contact or not. This system can be better understood in reference to figure 4.4 which shows a doubly-clamped beam brought into contact with the substrate by some means of actuation.

After the actuation means is removed, the system involves two energy terms, elastic strain energy in the beam and the adhesion energy ( $U_{total} = U_{strain} + U_{sticking}$ ). Through energy minimization considerations, the balance of these terms determines the equilibrium condition of the beam, i.e. whether more contact is preferred or not. The strain energy has two components ( $U_{strain} = U_{bending} + U_{tension}$ ). The first is from the beam bending,  $U_{bending}$ , and is dependent on the modulus of elasticity, the moment of inertia, and on the amount of bending or curvature in the beam. Secondly, since the beams can have a built-in tensile force, there is the added strain energy,  $U_{tension}$ , which depends on the amount of tension times the amount of stretching in the beam. The energy term due to surface attraction,  $U_{stick}$ , is negative; it is simply the adhesion energy per unit area times the area of contact. From figure 4.4, we see that the area is the width times the length of the beam touching the substrate,  $2x_s$  in this case. The condition for peeling is determined by taking the derivative of the total energy with respect to the contact length,  $x_s$ . Since this derivative is monotonic for all values of  $x_s$ , then if its value is positive at the point of initial contact,  $x_s = 0$ , then the system will tend towards avoiding this contact, i.e. the beam will peel. The above peel condition for doubly-clamped beams is met if:

$$N_P = \left( \frac{128 E h^2 t^3}{5 \gamma_s l^4} \right) \left[ 1 + \frac{4}{21} \left( \frac{\sigma l^2}{E t^2} \right) + \frac{256}{2205} \left( \frac{h^2}{t^2} \right) \right] > 1 \quad (4.15)$$

where the additional parameter  $\sigma$  is the tensile stress in the beam. Once again, if the peel number is greater than unity then the microbridges will peel from the substrate; otherwise, stiction will occur.

In order to more clearly illustrate the balance of stiction force versus the beam's restoring force, we re-arrange the above identity. Noting that the condition for peeling requires that  $N_P$  be greater than one, we rearrange the new inequality by putting the surface adhesion energy to one side such that:

$$\gamma_s < \left( \frac{128 E h^2 t^3}{5 l^4} \right) \left[ 1 + \frac{4}{21} \left( \frac{\sigma l^2}{E t^2} \right) + \frac{256}{2205} \left( \frac{h^2}{t^2} \right) \right] \quad (4.16)$$

This way we see that the stiction is prevented if the surface adhesion energy per unit area is less than the other three energy terms on the right. The first term in the above



inequality corresponds to the energy contribution of the linear beam bending, which is simply dependent on the material's modulus of elasticity, its moment of inertia, the length of the beam, and the amount of deformation experienced (hence, the  $h^2$  term). The second term, is the energy due to the built-in stress of the nitride film, and its value can be engineered to be dominant over the bending moment term. This term is less dependent on the beam length. Finally, the last term is the second-order contribution of the non-linear beam bending. This term is normally much smaller than the linear bending term and can often be neglected. In fact, for the GLV case, the stress term is normally dominant even over the bending term by an order of magnitude.

As in the cantilever case of section 4.3.1, relation (4.16) leads to an expression for the adhesion energy as a function of the displacement length if  $l$  is replaced by  $l_d$  and the inequality is replaced by an equality because  $N_p = l$  when  $l = l_d$ .

#### 4.3.2 Range of Values for Various Polysilicon-Silicon Systems

Mastrangelo used the cantilever test structures to evaluate adhesion energies for polysilicon-silicon systems. Their experiments were carried out with hydrophilic and hydrophobic systems and their measured values for  $\gamma_s$  were around  $140 \pm 70 \text{ mJ/m}^2$  for both systems (using a value of  $E=170 \text{ GPa}$ ). They were surprised that the hydrophobic system did not have lower values than the hydrophilic one, and this might be accounted for by the fact that they rinsed the freshly HF dipped wafers in water and allowed the water to dry off very slowly overnight. This process is likely to allow a hydrophilic oxide layer to grow. A similar observation and explanation was given by Torii *et al.* Another explanation could be that solid bridging occurred for the hydrophobic case and lead to similar attractive forces as that of liquid bridging in the hydrophilic case; however, we think that this is less likely because solid bridging is commonly thought to be a much stronger weld that would have given much higher values for adhesion energies.

The second paper of Mastrangelo [Mastrangelo, 1993b] gives another set of values of adhesion energies and these show a more understandable difference between the hydrophilic case ( $270 \pm 100 \text{ mJ/m}^2$ ) versus the hydrophobic case ( $100 \pm 60 \text{ mJ/m}^2$ ).

Some other researchers have published the results of their own measurements of adhesion energies per unit area for silicon systems. Legtenberg [Legtenberg, 1993] presented in Transducers '93 the results of his experiments using doubly clamped beam structures. On the other hand, Backlund [Backlund, 1992b] measured the adhesion energy of whole-wafer systems using crack propagation. The data of both these papers are tabulated above together with the results of Mastrangelo.

Rinse	Adhesion Energy at RT (mJ/m <sup>2</sup> )	Contact Angle with Water	Reference
BOE	42	N/A	[Backlund, 1992a]
Freshly HF dipped (no H <sub>2</sub> O)	79-97	70°	[Backlund, 1992a]
H <sub>2</sub> SO <sub>4</sub> :H <sub>2</sub> O <sub>2</sub>	136	8°	[Backlund, 1992a]
HF (no water rinse)	26	N/A	[Backlund, 1992b]
BOE; H <sub>2</sub> O	50 ± 5	70°	[Legtenberg, 1993]
BOE; HNO <sub>4</sub> ; H <sub>2</sub> O	260 ± 100	5°	[Legtenberg, 1993]
BOE; Isopropanol	100 ± 50	N/A	[Legtenberg, 1993]
BOE; HNO <sub>4</sub> ; Iso	240 ± 100	N/A	[Legtenberg, 1993]
HF	140 ± 70	N/A	[Mastrangelo, 1992]
HF	100 ± 60	N/A	[Mastrangelo, 1993b]
H <sub>2</sub> SO <sub>4</sub> :H <sub>2</sub> O <sub>2</sub>	270 ± 100	N/A	[Mastrangelo, 1993b]

**Table 4.1:** Adhesion energy values for silicon-to-silicon interfaces with varying rinse treatments based on references.

From the table above it can be noted that there is a wide-range of variability in the measured values. This is understandable given the above review discussion on adhesion models and their dependence on separation heights/roughness, relative humidity, and process rinses. None of the references above mentioned the values of roughness nor humidity.

In designing actual devices and requiring non-adhesion, designers are constrained to assume the worst case values of their material and rinse system and it would be advisable to perform one's own calibration measurements.

### 4.3.3 Dependence on Roughness

As early as 1989, Guckel [Guckel, 1989] had advocated the use of polysilicon and its controlled roughness as a means of engineering around the adhesion problem. Legtenberg models the effect of roughening on the various stiction mechanisms by calculating the value of the bonding energy versus surface separation. While roughened surfaces are not equivalent to greater surface separation, the average effect is very similar. Alley [Alley, 1993] points out the important statistical measures of surface roughness which are relevant to the stiction problem. Only rms surface roughness or the variance (and not slope nor curvature) is a parameter that is independent of sample area size. And the important statistical measures of roughness are variance ( $\sigma^2$ ), reduced skewness ( $Sk$ ) and reduced kurtosis ( $K$ ), which are described by the following relations and diagrams.

$$\sigma^2 = \int_{-\infty}^{\infty} p(z)[z - \bar{z}]^2 dz \quad (4.17)$$

$$Sk = \frac{1}{\sigma^3} \int_{-\infty}^{\infty} p(z)[z - \bar{z}]^3 dz \quad (4.18)$$

$$K = \frac{1}{\sigma^4} \int_{-\infty}^{\infty} p(z)[z - \bar{z}]^4 dz \quad (4.19)$$

where  $p(z)$  is the probability distribution of the surface height,  $z$ , and  $\bar{z}$  is the mean plane of the surface. For lowering the stiction force it is preferable to have a large variance, positive skew and positive kurtosis. Physically, this is illustrated in the diagrams below where it is seen that a larger variance means a rougher surface; a positive skewness means that most of the exposed surface is below the mean and so there are less asperities for another surface to come into actual contact with it; and, a higher kurtosis means that the asperities are sharp.

Raman [Raman, 1991] has shown that rms surface roughness does reduce stiction on magnetic recording disks up to a certain extent. In their paper, they have shown that below 40 nm, rms surface roughness reduces stiction and friction very considerably, but after 40 nm increased roughness did not improve the stiction problem.

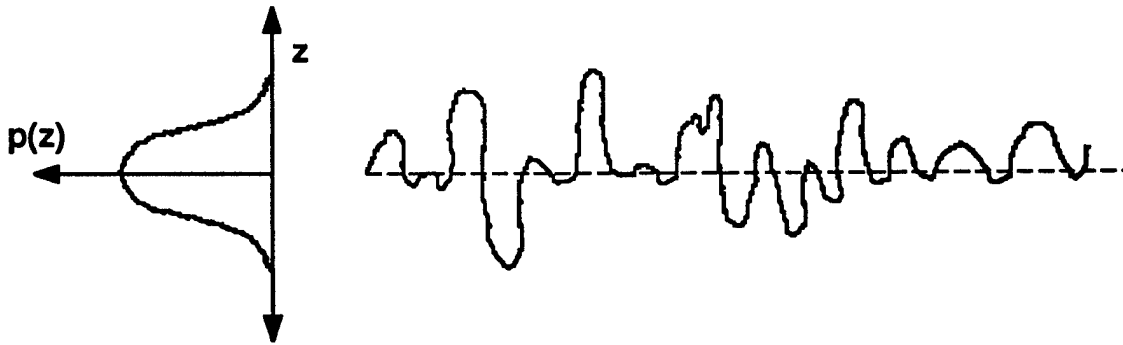


**Figure 4.5a:** Illustration of the physical significance of variance. Physically, the diagram above shows that a larger variance means greater separation of the surfaces on average.

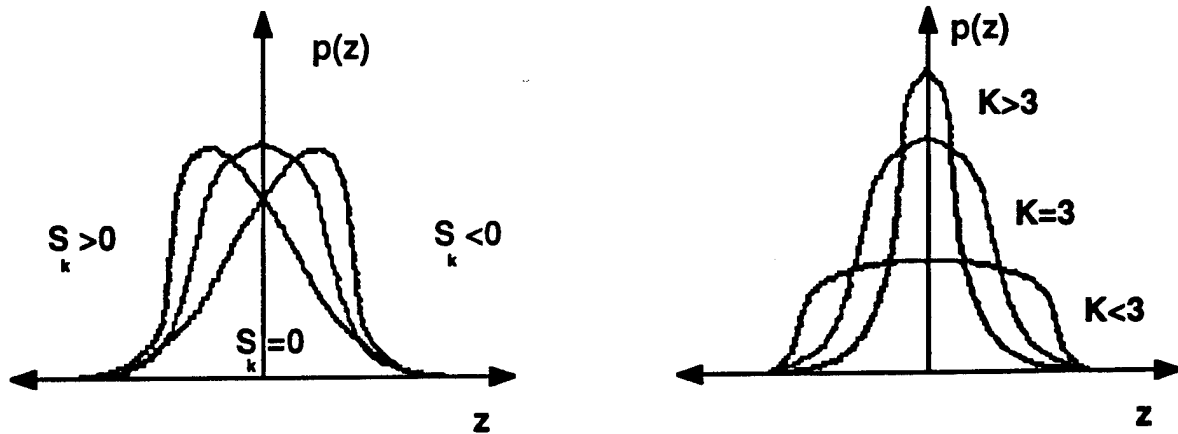


**Figure 4.5b, c:** Diagram describing the physical significance of Kurtosis and Skewness. A positive skewness means that most of the exposed surface is below the mean height; hence, there are less asperities for another surface to come into actual contact with it. A kurtosis greater than three means that the asperities are sharp.

#### 4.3.4 Roughening Experiments

Guckel has measured the surface rms roughness of fine-grained polysilicon and found it to be around  $8\text{\AA}$ . However it is well known that the graininess of polysilicon can be controlled by the deposition conditions, particularly temperature. Normally, there is a critical temperature between  $550^{\circ}\text{C}$  and  $600^{\circ}\text{C}$  (depending on the exact deposition system), above which the silicon is deposited in a grainy, polycrystalline way and below which one gets amorphous silicon which is normally smooth [Ibok, 1993]. After depositing a smoother amorphous layer one can still increase surface roughness by prolonged etching in HF or by annealing the silicon layer.

It must be remembered that if polysilicon is to be used as a roughening layer in a GLV beam that it has very different stress characteristics than silicon nitride. In fact, the anneal step is not only desirable to increase roughness but also because it anneals the normally compressive stress to a tensile state or even to a stress-free state [Guckel, 1988].

It has also been shown that etching can further increase the roughness of silicon or silicon nitride surfaces. This effect is expected to be enhanced for silicon if the structure is polycrystalline and if the etch is anisotropically dependent on crystalline orientation. This has been shown to be true in KOH and, even in HF [Haller, 1993].

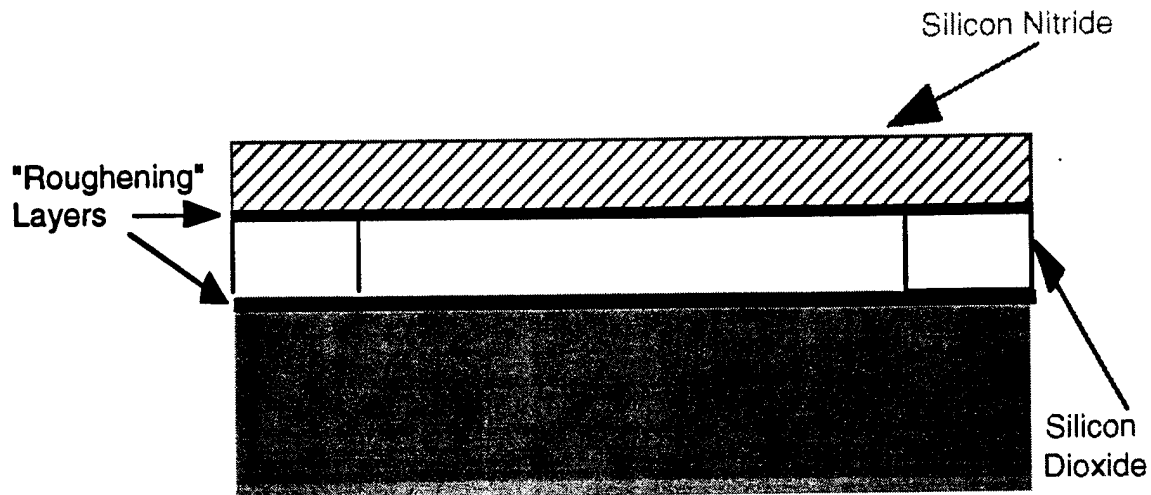


**Figure 4.6:** Diagram of test-structure used for adhesion energies of various material systems.

To experiment with surface adhesion energies and to test the roughening technique, we used a modified beam structure to compare various material systems. This structure is the same basic GLV beam with added surface layers placed at the interfaces (see figure 4.6). For the top and bottom layers we used the following materials: low-stress silicon nitride, high-stress silicon nitride, amorphous silicon, annealed polysilicon, and bare silicon (only for the substrate). The beam material is still silicon nitride with a significant stress level and is made much thicker than the coating layer such that the beam stiffness in each system will be approximately the same.

On a relative scale, it was found that the roughest interface (annealed polysilicon to annealed polysilicon) gave the lowest adhesion energies, while the smoothest (nitride to bare silicon) gave the worst results. However, due to experimental difficulties the exact adhesion energies could not be ascertained for this experiment. Nevertheless, similar runs were made for materials closer to the GLV's and the results are shown in figure 4.7. This chart of the adhesion energy values was made using the harp structures of doubly-clamped beams with typical GLV geometries (widths around  $1\text{ }\mu\text{m}$  to  $1.75\text{ }\mu\text{m}$ , and thickness around  $132\text{ nm}$ ). In general, results from the harp structure releasing showed that the smooth nitride on a bare silicon surface gave the strongest adhesion energies, and that an annealed roughened polysilicon was better against stiction than an unannealed silicon layer. The chart indicates a value of  $> 53\text{ mJ/m}^2$  for the plain nitride case because the test wafer V4's test structures only allowed measurements up to this value. On other wafer runs with plain nitride, the measured values ranged from  $80$  to  $100\text{ mJ/m}^2$ .

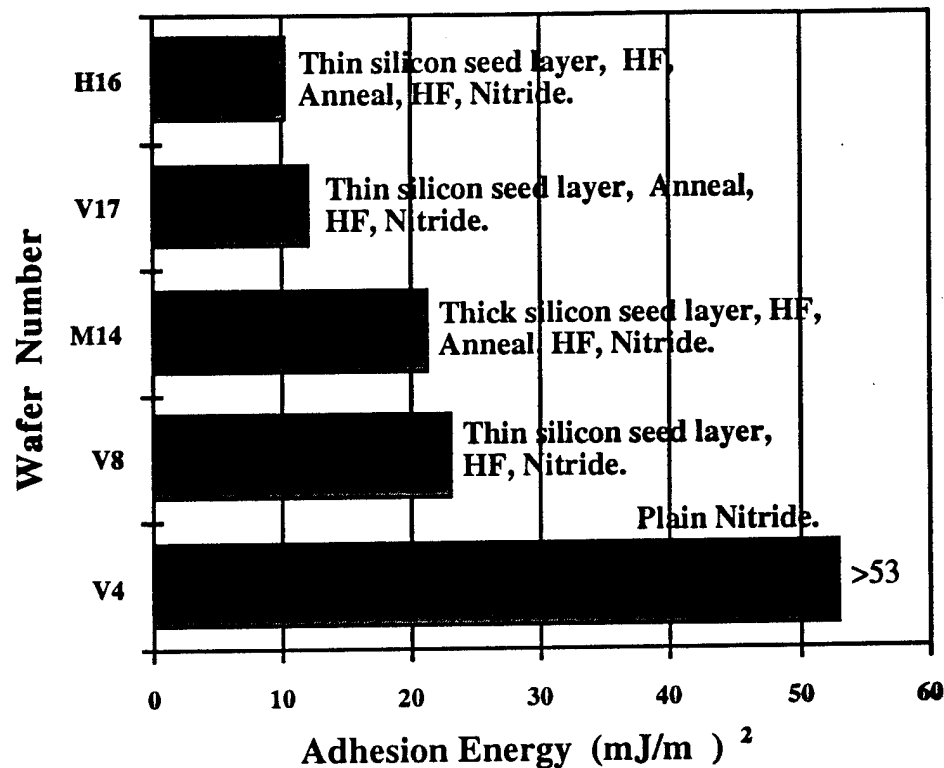


**Figure 4.7:** Chart of adhesion energy per unit area for various material systems (in  $\text{mJ/m}^2$ ).

At first, it was surprising that a thicker silicon seed layer was less effective in preventing stiction, since it gave a rougher top surface, especially when annealed. However, a TEM picture of silicon deposited on oxide (Photo 4.4) shows that the top surface is indeed rough but the bottom surface adopts the oxide surface's smoother morphology. The thinner seed layer works better because it does not fully cover the entire surface. A subsequent HF dip before the nitride deposition etches cavities in the exposed portions of oxide. The subsequently deposited nitride will fill in these cavities in the oxide layer and will therefore have a rougher bottom surface once the oxide is etched away.

In conclusion, the values for adhesion energy per unit area for silicon based systems vary in the range of 10 to  $100 \text{ mJ/m}^2$  (measured in a clean room environment with about 50 % relative humidity). Experimentally, it had been noted that these values can vary significantly on a run-to-run basis but clear trends such as those depicted in figure 4.7 were observed. Relative to other systems using the same wet chemistry, a thin roughening polysilicon seed layer lowered the adhesion energy by at least a factor of five

relative to plain and smooth nitride beam. This translates to beam displacement lengths of at least twice the original value.

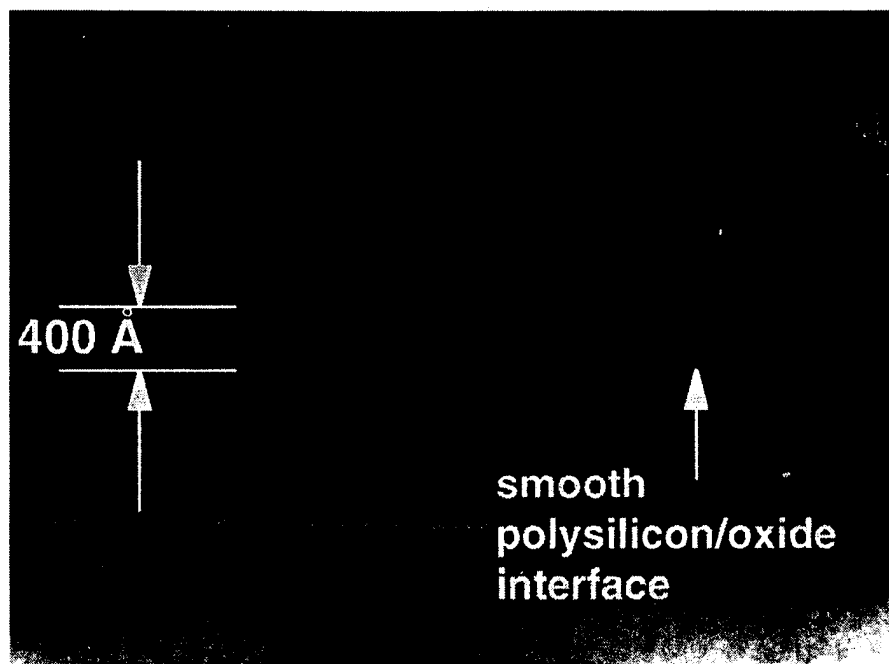


**Photo 4.4:** TEM picture of a smooth polysilicon/oxide interface. About 400 Å of amorphous silicon was LPCVD deposited at 250 mT and 580°C (done by Dave Koester of MCNC).

#### 4.4. Stiction and the GLV

The stiction problem has been addressed by many researchers in the MEMS area; however, the GLV system is more demanding than other MEMS cases because the device requires smooth surfaces, very thin, compliant structures and sub-micron spaces. Normally, other MEMS devices (e.g. diaphragms and motors) have worked with thicknesses on the order of 1  $\mu\text{m}$  or more, and with air gaps of the same magnitude. The GLV, on the other hand, is an optical device and relies on the interference of visible light; therefore, the dimensions of the microstructures are around 130 nm, eight times less than what had previously been worked with. Furthermore, the optical flatness requirement limits the amount of rms surface roughening to about 5 nm.

A very special GLV case is that of an optical modulator. In this case, the system does not normally require large modulation depths and contrast ratios; also, large voltage swings can be tolerated for systems with few elements. In this case, the GLV can be operated in a non-contact mode; and so, freeze-drying or other similar release techniques

will be sufficient to yield working devices [Sandejas, 1992]. On the other hand, for display applications where efficiency and contrast are of primary importance, the preferred mode of operation involves surface contact. Engineering solutions are required to circumvent the stiction problem given GLV display system requirements and the constraints of the material systems (particularly, the adhesion energy values). Essentially the problem is to overcome the stiction force with the beam restoring force.

The first solution is to simply increase the restoring force. From the discussion on GLV electromechanics, beam stiffness is proportional to the stress in the beam and inversely proportional to the square of the beam length. Figure 3.5 shows us that we can engineer the beam stress to be about 1 GPa, giving 20 V switching voltages for 15  $\mu\text{m}$  long beams. However, driver circuit considerations point towards lower stress levels and switching voltages, preferably around 5 V. Furthermore, tensile strength of the nitride and air dielectric breakdown at the device edges and in the spacing layer are other issues that constrain the maximum stress allowable in the beam material.

Therefore, it becomes necessary to also lower the adhesion energy. The preceding sections have already pointed out that this can be lowered by proper processing and insuring that the adhesion mechanism is either van der Waals or hydrogen bonding. When this is done, the process engineer is close to the fundamental limit of the adhesion force and engineering solutions must be utilized if further yield improvements are to be attained.

Noting that the stiction force is proportional to area of surface contact, a logical approach is to reduce this area. In effect, the microscopic scale roughening discussed in section 4.3 produces does this to a certain extent. However, macroscopic patterning provides techniques which can further reduce this area of surface contact by more than 95%. The last approach is a significant step for GLV processing since it brought device yields well beyond the borderline between stiction and peeling. A number of processes were developed to pattern sub-micron supports underneath a 1  $\mu\text{m}$  beam and these are discussed in the next section.



## 4.5. Engineering Solution to Stiction: Lessen Area of Contact

### 4.5.1. Incorporating the surface reduction parameter into the Mastrangelo Model.

The peel condition of Mastrangelo in equation (4.15) must now be modified to incorporate a factor that will describe the effect of contact area reduction. This can be simply done by multiplying the adhesion energy by the a factor that is equal to the percentage of actual area brought into contact over the whole beam length. Therefore, we can re-write relation (4.16) as:

$$\eta_{ar} \gamma_s < \left( \frac{128 E h^2 t^3}{5 l^4} \right) \left[ 1 + \frac{4}{21} \left( \frac{\sigma l^2}{E t^2} \right) + \frac{256}{2205} \left( \frac{h^2}{t^2} \right) \right] \quad (4.20)$$

where we have introduced the percentage area reduction factor  $\eta_{ar}$  to describe the overall effect of area reduction (hence, the subscript “ar”) on the peel condition. For example, for a 1  $\mu\text{m}$ -wide beam of any length, if there are 1  $\mu\text{m}^2$  contact points every 5  $\mu\text{m}$  along its length, then only 20% of the beam will touch the substrate if the beam is deflected (we, assume that the beam does not collapse in between the 1  $\mu\text{m}^2$  supports). In effect, we have reduced the adhesion energy per unit area to 20 % of its original value.

Since the material systems are not being altered, the adhesion energy is not actually being lowered; however with the help of area reduction techniques it is easier to insure that the adhesion energy increase per unit length of beam collapse (left-hand-side of (4.20)) is less than the strain energy lost per unit length (right-hand-side). Relation (4.20) now states that given a particular beam geometry and adhesion energy, peeling can be guaranteed by adjusting both the stress levels and the percentage of surface area actually brought into contact.

If relation (4.20) is turned into an equality and the length is replaced by the displacement length,  $l_d$ , it can be used to engineer the required area reduction for a GLV beam of a given geometry, material, and manufacturing process. We initially assume that there is no area reduction factor and plot adhesion energy as a function of displacement lengths and stress levels. Figure 4.8 is family of plots corresponding to the two stress levels. To interpret the plots, for a given stress curve, the space to the right and above corresponds to the stuck state and the space to the left and below corresponds to the

released state. Going to the right means having longer beams and going up means increasing the adhesion energy.

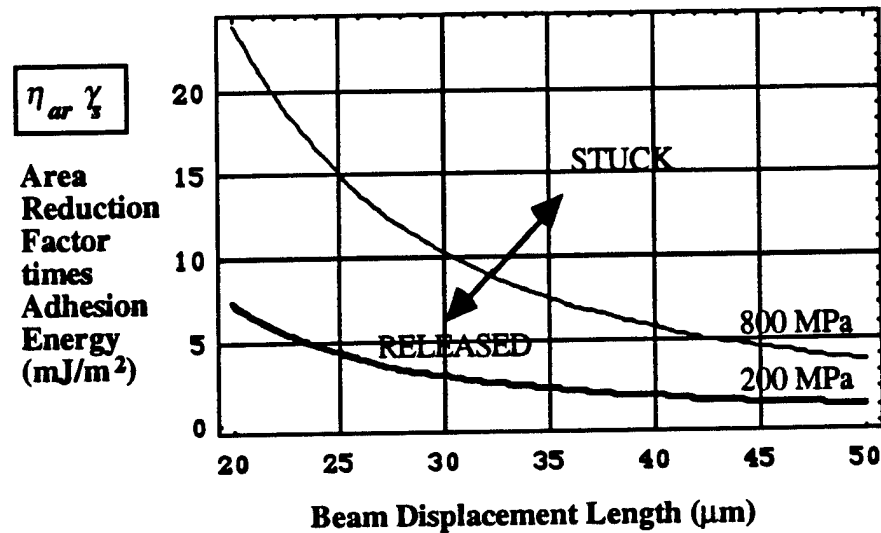


**Figure 4.8:** Plot of surface adhesion energy as a function of GLV beam displacement lengths. The lighter line above is calculated for a nitride beam system with  $h = t = 132$  nm,  $\sigma = 800$  MPa,  $E = 225$  GPa. The bottom plot is for the same system with a stress of 200 MPa.

As an example, we calculate the amount of surface reduction required for 25 μm beams to peel. The desired stress is 200 MPa to get the switching voltages below 10 V for 25 μm long beams. The material and process involved (including the rinse step) determine the adhesion energy. This can be easily measured by picking a system of a known geometry and stress and observing the displacement length. If an experiment is done with  $h = t = 132$  nm,  $E = 225$  GPa, and  $\sigma = 800$  MPa and the beam displacement length was found to be 20 μm, then the adhesion energy for that process is about 24 mJ/m<sup>2</sup>, as can be seen in the upper plot in figure 4.8. Now, if the same process is to be used but the stress is to be reduced to 200 MPa, then the second (darker) plot in figure 4.8 can be used to estimate the area reduction needed to yield the 25 μm-long working devices. The 200 MPa plot shows that the adhesion energy needs to be at most 4 mJ/m<sup>2</sup>

to get a displacement length of 25  $\mu\text{m}$ . Since this is not possible without changing the process, then  $\eta_{ar}$  can be used to effectively lower the adhesion energy per unit area and increase the displacement length to about 25  $\mu\text{m}$ . In this case,  $\eta_{ar}$  should be at most  $4/24 = 1/6$ . From experience, different processes show large different variations in the yields and so the worst case adhesion energy should be used for this type of calculation and tolerances must be very forgiving.

#### 4.5.2. Limits to the Surface Patterning Technique

From the above discussion, it is obvious that to increase the area reduction ratio one would want to make smaller contact points and separate them further. What are the constraints on how much one can reduce the contact area?

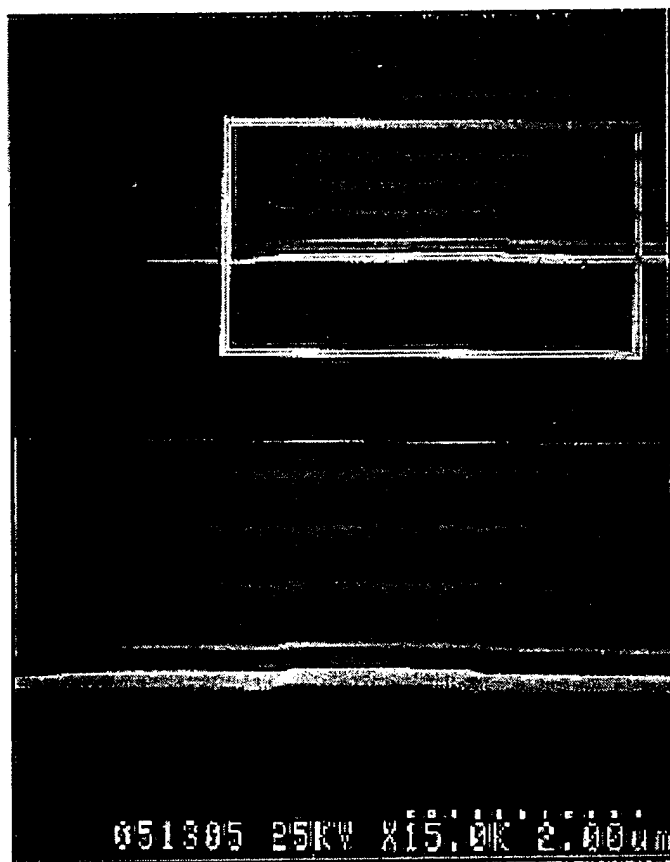
The first limit is determined by the ability of the support to absorb the pressure of the beam's weight slamming into the substrate. There has to be enough support area to distribute the pressure impulse without creating strains beyond the elastic limits of the materials.

The second constraint was hinted at above when we assumed that the sub-beam system does not collapse when the actuation mechanism pulls the whole beam assembly down to the substrate. In this case, the so-called "sub-beam system" is composed of that portion of the beam length supported by the contact points. For the GLV beam with a voltage actuation mechanism, the maximum separation between the supports is determined by insuring that switching voltage of the sub-system be larger than the maximum voltage applied to the GLV, normally around the switching voltage of the larger beam system. Using the Apte mechanical beam model [Apte, 1994], the maximum spacing between supports is about 5  $\mu\text{m}$  for a 25  $\mu\text{m}$ -long beam with 800 MPa of stress, and nitride and oxide spacer thicknesses of 132 nm.

The final constraint is more a practical issue: how small can the supports be made? This is determined by the process used to define these supports. It turned out that this was the more difficult portion of this work. The following sections discuss the GLV processes developed to define sub-micron contact points aligned to 1  $\mu\text{m}$ -wide beams.

### 4.5.3. Striations

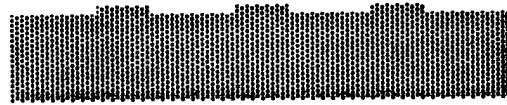
The first process technique employed was a modification of the bushing or stand-off bumps process suggested by Fan for micromachined motors [Howe, 1991; Fan, 1989]. However, since it is demanding to align sub-micron bumps on a  $1\text{ }\mu\text{m}$  wide-beam, we patterned the silicon substrate with  $1\text{ }\mu\text{m}$  wide striations spaced  $5\text{ }\mu\text{m}$  apart running perpendicular to the length of the GLV beams. Photo 4.5 is a two-part SEM photograph of a cross-section cut along the length of one GLV beam. The bottom part is a 2x close-up of the striation area. It shows striations which are  $200\text{ }\text{\AA}$  high,  $1\text{ }\mu\text{m}$ -wide and spaced  $5\text{ }\mu\text{m}$  apart. When the beams are pulled down by a voltage force they will contact the substrate only at the top of these striations.



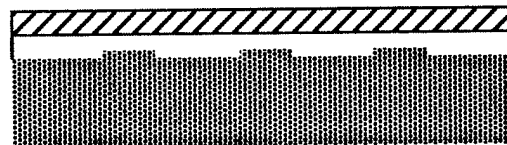
**Photo 4.5:** Two-part SEM photograph of a successful striated substrate. The bottom part is a 2x close-up of the striation area shown in the top section. Note that the GLV micro-beam is partially conformal to the striation in the silicon.

Figure 4.9 describes the fabrication process. It is identical to the basic GLV process described in section 4.1, with the addition of a silicon etch before the oxide is grown or deposited. The  $\langle 100 \rangle$  silicon wafer is first cleaned, photoresist is spun-on and patterned leaving resist over areas where the stripes are to be formed. The silicon wafer is then placed in a  $\text{CF}_4$  and  $\text{O}_2$  plasma silicon etch for about 15 seconds to remove about 20 nm. The resist is cleaned and the normal GLV process begins with a low-temperature oxide (LTO) deposition. Then we deposit silicon nitride and pattern the gratings in a dry nitride etch. Finally, the release etch is done in a 6:1 buffered oxide etch (BOE) for about 8 minutes; then, the wafer is dump-rinsed six times in water and finally spun-dry.

**1. Pattern silicon substrate.**



**2. Deposit oxide and nitride.**



**3. Pattern nitride and dry etch.**

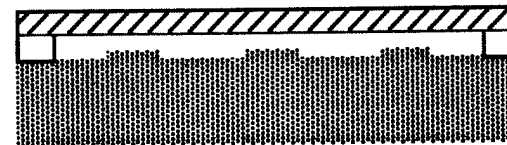


**Figure 4.9:** Process flow for the striated substrate technique.

A thermal oxidation step could still be used for the spacer layer instead of the LTO; however, it was noted that the silicon nitride beams formed using this process were partially conformal to the stripes. If the two surfaces are perfectly conformal then the process will only worsen the adhesion problem by providing a notch-fit for the beam. The use of LTO avoids this problem since it can be planarized.

A better solution to the conformality problem is to use a process that is more akin to the original dimple process, where the dimples are only on the bottom of the microstructure but not on the substrate. This is described in figure 4.10. The process variation starts with a thermally oxidized, flat wafer. At this point, the oxide is masked with resist everywhere except in the  $1\text{ }\mu\text{m}$  striation line areas and the oxide in these areas is etched 20 nm downwards. Thus, when the nitride is now conformally deposited it will have the dimples at its bottom.

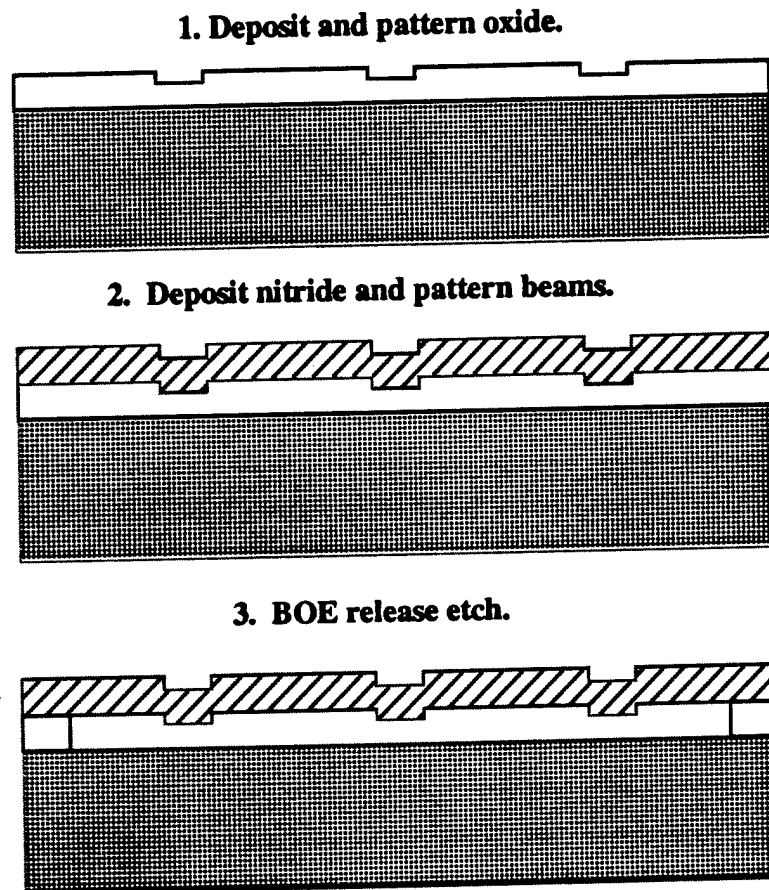


**Figure 4.10:** Process flow for the dimpled GLV beams.

The striation process is very simple to use and could easily further be optimized as described above. Using the first approach, we have been able to achieve an 80% reduction in contact area. The area reduction percentage was limited by the resolution of the lithographic process ( $1\text{ }\mu\text{m}$ ) and by the maximum length spacing between supports ( $5\text{ }\mu\text{m}$ ). Some disadvantages of this process are that it does not maintain an optically flat surface and

that the silicon etch has to be further improved to gain sub-5 nm control in a repeatable fashion.

#### 4.5.4. Self-aligned Side-wall Rails

As all the following processes, the self-aligned side-wall rail structures are a boon to GLV processing because it maintains optically flat surfaces and uses self-alignment techniques to micromachine truly nanometer-scale dimensions which are not dependent on photolithography.



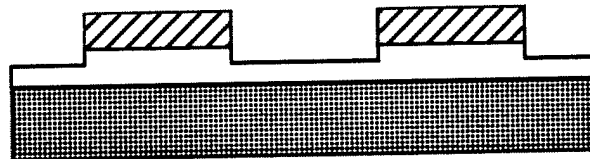
**Photo 4.6:** SEM of side-wall rails with sloped side-walls.

Photograph 4.6 is an SEM of the cross-section taken along the transverse direction of a GLV beam that is  $0.9\text{ }\mu\text{m}$ -wide. The photo is divided into two parts. The top slide shows a nitride beam sitting on top of an oxide layer that was partially etched away in hydrofluoric acid to enhance the contrast of the picture, but not fully etched away for support reasons. The two layers are on a silicon substrate. The bottom slide is a close-up of the left-edge of the nitride beam. Magnified by five times, the picture shows an inverted rail structure that spans the length of the beam edge. This rail is about 15 nm wide and extends about 20 nm below the bottom of the rest of the beam. Assuming that the beam does not sag towards

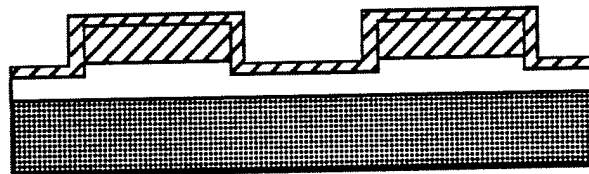
the center, the contact points will only be at the rails, thus reducing contact area by a percentage equal to the width of the rails over the width of the beam. In this particular case, it is on the order of 98 %.

The process for making side-wall rails is described in figure 4.11. It follows the basic GLV steps until the nitride etch step. For reasons that will be explained later, it is important that this nitride etch be anisotropic, giving very vertical side walls. We used a reactive ion etch with nitric fluoride,  $\text{NF}_3$ . The etch creates a protective polymer that protects the side-walls from etching. Finally, a BOE etch is done to release the beam. The etch is stopped at the oxide layer. Photoresist is stripped. The clean wafer is then placed in a dilute HF etch and precisely timed to etch the oxide to the level necessary for the desired rail. A second, conformal nitride layer is deposited, again in an LPCVD furnace. This second nitride layer is anisotropically etched with the same nitride etch process, removing only the vertically exposed nitride material.

1. Deposit oxide and nitride layers.
2. Dry etch nitride beams and part of oxide.



3. Deposit second side-wall nitride.



4. Anisotropic etch of side-wall nitride layer.
5. BOE release etch.

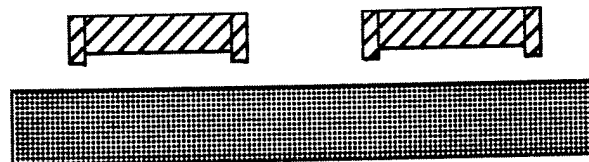
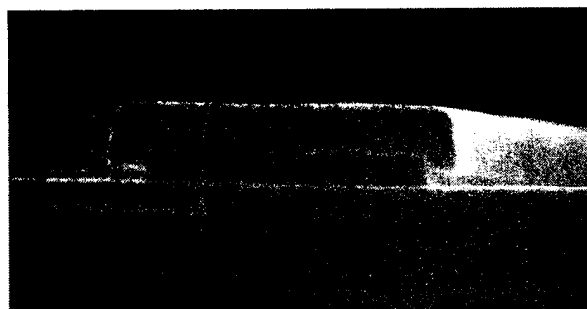


Figure 4.11: Process flow for the side-wall rails process.

It is obvious from figure 4.7, that this process requires very precise process control. For one, since the height of the beams are so important for good optical contrast, it is crucial to stop the second nitride etch at the desired thickness. Secondly, it would also be



desirable to gain control of the rail height. Ideally, the rail height will be equal to the downward oxide etch. However, since the side-wall has a finite slope to it, then the second nitride etch will actually start to etch away part of the side-wall that is exposed due to the sloped geometry. It is desirable to develop a process that will give better vertical side-walls. The wet isotropic oxide etch was used, for this reason. It undercuts the beam by a small amount, in a way creating a negative slope. Since the second nitride is conformal and will deposit also in the under-cut area, the wanted rail support structure is now protected by the beam material during the etch process. This provides better control of the rail height. Photograph 4.7 shows a rail supported beam with improved vertical side-walls and a rail height that was closer to its expected value.



**Photo 4.7:** SEM of side-wall rails with more vertical side-walls and more controllable rail heights. The width of the beam is 1  $\mu\text{m}$ .

Finally, it must be noted that if no insulator layer is placed between the beam metal and the substrate metal layers, then shorting occurs at the edges of the beams. Or, at the very least, dielectric breakdown is observed in the tiny air gap between these two metal layers. This problem is diminished by bad metal step coverage which is present if the side-walls are vertical or even negatively sloped.

In summary, the self-aligned side-wall rail process has succeeded in reducing contact area by at least 95 %. Because of this, we were able to operate GLV pixels with 100 MPa stress levels, giving switching voltages of 5 V for 25  $\mu\text{m}$ -long beams. This process however is difficult to control. Grating height tolerances will require the development of a stopping layer for the second nitride etch. Process development has to be done also for rail height control and for more vertical side-walls.

#### 4.5.5. Polysilicon T-Structures

The T-structure technique addresses the problem of shorting and height control. Photo 4.8 is an SEM of a T-structured grating beam. The T is composed of two different materials: the 1  $\mu\text{m}$ -wide horizontal portion is an 80 nm thick nitride layer, and the base of the T is a polysilicon layer, 50 nm thick and about 0.15  $\mu\text{m}$  wide. This polysilicon support structure runs the whole length of the beam and will be the contact point between the beam and the substrate. This T-structure approach also provides an additional isolation air gap between the beam metal and the substrate electrode to prevent arcing problems at high-voltage operation.



**Photo 4.8:** Cross-section SEM of polysilicon T-structures. The T is composed of two different materials: the 1  $\mu\text{m}$ -wide horizontal portion is an 80 nm thick nitride layer, and the base of the T is a polysilicon layer, 50 nm thick and about 0.15  $\mu\text{m}$  wide.

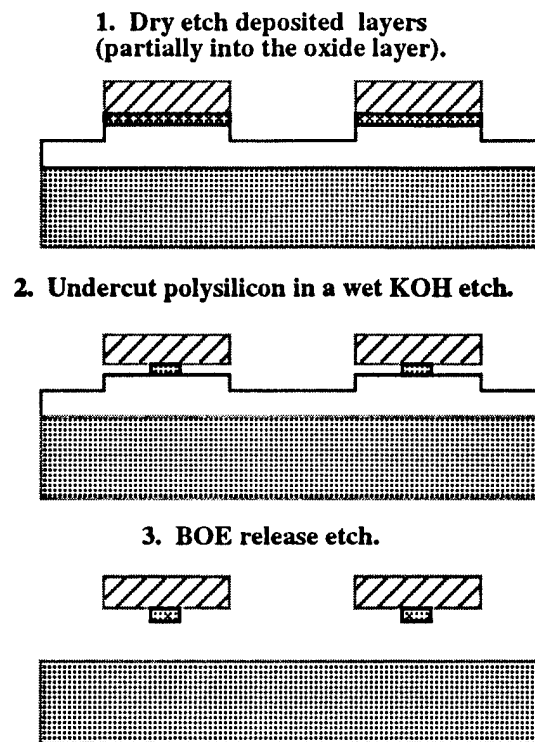


**Figure 4.12:** Process flow for fabricating polysilicon T-structure GLV beams (vertical dimensions exaggerated).

The fabrication of the T-structures starts off by growing a 132 nm thermal oxide. This is followed by the deposition of the silicon and silicon nitride layers. The targeted combined thickness of these two layers is also 132 nm. The silicon layer is normally deposited amorphous to get a smoother surface and annealed to lower the compressive stress [Guckel, 1988]. This anneal step will also roughen the layer to some extent [Ibok, 1993]. After film deposition, the nitride is RIE patterned to form the gratings. Another plasma etch is used to continue the grating patterning into the polysilicon layer. Then the photoresist is stripped. At this point, the oxide can be partially etched (Figure 4.12a) to prepare for the next step which is an isotropic KOH etch. This wet etch attacks the polysilicon in a side-ways fashion narrowing the base of our T-structure according to the etch time (Figure 4.12b). After the polysilicon etch, the beams are ready to be released and covered with evaporated aluminum (Figure 4.12c).

Since the KOH etch reduces the width of the polysilicon layer equally for all beam widths, the percentage reduction in contact area will vary for beams of varying widths. For 1  $\mu\text{m}$ -wide beams, variations in KOH etch times have yielded base supports ranging in

widths anywhere from 0.8  $\mu\text{m}$  to less than 0.1  $\mu\text{m}$ . Yield displacement lengths ranged from 17  $\mu\text{m}$  to greater than 65  $\mu\text{m}$ . The etch rate for annealed polysilicon was about 0.1  $\mu\text{m}/\text{min}$  in 45% KOH solution at 50°C.

The polysilicon T-structure support process is a good technique to reduce contact areas by more than 90 % with adequate process control of grating heights. As the side-wall rails process, it uses self-aligned processes to create sub-micron geometries without requiring an extra masking step. The problem encountered with this process is that if the bases are made narrow enough and there is sufficient torque applied to any side of the beam, the T-structure can tilt to one side (see photo 4.9). If this occurs when a voltage force is applied, then this contact at the edges can also lead to shorting and device failure.

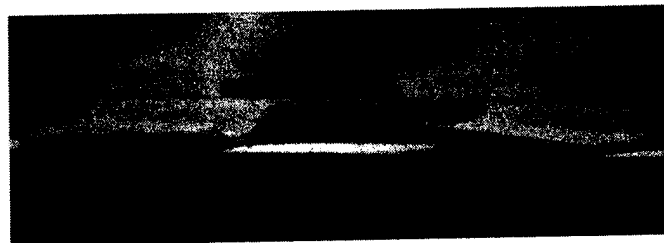


**Photo 4.9:** SEM of a transverse cross-section of two GLV beams fabricated using the T-process. The disadvantage of the T-structure process is that beams can tilt and shorting will occur if no insulating dielectric protects the substrate electrode.

#### 4.5.6. Staggered Polysilicon Supports

Since the self-aligned process used for the polysilicon T-structures proved very successful for stiction but suffered from tilting and shorting, we derived a new process based on the idea of the self-aligned sideways KOH polysilicon etch. Figure 4.13 is a cartoon that explains how the staggered polysilicon supports work. It is a ground view looking up at the bottom of the grating beams. For illustrative purposes the other support end of the beams and the silicon substrate have been cut from the picture. The beams in this case look like diving boards that have support structures protruding from underneath them. These supports are close to the edges and are positioned alternately on the left and the right. This provides support on both edges of the beam and prevents tilting.

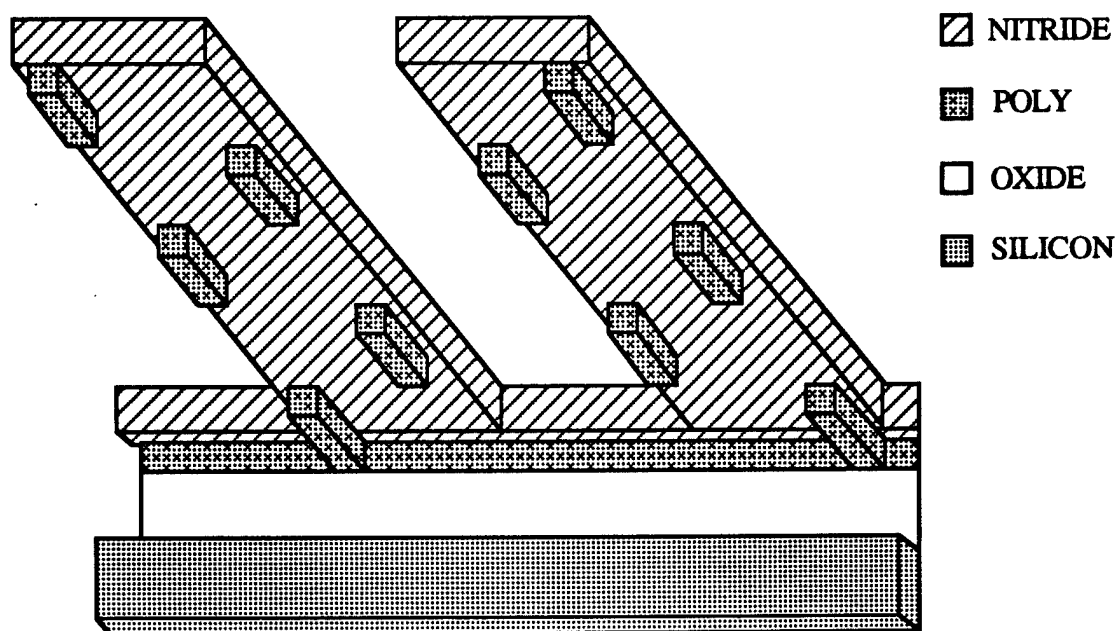
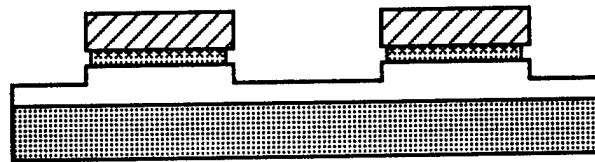


**Figure 4.13:** Ground view of the bottom of grating beams that have staggered polysilicon support structures at the edges of both sides of the beams.

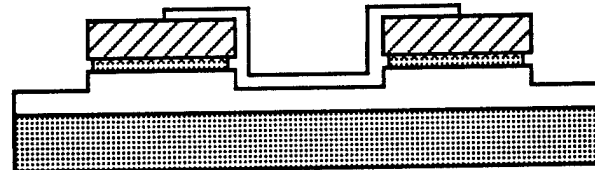
The process for the staggered polysilicon support structures is explained in figure 4.14. The process is identical to the T-structure process until the first KOH etch where the middle layer of polysilicon is etched only for one minute in 50°C KOH to undercut the nitride layer by about 0.1  $\mu\text{m}$  on both sides. The cross-section of the beam at this point will look like the top picture in figure 4.14. This break in the step minimizes the shorting of the aluminum layers evaporated later on. After this first polysilicon etch, a 50 nm low temperature silicon oxide (LTO) layer is deposited in an LPCVD furnace. This oxide layer

is photolithographically masked and etched in a 6:1 buffered oxide etch for 15 seconds to define a mask for the second KOH etch (see second cross-section in figure 4.14). Photograph 4.10 illustrates how from a top-view this mask produces a checkerboard pattern. The darker rectangles in the pattern are via holes in the oxide mask and will only allow the KOH to attack the polysilicon from alternating sides at different length segments along the beam. This second KOH etch is done in identical conditions as the first, however, the timing is based on the goal of leaving behind a few tenths of a micron of the polysilicon to act as a support structure for the beam when it comes into contact with the substrate. Finally, the whole wafer is placed in 6:1 BOE for about 6 minutes to remove the LTO mask and to release the GLV beams.

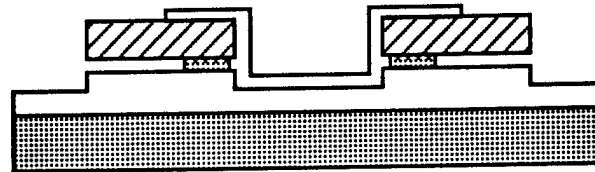
1. Pattern gratings, etching deposited layers.
2. KOH partial undercut of poly layer.



3. Deposit and pattern checkerboard oxide mask.



4. KOH undercut etch from selected sides.



5. BOE release.

**Figure 4.14:** Process flow for fabricating staggered polysilicon supports under GLV beams.

This process was tested on three different 4-inch <100> wafers with identical steps except for the second KOH etch where three wafers were etched for 5, 6, and 7 minutes, respectively. The thermal oxide was 133 nm. The polysilicon layer was about 50 nm, while the nitride thickness was 83 nm. On each wafer, we formed harp structures with

beam widths ranging from  $1.0\text{ }\mu\text{m}$  to  $1.75\text{ }\mu\text{m}$  in steps of  $0.25\text{ }\mu\text{m}$ . The polysilicon supports were staggered along the beam length at different periodicities. The checkerboard mask had boxes with varying lengths, from  $2\text{ }\mu\text{m}$  to  $5\text{ }\mu\text{m}$ . The beams were released in BOE, dump-rinsed in deionized water for six cycles, and spun-dried. Details of this process are included in appendix A.



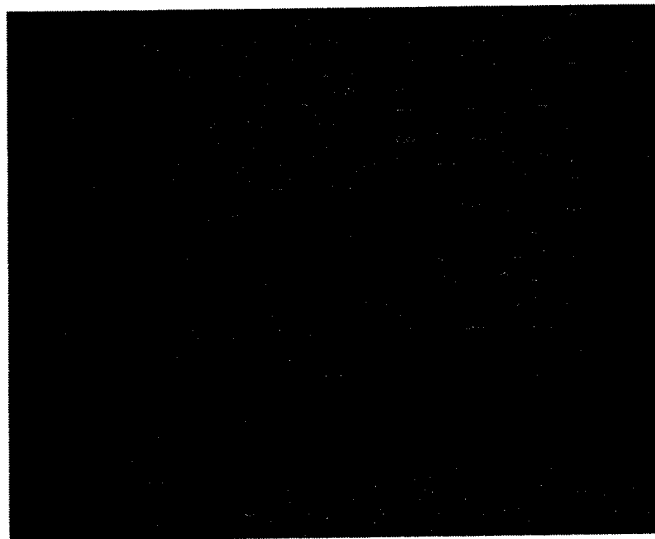
**Photo 4.10:** Optical microphotograph of a harp test structure with a checkerboard oxide mask pattern for the formation of staggered silicon supports in a KOH etch. The white portion is nitride over oxide covered with the oxide mask. The darker portions of the nitride correspond to areas where the oxide mask was removed to provide via etch holes for the KOH. The top-tick mark indicates the  $10\text{ }\mu\text{m}$  long beam.

Undercut length (in $\mu\text{m}$ )	Control all masked no KOH	T- structure unmasked	Staggered Supports columns arranged according to periodicity of supports			
			$10\text{ }\mu\text{m}$	$8\text{ }\mu\text{m}$	$6\text{ }\mu\text{m}$	$4\text{ }\mu\text{m}$
	covered	open				
0.35	15	65	20.5	20.5	22	23.5
0.62	16	22	31	25.5	24	28
0.85	16	20	62.5	48.5	37.5	32.5

**Table 4.2:** Beam displacement lengths (in  $\mu\text{m}$ ) as a function of the periodicity of the staggered support structures and of the KOH undercut etch length. All the beam widths in this case are  $1.25\text{ }\mu\text{m}$ . The difference in yields is due to two factors, the isotropic sideways etching of the KOH and the fact that if the supports are too far apart the beam sub-system tends to collapse.

Table 4.2 shows the displacement lengths taken from the inspection of the harp structures. It only includes data from the harp structures with  $1.25\text{ }\mu\text{m}$ -wide beams. Similar results were observed for beams of other widths, with the differences being determined by how much the polysilicon undercut etch reduced the contact area (see figure 4.16). The trends of this plot are illustrated in figure 4.15, where the undercut length of the polysilicon was converted into the area of contact provided by the silicon supports. It is clear that the displacement length increases as the contact area is reduced. Contact area

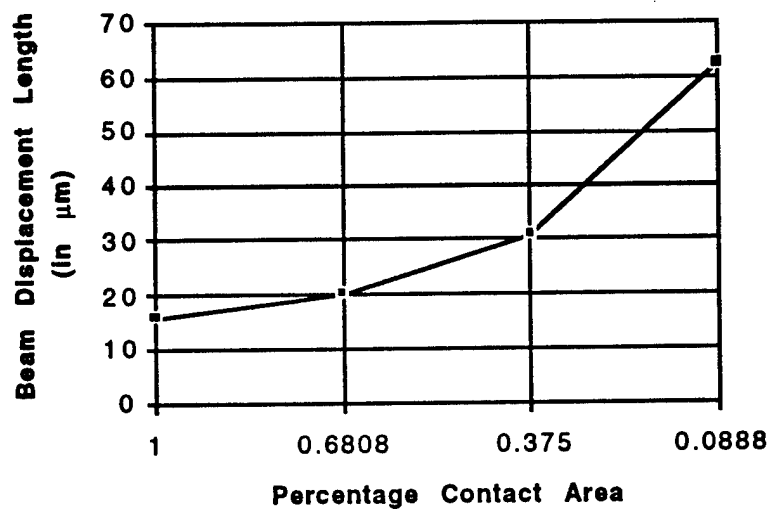
reduction serves the same function as reducing the adhesion energy per unit area of contact. Figure 4.15 has the exact same behavior as theoretically predicted in figure 4.8. A percentage value of 1.00 corresponds to the control case where the silicon underlayer is not patterned, while, a value of 0.089 corresponds to a beam where 91 % of the silicon layer beam was removed such that only 8.9 % percent of it will touch the substrate when it collapses. The staggered support structures were able to reduce area of surface contact to less than 5 % of the beam area and yielded displacement lengths beyond the limit of existing harp test structures (greater than 70  $\mu\text{m}$ ). These were successfully operated in the contact mode.



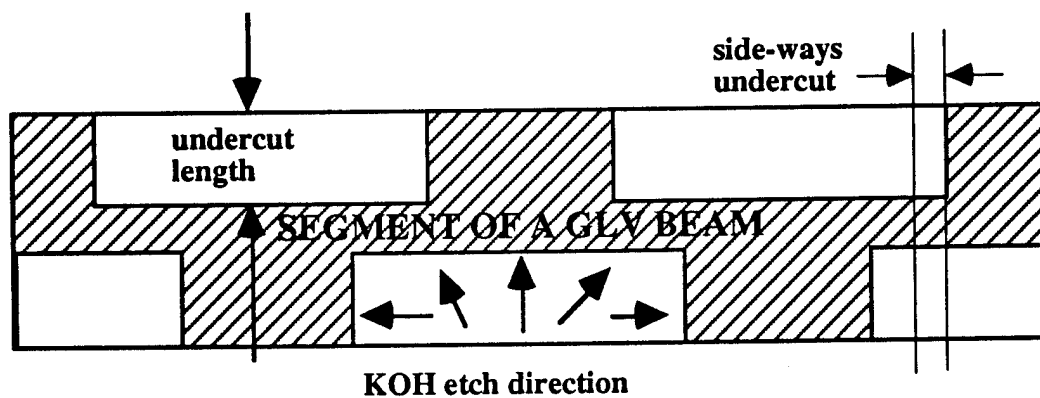
**Photo 4.11:** Optical microphotograph of harp structures showing the effectiveness of this process. Note that the color differences due to optical interference effects shows the process engineer where the polysilicon is still present under the beam.

Figure 4.16 illustrates why there is a difference between harps with staggered supports at different periodic spacings. As the side-ways etch reduces not only the width but also the length of the support, the overhang portion of the beam gets longer and forms another collapsible cantilever beam sub-system. This sub-system will tend to collapse and lead to stiction if the spacing between supports gets too large, which is the case in the finer periodic supports because of the geometry formed by the etch process.





**Figure 4.15:** Beam displacement length (in  $\mu\text{m}$ ) for  $1.25\ \mu\text{m}$  wide beams as a function of percentage contact area of the polysilicon staggered supports.



**Figure 4.16:** A segment of a GLV beam. Illustration of the KOH undercut etch process.

## 4.6. Summary and Conclusion

This chapter has reviewed the problem of stiction in MEMS devices. It has identified and modeled various adhesion mechanisms. Like many other MEMS devices, the GLV suffers from hydrogen bonding through liquid bridging and hydroxyl groups. Packaging devices in a dry environment will be important to lower the adhesion energy level from the liquid bridging case to the exclusively -OH-based hydrogen bonding case.

The fundamental physical limits to the adhesion problem were determined and for severe stiction problems, as found in the GLV device, engineering solutions are necessary. To lower the effect of the basic adhesion force one can resort to microscopic surface roughening, as with a LPCVD silicon roughening layer. With the optical constraint of a maximum rms roughness of 5 nm, this method was able to reduce the adhesion energy per unit area by at least 5 times the normal value. Adhesion energies of 10-20 mJ/m<sup>2</sup> were measured for roughened beams.

Further anti-stiction help is provided by macroscopic surface patterning to provide discrete contact points between two surfaces. Table 4.3 summarizes the results of the various engineering approaches to the stiction problem. The goal was to integrate into the GLV fabrication process a method for the formation of stand-off supports that could reduce the area of contact, avoid shorting, and maintain smooth, optically flat top surfaces.

Process Technique	Mask Steps	Self-Aligned?	Area Reduction	Problems?
Striations	2	No	20 %	Not Flat
Side-Wall Rails	1	Yes	> 90 %	Height Control
T-Structures	1	Yes	> 90 %	Tilting, Shorting
Staggered Si	2	Yes	> 90 %	NONE

**Table 4.3:** Summary of the engineering approaches to reducing area of surface contact between two contacting, optically-flat surfaces.

Other techniques can be useful for MEMS devices, but suffer particular disadvantages that make them incompatible for GLV use. Striations requires an additional masking step, is not self-aligned, provides a limited capacity to reduce contact area, and is not optically flat. Side-wall rails are attractive since they can provide very minimal contact area (demonstrated 98 % reduction); they are self-aligned and maintain optical flatness. The drawbacks of this process are that it is hard to control rail dimensions and grating heights; furthermore, it suffers a shorting problem. The T-structure process is almost ideal in that it

is a self-aligned, one-mask procedure that can provide more than 90 % reduction in surface contact area while still maintaining optical flatness and grating height control. In addition to this, the T-structure process allows the use of a roughening polysilicon layer for the contact areas. Its only problems are tilting and shorting.

The best method of engineering around the adhesion problem is the silicon staggered support structure technique. It has all the advantages of the T-structures, and by adding a non-critical masking step it avoids the tilting and shorting problem. This is the recommended approach to GLV fabrication. In the final integrated GLV process, an insulating layer will be included between the beam and the substrate to prevent shorting as they come in contact, and this might later make the T-structure process more competitive.

Obviously, the above process development only addresses a part of the total GLV integration problem. Further work is required to incorporate the staggered support structures with a full GLV process that includes two dimensional addressing and hermetic packaging. The main contribution of this work has been to demonstrate the success of the engineering approach to the stiction problem, i.e. microscopic roughening and macroscopic surface patterning. And in the general interest of MEMS research, three novel techniques have been developed to form true nano-scale stand-off structures self-aligned underneath 1  $\mu\text{m}$  wide beams whose top surfaces are kept optically flat.

## Chapter 5

# Conclusion and Future Work

The GLV research and development project at Stanford has been a very successful in many regards. Moving through the invention, engineering, manufacturing, and testing stages, the effort has brought together experience from multiple disciplines: optics, semiconductor process and device physics, mechanical engineering, surface chemistry, and even technology management. The success of the Grating Light Valve as a device is demonstrated by the commercial interest in this MEMS technology for fiber-telemetry, printer, and display applications. Before the publication of this document, at least three companies had licensed the GLV patent from the Office of Technology Licensing of Stanford University.

Certainly, bringing the GLV to market will involve much more beyond this thesis work. The emphasis of this work was in inventing and proving the commercial feasibility of the device. New issues now come to the fore.

Indeed, certain refinements can still be made to the electromechanical and optical models of the grating. And, it would be very interesting to build actual gratings that verify these models as they predict effects due to, for example, shadowing, non-scalar diffraction, duty-cycle errors, surface roughening, and the limited “aperture” or active area of a GLV pixel. However, the most significant issues facing GLV developers have to do with manufacturing: process integration, packaging, uniformity, repeatability, reliability, yields, failure analysis, and lifetime.

Upon the selection of the GLV application of interest, a completely integrated manufacturing process will have to be well designed to incorporate electrical isolation, addressing drive-circuitry (most probably 2-dimensional), anti-stiction mechanisms, and a hermetically sealed package.

The desire to integrate the drive circuitry with the GLV device makes it more attractive to consider GLV processes re-designed around low-temperature materials. As in most MEMS systems, the mechanical properties of the chosen ultra-thin film materials have to be better investigated. For each new type of film used, the Young's modulus, hardness, density, stress, dielectric strength, permittivity, yield strain, life-time, and even pin-hole density have to be experimentally measured.

Stiction is also still an important concern. In the effort to demonstrate the feasibility of the GLV technology, we have developed novel engineering solutions to the stiction problem. These particular solutions may not be directly transferable into a fully integrated GLV system; nevertheless, this work has shown the strength of the engineering approach to the adhesion problem: use surface roughening and self-aligned patterning to circumvent the fundamental limits of the adhesion forces. Moreover, the air damping and stiction problems emphasize the importance of hermetic packaging and sealing of the GLV devices.

Next, the complete manufacturing process and the actual devices will have to be tested for uniformity and repeatability, especially since these affect the GLV electromechanical behavior (e.g. switching voltages and hysteretic behavior), which, in turn, provides important specifications for the driver circuit designers. Finally, the whole process will have to be tested for reliability and life-time. Failure analysis may show strain fracture in the GLV beams, leakage in the package, or stiction, among other things.

Much work has still to be carried out before the GLV is seen in a commercial product. However, the felicitous note on which this thesis ends is the fact that there are companies and people in the semiconductor industry actually pouring time, experience, and finances into this follow-up work which will possibly take the GLV from the academic realm into the real world.

## Bibliography

- [Alley, 1992] R.L. Alley, G.J. Cuan, R.T. Howe and K. Komvopoulos, "The Effect of Release-Etch Processing on Surface Stiction," *Proceedings IEEE Solid-State Sensor and Actuator Workshop*, Hilton Head, South Carolina, U.S.A., June 21-25, 1992, pp. 202-207.
- [Alley, 1993] R.L. Alley, P. Mai, K. Komvopoulos, and R.T. Howe, "Surface Roughness Modification of Interfacial Contacts in Polysilicon Microstructures," *Technical Digest of The 7th International Conference on Solid-State Sensors and Actuators (Transducers '93)*, Yokohama, Japan, June 7-10, 1993, pp. 288-291.
- [Apte, 1993] R.B. Apte, F.S.A. Sandejas, W.C. Banyai, and D.M. Bloom, "Deformable Grating Light Valves for High Resolution Displays," *Digest of Technical Papers of the Society for Information Displays International Symposium*, Seattle, WA, May 18-21, 1993, pp. 807-808.
- [Apte, 1994a] R.B. Apte, F.S.A. Sandejas, W.C. Banyai, D.M. Bloom, "Deformable Grating Light Valves for High Resolution Displays", *Proceedings IEEE Solid-State Sensor and Actuator Workshop*, Hilton Head, South Carolina, U.S.A., June 13-16, 1994, pp. 1-6.
- [Apte, 1994b] R.B. Apte, "Grating Light Valves for High Resolution Displays," Ph.D. Dissertation, Stanford University, 1994.
- [Backlund, 1992a] Y. Backlund, K. Hermansson, and L. Smith, "Bond Strength Measurements Related to Silicon Surface Hydrophilicity," *Journal of the Electromechanical Society*, Vol. 139, No. 8 (1992), pp. 2299-2301.
- [Backlund, 1992b] Y. Backlund, K. Ljungberg, and A. Soderbarg, "A suggested mechanism for silicon direct bonding from studying hydrophilic and hydrophobic surfaces," *Journal of Micromechanics and Microengineering*, 2 (1992), pp. 158-160.

- [Beck, 1990] P.A. Beck, S.M. Taylor, J.P. McVittie, and S.T. Ahn, "Low Stress Silicon Nitride and Polysilicon Films for Micromachining Applications," *Proceedings of the Materials Research Symposium*, Vol. 182, pp. 207-212, 1990.
- [Benecke, 1991] W. Benecke, "Silicon Microactuators: Actuation Mechanisms and Scaling Problems," *Technical Digest of the 6th International Conference on Solid-State Sensors and Actuators (Transducers '91)*, San Francisco, California, U.S.A., June 24-27, 1991, pp. 46-50.
- [Bloom, 1994] D.M. Bloom, F.S.A. Sandejas, O. Solgaard, "Method and Apparatus for Modulating a Light Beam," *United States Patent*, No. 5,311,360, May 10, 1994.
- [Born, 1989] M. Born and E. Wolf, *Principles of Optics*, Sixth Edition, Pergamon Press, Oxford, pp. 401-406, 1989.
- [Bower, 1993] R. Bower, M.S. Ismail, B.E. Roberds, "Low Temperature Si<sub>3</sub>N<sub>4</sub> direct bonding," *Applied Physics Letters*, Vol. 62, No. 26 (1993), pp. 3485-3487.
- [Bowling, 1985] R. A. Bowling, "An Analysis of Particle Adhesion on Semiconductor Surfaces," *Journal Electrochemical Society on Solid-State Science and Technology*, Vol. 132, No. 9 (1985), pp. 2208-2214.
- [Deng, 1992a] K. Deng and W.H. Ko, "A study of static friction between silicon and silicon compounds," *Journal of Micromechanics and Microengineering*, 2 (1992), pp. 14-20.
- [Deng, 1992b] K. Deng and W.H. Ko, "Static friction of diamond-like carbon films in MEMS," *Sensors and Actuators A*, 35 (1992), pp.45-50.
- [DePalma, 1989] V. DePalma and N. Tillman, "Friction and Wear of Self-Assembled Trichlorosilane Monolayer Films on Silicon," *Langmuir*, 5 (1989), pp. 868-872.
- [English, 1994] G.R. English, "Measuring the Young's Modulus of Silicon Nitride," Personal Communication, May 1994.
- [Findler, 1992] G. Findler, J. Muchow, M. Koch, and H. Munzel, "Temporal Evolution of Silicon Surface Roughness During Anisotropic Etching Processes," *Proceedings IEEE Micro Electro Mechanical Systems*, Trarumunde, Germany, February 4-7, 1992, pp. 62-66.
- [Gerhard-Multhaupt, 1990] R. Gerhard-Multhaupt, W. Brinker, H.-J. Ehrke, W.-D. Molzow, H. Roeder, T. Rosin, and R. Tepe, "Viscoelastic Spatial Light Modulators and Schieleren-Optical Systems for HDTV Projection Displays," *Proceedings of the SPIE Conference on Large-Screen Projection Displays II*, Vol. 1255 (1990), pp.69-78.
- [Grunder, 1986] M. Grunder and H. Jacob, "Investigations on Hydrophilic and Hydrophobic Silicon (100) Wafer Surfaces by X-Ray Photoelectron and High-Resolution Electron Energy Loss-Spectroscopy," *Applied Physics A*, Vol. 39 (1986), pp. 73-82.

- [Guckel, 1988] H. Guckel, D.W. Burns, C.C.G. Visser, H.A.C. Tilmans and D. Deroo, "Fine-Grained Polysilicon Films with Built-In Tensile Strain," *IEEE Transactions on Electron Devices*, Vol. 35, No.6 (1988), pp. 800-801.
- [Guckel, 1989] H. Guckel, J.J. Sniegowski, T.R. Christenson, S. Mohny, and T.F. Kelly, "Fabrication of Microelectromechanical Devices from Polysilicon Films with Smooth Surfaces," *Sensors and Actuators*, A20 (1989), pp. 117-122.
- [Guckel, 1990] H. Guckel, J.J. Sniegowski, T.R. Christenson, and F. Raissi, "The Application of Fine-grained, Tensile Polysilicon to Mechanically Resonant Transducers," *Sensors and Actuators*, A21-A23 (1990), pp. 346-351.
- [Haller, 1993] M. Haller, "HF Roughening of Silicon Surfaces to Prevent Stiction," Personal Communication, October 31, 1993.
- [Haisma, 1989] J. Haisma, G.A.C.M. Spierings, U.K.P. Biermann, and J.A. Pals, "Silicon-on-Insulator Wafer Bonding-Wafer Thinning Technological Evaluations," *Japanese Journal of Applied Physics*, Vol. 28, No. 8 (1989), pp. 1426-1443.
- [Hartog, 1961] J.P.D. Hartog, *Strength of Materials*, Dover, New York, 1961.
- [Hemenway, 1990] B.R. Hemenway, "Integrated Silicon Light Modulator for Fiber-Optic Interconnects at 1.3 micron Wavelength," Ph.D. Dissertation, Stanford University, May 1990.
- [Hermansson, 1991] K. Hermansson, U. Lindberg, B. Hok, and G. Palmkog, "Wetting Properties of Silicon Surfaces," *Technical Digest of the 6th International Conference on Solid-State Sensors and Actuators (Transducers '91)*, San Francisco, California, U.S.A., June 24-27, 1991, pp. 193-196.
- [Ho, 1990] S.T. Ho, S.L. McCall, R.E. Slusher, L.N. Pfeiffer, and K.W. West, "High index contrast mirrors for optical microcavities," *Applied Physics Letters*, Vol. 57, No. 14 (1990), pp. 1387-1389.
- [Hornbeck, 1991a] L.J. Hornbeck, "Spatial Light Modulator and Method," *United States Patent*, Number 5,061,049. Issued: October 29, 1991.
- [Hornbeck, 1991b] L.J. Hornbeck and W.E. Nelson, "Spatial Light Modulator System," *United States Patent*, Number 5,028,939. Issued: July 2, 1991.
- [Howe, 1987] R.T. Howe, "Resonant Microsensors," *Technical Digest of the 4th International Conference on Solid-State Sensors and Actuators (Transducers '87)*, Tokyo, Japan, 1987, pp. 843-848.
- [Howe, 1991] R.T. Howe, "Dimple Structures to Prevent Stiction," Personal Communication, February 1991.



- [Ibok, 1993] E. Ibok and S. Garg, "A Characterization of the Effect of Deposition Temperature on Polysilicon Properties," *Journal of the Electrochemical Society*, Vol. 140, No. 10 (1993), pp.2927-2937.
- [Israelachvili, 1972a] J.N. Israelachvili and D. Tabor, "The measurement of van der Waals dispersion forces in the range 1.5 to 130 nm," *Proceedings of the Royal Society of London A*, 331 (1972), pp. 19-38.
- [Israelachvili,1972b] J.N. Israelachvili, "The calculation of van der Waals dispersion forces between macroscopic bodies," *Proceedings of the Royal Society of London A*, 331 (1972), pp. 39-55.
- [Israelachvili,1992] J.N. Israelachvili, *Intermolecular and Surface Forces, 2nd Edition*, Academic Press Limited, London, UK, 1992.
- [Jerman, 1991] J.H. Jerman, D.J. Clift, "Miniature Fabry-Perot Interferometer Micromachined in Silicon for use in Optical Fiber WDM Systems," *Technical Digest of the 6th International Conference on Solid-State Sensors and Actuators (Transducers '91)*, San Francisco, California, U.S.A., June 24-27, 1991, pp. 372-375.
- [Kendall, 1971] K. Kendall, "The Adhesion and Surface Energy of Elastic Solids," *Journal of Physics D: Applied Physics*, Vol. 4 (1971), pp. 1186-1195.
- [Legtenberg, 1993] R. Legtenberg, J. Elders, and M. Elwenspoek, "Stiction of Surface Micromachined Structures After Rinsing and Drying: Model and Investigation of Adhesion Mechanisms," *Technical Digest of The 7th International Conference on Solid-State Sensors and Actuators (Transducers '93)*, Yokohama, Japan, June 7-10, 1993, pp. 198-201.
- [Linford, 1993] M.R. Linford and C.E.D. Chidsey, "Alkyl Monolayers Covalently Bonded to Silicon Surfaces," *Journal of the American Chemical Society*, Vol. 115, No. 26 (1993), pp. 12631-12632.
- [Lober, 1988] T.A. Lober and R.T. Howe, "Surface Micromachining Processes for Electrostatic Microactuator Fabrication," *Technical Digest of the 1988 Solid-State Sensor and Actuator Workshop*, Hilton Head Island, South Carolina, USA, June 6-9, 1988, pp. 59-62.
- [Mastrangelo, 1992] C. H. Mastrangelo and C.H. Hsu, "A Simple Experimental Technique for the Measurement of the Work of Adhesion of Microstructures," *Proceedings IEEE Solid-State Sensor and Actuator Workshop*, Hilton Head, South Carolina, U.S.A., June 21-25, 1992, pp. 208-212.
- [Mastrangelo, 1993a] C.H. Mastrangelo and C.H. Hsu, "Mechanical Stability and Adhesion of Microstructures Under Capillary Forces - Part I: Basic Theory," *Journal of Microelectromechanical Systems*, Vol. 2, No. 1 (1993), pp. 33-43.
- [Mastrangelo, 1993b] C.H. Mastrangelo and C.H. Hsu, "Mechanical Stability and Adhesion of Microstructures Under Capillary Forces - Part II: Experiments," *Journal of Microelectromechanical Systems*, Vol. 2, No. 1 (1993), pp. 44-55.

- [Mullhern, 1993] G.T. Mullhern, D.S. Soane, and R.T. Howe, "Supercritical Carbon Dioxide Drying of Microstructures," *Technical Digest of The 7th International Conference on Solid-State Sensors and Actuators (Transducers '93)*, Yokohama, Japan, June 7-10, 1993, pp. 296-299.
- [Orpana, 1991] M. Orpana and A.O. Korhonen, "Control of Residual Stress of Polysilicon Thin Films by Heavy Doping in Surface Micromachining," *Technical Digest of the 6th International Conference on Solid-State Sensors and Actuators (Transducers '91)*, San Francisco, California, U.S.A., June 24-27, 1991, pp. 957-960.
- [Petersen, 1982] K.E. Petersen, "Silicon as a Mechanical Material," *Proceedings of the IEEE*. Vol. 70, No. 5 (1982), pp. 420-457.
- [Raman, 1991] V. Raman, W.T. Tang, D. Jen, T.R. Reith, "The dependence of stiction and friction on roughness in thin-film magnetic recording disks," *Journal of Applied Physics*, Vol. 70, No. 3 (1991), pp.1826-1836.
- [Sampsell, 1993] J.B. Sampsell, "The Digital Micromirror Device and Its Application to Projection Displays," *Technical Digest of The 7th International Conference on Solid-State Sensors and Actuators (Transducers '93)*, Yokohama, Japan, June 7-10, 1993, pp. 24-27.
- [Sandejas, 1992] F.S.A. Sandejas, O. Solgaard, D.M. Bloom, "Deformable Grating Optical Modulator," in the Conference on Lasers and Electro-Optics CLEO '92; May, 1992; Anaheim, CA.
- [Sandejas, 1993] F.S.A. Sandejas, R.B. Apte, W.C. Banyai, D.M. Bloom, "Surface Microfabrication of Deformable Grating Light Valves for High Resolution Displays," *Abstracts of Late News Papers of the 7th International Conference on Solid-State Sensors and Actuators (Transducers '93)*, , pp. 6-7, Yokohama, Japan, June 7-10, 1993.
- [Scheeper, 1992] P.R. Scheeper, J.A. Voorthuyzen, W. Olthius and P. Bergveld, "Investigation of attractive forces between PECVD silicon nitride microstructures and an oxidized silicon substrate," *Sensors and Actuators A*, 30 (1992), pp. 231-239.
- [Schmidt, 1994] M. A. Schmidt , "Silicon Wafer Bonding for Micromechanical Devices," *Technical Digest of the Solid-State Sensor and Actuator Workshop*, Hilton Head Islabd, South Carolina, USA, June 13-16, 1994, pp.127-131.
- [Shimbo, 1986] M. Shimbo, K. Furukawa, K. Fukuda, and K. Tanzawa, "Silicon-to-silicon direct bonding method," *Journal of Applied Physics*, Vol. 60, No. 8 (1986), pp. 2987-2989.
- [Solgaard, 1992a] O. Solgaard, "Integrated Semiconductor Light Modulators for Fiber-Optic and Display Applications," Ph.D. Dissertation, Stanford University, 1992.
- [Solgaard, 1992b] O. Solgaard, F.S.A. Sandejas, and D.M. Bloom, "A Deformable Grating Optical Modulator," *Optics Letters*, Vol. 17, No. 9 (1992), p. 688.

- [Staker, 1995] B. Staker, "GLV Contrast Simulation," Personal Communication, April 14, 1995.
- [Stengl, 1989] R. Stengl, T. Tan, and U. Goselle, "A Model for the Silicon Wafer Bonding Process," *Japanese Journal of Applied Physics*, Vol. 28, No. 10, (1989), pp. 1735-1741.
- [Sze, 1988] S.M. Sze, *VLSI Technology, 2nd Edition*, McGraw-Hill Book Company, New York, 1988.
- [Tian, 1993] H. Tian and T. Matsudaira, "The Role of Relative Humidity, Surface Roughness and Liquid Build-Up on Static Friction Behavior of the Head/Disk Interface," *ASME Journal of Tribology*, Vol. 115, January 1993, pp. 28-35.
- [Tillman, 1988] N. Tillman, A. Ulman, J.S. Schildkraut, and T.L. Penner, "Incorporation of Phenoxyl Groups in Self-Assembled Monolayers of Trichlorosilane Derivatives: Effects on Film Thickness, Wettability, and Molecular Orientation," *Journal of the American Chemical Society*, 110 (1988), pp. 6136-6144.
- [Torii, 1993] A. Torii, M. Sasaki, K. Hane, and S. Okuma, "Adhesive Force of the Microstructures Measured by the Atomic Force Microscope," *Proceedings IEEE Micro Electro Mechanical Systems*, Fort Lauderdale, FL, U.S.A., 7-10 Feb., 1993, pp. 111-116.
- [Vlassak, 1992] J.J. Vlassak and W.D. Nix, "A new bulge test technique for the determination of Young's modulus and Poisson's ratio of thin films," *Journal of Materials Research*, Vol.7, No.12 (1992), pp. 3242-3249.
- [Watanabe, 1989] M. Watanabe, M. Hamano, and M. Harazano, "The Role of Atmospheric Oxygen and Water in the Generation of Water Marks on the Silicon Surface in Cleaning Processes," *Materials Science and Engineering*, B4 (1989), pp. 401-405.
- [Weisenhorn, 1992] A.L. Weisenhorn, P. Maivald, H.J. Butt, and P.K. Hansma, "Measuring adhesion, attraction, and repulsion between surfaces in liquids with and atomic-force microscope," *Physical Review B*, Vol. 45, No. 19 (1992), pp.11226-11232.

## Appendix A

### Definition of Terms

$A$  = Area = area =  $wl$  for a beam  
 $A$  = short-range Hamaker constant  
 $B$  = long-range Hamaker constant  
 $E$  = Young's modulus  
 $I = wt^3/12$  = beam's moment of inertia  
 $K$  = kurtosis  
 $N_{EC}$  = Elastocapillary number used for the elastocapillary bound ( $N_{EC} > 1$ )  
 $N_P$  = Peel number used for determining the peeling condition ( $N_P > 1$ )  
 $Sk$  = skew  
 $V$  = Voltage  
 $W = \gamma_s$  = work of adhesion per unit area (also called adhesion energy)  
 $d$  = grating pitch or periodicity  
 $f_{res}$  = resonance frequency  
 $h$  = silicon oxide spacer, also initial air gap between bottom microbeam and substrate  
 $l$  = beam length  
 $s$  = stress force (+ve is tensile)  
 $t$  = thickness of microbeam  
 $w$  = beam width  
 $z$  = beam displacement  
 $\epsilon_{nit}$  = relative permittivity of silicon nitride  
 $\epsilon_o$  = permittivity of air  
 $\gamma$  = liquid surface tension,  
 $\gamma_s = W$  = adhesion energy per unit area (also called work of adhesion)  
 $\eta_{ar}$  = percentage area reduction factor  
 $\theta_c = \theta_1 = \theta_2$  = liquid contact angle with solids 1 and 2  
 $\rho$  = mass density (Chapter 3) or surface charge density (Chapter 4)

**$\sigma$  = tensile stress, also**

**$\sigma^2$  = RMS surface roughness as a variance in surface height**

**AFM = atomic force microscope**

**BOE = buffered oxide etch**

**CIS = Stanford University's Center for Integrated Systems**

**DMD = Texas Instruments' Digital Mirror Device**

**GLV = grating light valve**

**MEMS = microelectromechanical systems**

**RIE = reactive ion etch**

**SIMOD = silicon modulator**

**TI = Texas Instruments**

## Appendix B

### Sample CIS Process Sheet for the Staggered Support Structures

#### SCRIBE

Take L-Test wafers.  
Scribe from H1-H25.  
L-Test is 100-p-type with low resistivity (10-20).

#### WBNONMETAL: ORGANIC CLEAN

H<sub>2</sub>SO<sub>4</sub>/H<sub>2</sub>O<sub>2</sub> (9:1) for 20 mins.  
Dump/Rinse in DI water 6x.

#### WBDIFF: DIFFUSION CLEAN FOR OXIDATION

H<sub>2</sub>SO<sub>4</sub>/H<sub>2</sub>O<sub>2</sub> (4:1) for 10 mins.  
Buffered Oxide Etch (50:1) for 30 secs.  
H<sub>2</sub>O/H<sub>2</sub>O<sub>2</sub>/HCl (5:1:1) for 10 mins.

#### TYLAN: THERMAL OXIDATION

tvar = 00:14:10 mins (actual wet deposition time)  
target thickness = 1325 Å

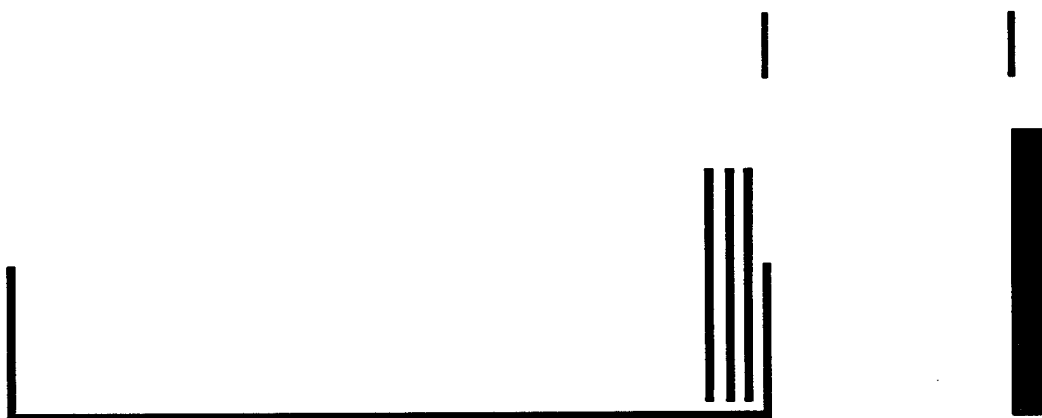
Use WET1000 in tyland

T = 1000 C  
gas flow: dry oxidation: O<sub>2</sub> = 2500 sccm  
wet oxidation: H<sub>2</sub> = 1500 sccm  
O<sub>2</sub> = 1000 sccm

dry oxidation:  $O_2 = 2500$  sccm  
 (a 10 min dry oxidation step preceeds and follows the wet oxidation step of tvar  
 duration)

time in = \_\_\_\_\_ time out = time in + 2 hours = \_\_\_\_\_

Mark order and positions of wafers in the boat below:



### **NANOSPEC: INSPECTION OXIDE THICKNESSES**

(use index n from ellipsometer measurement above for  $SiO_2$  - about 1.45)

Wafer	Thickness	Wafer	Thickness

### **WBDIFF: DIFFUSION CLEAN FOR POLYSILICON DEPOSITION**

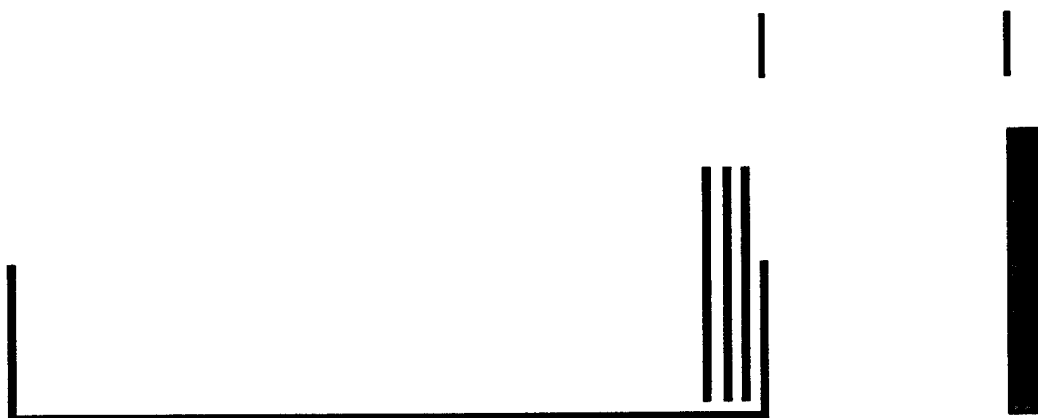
$H_2SO_4/H_2O_2$  (4:1) for 10 mins.

$H_2O/H_2O_2/HCl$  (5:1:1) for 10 mins.

Buffered Oxide Etch (50:1) for 30 secs.





**TYLAN: 850 ANNEAL****tvar = 02:00:00****Use 850AN in tytan4****T = 850°C****WBDIFF: DIFFUSION CLEAN FOR NITRIDE DEPOSITION****H<sub>2</sub>SO<sub>4</sub>/H<sub>2</sub>O<sub>2</sub> (4:1) for 10 mins.****H<sub>2</sub>O/H<sub>2</sub>O<sub>2</sub>/HCl (5:1:1) for 10 mins.****Buffered Oxide Etch (50:1) for 30 secs.****Spin dry.****TYLAN 10: NITRIDE DEPOSITION (LPCVD furnaces)****tvar = 00:19:00****target thickness = 825 Å.****Use SIN1.0 on tytan 10****T = 785C****gas: NH<sub>3</sub> = 100 sccm****DCS (dichlorosilane) = 100 sccm****Include dummy wafers for stress and thickness measurements.****Mark position and order of the wafers in the boat.****Distribute the dummy wafers evenly.****ELLIPSOMETER MEASUREMENT OF NITRIDE**

wafers	tox/nf @ ctr	top	bottom	left	right

--	--	--	--	--	--

Remove wafer(s) \_\_\_\_\_ for composite layer stress measurements.

**SVGCOAT: RESIST COAT.**

Program #1 in both stages.

(Dehydration bake, HMDS, spin PR, prebake)

**ULTRATECH: PATTERN NITRIDE GRATINGS**

Ultratech stepper.

Paco Sandejas Disk. Program: mix.2 (for a mix of colorbar arrays 15, 20, and 25 micron-long bridges and 6 micron long cantilevers).

COLORBAR2 #1 Mask. 1.0 micron lines, 1.0 micron spaces, die 5 x13 mm<sup>2</sup>.

Use \_\_\_\_\_ as dummy wafers for test matrix (run mode 3) to verify exposure and focus.

Exposure (110 mJ) = \_\_\_\_\_

Focus (0.0  $\mu$ m) = \_\_\_\_\_

**SVGDEV: RESIST DEVELOP**

Program #1 in both stages.

**UV RESIST HARDEN**

UV Expose 4 wafers at a time for 20 minutes each.

Post-bake at 110 C for 1 hr.

Circle wafer when done:

**AMT: PLASMA NITRIDE ETCH.**

in the AMT Loaded in Process #4:

Cryo Pump = Y.

Base Press = Y, 0.20

Warm Vent Y

Hold Pumpdown = N

Warm Step = N

Gas 5 (NF3) = 35 sccm.

Servo Press = Y, 50 mTorr

Servo Bias = Y, -200 V

Max RF = 750 W

time = 4.6 min (for 1325 Å with 10% over-etch at 300 Å/min for B slots in

Columns B, D and F)

AMT Run number = \_\_\_\_\_

Measure etch rate:

Use Nanospec to measure thickness of nitride with the index nf from the Ellipsometer measurement.

K19:

to = \_\_\_\_\_

tf = \_\_\_\_\_ after 1 minute etch

dt1 = \_\_\_\_\_ for 1st minute

K20:

to = \_\_\_\_\_

tf = \_\_\_\_\_ after 2 minute etch

$dt2 = \underline{\hspace{2cm}}$  for 2 minute etch  
 rate after the first minute =  $dt2 - dt1$  take this to be the stable etch rate.  
 time required =  $1 \text{ min} + [(thickness \times 110\%) - dt1]/rate = \underline{\hspace{2cm}}$

Circle wafers when done:

### **DRYTEK2: POLYSILICON ETCH**

In DRYTEK2 all in SLOT #2 one at a time!

Recipe: Polysilicon etch.

Process #2.

RF Actual = 375/20 set to standard settings

Pressure = 150 mTorr

SF6 = 50 set at

C2CLF5 = 50 set at

Coil = standard setting

Cap = standard setting

try: (approx. 2000Å/min after power-up)

Measure etch rate:

Use Nanospec to measure thickness of poly for dummy wafer(s):

$to = \underline{\hspace{2cm}}$   
 $tf = \underline{\hspace{2cm}}$  after 1 minute etch  
 $dt1 = \underline{\hspace{2cm}}$  for 1st minute

$to = \underline{\hspace{2cm}}$   
 $tf = \underline{\hspace{2cm}}$  after 2 minutes  
 $dt2 = \underline{\hspace{2cm}}$  for 2 minute etch

etch rate =  $dt2 - dt1 = \underline{\hspace{2cm}}$

time required =  $1 \text{ min} + [(thickness \times 110\%) - dt1]/rate = \underline{\hspace{2cm}}$

### **DRYTEK2 POLYMER CLEAN-UP**

In the Drytek 2 machine.

Process #1

O2 = 100 sccm in channel 4.

Pressure = 150 mtorr.

RF Power = 500 W.

Matching network: Coil = 328 and Cap = 850.

time = 2:30

Circle wafers when done:

### **RESIST STRIP/ORGANIC CLEAN**

### **POLYSILICON WET ETCH (KOH)**

Etch rate = 1000Å/min. (@50°C)

Etch in KOH (50°C) for 1 min.

dump rinse H2O 6 times.

spin dry.  
remove wafer \_\_\_\_\_ for SEM.

**TYLAN 11: LOW TEMP OXIDE DEPOSITION**

Target Thickness = 500A

tvar = 00:02:30

Recipe = LTO400

Deposition Rate = 212A/min

Time in = \_\_\_\_\_ Time out = Time in + tvar + 65:30' = \_\_\_\_\_

Mark the positions and order of wafers in the boat below. For this run J17, K13  
and K18 are the measurement wafers, so distribute them in the front, middle  
and back.

Flats down.

Dummy wafer = \_\_\_\_\_

**SVGCOAT: RESIST COAT.**

Program #1 in both stages.

(Dehydration bake, HMDS, spin PR, prebake)

**ULTRATECH: PATTERN CHECKERBOARD MASK FOR KOH ETCH**

Ultratech stepper.

Ishida Disk. Program: (the one corresponding to the 4th reticle)

TERA4 mask..

Use \_\_\_\_\_ as dummy wafers for test matrix (run mode 3) to verify exposure and  
focus.

Exposure (110 mJ) = \_\_\_\_\_

Focus (0.0  $\mu\text{m}$ ) = \_\_\_\_\_

**SVGDEV: RESIST DEVELOP**

Program #1 in both stages.

**WBNONMETAL: BOE6:1 OXIDE ETCH**

Etch away oxide for KOH via holes forming checkerboard oxide mask.

**RESIST STRIP/ORGANIC CLEAN****POLYSILICON WET ETCH (KOH)**

Etch rate = 1000Å/min. (@ 50°C)

Etch in KOH (50°C) for 5,6,7 min.

dump rinse in H<sub>2</sub>O 6 times.

spin dry.

remove wafer \_\_\_\_\_ for SEM.

**BOE 6:1 PARTIAL RELEASE ETCH**

time (1000Å/min for thermal oxide) = \_\_\_\_\_

dump rinse H<sub>2</sub>O 6 times.

spin dry.

Remove wafer(s) \_\_\_\_\_ for SEM.

**BOE 6:1 FINAL RELEASE ETCH**

BOE 6:1 for \_\_\_\_ mins.  
dump rinse H<sub>2</sub>O 6 times.  
spin dry.  
Circle wafers when done:

**INSPECTION OF HARP STRUCTURES**

Look at the shortest stuck bridge in the harp structures in the indicated positions for the following wafers.

wafer #	center	top	bottom	left	right

**EVAPORATE THIN ALUMINUM**

Ginzton Lab.  
target thickness = 250 Å.  
Circle wafers when done: